Technische Universität München

TUM School of Engineering and Design

Predictive Control of Back-to-Back Power Converter for Electrical Machine

Yingjie He

Vollständiger Abdruck der von der TUM School of Engineering and Design der Technischen Universität München zur Erlangung eines

Doktors der Ingenieurwissenschaften

genehmigten Dissertation.

Vorsitz: Prof. Dr.-Ing. Rolf Witzmann
Prüfer der Dissertation:
1. Prof. Dr.-Ing. Dr. h.c. Ralph Kennel
2. Prof. Dr.-Ing. Fengxiang Wang

Die Dissertation wurde am 14.09.2023 bei der Technischen Universität München eingereicht und durch die TUM School of Engineering and Design am 03.05.2024 angenommen.

Acknowledgment

I would like to express my deep gratitude to everyone who has supported me throughout my journey to completing my doctoral project.

First and foremost, I would like to thank Prof. Dr.-Ing. Ralph Kennel for accepting me as a Ph.D. candidate at the Institute for Electrical Drive Systems and Power Electronics at Technische Universität München (TUM). I am extremely grateful for the freedom he gave me to choose my doctoral topic and for his continuous encouragement and guidance throughout my doctoral period. The international atmosphere of the institute has provided me with a great opportunity to learn from different cultures and make friends from different parts of the world.

I would like to express my sincere gratitude to Prof. Dr.-Ing. Fengxiang Wang for his invaluable support and guidance throughout my research journey. He has provided me with constant encouragement, insightful feedback, and invaluable knowledge. I am particularly grateful for the trust he placed in me, which enabled me to take on more responsibility and develop my research skills. His trust in my abilities has been a constant source of motivation for me, and I am grateful for the freedom he gave me to organize certain aspects of the research. I am truly honored to have had the opportunity to work under Prof. Dr.-Ing. Fengxiang Wang's supervision, and I am indebted to him for his contribution to my academic and professional development.

I would like to express my sincere gratitude to my colleagues at EAL who have provided me with unwavering support throughout my academic research and daily life in Germany. In particular, I would like to extend my special thanks to Qing Chen, Haotian Xie, Xiaonan Gao, Wei Tian, and Dehao Kong. Their kindness and generosity have made my time at the institute memorable and enjoyable. Their support has been a source of comfort and inspiration for me, and I am grateful for their friendship.

Last but not least, I would like to express my heartfelt gratitude to my beloved family, especially my wife, Ying Tang, for her understanding, love, and unwavering support throughout my academic journey.

Once again, thank you to everyone who has contributed to my success in completing my graduation thesis.

Munich, Germany in March 2023
Yingjie He

Abstract

This dissertation focuses on the predictive control of back-to-back (BTB) converter for electrical machine systems, and two types of electrical machine are researched, namely, the Permanent Magnet Synchronous Machine (PMSM) and non-PM Switched Reluctance Machine (SRM). PMSM system is researched due to its high torque density and efficiency, and SRM system is also researched in view of its suitability in high-speed and high-temperature applications. The predictive control is generally adopted as an inner loop of the outer proportional-integral (PI) controller to track the power reference, so a DC-link voltage PI controller is always necessary to control the BTB converter-fed PMSM drive in the conventional predictive control strategies. It is a cascaded control structure since the inner predictive control is nested within the outer voltage control loop. For better dynamic response, a modified dynamic reference predictive control (DRPC) strategy with dynamic horizon, a cascade-free method, is proposed. The outer DC-link voltage control loop is removed by specifying the voltage and power references of every instant. Additionally, to further increase the dynamic response, a direct predictive voltage control (DPVC) strategy, which merges the DC-link voltage regulation and power regulation terms into one newly-defined cost function, is proposed. To cope with the mismatch between the actual and nominal parameters, Kalman filter is added to compensate for the steady-state error. Besides, to enhance the dynamic performance and to save the effort of parameter tuning, the weighting factor is further eliminated from the cost function by sorting the terms into two groups and independently evaluating each group in turn. Due to the structural characteristics of SRM, the BTB converter-fed SRM system is researched as well, and a centralized predictive deadbeat power control (P-DBPC) strategy is proposed to simplify the control structure. By building a direct power connection between the front-end VSR and back-end SRM, it fulfils the motor regulation, grid-side power factor correction, and current harmonic restraint simultaneously in one control structure.

Kurzfassung

Diese Dissertation befasst sich mit der prädiktive Regelung von Back-to-Back (BTB) Umrichtern für elektrische Antriebssystem, wobei zwei Arten von elektrischen Maschinen untersucht werden, nämlich die Permanentmagnet-Synchronmaschine (PMSM) und die nicht-permanenterregte Geschaltete Reluktanzmaschine (SRM). Das PMSM-System wird aufgrund seiner hohen Drehmomentdichte und Effizienz erforscht, und das SRM-System wird ebenfalls im Hinblick auf seine Eignung für Anwendungen bei hohen Geschwindigkeiten und hohen Temperaturen untersucht. Überlagert wird dieser von einem PI-Regler, der die Zwischenkreisspannung, durch Regelung des Leistungsflusses, konstant hält. Daher ist dieser PI-Regler bei Verwendung von herkömmlichen prädiktiven Regelungsstrategien für den Betrieb eines PMSM mit BTB-Umrichter stets erforderlich. Für ein schnelleres Ansprechverhalten wird eine modifizierte dynamische prädiktive Referenzregelungsstrategie (DRPC) mit variablem Horizont vorgestellt. Dabei handelt es sich um ein nicht kaskadiertes Regelungsverfahren. Dazu wird der äußere Regelkreis für die Zwischenspannung entfernt und stattdessen eine direkte prädiktive Spannungsregelung (DPVC) implementiert. Angesichts der guten Dynamik und der Möglichkeit verschiedene Einschränkungen zu integrieren, wird die modellprädiktive Regelung herangezogen. Die Regelgrößen Zwischenkreisspannung und Leistung werden gemeinsam in einer Kostenfunktion berücksichtigt. Um die Auswirkungen von Parameterabweichungen zu kompensieren, wird zudem ein Kalman-Filter eingefügt. Außerdem wird zur Verbesserung der Dynamik und um auf Parameteranpassungen verzichten zu können die Kostenfunktion in zwei Teile zerlegt und beide unabhängig voneinander bewertet. Auf diese Weise können die Gewichtungsfaktoren aus der Kostenfunktion eliminiert werden. Um die Regelungsstruktur zu vereinfachen, wird für das BTB-Umrichter gespeiste Hochgeschwindigkeits-SRM-Antriebssystem eine zentralisierte prädiktive Deadbeat-Leistungsregelungsstrategie (P-DBPC) eingeführt. Indem eine direkte Energieübertragung zwischen Front-End-VSR und Back-End-SRM aufgebaut wird, ist es so möglich, die Motorregelung, die netzseitige Leistungsfaktorkorrektur und die Reduzierung der Stromoberschwingungen in einem Regelkreis zu bewältigen.

Contents

CHAPTER 1

Introduction

This dissertation focuses on control techniques for grid-connected Back-to-Back (BTB) power converter-fed electrical machine. The main objective of this work is to develop effective control strategies that can enhance the performance and reliability of the system. In this chapter, the background, research focus, and contribution of this dissertation are introduced. The outline indexed to each of the following chapters have been summarized as well.

1.1 Electrical machine

Induction Machines (IM) and Permanent Magnet Synchronous Machine (PMSM) are the predominant choices for machine drive systems in industrial, residential, commercial, and transportation applications. Fig. 1.1 provides the conventional structure of these machines and compares them with the Switched Reluctance Machine (SRM). All these machines share common elements of a stator, winding, and rotor, but the SRM stands out with its simplified design. For PMSM, magnets are inserted in the rotor to provide rotor excitation. For IM, the rotor bars are designed to generate magnetic induction and produce torque on the rotor. In contrast, the SRM does not utilize permanent magnets or conductors on the rotor.

1.1.1 Induction machine

IM is widely used in many different applications. There are primarily two types of IMs. In wound-rotor IMs, the rotor circuit is made up of three-phase windings. The rotor windings are then short circuited by slip rings. In squirrel-cage IMs, the rotor bars are inserted by die casting, where melted aluminum is molded in the rotor slots. End rings then short circuit the bars. IM, also known as asynchronous machine, operates based on the relative motion between the rotating magnetic field of the stator and the rotor. When IM is not at the synchronous speed, a relative speed difference occurs between the rotating magnetic field of stator and rotor.

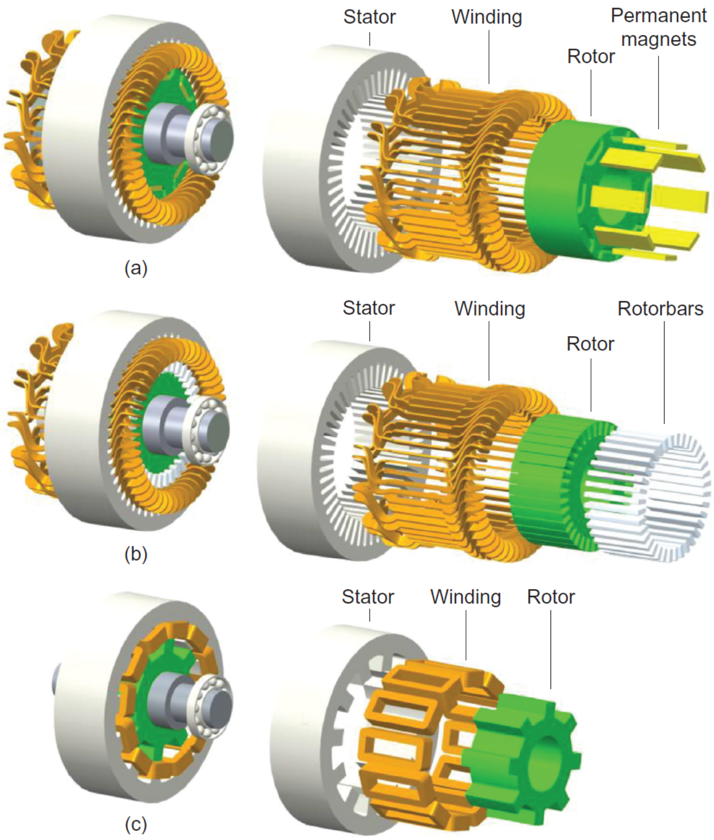

Figure 1.1: Typical structure of electric machine types [1]. (a) Interior PMSM. (b) IM. (c) SRM.

This speed difference is called "slip", denoted as a percentage of the synchronous speed. The presence of slip make the magnetic field of the stator move at a different speed than that of the rotor. As a result, the rotor conductors experience a time-changing magnetic field. This time-varying magnetic field induces a voltage across the rotor bars or windings. The magnitude of this induced voltage depends on the rate of change of the magnetic field and the number of turns in the rotor winding. Since the rotor conductors are short-circuited by the end rings (in the case of squirrel-cage IMs), this induced voltage causes current to circulate in closed loops within the rotor circuit. This circulating current creates its own magnetic field in the rotor, known as the "rotor magnetic field". The stator's rotating magnetic field induces a current in the rotor, resulting in the creation of the rotor magnetic field. The interaction between these two magnetic fields causes a force that produces mechanical torque on the rotor. This torque causes the rotor to rotate and follow the rotating magnetic field of the stator, albeit at a slower speed due to the slip. Due to induced currents on the rotor conductors, there are non-negligible rotor copper losses in IM. These losses can become significant, particularly in high-torque and high-power-density applications. The main challenge posed by rotor copper losses is the efficient extraction of heat from the machine to prevent overheating and maintain optimal performance.

1.1.2 Permanent magnet synchronous machine

Maintaining a strong magnetic field in the air gap is crucial for generating higher torque and, consequently, achieving higher torque density in an electrical machine. The permanent magnets on the rotor of PMSM, which serve as an independent source of magnetic field, play a significant role in this aspect. Depending on the material used for the permanent magnets, they can produce a powerful magnetic field in the air gap without the need for coils on the rotor. This characteristic enables less copper losses within the rotor, leading to a higher overall efficiency for PMSM, than other types of machines that rely on electromagnetic excitation. This efficiency advantage makes PMSM particularly well-suited for various high-performance applications where energy conservation and optimal performance are crucial. In interior PMSM, these magnets are embedded within the rotor. A well-thought-out design for the layout of the permanent magnets can take full advantage of the reluctance torque, resulting in improved output torque at higher speeds. In residential and commercial applications, surface PMSM is commonly employed, and the permanent magnets are positioned on the surface of the rotor, which will not cause the difference between d-axis inductance and q-axis inductance.

PMSM achieves high torque density and efficiency by using high-energy rare-earth magnets like Neodymium Iron Boron and Samarium Cobalt. However, the use of these magnets comes with several disadvantages. Firstly, their sensitivity to temperature limits the machine's operation in high-temperature environments. When the temperature of the NdFeB magnet reaches around 160°C, the output torque can drop significantly, up to 46% [2]. Secondly, permanent magnets contribute to a substantial portion of the total cost of a PMSM, even though they represent only a small fraction of the machine's total weight. For example, in an 80 kW interior PMSM designed for a traction application, the rotor magnets may account for only 3% of the mass but a significant 53% of the total cost for that specific application [1]. The high cost of permanent magnets poses a significant challenge in terms of machine affordability and accessibility. Additionally, there are supply chain issues with rare-earth elements, leading to fluctuations in their prices from time to time. These fluctuations can significantly impact the overall cost of PMSMs and may lead to uncertainties in production costs. Considering these drawbacks, there is a need to explore other machines that do not rely on permanent magnets and offer a simple construction in order to meet the demands of high-speed and high-temperature operations.

1.1.3 Switched reluctance machine

The SRM has a simple, cost-effective, and robust construction. Its stator is salient pole structure with the concentrated windings, while the rotor is a salient pole structure without windings or permanent magnets. These unique stator and rotor designs make the SRM highly suitable for high-speed applications. In contrast, the high-speed applications of PMSM is significantly hindered by rotor displacement and rotational stress. When the rotor operates at high speeds, centrifugal forces of PMSM become predominant, subjecting the magnet slots and bridges (the sections between the magnet slot and the air gap in the rotor core) to considerable stress. Careful design for rotor is essential to withstand the centrifugal forces and prevent flux leakage. Due to the simple rotor structure, the SRM circumvents these limitations, making it an excellent choice for high-speed operations. Its robust construction allows it to handle the demands of such applications without the added complexities associated with permanent magnets or windings on the rotor. Besides, SRM offers superior suitability for operation in high-temperature conditions compared to PMSM. In PMSM, the magnetic properties of permanent magnets, such as NdFeB magnets, are highly sensitive to temperature changes. As the temperature increases, the flux density and coercivity of the magnets decrease, directly impacting the output torque and leading to potential demagnetization issues. To address this, PMSM using NdFeB magnets are usually designed to maintain the magnet temperature around 100°C during continuous operation. In contrast, the rotor of SRM constructed just with laminated steel can withstand temperatures in the range of 200°C–400°C. This robust thermal tolerance makes SRM particularly well-suited for high-temperature applications.

1.2 Configuration of BTB converter-fed electrical machine system

The BTB converter-fed electrical machine system shown in Fig. 1.2 is a popular configuration, which can be used to transfer the energy from grid side into electrical machine for motor driving or can be used to transfer the energy generated by the electrical machine into grid side. This configuration offers several advantages, including higher efficiency, improved power quality, and better control of power flow. In this system, the converter connected to the grid is called the Grid-side Converter (GSC), and the converter connected to electrical machine called the Machine-side Converter (MSC).

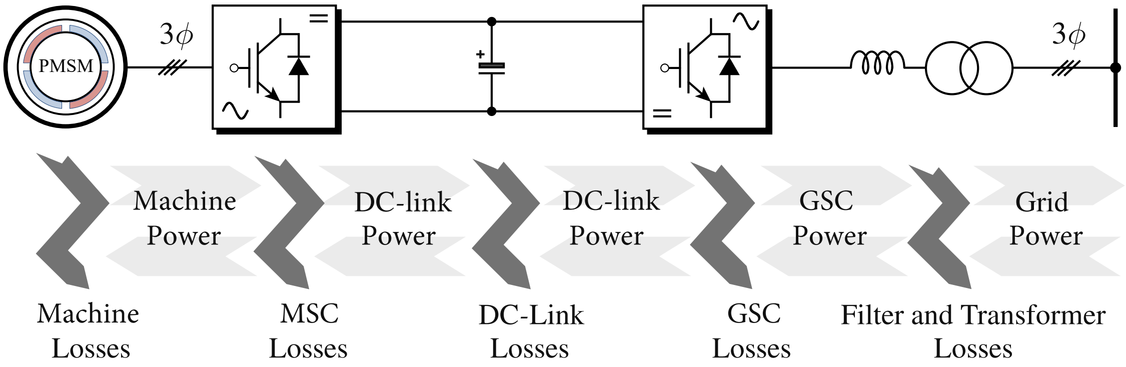

Figure 1.2: Sankey diagram for power flow in BTB converter-fed electrical machine system.

With specific power conversion stages and losses between the stages, the Sankey diagram in Fig. 1.2 shows the power flow in grid-connected BTB converters-fed electrical drive system [3]. For the generation application, power flows in the way from the electrical machine to the three-phase grid, and in the reverse direction for the motor drive application. However, losses occur during power conversion and transmission. These losses include electrical machine losses, MSC losses, DC link losses, GSC losses, filter losses, and transformer losses.

Electrical Machine losses are caused by internal resistance, hysteresis loss, and eddy currents in the machine, as well as the other losses in the bearings, mechanical components, etc. These losses can also be significant, especially in high-power applications, and can affect the overall system efficiency.

MSC losses are caused by the switching losses and conduction losses consumed during the voltage conversion from AC to DC (in generation application) or from DC to AC (in motor drive application). These losses can be minimized by using high-efficiency MSC, such as the MSC with Gallium Nitride (GaN) power module or Silicon Carbide (SiC) power module, but these losses still represent a significant source of power conversion losses in the BTB converter-fed electrical machine system.

DC link losses are caused by the resistance and capacitance of the DC link used to connect the MSC and GSC. These losses can be minimized by using low-resistance and high-capacity DC links.

GSC losses are caused by the switching losses and conduction losses used to convert the DC output of the DC link back to AC for connection to the grid. Similar to MSC, GSC can realized high efficiency by adopting the GaN power model or SiC power model for converter construction.

Filter and transformer losses are caused by the resistance and impedance of the filters and transformers used to smooth and regulate the AC voltage at grid side. These losses can be minimized by using high-quality filters and transformers.

In high-power applications, these losses can be significant and can reduce the overall system efficiency. However, with careful design and selection of components, it is possible to achieve high conversion efficiencies in a BTB converter-based electrical machine system.

1.2.1 BTB converter-fed PMSM system

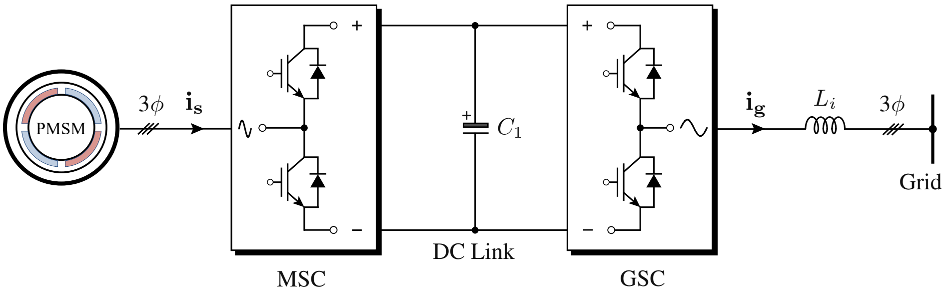

Figure 1.3: Drive topology of a two-level BTB converter-fed PMSM system.

Fig. 1.3 presents the drive topology of a BTB converter-fed PMSM system for low-voltage operation [4]. The MSC of this system is a two-level Voltage-Source Rectifier (VSR), which converts an AC input into a DC output, and the GSC is a two-level Voltage-Source Inverter (VSI), which converts a DC input into an AC output [5,6]. These two Voltage-Source Converters (VSCs) are connected through a DC-link capacitor C_1. The VSR converts the variable voltage and frequency output from the PMSM into DC, while the VSI inverts this DC into fixed voltage and frequency suitable for grid connection. Both VSR and VSI are constructed and assembled similarly, producing two-level voltage waveforms with two Insulated Gate Bipolar Transistors (IGBTs) per phase. The VSI should be operated in a way which balances the switching losses and Total Harmonic Distortion (THD) of grid current. Typically, this topology is used for power ratings up to 750 kW. It provides an effective way to convert the variable output from PMSM into fixed voltage and frequency suitable for grid. To increase power ratings, multiple BTB converters can be connected in parallel [7].

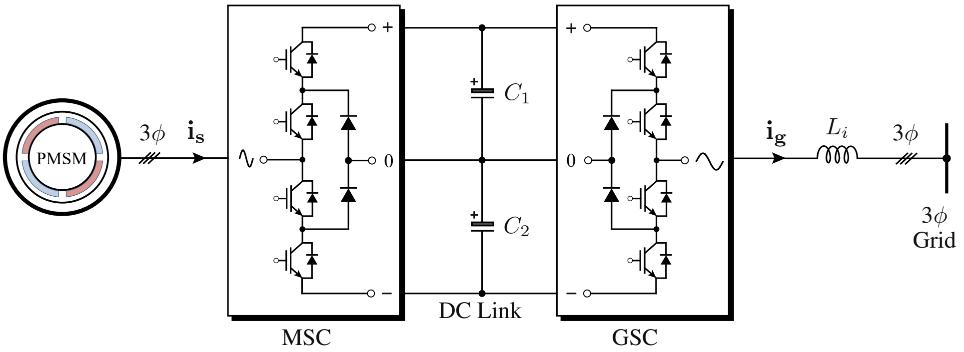

Figure 1.4: Drive topology of a three-level BTB converter-fed PMSM system

Fig. 1.4 presents the drive topology of a BTB converter-fed PMSM system for medium-voltage operation [8–10]. The MSC of this system is a three-level Neutral-Point-Clamped (NPC) VSR, and the GSC is a three-level NPC VSI. The three-level VSCs have several advantages such as low dv/dt, minimal electromagnetic interference, and high power quality [11]. The NPC converter is connected to the MV grid through an L or LCL filter. Fast-recovery diodes serve as clamping devices [12]. The voltage rating of semiconductor switches and diodes is half the net DC-bus voltage when DC-link capacitors share voltage evenly. However, switching operations of rectifier and inverter can cause DC-link capacitor voltage to drift, resulting in an imbalance in capacitor voltage, and this issue is addressed through employing digital control schemes. Typically, the BTB NPC converters have power ratings of 6.0 MW and operational voltages of 3-4 kV in practical applications [13].

1.2.2 BTB converter-fed SRM system

Due to the structural characteristics of SRM described in 1.1.3, the BTB converter-fed SRM system is also researched considering its suitability in high-speed applications. Fig. 1.5 presents the drive topology of a BTB converter-fed SRM system. For motor mode, the GSC of this system is a two-level VSC which converters the grid-side AC voltage with fixed frequency into a stable DC-link voltage, and the MSC is a SRM converter which switches the DC-link voltage to energize the winding in the correct position region. The front-end GSC and back-end MSC are connected through a DC-link capacitor C_1. As can be seen from the topologies, same VSC can be used as GSC for the BTB converter-fed SRM system and BTB converter-fed PMSM system. However, a DC/DC power converter topology should be adopted as the MSC for SRM system due to the operational principle of SRM, while a AC/DC power converter should be adopted as the MSC for PMSM system.

In order to produce a continuous torque in SRM, it is essential to conduct the winding of each phase sequentially to let the stator magnetic field rotate continuously in the air gap. To achieve this, a DC/DC power converter is necessary to accurately switch the phase current on and off. The Asymmetrical Half-Bridge (ASHB) converter is a commonly used DC/DC power converter for SRMs due to its control flexibility. Fig. 1.6 shows the circuit diagram of the

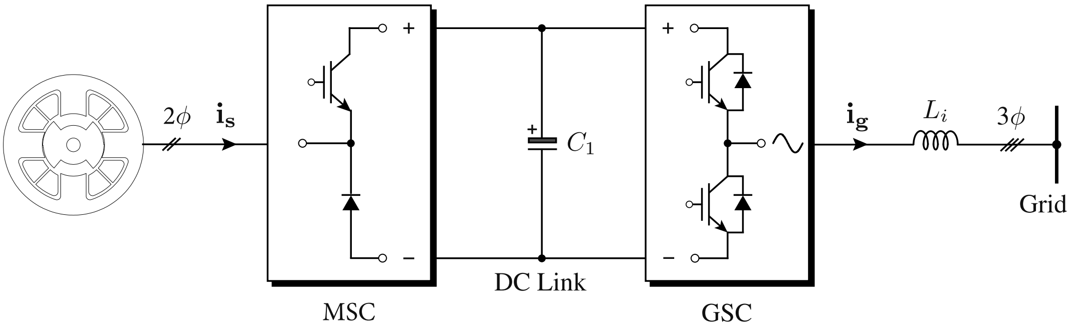

Figure 1.5: Drive topology of a BTB converter-fed SRM system.

ASHB converter designed for a two-phase SRM, comprising four power switches and four diodes. In the magnetization mode, the ASHB converter applies the full DC-link voltage to the winding by turning on the power switches S_1 and S_2, as depicted by the red path. This leads to a significant increase in winding current, particularly when the rotor is at an unaligned angle. In the demagnetization mode, S_1 and S_2 are switched off simultaneously, following the blue path. In this state, the energy stored in the phase causes diodes D_1 and D_2 to become forward biased, resulting in a negative DC-link voltage being applied to the phase winding. The winding current continues to flow through the diodes, returning to the DC link until it reaches zero. The freewheeling mode involves only one pair of switches and diodes being on, as shown by the yellow path. The phase winding is disconnected from the DC link, preventing energy from flowing back to it. Since the voltage across the phase terminals is zero and the phase is shorted, the current only encounters the winding resistance, leading to a relatively slower rate of decrease compared to the demagnetization mode with a negative DC-link voltage. It can be seen from above that the ASHB converter enables unidirectional current flow in the machine winding, and each phase's winding current can be electrically isolated from one another in this type of converter. Therefore, to create a multi-phase SRM, duplicating the single-phase ASHB topology on the DC link can be implemented.

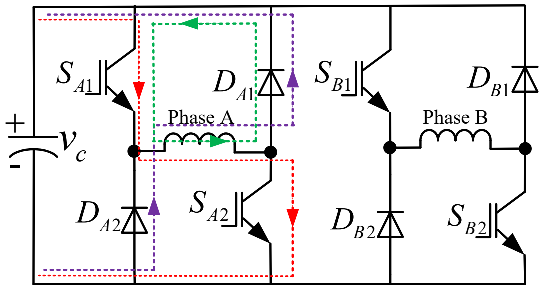

Figure 1.6: Conduction modes of ASHB converter.

1.3 Control techniques

Several commonly-used control techniques for BTB converter-fed electrical machine systems is described here, and the choosing of an appropriate control technique depends on the specific application and requirements of the system.

1.3.1 Hysteresis control

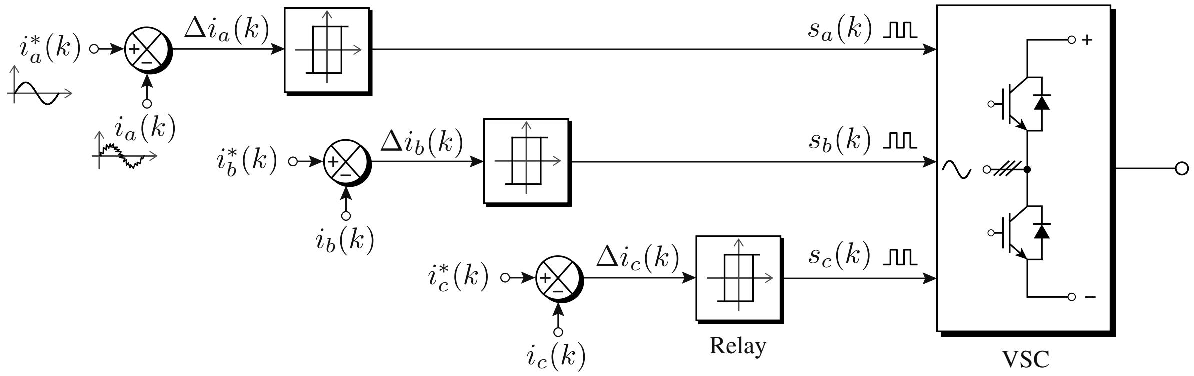

Figure 1.7: Hysteresis current control.

The hysteresis control scheme illustrated in Fig. 1.7 [14] is a widely used method for regulating three-phase load currents in power electronic systems [15, 16]. This nonlinear control technique compares the measured load currents (i_a, i_b, and i_c) with their corresponding reference currents (i_a^*, i_b^*, and i_c^*), and then feeds the error signals (Δi_a, Δi_b, and Δi_c) to the hysteresis comparators or bang-bang controllers.

Each relay in the scheme generates the switching signals to ensure that the load currents remain within the upper and lower limits defined by hysteresis bandwidth. The hysteresis bandwidth determines the range within which the load currents can vary without triggering a change in the switching signals. If the load currents exceed the upper or lower limits, the relays switch the output signal, turning on or off the switching device, thus regulating the load currents.

Hysteresis control is a straightforward and robust control technique that requires minimal computation and is not sensitive to parameter variations and disturbances. However, it is prone to chattering, a phenomenon where the switching signals rapidly alternate near the upper and lower limits of the hysteresis bandwidth. Chattering can result in unwanted noise and vibration, which can negatively impact the system's performance and reliability.

1.3.2 Field/voltage oriented control

This subsection discusses two common control strategies used in electric machines for achieving independent control of torque and flux or active and reactive power: Field-oriented Control (FOC) [17] for MSC and Voltage-Oriented Control (VOC) [18] for GSC, both with modulators.

FOC is commonly employed in AC machines such as IM and PMSM. It involves separating the stator current into two components: one component aligned with the rotor flux vector and the other orthogonal to it. These two components are then independently controlled using a current controller. On the other hand, VOC is commonly used in grid-connected converters. It involves separating the grid-side current into two components: one component aligned with the grid voltage vector and the other is orthogonal to it. Similar to FOC, these two components are independently controlled using a current controller. Both FOC and VOC have the advantage of decoupling the highly coupled and nonlinear control target, making them easier to control. This feature allows for precise control performance, making it more efficient and effective in its applications.

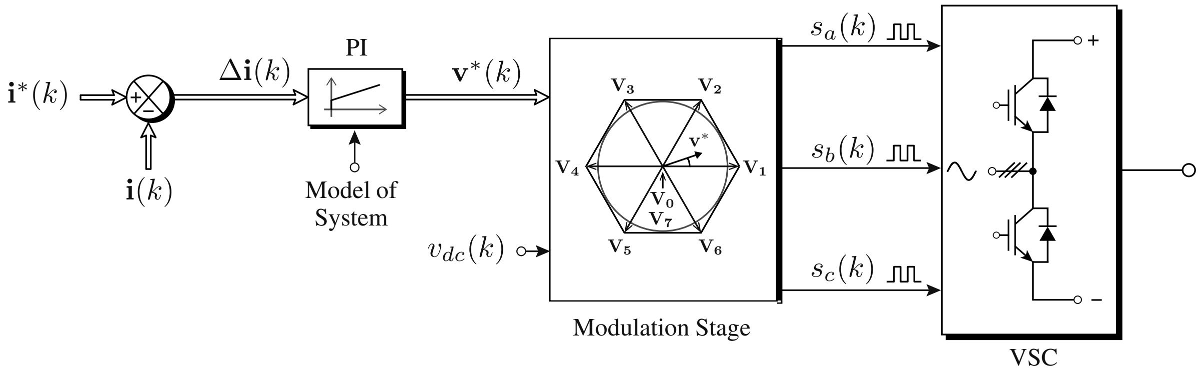

Figure 1.8: FOC scheme using PI regulator and modulator.

Fig. 1.8 [14] illustrates a linear current control scheme that employs a PI regulator and modulation stage. The control scheme involves comparing the measured load currents $\mathbf{i}(k)$ with the reference currents $\mathbf{i}^*(k)$ and sending the current error $\Delta\mathbf{i}(k)$ to the PI controller. The PI controller then processes the current error and generates reference voltage $\mathrm{v}^*(k)$ for the modulation stage. For Sinusoidal Pulse Width Modulation (SPWM) method, the modulation stage consists of a carrier waveform, DC-link voltage v_{dc}, reference frame transformation, comparators, and switching logic. The gating signals generated by the modulation stage are used to control the VSC, with the SVM modulation scheme being the most commonly used. The linear control scheme with SVM operates at a fixed switching frequency determined by the carrier frequency. The performance of FOC scheme depends heavily on the PI controller parameters and the modulation type used. Proper tuning of the PI controller is essential to ensure stable and accurate control of the converter, and the choice of modulation scheme affects the converter's efficiency and harmonic distortion.

A common method combines VOC and FOC for controlling a BTB converter-fed PMSM system can achieve good steady-state performance. However, this approach has some limitations, including:

1) Limited bandwidth: The cascaded structure used in this approach can limit the bandwidth of the control system, resulting in slower response times and reduced dynamic performance.

2) Modulator: The modulator used in this method is typically based on the time-averaged principle, which can be complex to design, particularly for multilevel power converters. Moreover, at low switching frequencies, the modulator can cause problems due to the limited resolution of the time-averaging process.

Despite these challenges, the combination of VOC and FOC is still widely used for controlling BTB converter-fed PMSM systems due to its effectiveness in achieving good steady-state performance. However, researchers are continually developing new control techniques and modulators to overcome these limitations and improve the dynamic response of the system.

1.3.3 Direct torque/power control

Unlike other control techniques that use modulators, Direct Torque Control (DTC) [19] and Direct Power Control (DPC) [20] directly manipulate the switching states of the power electronic converters using an offline-designed switching table.

DTC does not require a synchronous coordinate transformation like vector-oriented control, instead, it uses hysteresis controllers to replace linear PI controllers. This results in a larger bandwidth for the inner control loop, providing faster torque response. DPC, derived from DTC using the instantaneous power theory, does not require a coordinate transformation or inner PI control loops. Instead, it uses a hysteresis controller and the grid voltage vector location to select the switching sequence based on the instantaneous active and reactive power errors.

While DTC and DPC have their benefits, they also have their limitations. One disadvantage is the requirement for an offline-designed switching table, which can be challenging to design and implement, especially for multilevel power converters. Additionally, variable switching frequency and control variable ripple can affect the filter design and require a higher sampling frequency to achieve comparable steady-state performance. The use of hysteresis controllers instead of linear PI controllers can also result in some loss of precision in control, especially in the presence of disturbances. Moreover, the method may not be suitable for applications that require flexibility in the control algorithm since the switching table is designed offline and may not be easily modified or adapted to changes in the system or control requirements.

1.3.4 Sliding mode control

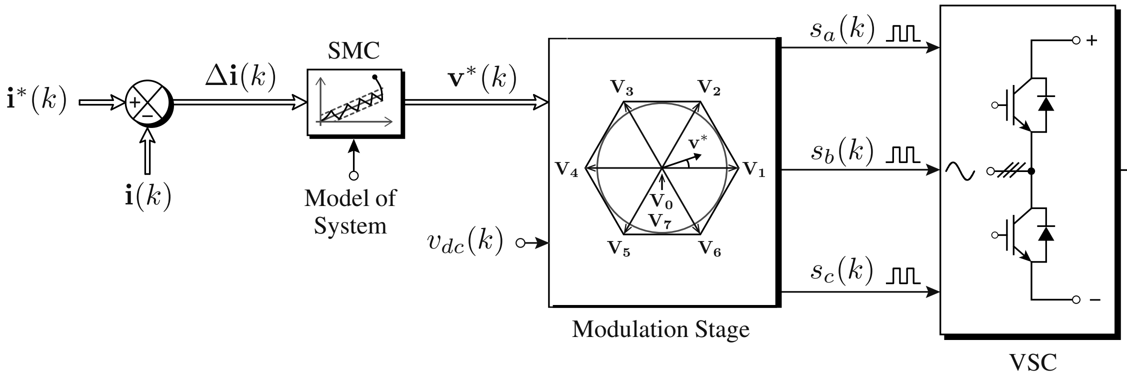

Figure 1.9: Block diagram of SMC with a modulator.

The block diagram of Sliding Mode Control (SMC) with a modulation stage for the load current of a VSC [21] is shown in Fig. 1.9. SMC is a digital control technique that belongs to the family of variable structure control and adaptive control, and it is a discrete and nonlinear control method. It is widely used in power electronic systems due to its ability to handle the nonlinearity of power converters.

SMC replaces the traditional PI controller in linear control and requires the converter model and system parameters. The current errors are processed by SMC, which generates the load voltage references $\mathbf{v}^*$ to force the control variable (load current) to track or slide along the predefined trajectory. The structure of the controller is intentionally changed according to a preset structure control law to achieve a robust and stable response during system parameter variations and load disturbances.

However, SMC has some disadvantages and limitations:

1) Chattering: SMC can suffer from chattering, which is a phenomenon where the control output rapidly switches between two values. This can lead to high-frequency noise and mechanical stress in the system. Chattering can be reduced by selecting appropriate control parameters, but this can be challenging.

2) Complexity: SMC requires complex mathematical modeling, and designing the control law can be difficult. In some cases, it may not be possible to design a satisfactory control law that meets all system requirements.

3) Sensitivity to parameter variations: SMC can be sensitive to variations in system parameters, such as load and converter parameters. These variations can lead to instability and degraded performance of the control system.

1.3.5 Model predictive control

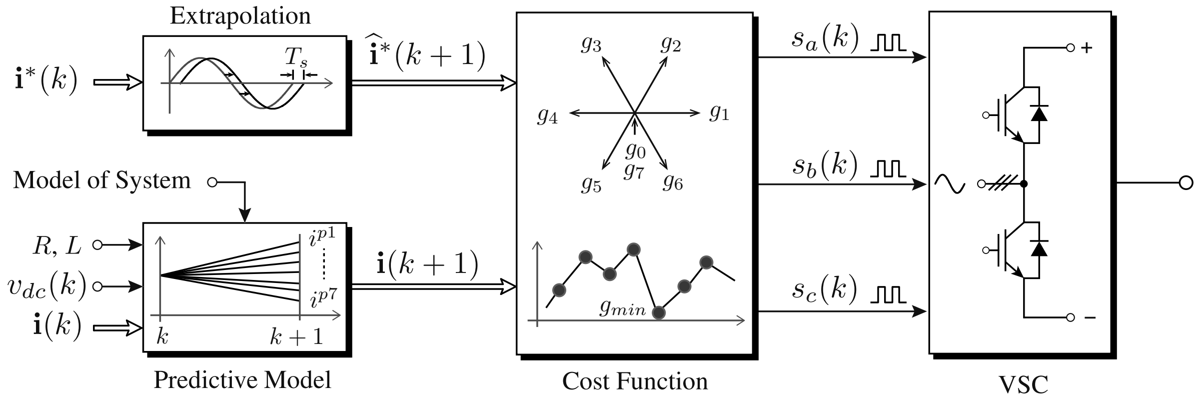

Figure 1.10: Block diagram of FCS-MPC for regulating load currents.

The Finite Control-Set Model Predictive Control (FCS-MPC) shown in Fig. 1.10 [22], is a control technique that can effectively manage power converters without the use of linear PI regulators and a modulation stage. Unlike traditional linear control techniques, FCS-MPC takes advantage of the discrete nature of power converters to evaluate the effect of each possible switching state on the concerned variables in a predefined criterion and selects the optimal one that can minimize the differences between the concerned variables and their references. Its main advantages are listed as blew: 1) The concept of FCS-MPC is very simple and intuitive. 2) FCS-MPC allows one to address multi-control objectives via the cost function. Thus, unlike PI-type controllers, MPC is a multi-variable control method that is ideally suited for multiple-input and multiple-output systems. 3) FCS-MPC allows flexible integration of various hard constraints and actuation constraints, e.g., the hard constraints of power limitation for system protection and actuation constraints of switching frequency minimization for switching loss reduction.

The FCS-MPC technique is composed of several parts, including the reference generator, prediction model, cost function, and switching signal generator. This control method is made up of the following steps:

1) Extrapolate the reference currents from $(k)^{\text{th}}$ to $(k+1)^{\text{th}}$ control period. 2) Predict future currents based on predictive model. 3) Evaluate cost function and generate gating signals.

The prediction model is utilized to forecast future current values. Because there are a finite number of switching states, these values can be enumerated for all possible switching states. Following that, the predicted load currents are assessed using a cost function defined as the absolute error between the reference and predicted currents:

$$J(k) = |\boldsymbol{y}^*(k+1) - \boldsymbol{y}(k+1)|^2 . \tag{1.1}$$

where $\boldsymbol{y}^*$ is the extrapolated reference command, and $\boldsymbol{y}$ is the predicted value of the control variable, and both of them correspond to the $k+1$ control period.

1.3.6 Comparison of different control techniques

Table 1.1: Summary of main features of different control techniques

	Hysteresis	FOC/VOC	DTC/DPC	SMC	FCS-MPC
Control Complexity	Low	Medium	Low	High	Low-Medium
Model & Parameters	Not Needed	Needed	Not Needed	Needed	Needed
Prior Knowledge	Not Needed	Not Needed	Not Needed	Not Needed	Not Needed
Modulation Stage	Not Needed	Needed	Not Needed	Needed	Not Needed
Constraint Inclusion	Not Possible	Not Possible	Not Possible	Possible	Possible
Dynamic Response	Excellent	Average	Excellent	Good	Excellent
Switching Frequency	Variable (Uncontrollable)	Fixed	Variable	Fixed	Variable (Controllable)

Table 1.1 presents a comparison of different control techniques . Traditional control strategies, such as hysteresis and FOC/VOC, are widely used in the power electronics industry. However, advanced control techniques, such as SMC and FCS-MPC, have gained significant attention in recent years due to their superior performance. FOC/VOC is expected to be implemented with compensating terms and space vector modulation. Hysteresis control is a basic control strategy that does not require a system model and parameters, making them simpler to use. However, SMC and FCS-MPC require more powerful microprocessors and intricate computations. Although SMC and FCS-MPC can both incorporate constraints into the controller architecture, FCS-MPC is more adaptable and easier to use. Hysteresis control and FCS-MPC operate without a modulator, resulting in better dynamic responses. However, hysteresis and FCS-MPC methods have variable switching frequencies. To regulate switching frequency, the FCS-MPC cost function can be penalized. The selection of a control technique depends on the application, as well as the trade-offs between precision, flexibility, and implementation complexity.

1.4 Research status and contributions

Many researches have been developed to enhance the performance of the BTB converter-fed PMSM system. One research interest focuses on improving system performance when abnormal conditions, e.g., unbalanced and distorted grid voltage, happen in grid [23, 24]. One research interest focuses on open-switch fault diagnosis, namely, locating the faulty switches of power converter [25]. One research interest focuses on fault-tolerant control, which aims to fulfill post-fault operation once open-switch fault arises in power module [26,27]. One research interest focuses on realizing high-performance control under balanced grid condition [28, 29]. For high-performance control strategy, the double closed-loop control based on PI controller is a conventionally adopted strategy [30]. However, the response time is limited due to the nested control structure. To improve the dynamics, DTC/DPC selecting the optimal vector from a pre-defined switching table is developed to replace the inner PI controller. In [31], newly-defined switching tables are developed and the absolute errors of reactive power, stator flux, and electromagnetic torque are used to specify the priority to control MSC and GSC.

Due to the fast dynamic response and flexible integration of various constraints, MPC is also a good candidate to realize the tracking of references [32]. In [33], a MPC with multi-vector modulation and fixed switching frequency is developed, which allows the adjustment of dynamic response time and overmodulation. In [34], the new direct model predictive flux and power control are developed in combination with the direct torque and power control to narrow the range of vector selection. In [35], the predictive current control is applied to both GSC and MSC, and the redundant switching states are fully evaluated in the cost function to achieve the neutral-point balance on DC link. However, most MPCs in literature are generally developed as an inner controller to cooperate with the outer PI controller, thereby forming the conventional PI controller-based model predictive control (PI-MPC). It is a cascaded structure since the inner MPC is nested within the outer PI control loop [36]. To further improve the dynamic response, a cascade-free algorithm without the outer speed PI controller is developed in [37]. A new cost function, which consists of the errors between references and predictive variables in an intuitive manner, is designed for vector evaluation, and a torque suppression coefficient is introduced into the cost function to avoid overshoots in transient state. However, the load torque observer is essential for speed prediction. In [38], a cost function constructed by a steady-state term and a transient term is developed to get rid of the cascade control structure, but five weighting factors are required due to the complex cost function, which undoubtedly complicates the algorithm. In [39], a dynamic references concept is developed to define the temporary references of every instant in the cost function, thus removing the outer PI controller. This idea is further developed into the neutral-point-clamped converter and BTB power converter in [40] and [41], respectively. In [41], the trajectory of the temporary DC-link voltage references is specially designated, and the temporary active power references involved in the cost function are estimated correspondingly by adding the load power and capacitor power together. Thus, the final DC-link voltage reference is reached by following the renewed references at every instant. However, the steady-state voltage deviations exist since the converter conduction loss, switching loss, etc. are ignored in the calculation of temporary active power reference. If a load that consumes power is connected at the load side, less power than necessary can be provided to the load due to the power loss of converter. Thus, the regulated DC-link voltage will be lower than its reference. If a load that generates power is connected at the load side, more power will be fed into the grid due to the power loss of converter, which also makes the regulated DC-link voltage lower than its reference. To get rid of the steady-state voltage deviation in [41], the accumulated voltage error is used in a Revised Quasi-Centralized Direct Model Predictive Control (RQC-DMPC) approach in [42], whereas the reference prediction horizon limits its dynamic response to some extent.

Due to the structural characteristics of SRM, the BTB converter-fed SRM system is also researched considering its suitability in high-speed application. Conventionally, the DC source required by the SRM power converter is supplied through the diode rectifier. Although the adoption of the diode rectifier reduces system cost, a large amount of reactive power and current distortion is induced into the grid, which is incredibly harmful to the system [43]. The reactive power leads to additional wattage losses along the lines, increased costs for energy and installation, reduced kVA capacity, and reduced available active power transmitted. High current distortion not only causes overheating and failure at operating conditions below their ratings, but also results in decreased power factor (PF). Besides, the energy feedback, which is beneficial to the motor drive system, cannot be realized via the diode rectifier. To get a satisfactory gird-side power quality, the DC bus capacitor in [44] is moved to the back of the SRM converter, and a power switch is inserted between converter's legs to control the capacitor, but the experimental results are not ideal. Besides, several diode rectifier-connected DC-DC topologies are developed to place in front of the SRM converter for power factor correction (PFC). In [45], a modified Z-source converter with peak current control is employed to enhance the grid-side PF for the SRM drive system in which the magnetizing and demagnetizing time of SRM is controllable. In [46], the front end supplying two equal output voltages for the back-end midpoint converter is adopted for power quality improvement. However, since each capacitor on the DC bus manages the energizing for one phase of SRM, the symmetry of capacitor voltages must be emphasized. Moreover, the computation burden caused by the enumeration algorithm is heavy for the controller. In [47], by adding the high-frequency capacitor and adequately designing the bulky capacitor in the switch-mode rectifier, the voltage spikes on the DC bus are damped to facilitate the improvement of the line drawn power quality. Nevertheless, the inter-phase control independence is weakened due to the coupling between excitation mode and demagnetizing mode in the back-end SRM converter. In [48], the developed SRM drive system performs harmonic cancellation by treating the line current and ripples as disturbances, yet several control schemes are simultaneously employed. In [49] and [50], a circuit modified on the single-ended primary inductor converter is researched, but the speed in [49] is not directly governed in the control scheme. The diode rectifier-connected topologies also can be replaced with AC-DC topologies to enhance the power quality. In [51], the three-level converter is developed to drive the SRMs, but many power devices are employed in the system, which is low cost-effective. The drive circuit in [52], which is made up of two Cuk circuits, is developed to generate dual equal output voltages for SRM midpoint converter. However, an additional controller is requisite to keep the upper and lower capacitor on DC bus balanced.

This dissertation aims to develop control strategies that can further improve the performance of BTB converter-fed electrical machine systems and the main contributions are as follows:

- **Define a new cost function, thereby removing the conventional cascade control structure**

  As mentioned earlier, most MPCs in literature are developed as an inner controller to cooperate with the outer PI controller, which is the typical control structure of PI-MPC. A DC-link voltage PI controller is always necessary to control the BTB converter with PI-MPC, which is a cascaded control structure since the inner MPC is nested within the outer voltage PI control loop. Instead of adopting the cascade control structure, the Direct

Predictive Voltage Control (DPVC) strategy, which directly regulates the DC-link voltage and power flows within a newly-defined cost function, is proposed in this dissertation. By evaluating the newly-defined cost function, the switching state, which not only will generate a DC-link voltage closer to its reference but will generate the active power capable of further reducing that voltage error, is selected for the future instant. Consequently, well-regulated DC-link voltage and controllable power can be achieved within one cost function.

- **Remove the weighting factor**

  The weighting factor in cost function is generally determined based on trial and error procedures, which are empirical and time-consuming. Besides, additional tuning effort for weighting factor is necessary in order to perform well in various operating conditions. In this dissertation, the weighting factor is removed from the proposed strategy by sorting the terms of cost function into two groups and independently evaluating each group separately, which gets rid of the empirical tuning procedures and ensures fast dynamic performance.

- **Compensate for errors caused by mismatched parameter**

  The mathematical model for prediction is accurate when actual values of inductor and resistor are adopted. However, it is actually the nominal values involved in the prediction since the actual values are unknown, and it is also possible that the actual values change during the operation, which causes the steady-state error in the system. To address this problem, Kalman filter is added to the proposed strategy. The disturbances caused by mismatched parameters are estimated via Kalman filter and used to correct the power expressions, thus compensating for the steady-state power error.

- **Reduce the dynamic response time for DRPC**

  For the scheme based on dynamic reference concept, the DC-link voltage tracking performance heavily depends on the reference prediction horizon. To improve its dynamic performance, a modified Dynamic Reference Predictive Control (DRPC) is proposed, in which a dynamic reference prediction horizon is adopted to update the DC-link voltage reference of every time instant to reduce the response time in transients while achieving a satisfying steady-state DC-link voltage control performance.

- **Realize a centralized power control strategy**

  To fulfill the bidirectional power flow, the VSR is generally adopted to connect with SRM converter, which forms the BTB converter for SRM. Conventionally, the front-end VSR and back-end SRM converter are two separate control units with their respective control schemes, which means the control scheme of the VSR regulates the grid-side power quality and the control scheme SRM converter regulates the motor speed. In this dissertation, a direct power connection is built between VSR and SRM, and a centralized control strategy, which treats the VSR and the SRM converter as a whole, is proposed so that the SRM regulation, AC-side power factor correction, and current harmonics restraint can be realized simultaneously in the proposed control strategy.

1.5 Outline

The outline of this dissertation is as follows:

In Chapter 2, the modeling of the BTB converter-fed PMSM system and SRM system is described thoroughly, which provides the theoretical basis for the subsequent controller design. Besides, the self-designed testbench on which the control strategies are validated is presented in detail.

In Chapter 3, the principles of the conventional model-based control strategies, i.e., PI-MPC, and Proportional Integral Deadbeat Predictive Control (PI-DBPC) are revisited.

In Chapter 4, a DRPC, which removes the outer PI controller by updating the voltage and power references of every instant, is described. To further improve its dynamic performance, a modified DRPC is proposed, which adopts a dynamic reference prediction horizon for DC-link voltage reference calculation.

In Chapter 5, a cascade-free DPVC strategy, which realizes controllable DC-link voltage, bidirectional power flow, and sinusoidal current simultaneously within a single cost function of MPC, is proposed.

In Chapter 6, to further enhance the control performance of DPVC strategy, the weighting factors are removed from the cost function to save the factor tunning effort while ensuring a fast dynamic response. Moreover, the Kalman filter is added to DPVC strategy to improve the robustness of the system with mismatched parameters by estimating the disturbances in power expression.

In Chapter 7, a centralized P-DBPC, which builds a direct connection of power between the front-end VSR and back-end SRM converter in the BTB converter-fed SRM system, is proposed to simplify the control structure of the BTB converter-fed high-speed SRM drive system.

At last, the whole work is summarized in Chapter 8.

CHAPTER 2

System modeling and physical system description

The mathematical expressions of system modeling, which provides the theoretical basics for the control strategies in the subsequent chapters, is explained in this chapter.

- Firstly, the revisits the basics for system modeling including coordinate transformations and mathematical models in abc, $\alpha\beta$, and dq frames (see Sec. 2.1), are revisited by taking VSC as an example.
- Secondly, the instantaneous power theory (Sec. 2.2), and the continuous and discontinuous models of the BTB converter-fed PMSM system and SRM system are described (Sec. 2.3).
- Finally, the lab-constructed testbench of the BTB converter-fed electrical machine system, which is used to experimentally verify the control strategies discussed in the following chapters, is depicted (Sec. 2.4).

2.1 Mathematical basics for system modeling

2.1.1 Three-phase system coordinate transformation

Fig. 2.1 shows three coordinate systems, where abc (in red), $\alpha\beta$ (in blue), and dq (in green) are the stationary three-phase, stationary two-phase, and rotational two-phase coordinates, respectively. These coordinate systems are commonly used in power systems analysis to represent different quantities, such as voltage, current, and magnetic fields.

In abc coordinate system, the three phases are represented as vectors that are separated by 120 degrees, and the origin of the coordinate system is typically located at the center of the three-phase source.

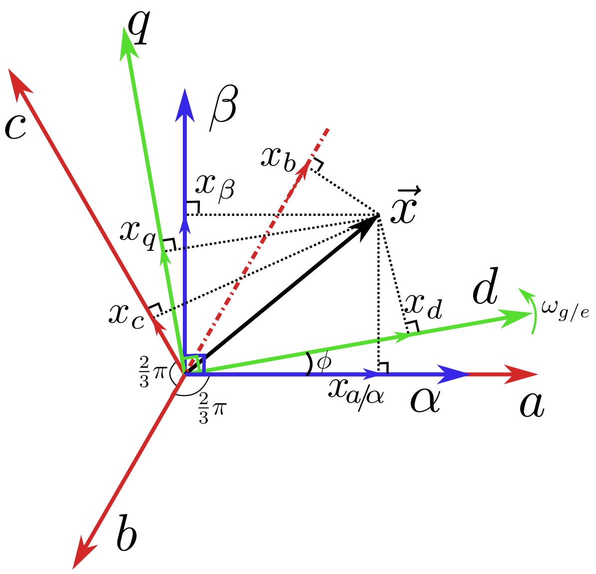

Figure 2.1: Coordinate transformations.

In $\alpha\beta$ coordinate system, the two phases are represented as vectors that are orthogonal to each other, and the origin of the coordinate system is typically located at the center of the two-phase source. The $\alpha\beta$ coordinate system is used to simplify the analysis of three-phase systems by transforming them into a two-phase system.

In dq coordinate system, the two phases are represented as vectors that are orthogonal to each other and rotate with the rotor of the machine. The dq coordinate system is used to simplify the control by transforming the variable parameters in three-phase system into constant parameters.

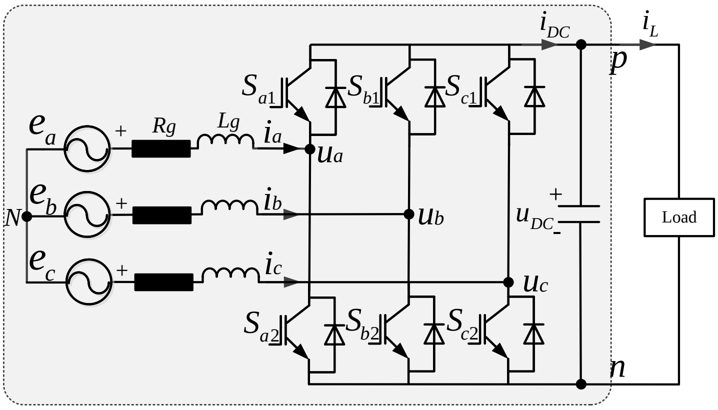

Figure 2.2: Three-phase VSC.

2.1.2 Mathematical model in abc frames

Taking the circuit topology of the three-phase three-wire VSC (see Fig. 2.2) as an example, the following expression can be obtained by applying Kirchhoff's Voltage Law (KVL) to the AC side

$$\begin{cases} L\frac{di_a}{dt} = e_a - Ri_a - u_{aN} \\ L\frac{di_a}{dt} = e_b - Ri_b - u_{bN} \\ L\frac{di_a}{dt} = e_c - Ri_c - u_{cN} \end{cases} \tag{2.1}$$

where $u_{aN} = u_{an} + u_{nN} = S_a u_{DC} + u_{nN}, u_{bN} = u_{bn} + u_{nN} = S_b u_{DC} + u_{nN}, u_{cN} = u_{cn} + u_{nN} = S_c u_{DC} + u_{nN}; u_{nN}$ is the voltage between the node of the lower bridge arm n and the neutral point of the power supply N.

For a three-phase symmetrical power system, $e_a + e_b + e_c = 0, i_a + i_b + i_c = 0$, So

$$u_{nN} = -\frac{1}{3}u_{DC} \sum_{i=a,b,c} S_i. \tag{2.2}$$

The voltage of (2.1) can be rewritten as

$$\begin{cases} u_{aN} = u_{DC}\left(S_a - \frac{1}{3}\sum\limits_{i=a,b,c} S_i\right) \\ u_{bN} = u_{DC}\left(S_b - \frac{1}{3}\sum\limits_{i=a,b,c} S_i\right) \\ u_{cN} = u_{DC}\left(S_c - \frac{1}{3}\sum\limits_{i=a,b,c} S_i\right) \end{cases} \tag{2.3}$$

In addition, applying Kirchhoff's Current Law (KCL) to the DC side in Fig. 2.2 gives

$$C\frac{du_{DC}}{dt} = i_{DC} - i_L. \tag{2.4}$$

where $i_{DC} = S_a i_a + S_b i_b + S_c i_c$. For resistive loads $i_L = u_{DC}/R_L$.

Combining (2.1) and (2.4), the mathematical model of VSC in abc frames is

$$\begin{cases} L\frac{di_a}{dt} = e_a - Ri_a - d_a u_{DC} \\ L\frac{di_a}{dt} = e_b - Ri_b - d_b u_{DC} \\ L\frac{di_a}{dt} = e_c - Ri_c - d_c u_{DC} \\ C\frac{du_{DC}}{dt} = S_a i_a + S_b i_b + S_c i_c - i_L \end{cases} \tag{2.5}$$

where $d_a = S_a - \frac{1}{3}\sum\limits_{i=a,b,c} S_i$, $d_b = S_b - \frac{1}{3}\sum\limits_{i=ab,c} S_i$, and $d_c = S_c - \frac{1}{3}\sum\limits_{i=a,b,c} S_i$.

2.1.3 Mathematical model in $\alpha\beta$ frames

In order to establish the mathematical model of the VSC in $\alpha\beta$ frames, the Clarke transformation is used to convert the variables of the converter in abc frames into $\alpha\beta$ frames. There are two methods for Clarke transformation, one is equal-amplitude vector transformation, and the other is equal-power vector transformation. Equal-amplitude vector transformation refers to the coordinate transformation in which the amplitude before and after the coordinate transformation is equal. Equal-power vector transformation refers to the coordinate transformation in which the power before and after the coordinate transformation is equal.

2.1.3.1 Equal-amplitude vector transformation in $\alpha\beta$ frames

The equal-amplitude vector transformation matrix $(\boldsymbol{M}_C)$ and its inverse matrix $\boldsymbol{M}_C^{-1}$ are

$$\boldsymbol{M}_C = \frac{2}{3}\begin{pmatrix} 1 & -\frac{1}{2} & -\frac{1}{2} \\ 0 & \frac{\sqrt{3}}{2} & -\frac{\sqrt{3}}{2} \end{pmatrix}, \quad \boldsymbol{M}_C^{-1} = \begin{pmatrix} 1 & 0 \\ -\frac{1}{2} & \frac{\sqrt{3}}{2} \\ -\frac{1}{2} & -\frac{\sqrt{3}}{2} \end{pmatrix}. \tag{2.6}$$

For a three-phase system, the converter model in the three-phase abc frames is transformed by $\boldsymbol{M}_C$, and the obtained mathematical model in $\alpha\beta$ frames is

$$\begin{cases} L\frac{di_\alpha}{dt} = e_\alpha - Ri_\alpha - u_{r\alpha} = e_\alpha - Ri_\alpha - S_\alpha u_{DC} \\ L\frac{di_\beta}{dt} = e_\beta - Ri_\beta - u_{r\beta} = e_\beta - Ri_\beta - S_\beta u_{DC} \\ C\frac{du_{DC}}{dt} = \frac{3}{2}\left(S_\alpha i_\alpha + S_\beta i_\beta\right) - i_L \end{cases} \tag{2.7}$$

where $e_\alpha = U_m \cos\omega t, e_\beta = U_m \sin\omega t$, $S_\alpha = \left(2S_a - S_b - S_c\right)/3$, and $S_\beta = \sqrt{3}\left(S_b - S_c\right)/3$.

2.1.3.2 Equal-power vector transformation in $\alpha\beta$ frames

The equal-power vector transformation matrix $(\boldsymbol{T}_C)$ and its inverse matrix $\boldsymbol{T}_C^{-1}$ are

$$\boldsymbol{T}_C = \sqrt{\frac{2}{3}}\begin{pmatrix} 1 & -\frac{1}{2} & -\frac{1}{2} \\ 0 & \frac{\sqrt{3}}{2} & -\frac{\sqrt{3}}{2} \end{pmatrix}, \quad \boldsymbol{T}_C^{-1} = \sqrt{\frac{2}{3}}\begin{pmatrix} 1 & 0 \\ -\frac{1}{2} & \frac{\sqrt{3}}{2} \\ -\frac{1}{2} & -\frac{\sqrt{3}}{2} \end{pmatrix}. \tag{2.8}$$

For a three-phase symmetrical power converter system, the converter model in abc frames is transformed by $\boldsymbol{T}_C$, and the obtained mathematical model in $\alpha\beta$ frames is

$$\begin{cases} L\frac{di_\alpha}{dt} = e_\alpha - Ri_\alpha - u_{r\alpha} = e_\alpha - Ri_\alpha - S_\alpha u_{DC} \\ L\frac{di_\beta}{dt} = e_\beta - Ri_\beta - u_{r\beta} = e_\beta - Ri_\beta - S_\beta u_{DC} \\ C\frac{du_{DC}}{dt} = S_\alpha i_\alpha + S_\beta i_\beta - i_L \end{cases} \tag{2.9}$$

where $e_\alpha = \sqrt{3/2}U_m \cos\omega t$, $e_\beta = \sqrt{3/2}U_m \sin\omega t$, $S_\alpha = \left(2S_a - S_b - S_c\right)/\sqrt{6}$, and $S_\beta = (S_b -S_c)/\sqrt{2}$.

2.1.4 Mathematical model in dq frames

The Park transformation matrix $(\boldsymbol{M}_P)$ and its inverse matrix $\boldsymbol{M}_P^{-1}$ are

$$\boldsymbol{M}_P = \begin{pmatrix} \cos\theta & \sin\theta \\ -\sin\theta & \cos\theta \end{pmatrix}, \quad \boldsymbol{M}_P^{-1} = \begin{pmatrix} \cos\theta & -\sin\theta \\ \sin\theta & \cos\theta \end{pmatrix}. \tag{2.10}$$

Thus, the mathematical model in dq frames with equal-amplitude vector transformation is

$$\begin{cases} L\frac{di_d}{dt} = e_d - Ri_d + \omega Li_q - u_{rd} \\ L\frac{di_q}{dt} = e_q - Ri_q - \omega Li_d - u_{rq} \\ C\frac{du_{DC}}{dt} = \frac{3}{2}\left(S_d i_d + S_q i_q\right) - i_L. \end{cases} \tag{2.11}$$

Considering $u_{rd} = S_d u_{DC}$, $u_{rq} = S_q u_{DC}$, and $i_L = u_{DC}/R_L$ (resistive load), then (2.11) can be changed to

$$\begin{cases} L\frac{di_d}{dt} = e_d - Ri_d + \omega L i_q - S_d u_{DC} \\ L\frac{di_q}{dt} = e_q - Ri_q - \omega L i_d - S_q u_{DC} \\ C\frac{du_{DC}}{dt} = \frac{3}{2}\left(S_d i_d + S_q i_q\right) - \frac{u_{DC}}{R_L}. \end{cases} \tag{2.12}$$

The mathematical model in dq frames with equal-power vector transformation is

$$\begin{cases} L\frac{di_d}{dt} = e_d - Ri_d + \omega L i_q - u_{rd} \\ L\frac{di_q}{dt} = e_q - Ri_q - \omega L i_d - u_{rq} \\ C\frac{du_{DC}}{dt} = S_d i_d + S_q i_q - i_L. \end{cases} \tag{2.13}$$

Considering $u_{rd} = S_d u_{DC}$, $u_{rq} = S_q u_{DC}$, and $i_L = u_{DC}/R_L$, then (2.13) can be changed to

$$\begin{cases} L\frac{di_d}{dt} = e_d - Ri_d + \omega L i_q - S_d u_{DC} \\ L\frac{di_q}{dt} = e_q - Ri_q - \omega L i_d - S_q u_{DC} \\ C\frac{du_{DC}}{dt} = S_d i_d + S_q i_q - \frac{u_{DC}}{R_L} \end{cases} \tag{2.14}$$

2.2 Instantaneous power theory

For power systems with sinusoidal voltages and currents, quantities such as active power, reactive power, etc., are based on the average concept [53]. Many contributors have attempted to redefine these quantities to deal with three-phase systems with distorted currents and voltages. Among them, Akagi et al. [54] have introduced an interesting concept of instantaneous power theory. This concept gives an effective method to control the instantaneous real and reactive power for three-phase systems, and the detailed definitions are presented as follows.

Consider the network whose terminal voltages and currents are $\vec{\boldsymbol{e}}_{abc} = \left[e_a, e_b, e_c\right]^T$ and $\vec{\boldsymbol{i}}_{abc} = \left[i_a, i_b, i_c\right]^T$, respectively. The instantaneous active power in the time domain is expressed as [55]

$$p(t) = e_a(t)i_a(t) + e_b(t)i_b(t) + e_c(t)i_c(t) \tag{2.15}$$

where $i_a + i_b + i_c = 0$. $\vec{\boldsymbol{e}}_{abc}$ and $\vec{\boldsymbol{i}}_{abc}$ in (2.15) can be expressed in terms of their corresponding space phasors $\boldsymbol{e}(t)$ and $\boldsymbol{i}(t)$

$$\begin{aligned} p(t) = {} & \Re\left\{\boldsymbol{e}(t)e^{j0}\right\}\Re\left\{\boldsymbol{i}(t)e^{j0}\right\} + \Re\left\{\boldsymbol{e}(t)e^{-j\frac{2}{3}\pi}\right\}\Re\left\{\boldsymbol{i}(t)e^{-j\frac{2}{3}\pi}\right\} \\ & + \Re\left\{\boldsymbol{e}(t)e^{-j\frac{4}{3}\pi}\right\}\Re\left\{\boldsymbol{i}(t)e^{-j\frac{4}{3}\pi}\right\} \end{aligned} \tag{2.16}$$

where
$\boldsymbol{e}(t) = \frac{2}{3}\left[e^{j0}e_a(t) + e^{j\frac{2}{3}\pi}e_b(t) + e^{j\frac{4}{3}\pi}e_c(t)\right]$ and $\boldsymbol{i}(t) = \frac{2}{3}\left[e^{j0}i_a(t) + e^{j\frac{2}{3}\pi}i_b(t) + e^{j\frac{4}{3}\pi}i_c(t)\right]$ are space phasors, and $\Re\{\ \}$ is the real-part operator. Based on the identity $\Re\left\{\boldsymbol{\xi}_1\right\}\Re\left\{\boldsymbol{\xi}_2\right\} = \left(\Re\left\{\boldsymbol{\xi}_1\boldsymbol{\xi}_2\right\} + \Re\left\{\boldsymbol{\xi}_1\boldsymbol{\xi}_2^{\star}\right\}\right)/2$, (2.16) is expressed as

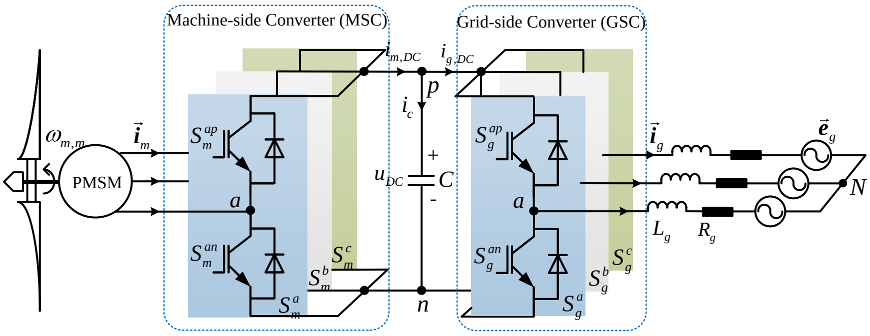

Figure 2.3: BTB converter-fed PMSM system.

$$p(t) = \frac{\Re\left\{\boldsymbol{e}(t)\boldsymbol{i}(t)e^{j0}\right\} + \Re\left\{\boldsymbol{e}(t)\boldsymbol{i}^\star(t)\right\}}{2} + \frac{\Re\left\{\boldsymbol{e}(t)\boldsymbol{i}(t)e^{-j\frac{4}{3}\pi}\right\} + \Re\left\{\boldsymbol{e}(t)\boldsymbol{i}^\star(t)\right\}}{2} + \frac{\Re\left\{\boldsymbol{e}(t)\boldsymbol{i}(t)e^{-j\frac{8}{3}\pi}\right\} + \Re\left\{\boldsymbol{e}(t)\boldsymbol{i}^\star(t)\right\}}{2} \tag{2.17}$$

where * indicates the conjugate complex. Since $e^{j0} + e^{-j\frac{4}{3}\pi} + e^{-j\frac{8}{3}\pi} \equiv 0$, (2.17) is simplified to

$$p(t) = \frac{3}{2}\Re\left\{\boldsymbol{e}(t)\boldsymbol{i}^\star(t)\right\}. \tag{2.18}$$

To achieve the analogy with conventional phasor analysis, the definitions of the instantaneous reactive power and the instantaneous complex power are given by [55]

$$q(t) = \frac{3}{2}\Im\left\{\boldsymbol{e}(t)\boldsymbol{i}^\star(t)\right\} \tag{2.19}$$

$$s(t) = p(t) + jq(t) = \frac{3}{2}\boldsymbol{e}(t)\boldsymbol{i}^\star(t) \tag{2.20}$$

where $\Im\{\ \}$ is the imaginary-part operator. $\boldsymbol{e}(t)$ and $\boldsymbol{i}^\star(t)$ in the above expressions also can be expressed in two-phase $\alpha\beta$ reference frame as below

$$\vec{\boldsymbol{e}}_{\alpha\beta}(t) = e_\alpha + je_\beta \tag{2.21}$$

$$\vec{\boldsymbol{i}}^*_{\alpha\beta}(t) = i_\alpha - ji_\beta. \tag{2.22}$$

To obtain equivalent expressions in terms of $\alpha\beta$-frame variables, the following expressions can be got by substituting (2.21) and (2.22) into (2.18) and (2.19)

$$p(t) = \frac{3}{2}\left[e_\alpha(t)i_\alpha(t) + e_\beta(t)i_\beta(t)\right] = \frac{3}{2}\Re\left(\vec{\boldsymbol{e}}_{\alpha\beta}(t)\vec{\boldsymbol{i}}^\star_{\alpha\beta}(t)\right) \tag{2.23}$$

$$q(t) = \frac{3}{2}\left[-e_\alpha(t)i_\beta(t) + e_\beta(t)i_\alpha(t)\right] = \frac{3}{2}\Im\left(\vec{\boldsymbol{e}}_{\alpha\beta}(t)\vec{\boldsymbol{i}}^\star_{\alpha\beta}(t)\right) \tag{2.24}$$

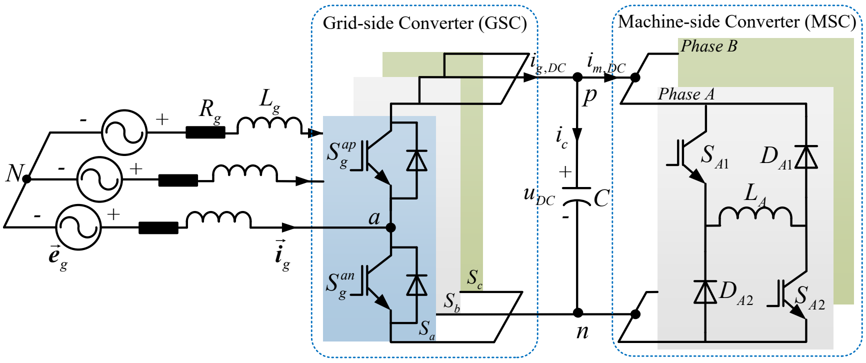

Figure 2.4: BTB converter-fed SRM system.

2.3 Modeling of BTB converter-fed electrical machine

In this section, the BTB converter-fed PMSM system shown in Fig. 2.3 and the BTB converter-fed SRM system shown in Fig. 2.4 are described in detail and the dynamic equations are given. To ease the modeling and controller design, the variables in abc stationary plane $\overrightarrow{\boldsymbol{\xi}}_x^{abc} = \left[\xi_x^a, \xi_x^b, \xi_x^c\right]^T$ are mapped into $\alpha\beta$ stationary plane $\overrightarrow{\boldsymbol{\xi}}_x^{\alpha\beta} = \left[\xi_x^\alpha, \xi_x^\beta\right]^T$ and dq rotating plane $\overrightarrow{\boldsymbol{\xi}}_x^{dq} = \left[\xi_x^d, \xi_x^q\right]^T$ by the matrices below

$$\begin{aligned} \overrightarrow{\boldsymbol{\xi}}_x^{\alpha\beta} &= \boldsymbol{M}_C \overrightarrow{\boldsymbol{\xi}}_x^{abc} \\ \overrightarrow{\boldsymbol{\xi}}_x^{dq} &= \boldsymbol{M}_P \overrightarrow{\boldsymbol{\xi}}_x^{\alpha\beta} \end{aligned} \qquad x \in \{m, g\} \tag{2.25}$$

where subscript x denotes machine-side variables (m) or grid-side variables (g), and θ denotes the angle between the rotating d-axis and stationary α-axis.

2.3.1 Dynamic models of GSC

The voltage model of GSC [56] is given by

$$\overrightarrow{\boldsymbol{e}}_g^{\alpha\beta}(t) = R_g \overrightarrow{\boldsymbol{i}}_g^{\alpha\beta}(t) + L_g \frac{d\overrightarrow{\boldsymbol{i}}_g^{\alpha\beta}(t)}{dt} + \overrightarrow{\boldsymbol{u}}_g^{\alpha\beta}(t) \tag{2.26}$$

where e_g, i_g, u_g, L_g, and R_g are grid-side voltage, current, converter voltage, filter inductor, and filter resistor, respectively. The converter voltage $\overrightarrow{\boldsymbol{u}}_g^{\alpha\beta}$ can be regulated by configuring the power switches in GSC

$$\overrightarrow{\boldsymbol{u}}_g^{\alpha\beta}(t) = \boldsymbol{M}_C \left(\overrightarrow{\boldsymbol{S}}_g^{abc}(t) - \frac{1}{3} \sum_{y=a,b,c} S_g^y(t) \right) u_{DC}(t) \tag{2.27}$$

where $\overrightarrow{\boldsymbol{S}}_g^{abc} = \left[S_g^a, S_g^b, S_g^c\right]^T$ and S_g^y denotes the phase switching state. S_g^y can be set to 1 or 0 by configuring the upper S_g^{yp} and lower switches S_g^{yn} on each leg of GSC. Thus, eight switching vectors can be obtained in GSC, namely $V_g \in \left\{[0,0,0]^T, [0,0,1]^T, \ldots, [1,1,0]^T, [1,1,1]^T\right\}$. In light of the instantaneous power theory, the instantaneous active power p_g and instantaneous reactive power q_g can be described by

$$\begin{pmatrix} p_g(t) \\ q_g(t) \end{pmatrix} = \underbrace{\frac{3}{2} \begin{bmatrix} e_g^{\alpha}(t) & e_g^{\beta}(t) \\ e_g^{\beta}(t) & -e_g^{\alpha}(t) \end{bmatrix}}_{\boldsymbol{A}_g} \overrightarrow{\boldsymbol{i}}_g^{\alpha\beta}(t) \tag{2.28}$$

where the equal-amplitude vector transformation is applied. For $\overrightarrow{e}_g^{\alpha\beta}$, the following relationship holds

$$\frac{d}{dt}\left(\overrightarrow{\boldsymbol{e}}_g^{\alpha\beta}(t)\right) = \begin{bmatrix} 0 & -1 \\ 1 & 0 \end{bmatrix} \omega_g \overrightarrow{\boldsymbol{e}}_g^{\alpha\beta}(t) \tag{2.29}$$

where $\omega_g = 2\pi f$ denotes the angular frequency of the grid-side voltage. Then the dynamic expression of p_g and q_g can be derived as follows by combining (2.26), (2.28), and (2.29) together

$$\frac{d}{dt}\begin{pmatrix} p_g(t) \\ q_g(t) \end{pmatrix} = \frac{\boldsymbol{A}_g}{L_g}\begin{pmatrix} e_g^{\alpha}(t) - u_g^{\alpha}(t) \\ e_g^{\beta}(t) - u_g^{\beta}(t) \end{pmatrix} + \begin{pmatrix} -\frac{R_g}{L_g}p_g(t) - \omega_g q_g(t) \\ -\frac{R_g}{L_g}q_g(t) + \omega_g p_g(t) \end{pmatrix} \tag{2.30}$$

In light of (2.30), the discrete power models of GSC of instant $k+1$ can be described as

$$\begin{aligned} \begin{pmatrix} p_g[k+1] \\ q_g[k+1] \end{pmatrix} &= \frac{3T_s}{2L_g}\begin{bmatrix} e_g^{\alpha}[k] & e_g^{\beta}[k] \\ e_g^{\beta}[k] & -e_g^{\alpha}[k] \end{bmatrix}\begin{pmatrix} e_g^{\alpha}[k] - u_g^{\alpha}[k] \\ e_g^{\beta}[k] - u_g^{\beta}[k] \end{pmatrix} \\ &+ \begin{pmatrix} p_g[k] - \frac{T_s R_g}{L_g}p_g[k] - T_s\omega_g q_g[k] \\ q_g[k] - \frac{T_s R_g}{L_g}q_g[k] + T_s\omega_g p_g[k] \end{pmatrix}. \end{aligned} \tag{2.31}$$

2.3.2 Dynamic models of PMSM

The dynamic models of the PMSM [57] are

$$\begin{cases} \frac{d}{dt}\left(\overrightarrow{\boldsymbol{i}}_m^{dq}(t)\right) = \begin{bmatrix} -\frac{R_{m,s}}{L_{m,s}} & \omega_{m,e}(t) \\ -\omega_{m,e}(t) & -\frac{R_{m,s}}{L_{m,s}} \end{bmatrix} \overrightarrow{\boldsymbol{i}}_m^{dq}(t) \\ \qquad + \frac{1}{L_{m,s}}\boldsymbol{I}_2 \overrightarrow{\boldsymbol{u}}_m^{dq}(t) + \begin{pmatrix} 0 \\ -\frac{\psi_r \omega_{m,e}(t)}{L_{m,s}} \end{pmatrix} \\ \frac{d}{dt}\left(\omega_{m,m}(t)\right) = \frac{1}{J_m}\left(\tau_{m,m}(t) - \tau_{m,e}(t)\right) \\ \tau_{m,e}(t) = 1.5 n_p \psi_r i_m^q(t) \end{cases} \tag{2.32}$$

where $i_m, u_m, \psi_r, R_{m,s}, L_{m,s}, J_m, \tau_{m,e}, \tau_{m,m}, \omega_{m,e}, \omega_{m,m}$, and n_p denote the stator current, stator voltage, flux linkage established by permanent magnet, stator resistance, stator inductance, motor inertia, electromagnetic torque, load torque, electrical angular speed, mechanical angular speed, and pole pairs of the generator, respectively, and $\boldsymbol{I}_2 = \mathrm{diag}(1,1)$. The stator voltage $\overrightarrow{\boldsymbol{u}}_m^{dq}$ can be regulated by configuring the power switches in MSC

$$\overrightarrow{\boldsymbol{u}}_m^{dq}(t) = \boldsymbol{M}_P \boldsymbol{M}_C \left(\overrightarrow{\boldsymbol{S}}_m^{abc}(t) - \frac{1}{3}\sum_{y=a,b,c} S_m^y(t)\right) u_{DC}(t) \tag{2.33}$$

where $\overrightarrow{\boldsymbol{S}}_m^{abc} = \left[S_m^a, S_m^b, S_m^c\right]^T$, u_{DC} denotes the DC-link voltage, and S_m^y denotes the phase switching state. S_m^y can be set to 1 or 0 by configuring the upper and lower switches on each leg of MSC

$$S_m^y = \begin{cases} 1 & (S_m^{yp}\ On,\ S_m^{yn}\ Off) \\ 0 & (S_m^{yp}\ Off,\ S_m^{yn}\ On) \end{cases} y \in \{a, b, c\}. \tag{2.34}$$

Thus, eight switching vectors can be obtained in MSC, namely $V_m \in \left\{[0,0,0]^T, [0,0,1]^T, \ldots, [1,1,0]^T, [1,1,1]^T\right\}$.

By applying the forward Euler discretization (i.e., $\frac{d}{dt}y(t) = \frac{y[k+1]-y[k]}{T_s}$) to the dynamic models in (2.32), the discretized current equation of PMSM in dq coordinate system is given by [57]

$$\begin{aligned} \begin{pmatrix} i_m^d[k+1] \\ i_m^q[k+1] \end{pmatrix} &= \begin{bmatrix} 1 - \frac{R_{m,s}T_s}{L_{m,s}} & w_{m,e}[k]T_s \\ -w_{m,e}[k]T_s & 1 - \frac{R_{m,s}T_s}{L_{m,s}} \end{bmatrix} \begin{pmatrix} i_m^d[k] \\ i_m^q[k] \end{pmatrix} \\ &+ \frac{T_s}{L_{m,s}} \boldsymbol{I}_2 \begin{pmatrix} u_m^d[k] \\ u_m^q[k] \end{pmatrix} - \begin{pmatrix} 0 \\ \frac{T_s \psi_r}{L_{m,s}} w_{m,e}[k] \end{pmatrix} \end{aligned} \tag{2.35}$$

where i_m, u_m, ψ_r, R_m, L_m, $\omega_{m,e}$, and T_s denote the stator current, stator voltage, permanent magnet flux linkage, stator resistor, stator inductor, electrical angular velocity, and sampling period, respectively, and $\boldsymbol{I}_2 = diag(1,1)$. The electromagnetic torque $\tau_{m,e}$ of PMSM depends on the q-axis current

$$\tau_{m,e}[k] = \frac{3}{2} n_p \psi_r i_m^q[k] \tag{2.36}$$

The mechanical angular velocity can be expressed by

$$w_{m,m}[k+1] = \frac{\tau_{m,m}[k] - \tau_{m,e}[k]}{M_m} T_s + w_{m,m}[k] \tag{2.37}$$

where M_m represents the machine inertia.

2.3.3 Dynamic models of SRM

The voltage equation of phase m, $m \in \{A, B\}$ of the SRM can be written as [58]

$$\begin{aligned} v_m &= r_m i_m + \frac{\partial \psi(i_m, \theta_r)}{\partial i_m} \frac{di_m}{dt} + \frac{\partial \psi(i_m, \theta_r)}{\partial \theta_r} \frac{d\theta_r}{dt} \\ &= r_m i_m + L_m(i_m, \theta_r) \frac{di_m}{dt} + \frac{\partial L_m(i_m, \theta_r)}{\partial \theta_r} \omega_r i_m \end{aligned} \tag{2.38}$$

where v_m, i_m, r_m, L_m, ω_r, and θ_r represent phase voltage, current, resistance, inductor, angular speed, and rotor position of SRM, respectively. The last term of the right-hand side of (2.38) is defined as the back Electromotive Force (back EMF) of the motor, which is speed dependent. The magnetization mode and double-voltage demagnetization mode are analyzed as examples.
1) Magnetization mode:

> When S_{m1} and S_{m2} shown in Fig. 2.4 are switched on (phase switching state S_m is 1 in this case), the capacitor voltage v_{DC} is applied to the winding of phase m. Supposing the

capacitor voltages on DC-link are well controlled, the voltage and current equations of this mode are given by

$$\begin{cases} v_m = v_{DC} = r_m i_m + L_m(i_m, \theta_r)\frac{\partial i_m}{\partial t} + \frac{\partial L_m(i_m,\theta_r)}{\partial \theta_r}\omega_r i_m \\ i_m(t) = I_{m1\_ini}\, e^{-t/\tau_a} + \frac{v_{DC}}{R_{eq\_m}}(1 - e^{-t/\tau_a}) \\ R_{eq\_m} = r_m + \partial L_m(i_m, \theta_r)\omega_r / \partial \theta_r \\ \tau_a = L_m\,(i_m, \theta_r)/R_{eq\_m} \end{cases} \tag{2.39}$$

where I_{p1_ini} denote initial current. Regularly, the energy stored in phase winding is fully released at the end of every stroke, thus $I_{m1\_ini} = 0$.

2) Demagnetization mode:

When S_{m1} and S_{m2} are switched off (the phase switching state S_m is -1 in this case), a reversed DC-link voltage equaling to v_{DC} is applied to the winding of phase p and the mathematical model of this mode are given by

$$\begin{cases} v_m = -v_{DC} = r_m\, i_m + L_m(i_m, \theta_r)\frac{\partial i_m}{\partial t} + \frac{\partial L_m(i_m,\theta_r)}{\partial \theta_r}\omega_r i_m \\ i_m(t) = I_{m2\_ini}\, e^{-t/\tau_a} - \frac{v_c}{R_{eq\_m}}(1 - e^{-t/\tau_a}) \end{cases} \tag{2.40}$$

where I_{m2_ini} is the initial current in winding at the start of this mode. For high-speed SRM, fast demagnetization is extremely important for the reduction of current tailing time, which contributes to negative torque elimination.

The speed of the SRM is governed by the following first-order differential equation

$$\frac{d\omega_r(t)}{dt} = \frac{1}{J_m}(\tau_{e,m}(t) - \tau_l(t) - B_m\omega_r(t)) \tag{2.41}$$

where J_m, B_m, $\tau_{e,m}$, and τ_l represent motor inertia, friction coefficient, electromagnetic torque, and load torque, respectively.

2.3.4 Dynamic models of DC-link voltage

According to KCL and the definition of the positive current direction in Fig. 2.3, the following expression holds

$$i_c(t) = i_{g,DC}(t) - i_{m,DC}(t) = C\frac{du_{DC}(t)}{dt} \tag{2.42}$$

where C denotes the capacitance of DC-link capacitor, $i_{g,DC}$ denotes the current flowing out of GSC, $i_{m,DC}$ denotes the current flowing into MSC. $i_{g,DC}$ is related to switching state $\overrightarrow{\boldsymbol{S}}_g^{abc}$ and phase current $\overrightarrow{\boldsymbol{i}}_g^{abc}$ of GSC, and it can be calculated by

$$i_{g,DC}(t) = \overrightarrow{\boldsymbol{S}}_g^{abc}(t)^T \overrightarrow{\boldsymbol{i}}_g^{abc}(t). \tag{2.43}$$

$i_{m,DC}$ is related to the switching state and phase current of MSC. Therefore, for BTB converter-fed PMSM system shown in Fig. 2.3, $i_{m,DC}$ can be calculated by $\overrightarrow{\boldsymbol{S}}_m^{abc}$ and $\overrightarrow{\boldsymbol{i}}_m^{abc}$

$$i_{m,DC} = \overrightarrow{\boldsymbol{S}}_m^{abc}(t)^T \overrightarrow{\boldsymbol{i}}_m^{abc}(t). \tag{2.44}$$

Combining (2.42), (2.43) and (2.44) gives

$$C\frac{du_{DC}(t)}{dt} = \vec{\boldsymbol{S}}_g^{abc}(t)^T \vec{\boldsymbol{\imath}}_g^{abc}(t) - \vec{\boldsymbol{S}}_m^{abc}(t)^T \vec{\boldsymbol{\imath}}_m^{abc}(t). \tag{2.45}$$

Hence, the predictive model of DC-link voltage of instant $k+1$ is expressed as

$$u_{DC}[k+1] = u_{DC}[k] + \frac{T_s}{C}\{\underbrace{\left(\vec{\boldsymbol{S}}_g^{abc}[k]\right)^T \vec{\boldsymbol{\imath}}_g^{abc}[k]}_{i_{g,DC}[k]} - \underbrace{\left(\vec{\boldsymbol{S}}_m^{abc}[k]\right)^T \vec{\boldsymbol{\imath}}_m^{abc}[k]}_{i_{m,DC}[k]}\}. \tag{2.46}$$

For BTB converter-fed SRM system shown in Fig. 2.4, the current flowing into MSC can be calculated by

$$i_{m,DC} = \vec{\boldsymbol{S}}_m(t)^T \vec{\boldsymbol{\imath}}_m(t) \tag{2.47}$$

where $\vec{\boldsymbol{S}}_m = [S_A, S_B]^T$ and $\vec{\boldsymbol{\imath}}_m = [i_A, i_B]^T$. Combining (2.42), (2.43) and (2.47) gives

$$C\frac{du_{DC}(t)}{dt} = \vec{\boldsymbol{S}}_g^{abc}(t)^T \vec{\boldsymbol{\imath}}_g^{abc}(t) - \vec{\boldsymbol{S}}_m(t)^T \vec{\boldsymbol{\imath}}_m(t). \tag{2.48}$$

Hence, the predictive model of DC-link voltage of instant $k+1$ is expressed as

$$u_{DC}[k+1] = u_{DC}[k] + \frac{T_s}{C}\{\underbrace{\left(\vec{\boldsymbol{S}}_g^{abc}[k]\right)^T \vec{\boldsymbol{\imath}}_g^{abc}[k]}_{i_{g,DC}[k]} - \underbrace{\left(\vec{\boldsymbol{S}}_m[k]\right)^T \vec{\boldsymbol{\imath}}_m[k]}_{i_{m,DC}[k]}\}. \tag{2.49}$$

2.4 Lab-constructed testbench

All the control schemes concerning the BTB converter-fed PMSM system in this work are realized on the same testbench shown in Fig. 2.5. The testbench includes test instruments such as oscilloscope and power analyzer (left), control unit and power converters (middle), and controlled motor and its load (right). In addition, the controlled motor and load share the same DC bus, which helps to avoid energy waste. The braking resistors, if necessary, can absorb excess energy to avoid over-voltage faults on the DC bus.

Table 2.1: Hardware Configuration

Description	Producer	Type
Digital signal processor	TEXAS INSTRUMENTS	TMS320F28335
Insulated gate bipolar transistor	INFINEON	FS100R12KE3
Current transducer	LEM	LA25
Voltage transducer	LEM	LV25
Incremental encoder	HEIDENHAIN	ERO1420

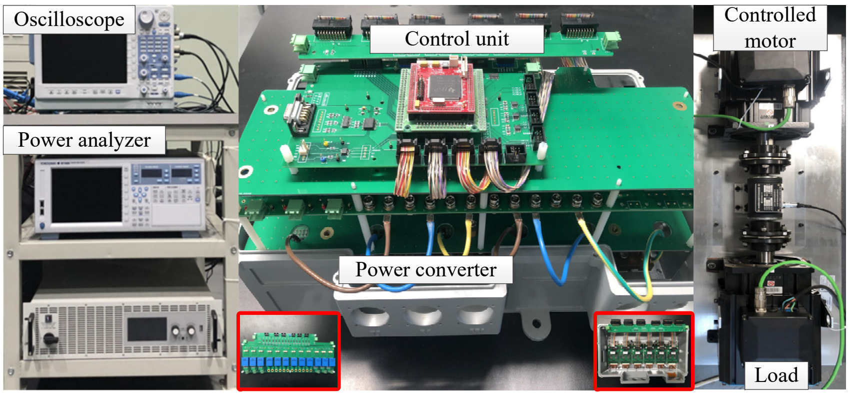

Figure 2.5: BTB converter-fed PMSM drive system.

Table 2.2: Experimental System Parameters

Description	Parameter	Value	Description	Parameter	Value
GSC			PMSM		
Voltage Frequency	ω_g(rad/s)	100π	Pole pairs	n_p	4
Filter resistance	$R_g(\Omega)$	0.1	PM flux linkage	ψ_r(Wb)	0.41
Filter inductor	L_g(mH)	15	Stator inductor	$L_{m,s}$(mH)	12
Phase voltage	e_g(V)	160	Stator resistance	$R_{m,s}(\Omega)$	0.85
DC-link capacitor	$C(\mu$F)	100	Rated torque	$\tau_{m,e}(N \cdot m)$	15
Control period	$T_s(\mu s)$	50	Rated speed	$n_{m,r}$(r/min)	1500

2.4.1 Testbench data

Table 2.1 presents the hardware configuration of the lab-constructed testbench. The experiment parameters concerning the drive system are given in Table 2.2.

2.4.2 Power converter design

Fig. 2.6(a) shows the self-designed BTB converter consisting of several boards for motor control. Fig. 2.6 shows the assembled BTB converter box with an aluminum housing that directly attaches to the power devices. The power converter is cooled using water. Fig. 2.6(b) shows a digital control board based on TMS320F28335, a 32-bit floating-point DSP. The control board has 12 PWM outputs, 16 ADC inputs, 2 DAC outputs, and decoding input for motor encoder, which is used for the control of the whole system. The board also has hardware protection for voltage and current through comparators. The IGBT gate drive board in Fig. 2.6(c) transmits the 12 channels of gate drive signals from control board to inverter through photocoupler. Fig. 2.6(d) is the current sampling board with 6 current sampling circuits. It uses LEM LA 25-NP as current sensor, which has a current sampling accuracy of ± 0.5 %. Fig. 2.6(e) is the voltage sampling board with 6 voltage sampling circuits. It uses LEM LV 25-NP as voltage sensor, which has a voltage sampling accuracy of ± 1 %. Fig. 2.6(f) is the IGBT power board with two integrated Infineon power modules FF300R12ME4.

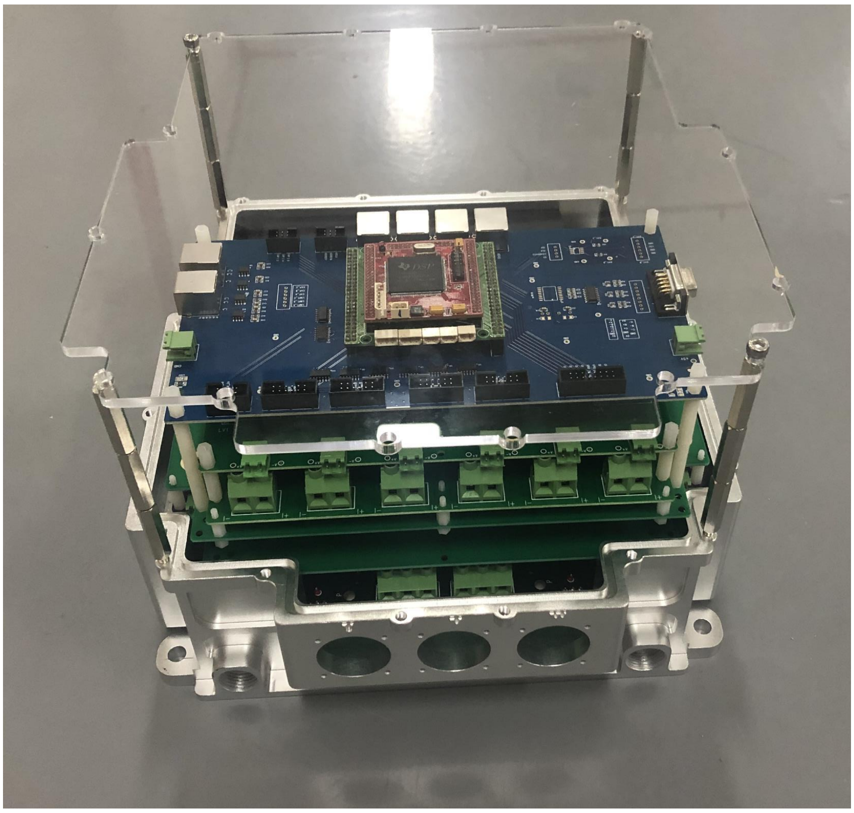

(a) BTB converter box.

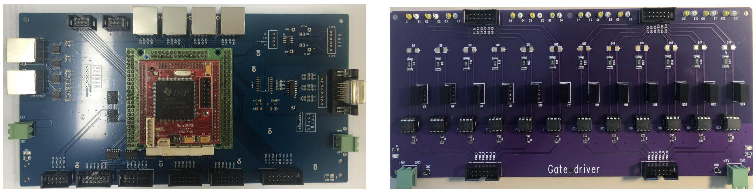

(b) Digital control board.
(c) Gate driver board.

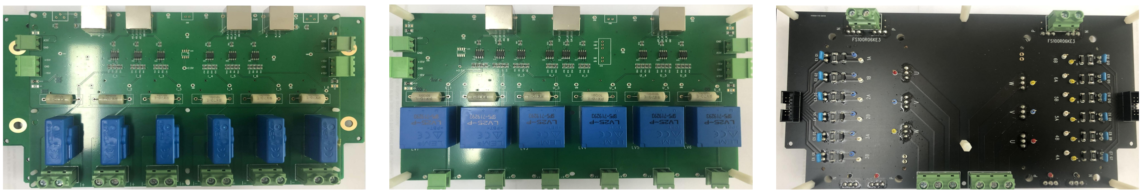

(d) Current sampling board.
(e) Voltage sampling board.
(f) Power board.

Figure 2.6: Self-designed BTB converter.

2.4.3 AC filter design

The primary role of the inductor (L_g) in the grid side is to filter out the switching frequency harmonics and smooth out the output power switches voltage. This is achieved by storing energy in the inductor during the switching ON time of the GSC and releasing it during the OFF time.

The current ripple, which is the difference between the maximum and minimum current in the inductor during each switching cycle, decides the amount of energy stored and released by the inductor. The inductor should be designed to handle the calculated current ripple without saturating the core material.

Fig. 2.7, showing one switching cycle waveform of the inverter output voltage with respect to the inductor current, can be used to analyze the performance of the inductor in the output filter. The waveform of the inductor current should have a relatively smooth and continuous shape, with minimal ripple and overshoot. Any excessive ripple or overshoot can indicate a design issue with the inductor, such as insufficient inductance or core saturation.

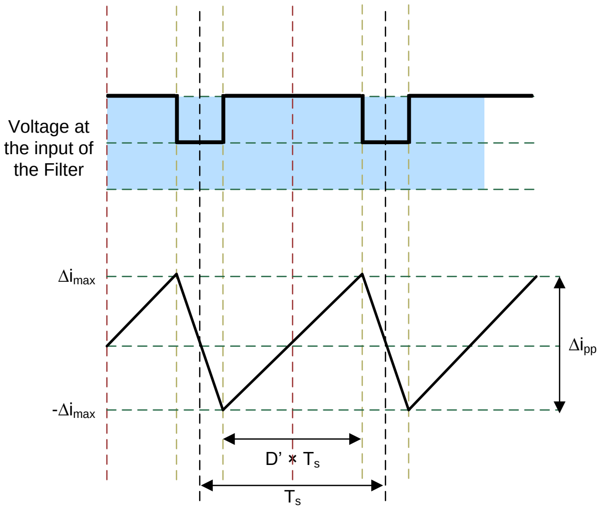

Figure 2.7: Current ripple calculation.

The voltage across the inductor is given by $u = L_g \times \frac{di}{dt}$. For VSR, this equation can be written as:

$$\left(\frac{u_{DC}}{2} - e_g\right) = L_g * \frac{\Delta \mathrm{i}_{\mathrm{pp}}}{D' * T_s} \tag{2.50}$$

where $T_s = 1/f_{sw}$ is the switching period and D' is the duty cycle for which the switches are ON. For control design, D is assumed to be the voltage at the other terminal of the inductor and is related to D' by $D' = 1 - D$. Rearranging the current ripple at any instant in the AC waveform is given as

$$\Delta \mathrm{i}_{\mathrm{pp}} = \frac{\mathrm{D}' * T_s * \left(\frac{u_{DC}}{2} - e_g\right)}{L_g}. \tag{2.51}$$

Now assuming the modulation index to be m_a the duty cycle can be given as $D' = m_a{}^* \sin(\omega t)$ and assuming that $e_g = \mathrm{D}'^* \, (u_{DC}/2)$, (2.51) can be revised.

$$\Delta \mathrm{i}_{\mathrm{pp}} = \frac{u_{DC} * T_s * m_a * \sin(\omega t) * (1 - m_a \sin(\omega t))}{2 * L_g}. \tag{2.52}$$

From (2.52) , it is clear that the peak ripple is a factor where the input AC is in the sinusoidal waveform. To get the maximum value differentiating the equation (2.52) with respect to time,

$$\frac{d\left(\Delta \mathrm{i}_{\mathrm{pp}}\right)}{dt} = \mathrm{K}\left\{\cos(\omega t) * (1 - m_a \sin(\omega t)) - m_a \sin(\omega t) * \cos(\omega t)\right\} = 0 \tag{2.53}$$

which gives the maximum ripple exists at $\sin(\omega t) = 1/\left(2 * m_a\right)$, substituting this value, (2.54) is derived.

$$\Delta \mathrm{i}_{\mathrm{pp}_{\max}} = \frac{u_{DC} * T_s}{8 * L_g} \Rightarrow L_g = \frac{u_{DC}}{8 * f_{sw} * \Delta \mathrm{i}_{\mathrm{pp}_{\max}}}. \tag{2.54}$$

2.4.4 DC-link capacitor design

The DC-link capacitor is an essential component in a power electronic converter, which helps to smooth out the DC-link voltage and reduce voltage ripple. The maximum input power is an important parameter that determines the minimum capacitance of the DC-link capacitor. This is because the energy stored in the capacitor must be sufficient to support the input power during transient periods. In addition to the maximum input power, the allowable voltage deviation limit is also an important factor that affects the minimum capacitance of the DC-link capacitor. The allowable voltage deviation limit is the maximum acceptable deviation in the DC voltage from its nominal value. This deviation can occur due to variations in the input voltage, load current, or switching frequency of the converter. The DC-link capacitor should be designed such that the voltage deviation stays within the acceptable limit. Ref. [59, 60] gives a detailed design method for the DC-link capacitor. The variation of energy in the DC-link capacitor over one PWM period is given by

$$\Delta W \approx \frac{\Delta P_{\max} \cdot T_d}{2} \tag{2.55}$$

where $\Delta P_{\max}$ is the maximum power variation of converter and T_d is the response time of voltage control loop (five to ten times the modulation period) [59]. In addition, the voltage deviation is expressed by

$$\Delta u_{DC} \approx \frac{\Delta W}{C u_{DC}} \tag{2.56}$$

where Δv_{DC} is the maximum allowable DC-link voltage deviation. Substituting (2.55) in (2.56), the minimum capacitance is calculated as

$$C_{\min} \geq \frac{\Delta P_{\max} T_d}{2 u_{DC} \Delta u_{DC}}. \tag{2.57}$$

2.5 Summary

In this chapter, the models for BTB converters-fed PMSM drive system have been explicitly developed in both continuous and discrete time forms. The lab-constructed testbench with the self-designed BTB converter box has also been depicted in detail. Overall, this chapter paves the way for the rest of the dissertation by providing the necessary mathematical models and experimental setups for testing and analyzing the behavior of the control strategies for the BTB converter-fed PMSM drive system.

CHAPTER 3

Classical predictive control techniques for BTB converter-fed PMSM system

This chapter discusses two classical predictive control strategies for the BTB converter-fed PMSM drive systems and presents their respective control performances in experimental evaluation.

- Firstly, the basic principle of the predictive control strategy without modulation, i.e., FCS-MPC, is discussed. The time delay compensation, which should be considered into the strategy to compensate for the errors caused by digital implementation in practical system, is also introduced. Besides, the specific application of FCS-MPC in the BTB converter-fed PMSM drive system, which involves the model predictive current control (MPCC) for the machine side and model predictive power control (MPPC) for the grid side (see Sec. 3.2), is described in detail in terms of the control block diagram, controller design, and experimental waveforms.
- Secondly, the basic principle of predictive control strategy with modulation, i.e., Deadbeat Predictive Control (DBPC), is described, and it is applied to both the machine side and grid side (see Sec. 3.3) in the BTB converter-fed PMSM drive system. By assuming the desired behavior can be reached at the next time instant, it directly calculates the voltage vector, which indicates a simple digital realization. Its control performance is also evaluated on the testbench presented in Chap. 2.

3.1 Background

The research works on predictive control of power electronic converters can be traced back to as early as the 1980s [61, 62], and a wide range of predictive control techniques with different control concepts have been developed over the years. The two most popular predictive control techniques are PI-MPC and PI-DBPC [63]. Predictive control techniques have gained popularity in power electronics applications due to their ability to provide optimized control actions by predicting the future behavior of the system according to mathematical models.

PI-MPC is a modulator-free predictive control technique. Considering its advantage of being able to reach a reference value with a fast dynamic response while satisfying a set of constraints, PI-MPC has been widely studied. By making use of the inherent discrete nature of power converters, PI-MPC evaluates the effect of each possible switching vector on the concerned variables in a predefined criterion and selects the optimal one that can minimize the differences between the concerned variables and their references.

PI-DBPC, on the other hand, is a modulator-based predictive control technique. The control objective of PI-DBPC is to achieve zero steady-state error in the converter output voltage or current. It generates control actions by predicting the future behavior of the system and calculating the control inputs that force the system to reach the desired output at the next time instant. This technique is very fast and accurate and is suitable for applications where the converter output needs to track a desired reference signal quickly.

3.2 Predictive control without modulation

3.2.1 Basic principle of FCS-MPC

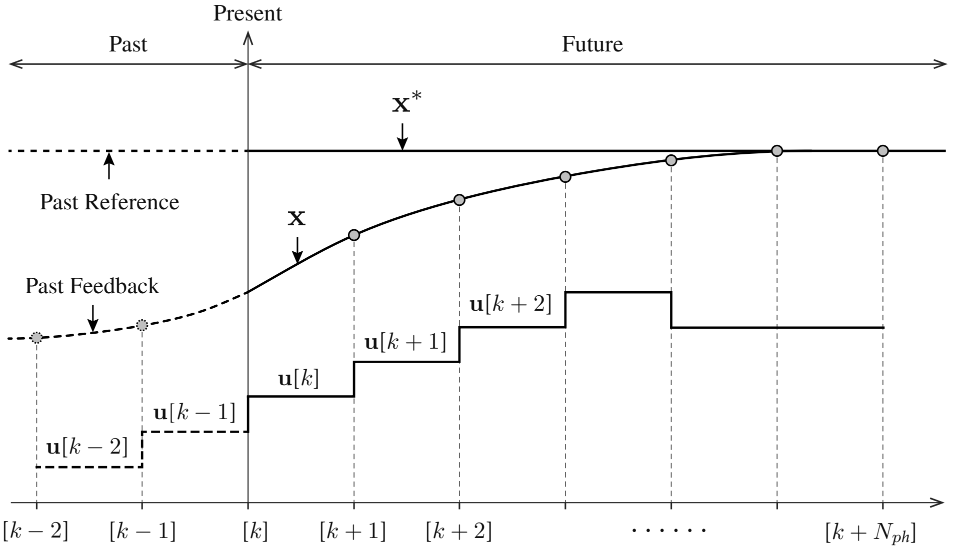

Figure 3.1: Operating principle of MPC (N_{ph} = prediction horizon).

The generic working principle of an FCS-MPC is shown in Fig. 3.1 [32]. The prediction of future errors and taking preventive control actions make the system more robust and efficient. The prediction horizon N_{ph}, which is a user-defined parameter, determines the length of the future prediction. The cost function is a critical component of the FCS-MPC strategy as it determines the optimization objective. The cost function can be formulated to reach various objectives, such as minimizing the error between the reference and the predicted output. FCS-MPC provides a systematic way to handle constraints on the control inputs and the system state variables. The constraints can be either hard or soft constraints and can be incorporated into the optimization problem. Solving the optimization problem provides the optimal control action sequence that can be applied to the system. The FCS-MPC strategy ensures that the control input sequence satisfies the constraints and drives the system to track the desired reference trajectory.

The working principle of FCS-MPC can be divided into three main components: prediction, optimization, and receding horizon strategy.

- **Prediction**: The FCS-MPC is based on numerical optimizations or online iterations. The future values of state variable $\boldsymbol{x}$ and control input sequence $\boldsymbol{u}$ are predicted for a prediction horizon N_{ph} by using the system model and feedback measurements at the $[k]^{\text{th}}$ instant.

- **Optimization**: The predictions are evaluated by a cost function that defines the system control objectives or desired behavior. A generic form of cost function is defined as a nonlinear function of reference, predicted, and input sequences:

$$J_x[k]=\boldsymbol{f}\left[\boldsymbol{x}^*[k],\cdots,\boldsymbol{x}^*\left[k+N_{ph}\right],\boldsymbol{x}[k],\boldsymbol{u}[k],\cdots,\boldsymbol{u}\left[k+N_{ph}\right]\right]. \tag{3.1}$$

The input control sequence that minimizes $J_x[k]$ is selected as an optimal actuation:

$$\boldsymbol{u}^{op}[k]=\arg\min_{\boldsymbol{u}} J_x[k]. \tag{3.2}$$

- **Receding horizon strategy**: The first element of the optimal input sequence $\boldsymbol{u}[k]=\boldsymbol{u}^{op}[k]$ is applied to the plant. As a result, the state variable $\boldsymbol{x}$ moves toward the reference trajectory $\boldsymbol{x}^*$. The process of measuring new feedback variables, predicting new system behavior, and optimizing performance cost is repeated during each sampling interval. This procedure is called the receding horizon strategy.

The well-known cost function $J_x, x\in\{m,g\}$ is the form with the prediction horizon of 1 , and its generalized form is

$$\begin{cases} J_x\left(\overrightarrow{\boldsymbol{S}}_x^{opt}[k]\right)=\min\limits_{\overrightarrow{\boldsymbol{S}}_x^{abc}\in V_x} J_x\left(\overrightarrow{\boldsymbol{S}}_x^{abc}[k]\right) \\ J_x\left(\overrightarrow{\boldsymbol{S}}_x^{abc}[k]\right)=\lambda_f\left\|F_x^*-f_x[k+1]\right\|^2+\zeta_x \end{cases} \tag{3.3}$$

where $f_x[k+1]$ denotes concerned variables predicted based on the possible switching state $\vec{S}_x^{abc}[k]$ of instant k, $\vec{S}_x^{\text{opt}}[k]$ denotes the optimal switching state of instant k, F_x^* denotes the references of the concerned variables, and ζ_x represents the constraint. According to their nature, the terms in the cost function can be classified into different groups to facilitate the adjustment procedure of weighting factors λ_f, and the branch and bound method illustrated in [35] is commonly used to tune λ_f in various cost functions (the cost function with equally important terms, the cost function with secondary term, etc.). ζ_x is introduced into the cost function to limit the concerned system variables within a safe range, and it is generally given by

$$\zeta_x=\begin{cases} 0, & \text{if } \left\|h_x\left(\overrightarrow{\boldsymbol{S}}_x^{abc}[k]\right)\right\|\leq\left\|h_x^{\max}\right\| \\ \infty, & \text{if } \left\|h_x\left(\overrightarrow{\boldsymbol{S}}_x^{abc}[k]\right)\right\|>\left\|h_x^{\max}\right\| \end{cases} \tag{3.4}$$

where h_x and $h_x^{\max}$ denote the mathematical expression and maximum of the concerned system variables, respectively.

In MPC, the effect of each possible converter switching state on the concerned variables is calculated according to the predictive model, and the optimal one, i.e., $\vec{\boldsymbol{S}}_x^{opt}[k]$, selected during $[k, k+1]$ should be applied during the entire time interval of $[k, k+1]$ in an ideal case. However, in a practical system, the time delay in digital implementation makes $\vec{\boldsymbol{S}}_x^{opt}[k]$ cannot be applied to power switches at instant k in time [64]. To address this problem, time delay compensation is considered into MPC so that the optimal switching state $\vec{\boldsymbol{S}}_x^{opt}[k]$ for interval $[k, k+1]$ can be calculated during interval $[k-1, k]$ and applied at instant k. The cost function with time delay compensation is defined as

$$\begin{cases} J_x\left(\vec{\boldsymbol{S}}_x^{opt}[k+1]\right) = \min\limits_{\vec{\boldsymbol{S}}_x^{abc}\in V_x} J_x\left(\vec{\boldsymbol{S}}_x^{abc}[k+1]\right) \\ J_x\left(\vec{\boldsymbol{S}}_x^{abc}[k+1]\right) = \lambda_f \left\|F_x^* - f_x[k+2]\right\|^2 + \zeta_x \end{cases} \tag{3.5}$$

It can be found that with the time delay compensation, the optimal switching state of each instant is calculated in the previous time interval and can be applied to converters at the exactly right instant, which improves the control accuracy.

3.2.2 PI-MPC strategy for BTB converter-fed PMSM systems

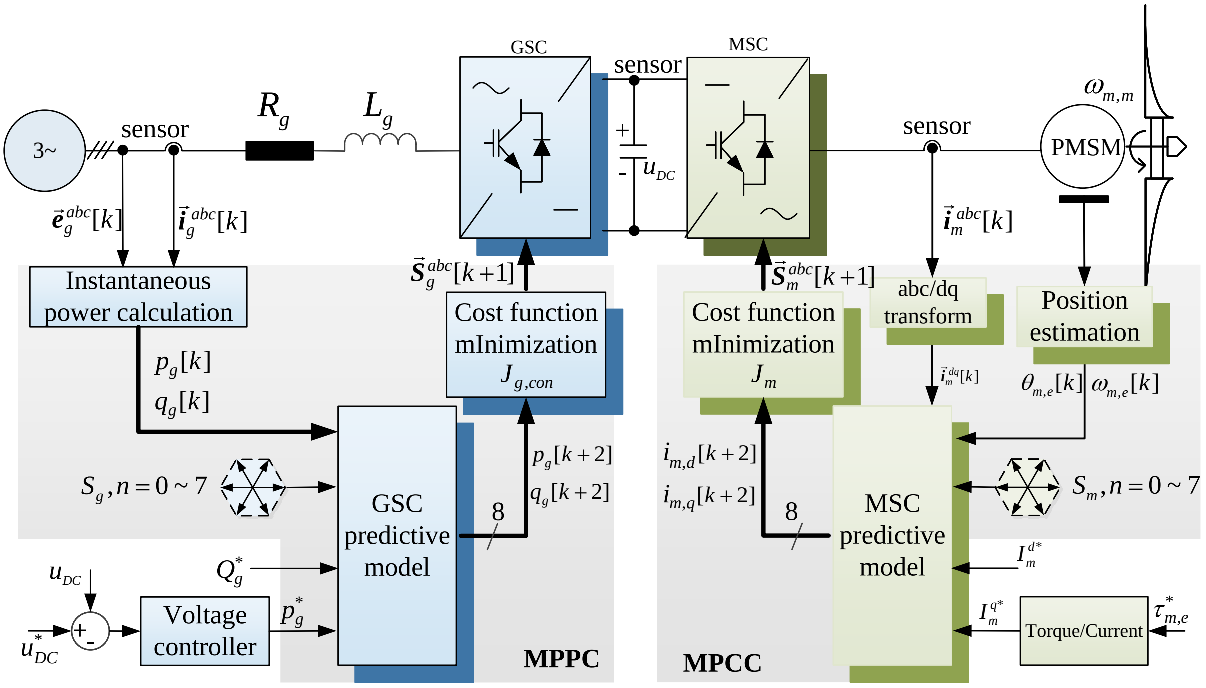

Figure 3.2: Control structure of PI-MPC strategy.

This section will present the BTB converter-fed PMSM systems based on PI-MPC strategy. Specifically, it will delve into the MPCC method for the machine side and the MPPC approach for the grid side. To visualize this control scheme, the control structure for the BTB converter-fed PMSM system based on PI-MPC strategy is depicted in Fig. 3.2. The control goals are to realize well-regulated DC-link voltage, electromagnetic torque, and reactive power. For GSC, the active power references (P_g^*) are obtained using a voltage PI controller. As the energy can flow in both directions, from the grid to the PMSM and vice versa, P_g^* can take positive or negative values. The reactive power reference Q_g^* is set to 0 Var to improve the PF for the system. MPPC is used to keep track of P_g^* and Q_g^* in the proposed system. For MSC, the torque reference ($\tau_{m,e}^*$) is tracked by controlling the current of the PMSM, and MPCC is used to keep track of $\boldsymbol{I}_m^{d*}$ and $\boldsymbol{I}_m^{q*}$.

3.2.2.1 MPCC for machine-side converter

The discretized current equation of PMSM in dq coordinate system at $(k+2)^{\text{th}}$ instant is given by

$$\begin{aligned}\begin{pmatrix} i_m^d[k+2] \\ i_m^q[k+2] \end{pmatrix} &= \begin{bmatrix} 1-\frac{R_m T_s}{L_m} & w_{m,e}[k+1]T_s \\ -w_{m,e}[k+1]T_s & 1-\frac{R_m T_s}{L_m} \end{bmatrix} \begin{pmatrix} i_m^d[k+1] \\ i_m^q[k+1] \end{pmatrix} \\ &+ \frac{T_s}{L_m}\boldsymbol{I}_2 \begin{pmatrix} u_m^d[k+1] \\ u_m^q[k+1] \end{pmatrix} - \begin{pmatrix} 0 \\ \frac{T_s \psi_r}{L_m} w_{m,e}[k+1] \end{pmatrix}\end{aligned} \tag{3.6}$$

where i_m, u_m, ψ_r, R_m, L_m, $\omega_{m,e}$ and T_s denote the stator current, stator voltage, permanent magnet flux linkage, stator resistor, stator inductor, electrical angular velocity, and sampling period, respectively, and $\boldsymbol{I}_2 = diag(1,1)$.

To achieve the tracking of torque reference $\tau_{m,e}^*$, the cost function of PMSM is defined as

$$\begin{aligned} J_m = \|I_m^{q*} - i_m^q[k+2]\|^2 + \left\|I_m^{d*} - i_m^d[k+2]\right\|^2 \\ + \underbrace{\begin{cases} 0, & \left\|\boldsymbol{i}_m^{dq}[k+2]\right\| \le \|i_m^{\max}\| \\ \infty, & \left\|\boldsymbol{i}_m^{dq}[k+2]\right\| > \|i_m^{\max}\| \end{cases}}_{h_{m,coni}} \end{aligned} \tag{3.7}$$

where $\boldsymbol{I}_m^{dq*}$ denotes the reference for stator current $\boldsymbol{i}_m^{dq}$, $h_{m,coni}$ denotes the constraint of stator current, i_m^{max} denotes the length limit of vector $\boldsymbol{i}_m^{dq}$ for system safety, and $\boldsymbol{I}_m^{dq*} = \frac{2\tau_{m,e}^*}{3n_p\psi_r}$. $\boldsymbol{i}_m^{dq}[k+2]$ of every switching vector $\boldsymbol{S}_m[k+1]$ are predicted in light of the expressions of $\boldsymbol{i}_m^{dq}$ of instant $k+2$, which can be obtained on the discrete models given in (3.6).

3.2.2.2 MPPC for grid-side converter

The discretized power equation of GSC in $\alpha\beta$ coordinate system at $(k+2)^{\text{th}}$ instant is given by

$$\begin{aligned}\begin{pmatrix} p_g[k+2] \\ q_g[k+2] \end{pmatrix} &= \frac{3T_s}{2L_g} \begin{bmatrix} e_g^\alpha[k+1] & e_g^\beta[k+1] \\ e_g^\beta[k+1] & -e_g^\alpha[k+1] \end{bmatrix} \begin{pmatrix} e_g^\alpha[k+1] - u_g^\alpha[k+1] \\ e_g^\beta[k+1] - u_g^\beta[k+1] \end{pmatrix} \\ &+ \begin{pmatrix} p_g[k+1] - \frac{T_s R_g}{L_g} p_g[k+1] - T_s \omega_g q_g[k+1] \\ q_g[k+1] - \frac{T_s R_g}{L_g} q_g[k+1] + T_s \omega_g p_g[k+1] \end{pmatrix}.\end{aligned} \tag{3.8}$$

MPC is generally adopted as the inner controller to track the active power reference P_g^* and reactive power reference Q_g^* in the GSC, and the cost function in conventional PI-MPC strategy is defined as [36]

$$\begin{aligned} J_{g,con} = & \left\|P_g^* - p_q[k+2]\right\|^2 + \left\|Q_g^* - q_g[k+2]\right\|^2 \\ & + \underbrace{\begin{cases} 0, & \|p_g[k+2]\| \le \left\|p_g^{\max}\right\| \\ \infty, & \|p_g[k+2]\| > \left\|p_g^{\max}\right\| \end{cases}}_{h_{g,conp}} \\ & + \underbrace{\begin{cases} 0, & \|q_g[k+2]\| \le \left\|q_g^{\max}\right\| \\ \infty, & \|q_g[k+2]\| > \left\|q_g^{\max}\right\| \end{cases}}_{h_{g,conq}} \end{aligned} \tag{3.9}$$

where $p_g[k+2]$ and p_g^{max} denote the value of instant $k+2$ and the allowable maximum of active power, respectively, and $q_g[k+2]$ and q_g^{max} denote the value of instant $k+2$ and allowable maximum of reactive power, respectively. $p_g[k+2]$ and $q_g[k+2]$ of every switching vector $\boldsymbol{S}_g[k+1]$ are predicted according to the expressions obtained via shifting forward by one T_s. P_g^* is produced by a DC-link voltage PI controller, and the load power is generally added to the output of voltage PI controller for fast dynamic response. $h_{g,conp}$ and $h_{g,conq}$ denotes the constraint of active power and reactive power, respectively, which is introduced into the cost function to limit the concerned system variables within a safe range. p_g, q_g, $p_g^{\max}$ and $q_g^{\max}$ denote the mathematical expression and maximum of the concerned system variables, respectively. As can be seen, a cascade control structure is adopted in this strategy, and an independent outer voltage PI controller is always necessary to provide the power reference for inner MPC.

3.2.3 PI parameters design for voltage control loop

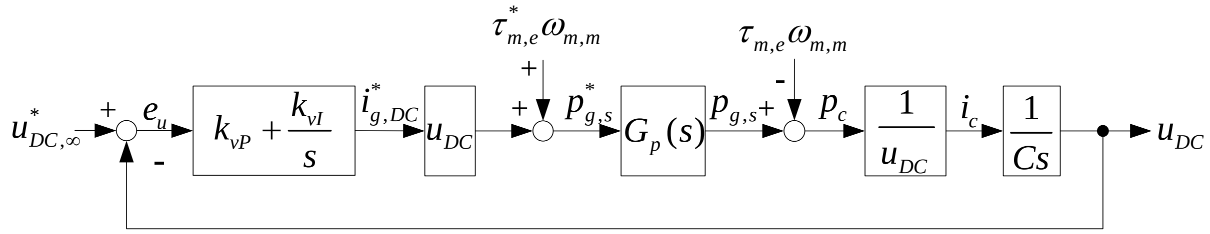

Figure 3.3: Block diagram of the system based on PI-MPC strategy.

Based on the control structure described in [42], the block diagram of the conventional PI-MPC system is presented in Fig. 3.3. The PI controller below is adopted as an outer control loop for DC-link voltage regulation

$$i_{DC}^* = k_{vP}e_u + k_{vI}\int e_u dt \tag{3.10}$$

where k_{vP} denotes proportional gain, k_{vI} denotes integral gain, and e_u denotes the difference between reference and actual value of DC-link voltage (namely, $e_u = u_{DC,\infty}^* - u_{DC}$). For

PI controller, the corresponding transfer function is $G_v(s) = k_{vP} + k_{vI}/s$. Then, the active power reference is calculated by $p^*_{g,s} = i^*_{g,DC}u_{DC} + \tau^*_{m,e}\omega_{m,m}$. The inner MPC controller can directly track the active power reference with fast response by applying the optimal switching state, so the transfer function of inner MPC controller can be treated as unity gain [65], namely, $G_p(s) = 1$. According to power balance, the following expression holds

$$p_{g,s} = \tau_{m,e}\omega_{m,m} + p_c \tag{3.11}$$

where $p_{g,s}$ is the power flowing out of GSC, $\tau_{m,e}\omega_{m,m}$ is the power consumed by PMSM, and p_c is the power consumed by DC-link capacitor. With the capacitor power, the capacitor current i_c can be calculated by

$$i_c = \frac{p_c}{u_{DC}} = C\frac{du_{DC}}{dt} \tag{3.12}$$

where C denotes the capacitance of DC-link capacitor. As an electromagnetic variable, the electromagnetic torque $\tau_{m,e}$ tracks its reference $\tau^*_{m,e}$ in a fast response, so $\tau_{m,e} \approx \tau^*_{m,e}$. Based on the above, the open-loop transfer function can be derived as

$$F_{ol}(s) = \left(k_{vP} + \frac{k_{vI}}{s}\right)\frac{1}{Cs}. \tag{3.13}$$

The cutoff frequency of the PI controller ω_{pi} is defined as

$$\omega_{pi} = \frac{k_{vI}}{k_{vP}}. \tag{3.14}$$

Generally, ω_{pi} is a fraction of the crossover frequency of voltage regulator ω_{vr}, so the PI controller can be approximated as follows at the vicinity of ω_{vr} in the frequency region

$$G_v(s) = k_{vP} + \frac{k_{vI}}{s} \approx k_{vP}, \quad \text{at } s = j\omega_{vr}. \tag{3.15}$$

Accordingly, the open-loop transfer function in (3.13) can be simplified as follows at the vicinity of ω_{vr}

$$F_{ol}(s) = k_{vP}\frac{1}{Cs}, \quad \text{at } s = j\omega_{vr}. \tag{3.16}$$

Since $|F_{ol}\left(j\omega_{vr}\right)| = 1$, the proportional gain k_{vP} of PI controller can be estimated by

$$k_{vP} = C\omega_{vr}. \tag{3.17}$$

The integral gain k_{vI} of PI controller can be set from the condition that the cutoff frequency ω_{pi} of PI controller should be a fraction of the crossover frequency ω_{vr} [66], namely

$$\omega_{pi} \le \frac{\omega_{vr}}{5}. \tag{3.18}$$

Thus, k_{vI} of PI controller can be estimated by

$$k_{vI} \le \frac{\omega_{vr}k_{vP}}{5}. \tag{3.19}$$

In testbench, the rough range of the gains of PI controller is firstly calculated based on the steps above and then the gains need to be further tuned in practical experiments.

3.2.4 Experimental verification

3.2.4.1 Steady-state performances

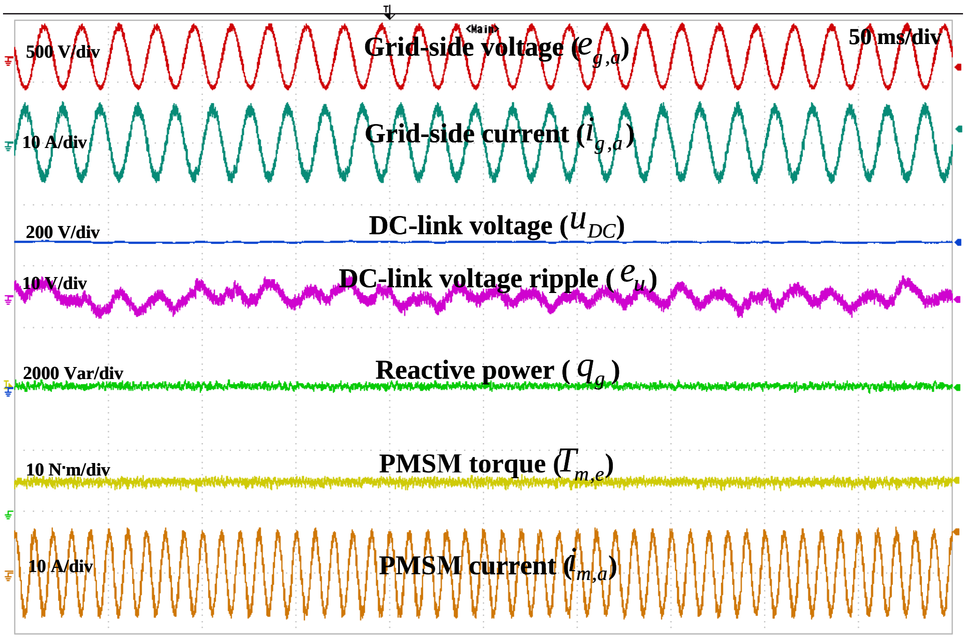

(a) Experimental waveforms.

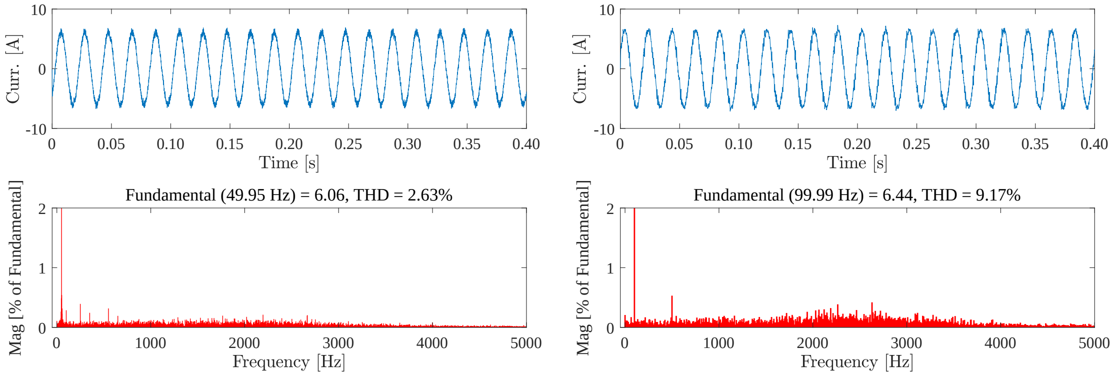

(b) Grid-side current spectrum. (c) Machine-side current spectrum.

Figure 3.4: Steady-state experimental results of the PI-MPC strategy.

The results presented in Fig. 3.4(a) demonstrate the control performance of the conventional PI-MPC strategy in regulating the PMSM and GSC. Achieving a sinusoidal stator current of 6 A, the PMSM operates at the rated speed of 1500 r/min and generates the required reference torque of -15 N·m. For GSC, the PI-MPC strategy ensures stable operation of the DC-link voltage by continuously transferring the energy generated by PMSM to the grid. The DC-link voltage is boosted to 480 V and regulated within ± 4 V, as shown by the error between the actual DC-link voltage and its reference (i.e., $e_u = u_{DC} - u^*_{DC,\infty}$). Moreover, the reactive power has been kept around 0 Var, resulting in a sinusoidal grid-side current in the opposite phase with the grid-side voltage. The current spectrum of the grid-side current is shown in Fig. 3.4(b) and the machine-side current is shown in Fig. 3.4(c). The equivalent switching frequency in this state is around 2.9 kHz. For the grid-side, the current is 6.06 A, and the THD is 2.63 %. For the machine-side, the current is 6.44 A, and the THD is 9.17 %.

3.2.4.2 Step change of DC-link voltage

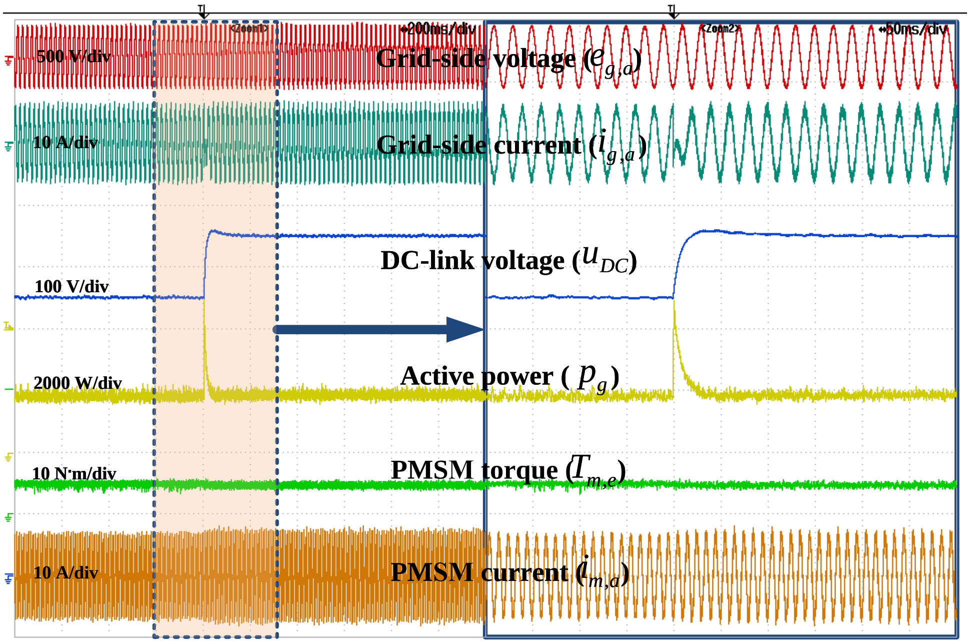

Figure 3.5: Experimental waveforms of PI-MPC strategy in the step change of DC-link voltage.

Fig. 3.5 presents the experimental waveforms of the conventional PI-MPC strategy in the step change of DC-link voltage (from 450 V to 550 V) at the rated operating condition. An offset has been added to the Digital-to-Analog Converter (DAC) output, and the short yellow dash with a "T" on it indicates 0 W for active power waveform. To boost the DC-link voltage quickly, the active power changes from around -2200 W to a positive value of around 900 W. That means the grid starts to provide active power along with the PMSM to charge the DC-link capacitor in a quick manner. The voltage overshoot during the regulation is around 10 V, and it takes around 90 ms for conventional PI-MPC strategy to reach the new voltage reference. It is worth noting that the control strategy is able to regulate the DC-link voltage to the new reference, despite the voltage overshoot. Therefore, further improvement is necessary to ensure robust and fast response of the system during such step changes.

3.2.4.3 Step change of torque

The experiment results of the conventional PI-MPC strategy under abrupt torque change at rated speed are shown in Fig. 3.6. The DC-link voltage increases at the moment when torque changes from 12 to -12 N·m since PMSM suddenly starts to generate power instead of consuming power.To reach the desired electromagnetic torque magnitude in the opposite direction,

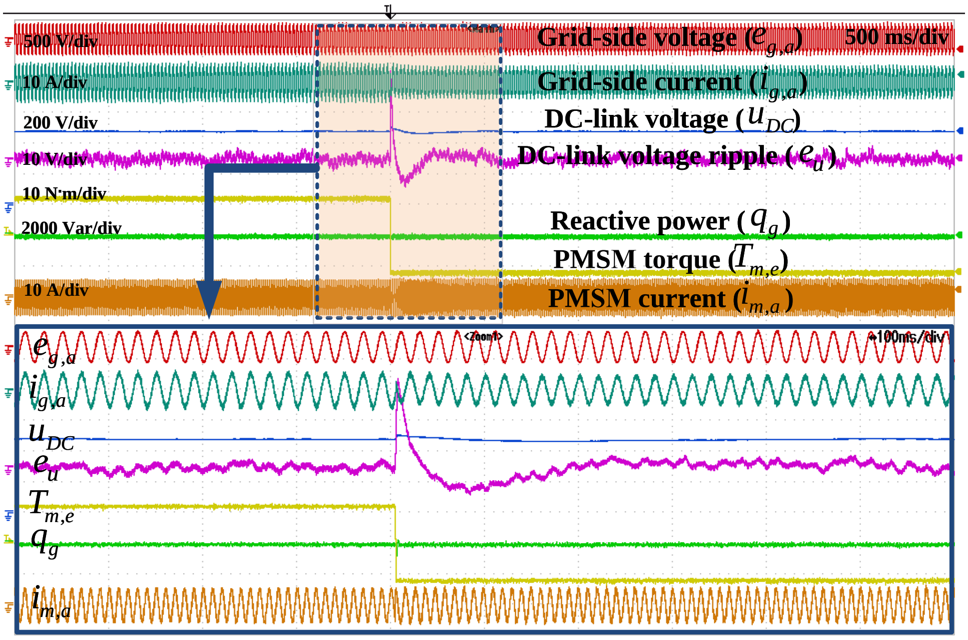

Figure 3.6: Experimental waveforms of PI-MPC strategy in the step change of torque (from 12 to -12 N·m).

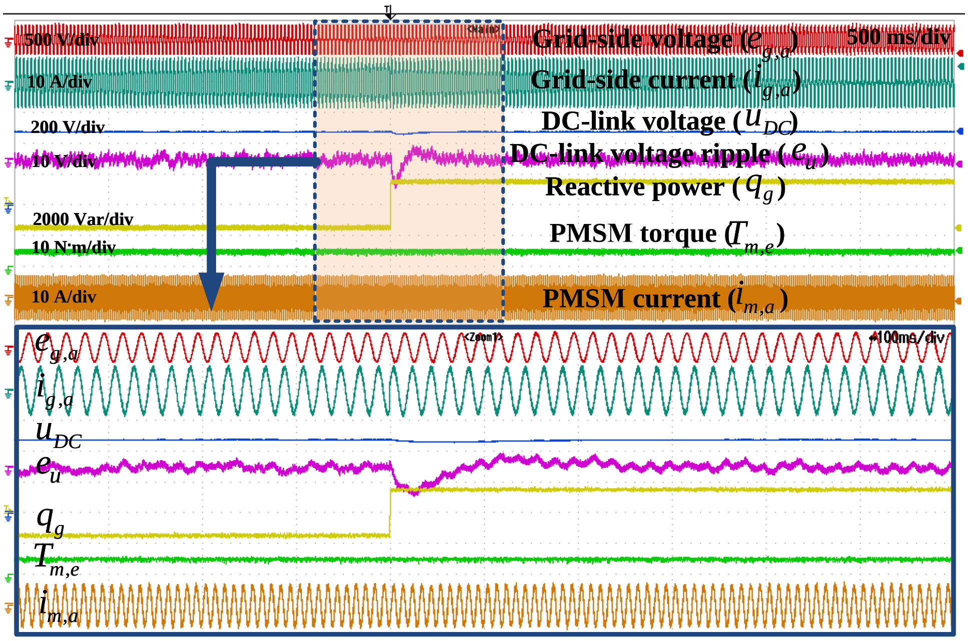

Figure 3.7: Experimental waveforms of PI-MPC strategy in the step change of reactive power.

the phase of PMSM current changes immediately once the new torque reference is issued. The PI-MPC strategy maintains a stable DC-link voltage by changing the direction of power flow. The active power waveform shows that the power is initially negative and then changes to positive as the PMSM starts to generate power. As can be seen from the curves, the peak errors of DC-link voltage e_u are 28 V for conventional PI-MPC strategy, and the recovery times of

DC-link voltage are around 200 ms.

3.2.4.4 Step change of reactive power

The reactive power changes cause a significant impact on the DC-link voltage regulation performance of the conventional PI-MPC strategy. In this case, the active power is also affected, and it takes a certain time to recover the active power to its reference value. As can be observed from Fig. 3.7, the DC-link voltage decreases rapidly after the reactive power reference changes from -1500 to 1500 Var, which results in an undershoot of around 10 V. The recovery time of the DC-link voltage in the conventional PI-MPC strategy is around 200 ms. Therefore, when reactive power changes abruptly, it can cause a disturbance DC-link voltage, and the control strategy should always control DC-link voltage overshoot within a small range for the safety of the system.

3.2.4.5 Step change of speed

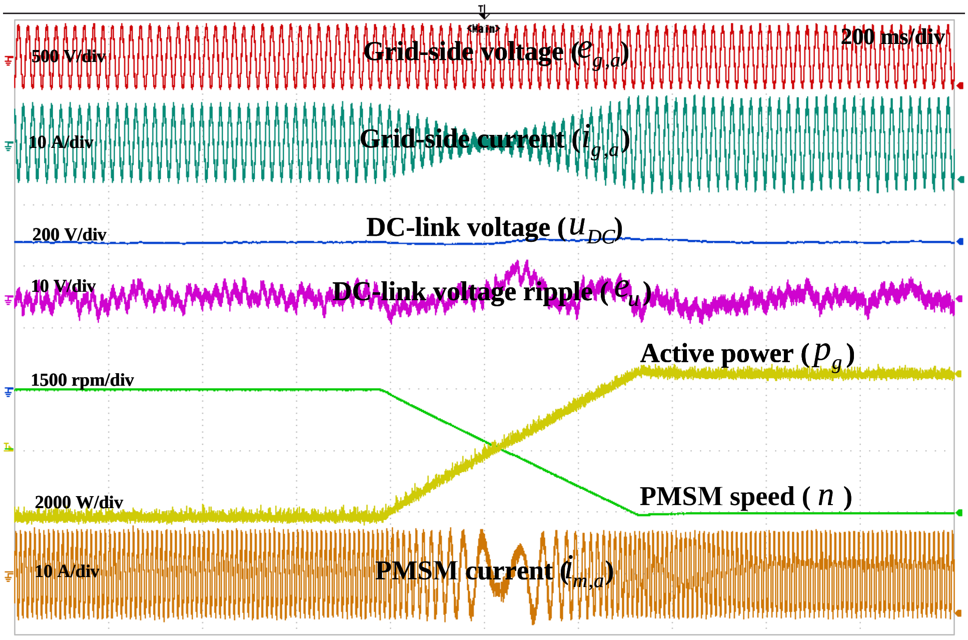

Figure 3.8: Experimental waveforms of PI-MPC strategy in the step change of speed.

The experiment results of the conventional PI-MPC strategy under abrupt speed changes are presented in Fig. 3.8. With the constant torque of -15 N·m, the operating status of machine changes from generating mode to motoring mode as the speed changes from 1500 to -1500 r/min. The grid-side current waveform also changes its phase angle as the direction of power flow reverses. In the motoring mode, the GSC needs to supply active power to PMSM to maintain the DC-link voltage, while in the generating mode, the GSC needs to absorb active power from the PMSM in order to avoid power accumulation on DC-link. It can be observed the peak errors of DC-link voltage are around 6 V, which indicates the effectiveness of the PI-MPC strategy in regulating the DC-link voltage under abrupt speed changes.

3.2.4.6 Robustness performance

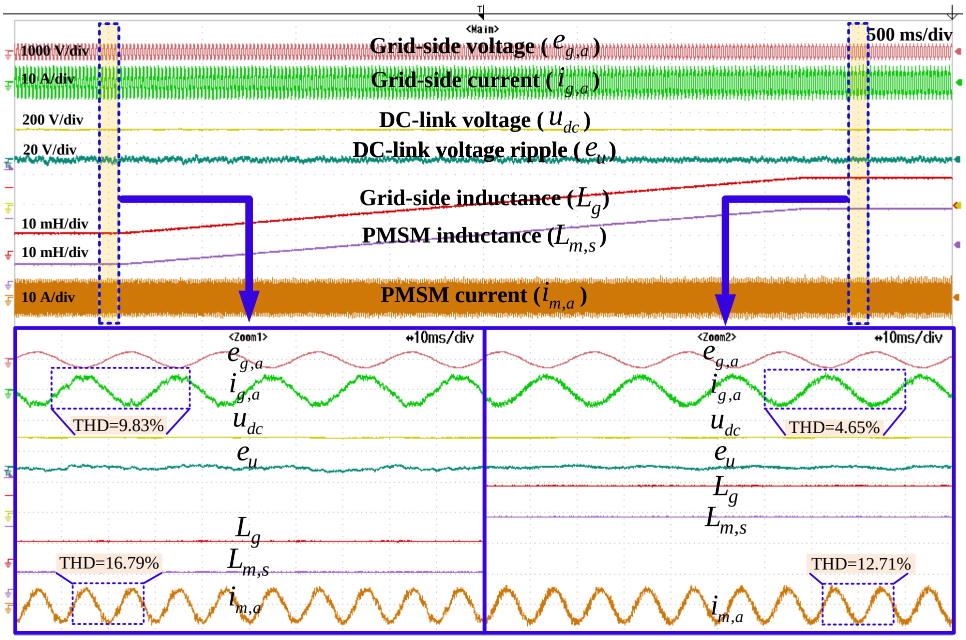

Figure 3.9: Experiment results of the PI-MPC strategy scheme under mismatched inductances.

The robustness of the control scheme is an important consideration in practical applications. The experiments with mismatched parameters help to evaluate the performance of the control scheme under different operating conditions. In addition to the inductance variation, the resistance variation also affects the system dynamics, but the effect of inductance variation is more significant. In this section, the values of grid-side inductor L_g and PMSM inductor $L_{m,s}$ are set to linearly increase from half of their actual value to twice their actual values (namely, from 50 % to 200 %) at the same time at the rated operating condition.

Fig. 3.9 shows the experimental results of the conventional PI-MPC strategy under mismatched inductances. It can be seen that the system remains controllable, even though the inductances deviate from their actual values. The current THDs are used to evaluate the system performance, and it is found that the current THDs become worse as the inductances deviate from their actual values. When L_g and $L_{m,s}$ are set to 50 % of their actual values, the grid-side current THDs increase to around 9.83 %, and the PMSM current THDs increase to around 16.79 %. When L_g and $L_{m,s}$ are set to 200 % of their actual values, the grid-side current THDs decrease to around 4.65 %, and the PMSM current THDs decrease to around 12.71 %. It is worth noting that the mismatched inductances will not exceed the range of 50 %-200 % of their actual values in practical systems. Therefore, the conventional PI-MPC strategy presents good robustness against mismatched inductances.

3.2.4.7 Current THDs and power factors

In addition to the steady-state performance at the rated operating condition, the experimental results of the conventional PI-MPC strategy at different operating speeds are also presented in Fig. 3.10. As the operating speed changes from 1000 to 1500 r/min with a constant electromagnetic

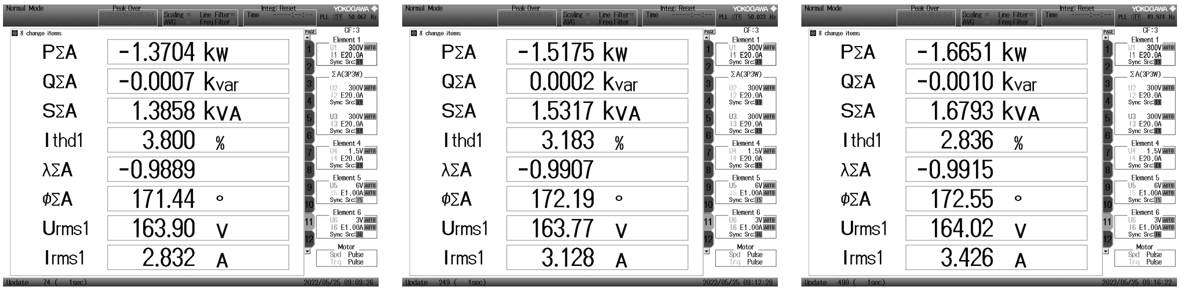

PΣA	-1.3704 kW
QΣA	-0.0007 kvar
SΣA	1.3858 kVA
Ithd1	3.800 %
λΣA	-0.9889
ϕΣA	171.44 °
Urms1	163.90 V
Irms1	2.832 A

PΣA	-1.5175 kW
QΣA	0.0002 kvar
SΣA	1.5317 kVA
Ithd1	3.183 %
λΣA	-0.9907
ϕΣA	172.19 °
Urms1	163.77 V
Irms1	3.128 A

PΣA	-1.6651 kW
QΣA	-0.0010 kvar
SΣA	1.6793 kVA
Ithd1	2.836 %
λΣA	-0.9915
ϕΣA	172.55 °
Urms1	164.02 V
Irms1	3.426 A

(a) 1000 r/min (b) 1100 r/min (c) 1200 r/min

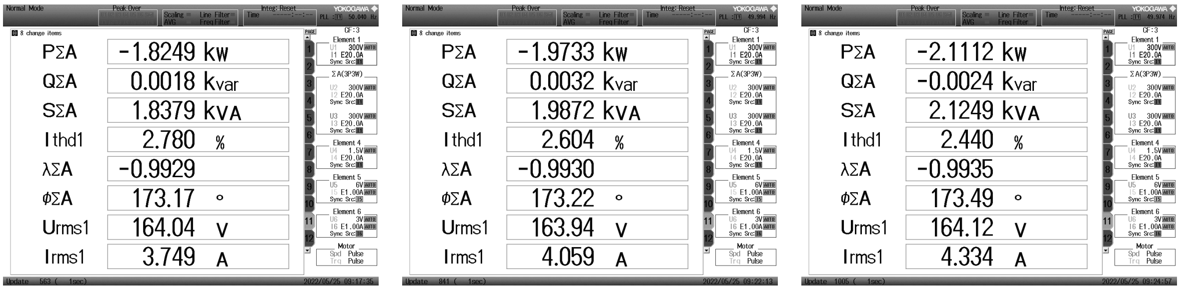

PΣA	-1.8249 kW
QΣA	0.0018 kvar
SΣA	1.8379 kVA
Ithd1	2.780 %
λΣA	-0.9929
ϕΣA	173.17 °
Urms1	164.04 V
Irms1	3.749 A

PΣA	-1.9733 kW
QΣA	0.0032 kvar
SΣA	1.9872 kVA
Ithd1	2.604 %
λΣA	-0.9930
ϕΣA	173.22 °
Urms1	163.94 V
Irms1	4.059 A

PΣA	-2.1112 kW
QΣA	-0.0024 kvar
SΣA	2.1249 kVA
Ithd1	2.440 %
λΣA	-0.9935
ϕΣA	173.49 °
Urms1	164.12 V
Irms1	4.334 A

(d) 1300 r/min (e) 1400 r/min (f) 1500 r/min

Figure 3.10: Power analyzer screenshots of PI-MPC strategy at different speeds.

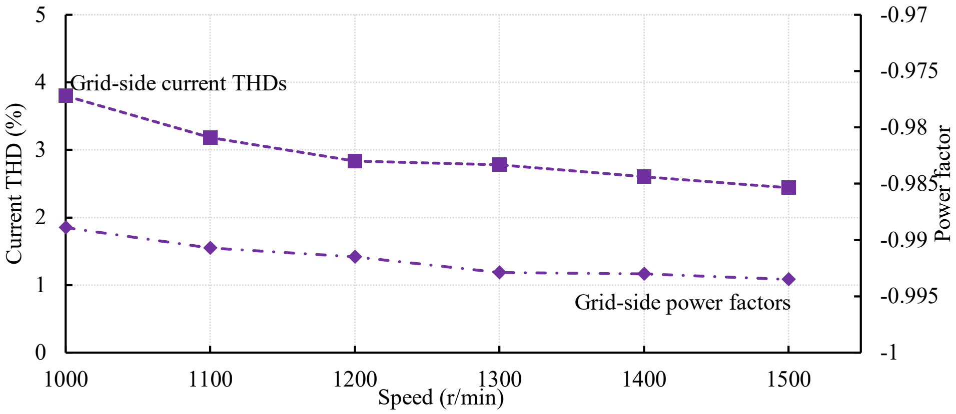

Figure 3.11: Current THDs and power factors of PI-MPC strategy.

torque of -15 N·m, the grid-side current THDs are controlled below 2.5%, and the grid-side power factors are controlled above 0.993 at the rated operation condition. The machine-side current THDs are around 9.17 % for all operating speeds, indicating well control performance. Furthermore, Fig. 3.11 summarizes the current THDs and power factors of the PI-MPC strategy at different operating conditions. In conclusion, the experimental results demonstrate that the conventional PI-MPC strategy can achieve good steady-state and dynamic control performance under different operating conditions, indicating its potential for practical applications in the BTB converter-fed PMSM system. However, its control performance is still limited, especially during the transients.

3.3 Predictive control with modulation

3.3.1 Basic principle of DBPC

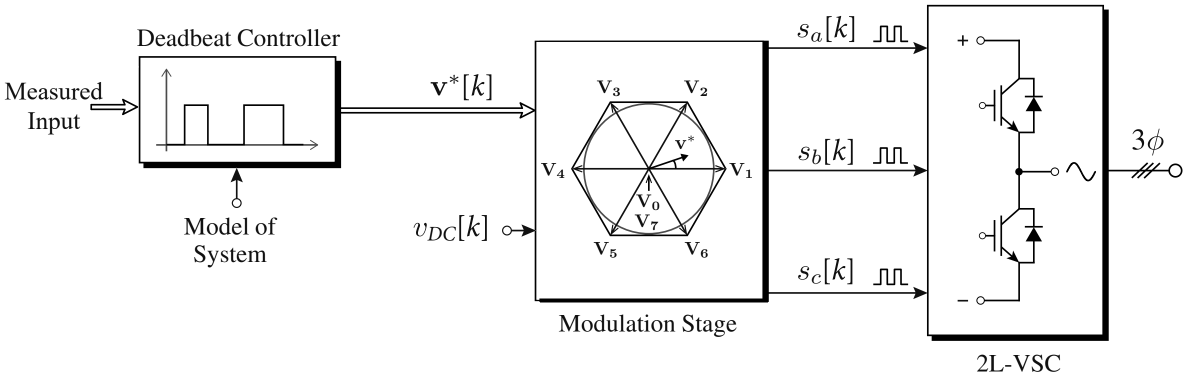

Figure 3.12: DBPC with a modulation.

Figure 3.12 [32] depicts a DBPC scheme with a modulation stage. The DBPC scheme is a popular choice for power converters due to its ability to provide fast and accurate responses, making it suitable for applications that require precise and rapid control [67]. Unlike the traditional PI controller, the deadbeat controller does not require a steady-state error to achieve the desired output. Instead, it aims to drive the output to the reference value within a single control cycle. Furthermore, the deadbeat controller takes advantage of the predictive nature by considering future behavior, which allows it to predict disturbances and make adjustments. However, the deadbeat controller also has some limitations [62]. Since it aims to achieve a zero steady-state error in a single cycle, it can be highly sensitive to system parameter mismatch and noise.

For a linear system, the following expression holds

$$\boldsymbol{x}[k+1] = \boldsymbol{A}\boldsymbol{x}[k] + \boldsymbol{B}\boldsymbol{u}[k] \tag{3.20}$$

where $\boldsymbol{x}$ is the state variable, and $\boldsymbol{u}$ is the input variable.

Then based on the concept of DBPC, the input can be directly calculated by

$$\boldsymbol{u}[k] = \boldsymbol{B}^{-1}\left[\boldsymbol{x}^*[k+1] - \boldsymbol{A}\boldsymbol{x}[k]\right] \tag{3.21}$$

where $\boldsymbol{x}^*[k+1]$ is the reference value.

Considering DBPC is one of the model-based predictive control, the time delay caused by digital implementation also exists in DBPC. Thus, the time delay compensation method [68,69] presented in FCS-MPC should also be included into DBPC to increase the prediction accuracy.

$$\boldsymbol{u}[k+1] = \boldsymbol{B}^{-1}\left[\boldsymbol{x}^*[k+2] - \boldsymbol{A}\boldsymbol{x}[k+1]\right] \tag{3.22}$$

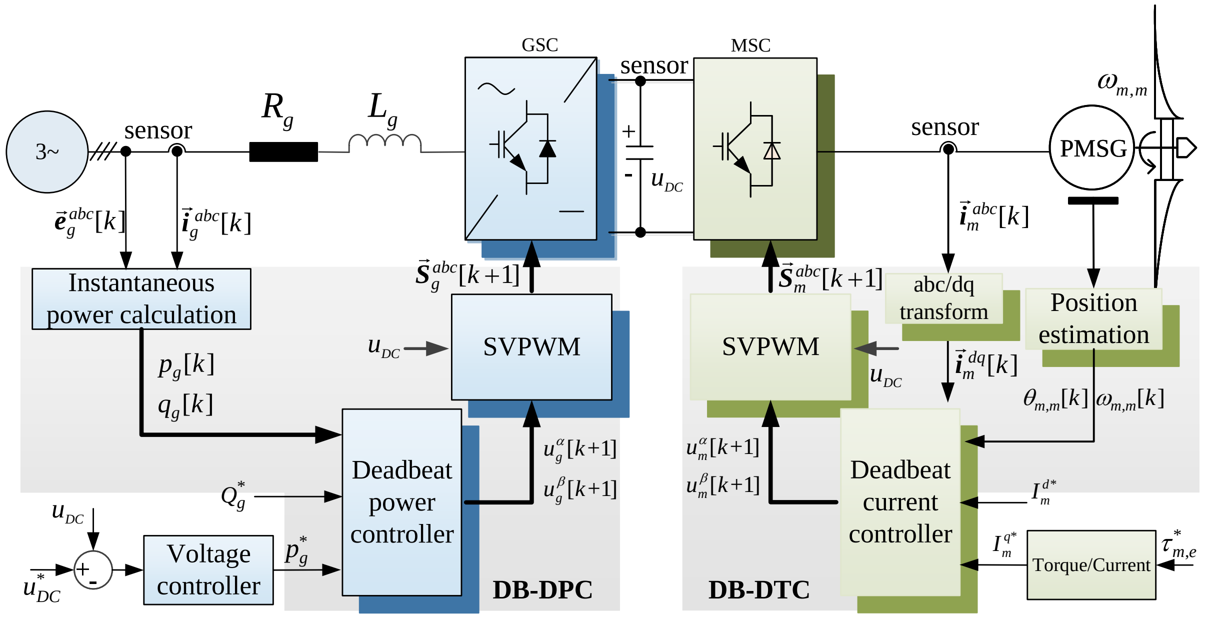

Figure 3.13: Control strategy of PI-DBPC strategy.

3.3.2 PI-DBPC strategy for BTB converter-fed PMSM systems

The control structure for the BTB converter-fed PMSM system based on PI-DBPC strategy is depicted in Fig. 3.13. To ensure a stable DC-link voltage, the grid active power reference P_g^* is calculated based on the PI voltage control loop. Additionally, the grid reactive power reference Q_g^* can be adjusted as per the system requirements to optimize the overall performance. The DC-link voltage reference u_{DC}^* is set based on the PMSM's requirements. By sampling real-time parameters and using mathematical models of the GSC and MSC, it is possible to predict the PMSM current, electromagnetic torque, DC-link voltage, and grid-side power for instant $k+2$. The switching state is then determined using the SVPWM technique and the corresponding IGBT is driven to generate the required output voltage. In the following, the deadbeat (torque) control (DB-DTC) for machine side and deadbeat (power) control (DB-DPC) for the grid side are introduced.

3.3.2.1 Deadbeat (torque) control for machine side

The DB-DTC is designed to regulate the current of PMSM to achieve a desired torque reference at the nest sampling interval. Its primary objective is to determine the appropriate voltage vector that needs to be assigned to the converter based on the system model and the desired reference. The generator model in discrete format is as below.

$$\begin{aligned}\vec{\boldsymbol{i}}_m^{dq}[k+2] = &\underbrace{\begin{bmatrix} 1-\frac{T_sR_m}{L_m} & T_s\omega_{m,e}[k+1] \\ -T_s\omega_{m,e}[k+1] & 1-\frac{T_sR_m}{L_m} \end{bmatrix}}_{=:\mathbf{A}_m[k+1]} \vec{\boldsymbol{i}}_m^{dq}[k+1] + \underbrace{\begin{bmatrix} \frac{T_s}{L_m} & 0 \\ 0 & \frac{T_s}{L_m} \end{bmatrix}}_{=:\mathbf{B}_m} \vec{\boldsymbol{u}}_m^{dq}[k+1] \\ &+ \underbrace{\begin{pmatrix} 0 \\ -\frac{T_s\psi_r}{L_m}\omega_{m,e}[k+1] \end{pmatrix}}_{=:\mathbf{H}_m[k+1]}\end{aligned} \tag{3.23}$$

$$\tau_{m,e}[k+1] = N_p\psi_r i_m^q[k+1] \tag{3.24}$$

The reference current can obtained by considering the torque equation of (3.24)

$$\overrightarrow{\boldsymbol{i}}_m^{dq*}[k+2] = \left(i_m^{d*}[k+2], \frac{\tau_{m,e}^*[k+2]}{N_p\psi_r}\right)^\top . \tag{3.25}$$

To compute the machine-side reference voltage vector, we can insert (3.25) into (3.23), and (3.26) can be got

$$\overrightarrow{\boldsymbol{u}}_m^{dq}[k+1] = \mathbf{B}_m^{-1}\left[\overrightarrow{\boldsymbol{i}}_m^{dq*}[k+2] - \mathbf{A}_m[k+1]\overrightarrow{\boldsymbol{i}}_m^{dq}[k+1] - \mathbf{H}_m[k+1]\right] . \tag{3.26}$$

It can be seen that, this process ensures that the reference voltage is calculated in a way that aligns with the system model.

The voltage vector to assign to a SVPWM can be calculated as $\overrightarrow{\boldsymbol{u}}_m^{\alpha\beta}[k+1] = \boldsymbol{M}_P^{-1}\overrightarrow{\boldsymbol{u}}_m^{dq}[k+1]$. Applying $\overrightarrow{\boldsymbol{u}}_m^{\alpha\beta}[k+1]$ would control the current to reach its reference $\overrightarrow{\boldsymbol{i}}_m^{dq*}[k+2]$ in the next sampling interval, thereby the torque reference is achieved, i.e., $\tau_{m,e}[k+2] = \tau_{m,e}^*[k+1]$.

3.3.2.2 Deadbeat (power) control for grid side

The discrete power models of GSC of instant $k+2$ can be described as

$$\begin{aligned}\begin{pmatrix} p_g[k+2] \\ q_g[k+2] \end{pmatrix} = &\frac{3T_s}{2L_g}\begin{bmatrix} e_g^\alpha[k+1] & e_g^\beta[k+1] \\ e_g^\beta[k+1] & -e_g^\alpha[k+1] \end{bmatrix}\begin{pmatrix} e_g^\alpha[k+1]-u_g^\alpha[k+1] \\ e_g^\beta[k+1]-u_g^\beta[k+1] \end{pmatrix} \\ &+\begin{pmatrix} p_g[k+1]-\frac{T_sR_g}{L_g}p_g[k+1]-T_s\omega_g q_g[k+1] \\ q_g[k+1]-\frac{T_sR_g}{L_g}q_g[k+1]+T_s\omega_g p_g[k+1] \end{pmatrix} .\end{aligned} \tag{3.27}$$

Deadbeat control is to calculate the desired variables by presuming that the system attains the intended behavior at the very end of every control period. Hence the desired voltage vector can be calculated by bringing $p[k+2] = P^*$ and $q[k+2] = Q^* = 0$ into (3.27)

$$\begin{aligned}\overrightarrow{\boldsymbol{u}}_g^{\alpha\beta}[k+1] = &\overrightarrow{\boldsymbol{e}}_g^{\alpha\beta}[k+1] - \frac{2L_g}{3T_s\left\|\overrightarrow{\boldsymbol{e}}_g^{\alpha\beta}[k+1]\right\|^2}\begin{bmatrix} e_g^\alpha[k+1] & e_g^\beta[k+1] \\ e_g^\beta[k+1] & -e_g^\alpha[k+1] \end{bmatrix} \\ &\cdot\begin{pmatrix} P_g^*-p_g[k+1]+\frac{T_sR_g}{L_g}p_g[k+1]+T_s\omega_g q_g[k+1] \\ Q_g^*-q_g[k+1]+\frac{T_sR_g}{L_g}q_g[k+1]-T_s\omega_g p_g[k+1] \end{pmatrix} .\end{aligned} \tag{3.28}$$

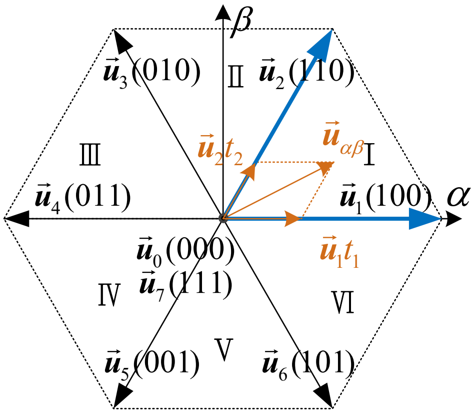

(a) Base vectors and sector division.

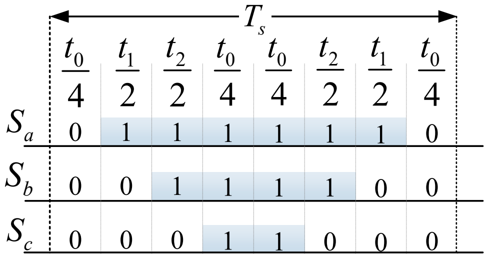

	$\frac{t_0}{4}$	$\frac{t_1}{2}$	$\frac{t_2}{2}$	$\frac{t_0}{4}$	$\frac{t_0}{4}$	$\frac{t_2}{2}$	$\frac{t_1}{2}$	$\frac{t_0}{4}$
S_a	0	1	1	1	1	1	1	0
S_b	0	0	1	1	1	1	0	0
S_c	0	0	0	1	1	0	0	0

(b) Switching patterns if $\vec{u}_{\alpha\beta}[k+1]$ locates in sector.

Figure 3.14: SVPWM.

$\vec{u}_g^{\alpha\beta}[k+1]$ should be applied to the VSC through SVPWM. The base vectors and sector division of SVPWM are shown in Fig. 3.14(a). The switching patterns of SVPWM when $\vec{u}_g^{\alpha\beta}[k+1]$ locates inside sector I are presented in Fig. 3.14(b), and there are eight switching patterns within a control period (T_s). t_0, t_1, and t_2 represent the dwell time for zero voltage vectors ($\vec{u}_0$ and $\vec{u}_7$), $\vec{u}_1$, and $\vec{u}_2$, respectively. Beginning and ending with the zero-voltage vector $\vec{u}_0$ (000), the SVPWM implements the other zero-voltage vector $\vec{u}_7$ (111) in the middle of T_s. Thus, the switching frequency of the SVPWM equals the control frequency, namely, $1/T_s$. Applying $\vec{u}_g^{\alpha\beta}[k+1]$ would (ideally) control the power to reach its reference at the end of the current control period, thereby achieving a dead-beat power control in $\alpha\beta$ frame.

3.3.3 Experimental verification

3.3.3.1 Steady-state performances

Within a sufficiently long period, the switching frequency of FCS-MPC is almost fixed in steady state. In the system with the PI-MPC strategy, the equivalent switching frequency is around 2.9 kHz at the rated operating condition. For a better comparison, the switching frequency of the PI-DBPC strategy is set to be the same as that of the PI-MPC strategy. The steady-state experiment waveform of the PI-DBPC strategy at the rated operating condition is presented in Fig. 3.15(a). The electromagnetic torque of PMSM has been set to -15 N·m at the speed of 1500 r/min, and the DC-link voltage has been regulated to 480 V. It is observed that the DC-link voltage ripple,

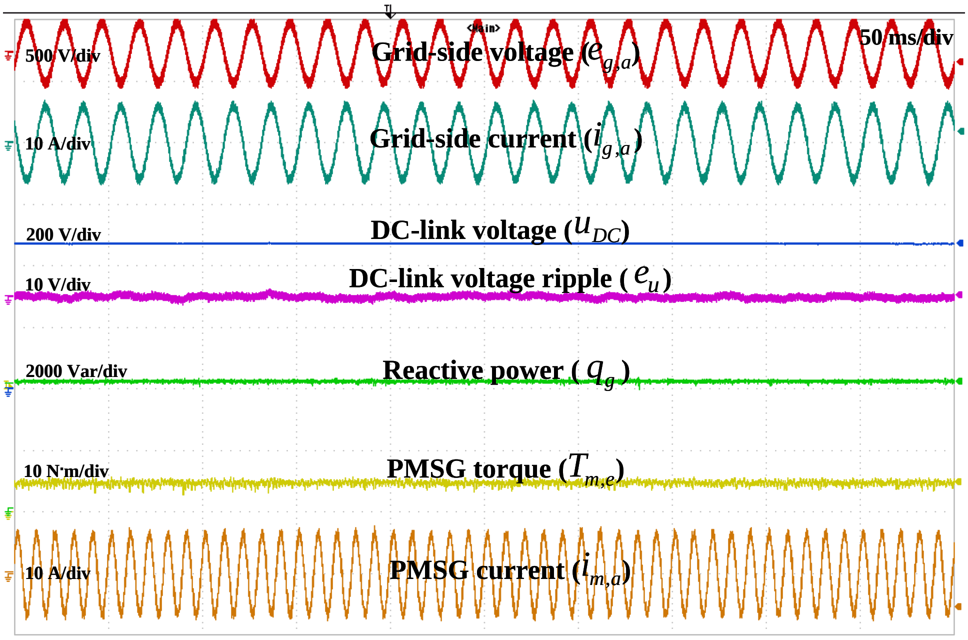

(a) Experimental waveforms.

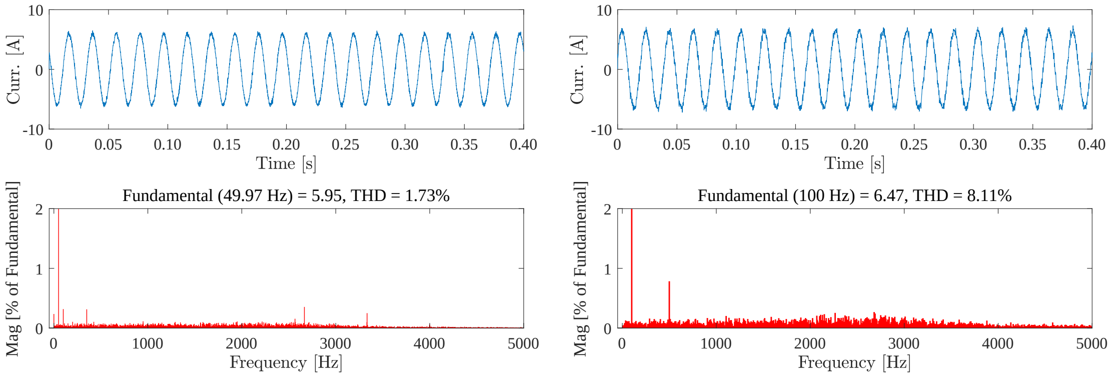

(b) Grid-side current spectrum. (c) Machine-side current spectrum.

Figure 3.15: Steady-state experimental results of the PI-DBPC strategy.

the voltage difference between the actual DC-link voltage and its reference, has been regulated within ± 2 V. Moreover, the reactive power has been kept around 0 Var, resulting in a sinusoidal grid-side current in the opposite phase with the grid-side voltage. The current spectrum of the grid-side current is shown in Fig. 3.15(b) and the machine-side current is shown in Fig. 3.15(c). For the grid-side, the current is 4.95 A, and the THD is 1.73 %. For the machine-side, the current is 5.47 A, and the THD is 8.11 %.

3.3.3.2 Step change of torque

Fig. 3.16 presents the experimental results of the PI-DBPC strategy under abrupt torque change. The DC-link voltage increases at the moment when torque decreases from 12 to -12 N·m since PMSM suddenly starts to produce power instead of consuming power. Although the direction

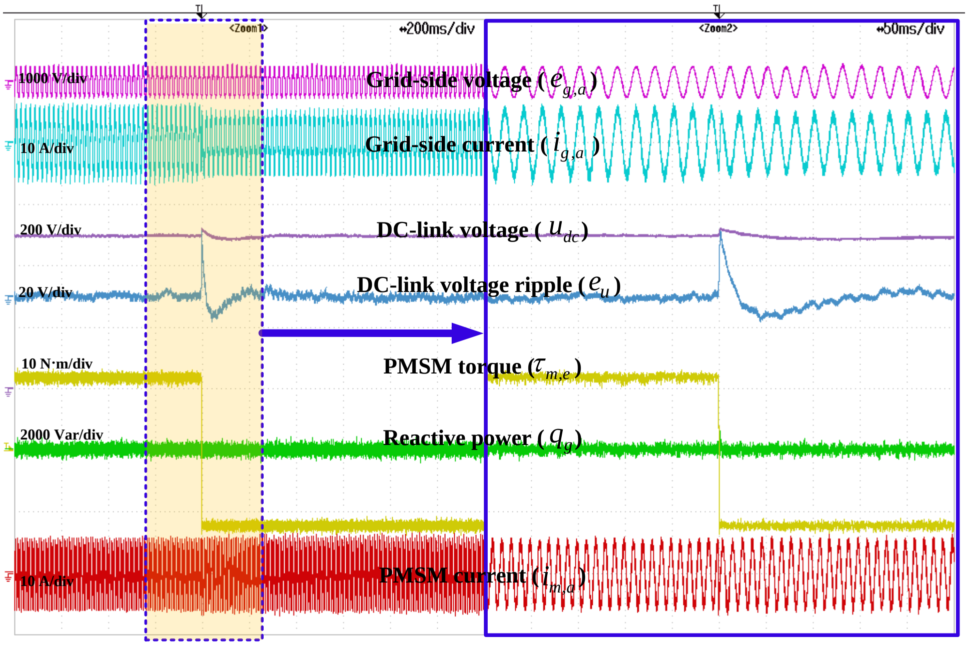

Figure 3.16: Experimental waveforms of PI-DBPC strategy in the step change of torque.

of active power flow is reversed under the abrupt torque changes, the DC-link voltage can be pulled back to its reference by transmitting the active power to the grid in time. The DC-link voltage is pulled back to its referenced within around 300 ms and the peak error is around 22 V during the regulation.

3.3.3.3 Step change of reactive power

Fig. 3.17 presents the experimental results of the PI-DBPC strategy under abrupt reactive power changes from -1000 to 1000 Var. The step change of reactive power disturbs DC-link voltage due to the coupling between active and reactive power. A disturbance, which is around 7 V, shows in the DC-link voltage waveform, and it takes 350 ms for the scheme to recover back to the steady state.

3.3.3.4 Step change of speed

Fig. 3.18 presents the experimental results of the PI-DBPC strategy under abrupt speed changes at -12 N·m . When the speed of PMSM is commanded to reverse from 1500 to -1500 r/min at the rated torque, the machine state is changed from generating power to consuming power, and the direction of grid-side active power changes correspondingly to keep the DC-link voltage constant. In this case, the DC-link voltage fluctuates with a peak error of 6 V during the regulation, and it takes around 400 ms for DC-link voltage to recover back to its original reference value.

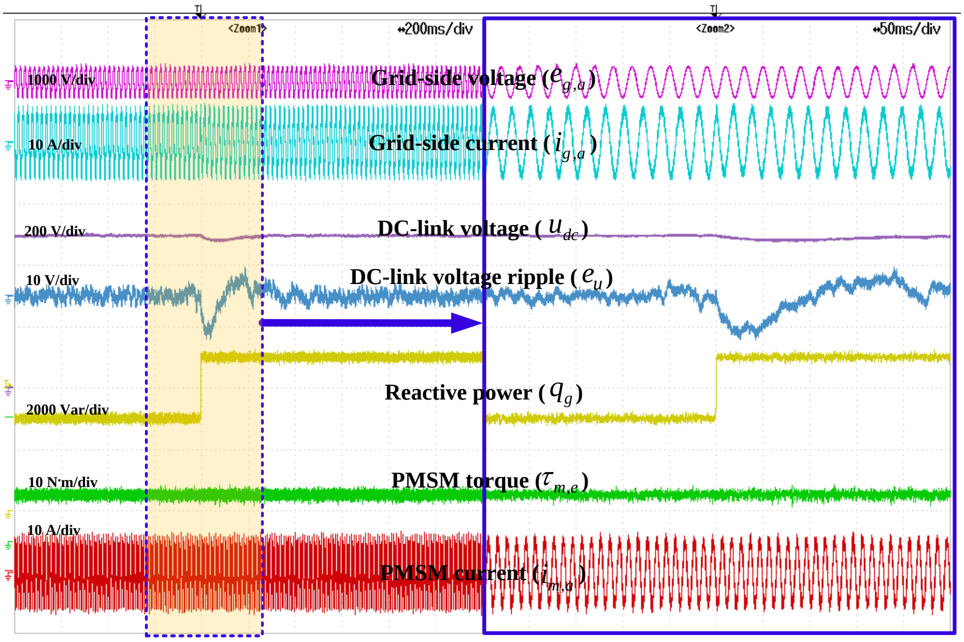

Figure 3.17: Experimental waveforms of PI-DBPC strategy in the step change of reactive power.

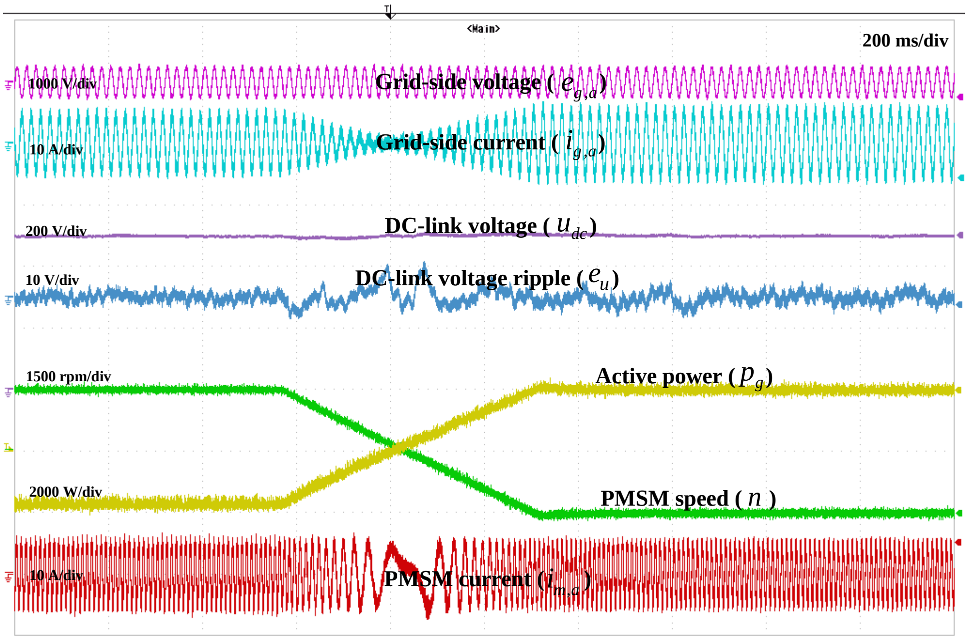

Figure 3.18: Experimental waveforms of PI-DBPC strategy in the step change of speed.

3.3.3.5 THDs and power factors analysis

In addition to the steady-state performance at the rated operating condition, the experimental results of the PI-DBPC strategy at different operating speeds are also presented in Fig. 3.19. The grid-side current THDs are controlled below 1.8%, and the grid-side power factors are controlled above 0.997 at the rated operating condition. The machine-side current THDs are around

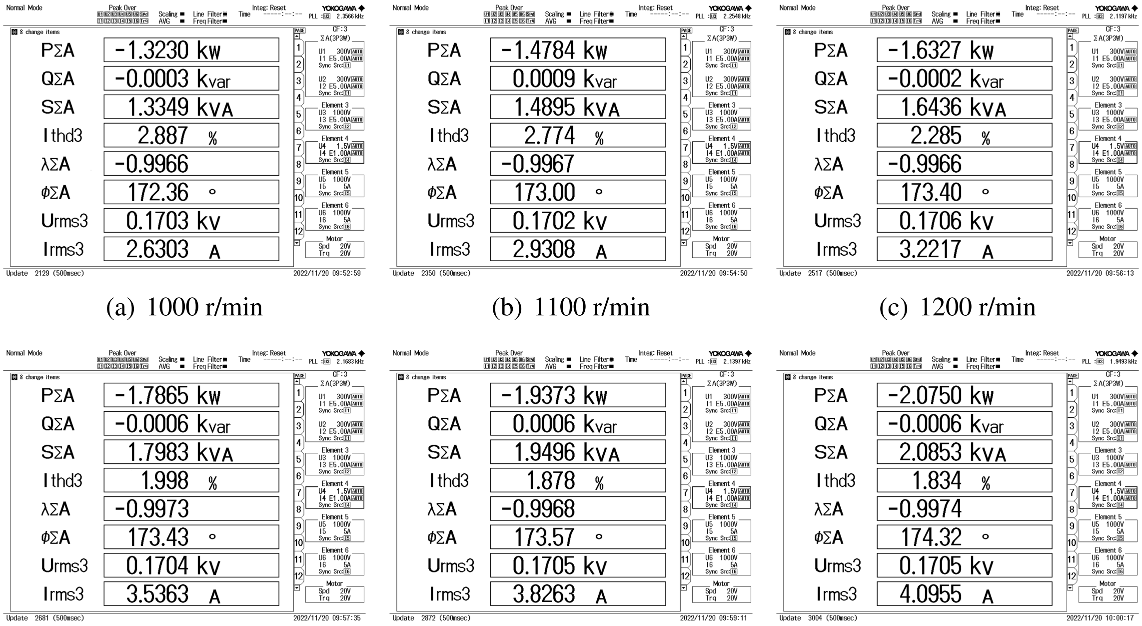

PΣA -1.3230 kW
QΣA -0.0003 kvar
SΣA 1.3349 kVA
Ithd3 2.887 %
λΣA -0.9966
ΦΣA 172.36 °
Urms3 0.1703 kV
Irms3 2.6303 A
Update 2129 (500msec) 2022/11/20 09:52:59

(a) 1000 r/min

PΣA -1.4784 kW
QΣA 0.0009 kvar
SΣA 1.4895 kVA
Ithd3 2.774 %
λΣA -0.9967
ΦΣA 173.00 °
Urms3 0.1702 kV
Irms3 2.9308 A
Update 2350 (500msec) 2022/11/20 09:54:50

(b) 1100 r/min

PΣA -1.6327 kW
QΣA -0.0002 kvar
SΣA 1.6436 kVA
Ithd3 2.285 %
λΣA -0.9966
ΦΣA 173.40 °
Urms3 0.1706 kV
Irms3 3.2217 A
Update 2517 (500msec) 2022/11/20 09:56:13

(c) 1200 r/min

PΣA -1.7865 kW
QΣA -0.0006 kvar
SΣA 1.7983 kVA
Ithd3 1.998 %
λΣA -0.9973
ΦΣA 173.43 °
Urms3 0.1704 kV
Irms3 3.5363 A
Update 2681 (500msec) 2022/11/20 09:57:35

(d) 1300 r/min

PΣA -1.9373 kW
QΣA 0.0006 kvar
SΣA 1.9496 kVA
Ithd3 1.878 %
λΣA -0.9968
ΦΣA 173.57 °
Urms3 0.1705 kV
Irms3 3.8263 A
Update 2872 (500msec) 2022/11/20 09:59:11

(e) 1400 r/min

PΣA -2.0750 kW
QΣA -0.0006 kvar
SΣA 2.0853 kVA
Ithd3 1.834 %
λΣA -0.9974
ΦΣA 174.32 °
Urms3 0.1705 kV
Irms3 4.0955 A
Update 3004 (500msec) 2022/11/20 10:00:17

(f) 1500 r/min

Figure 3.19: Power analyzer screenshots of PI-DBPC strategy at different speeds.

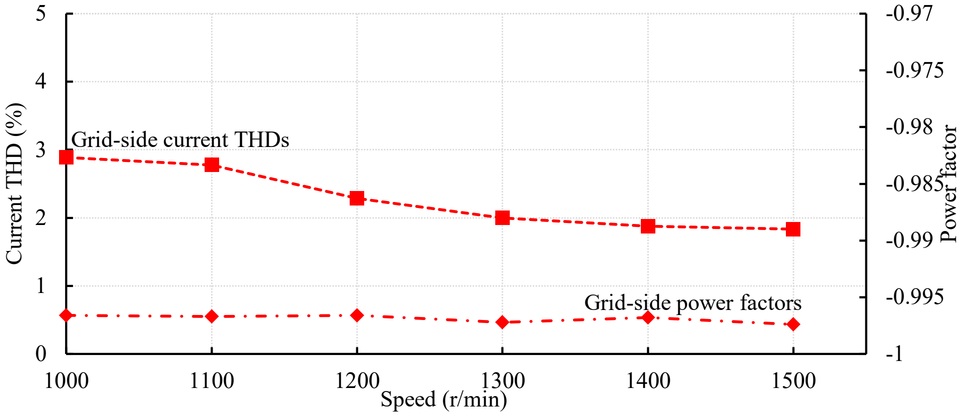

Figure 3.20: Current THDs and power factors of PI-DBPC strategy.

8.11 % for all operating speeds, indicating good control performance. Furthermore, Fig. 3.20 summarizes the current THDs and power factors of the PI-DBPC strategy at different operating conditions. In conclusion, the experimental results demonstrate that the PI-DBPC strategy can achieve good steady-state and dynamic control performance under different operating conditions.

3.4 Summary

Both PI-MPC and PI-DBPC are promising predictive control strategies that have been widely used in power electronics applications. One difference between the two strategies is that PI-MPC is a modulator-free technique while PI-DBPC is a modulator-based technique. Another difference is their control objectives. The control objective for PI-MPC is to minimize the cost function subject to system constraints and desired control behaviors. This signifies a high flexibility in defining the cost function and also means that an optimal voltage vector can be got while taking multiple performance criteria and restraints into account. The computational burden during the enumeration is a demerit, but it is unimportant since computing capacity needed by PI-MPC can be handled by contemporary industrial digital controller. In contrast, PI-DBPC has a more specific control objective of achieving zero steady-state error for the desired system behaviors. Thus, without online optimizations or enumeration, PI-DBPC calculates the reference vector directly according to the measurements and desired control behaviors. As can be seen from the experimental waveforms, the PI-DBPC has a slightly better steady-state regulation performance than the PI-MPC at the same switching frequency, but it has the slower regulation performance in transients. However, the steady-state performances of the PI-MPC are comparable to that of the PI-DBPC since the PI-MPC also can regulate the current THDs below 3 % and regulate the grid-side power factors above 0.99 at the rated operating condition.

CHAPTER 4

Modified DRPC strategy for BTB converter-fed PMSM system

This chapter presents the modified Dynamic Reference Direct Model Predictive Control (DRPC) methods for BTB converter-fed PMSM system, based on the dynamic reference generation concept.

- In Sec. 4.2, the control structure of the modified DRPC strategy is illustrated firstly. Then, the concept of dynamic reference is introduced, based on which the actual references of DC-link voltage and active power are calculated at each instant, and the cost function that manages the DC-link voltage without outer voltage PI controller is explained. A dynamic reference prediction horizon is specially adopted to accelerate the power flow for fast dynamic response.
- In Sec. 4.3, the comparisons between conventional PI-MPC strategy and modified DRPC strategy are given to show the characteristics of these two strategies.
- In Sec. 4.4, the modified DRPC is verified on the testbench using a DSP-based solution, and the experimental waveforms are shown.

4.1 Background

Considering its advantage of being able to reach a reference value with a fast dynamic response while satisfying a set of constraints, MPC has been widely studied. In [70], a long prediction horizon MPC is developed to control the BTB converter-fed PMSM system. Although the increased prediction horizon helps enhance the steady-state control performance, solving optimization problem is challenging and time-consuming since the associated computational burden increases exponentially with the length of the prediction horizon. Thus, the finite control set MPC is the most commonly applied [71]. Predictive direct power control is a widely applied method in various drive systems. In [72–74], it is adopted to control the rotor side converter in the doubly fed induction generator drive system. In [75], instead of selecting a certain switching vector, the developed strategy adopts the switching time in addition to the switching vector to minimize the deviations from reference for the regulation of a three-level T-type inverter. Though an additional degree of freedom is enabled by choosing a variable switching point, the method complexity is also increased. In [76], a model predictive direct flux/power control is developed to reduce the computation burden by only evaluating the switching vectors selected from the newly-designed switching tables. However, most MPCs in literature, including the references above, are adopted as an inner loop of the outer PI controller, which constructs the conventional PI-MPC. A DC-link voltage PI controller is always necessary to generate reference for MPC to control the BTB converter with PI-MPC [36]. This is a typical cascaded control structure because MPC is nesting inside the external voltage PI control loop [77, 78].

In order to further enhance the dynamic response of the system, a cascade-free DRPC strategy for BTB converter-fed PMSM systems is introduced in this chapter to remove the external DC voltage control loop. The core of this strategy is to generate appropriate references for the active power and DC-link voltage without the need for additional control loops. The proposed strategy can limit the maximum power levels, avoiding performance degradation due to windup issues that are common in PI control loops [79]. To further improve the dynamic performance of the DRPC, a modified DRPC strategy is proposed, which adopts a dynamic reference prediction horizon to compute the actual DC-link voltage reference of each instant. It aims to reduce the dynamic response time by reducing the reference prediction horizon while achieving a satisfying steady-state DC-link voltage control performance.

4.2 Basic principle of modified DRPC

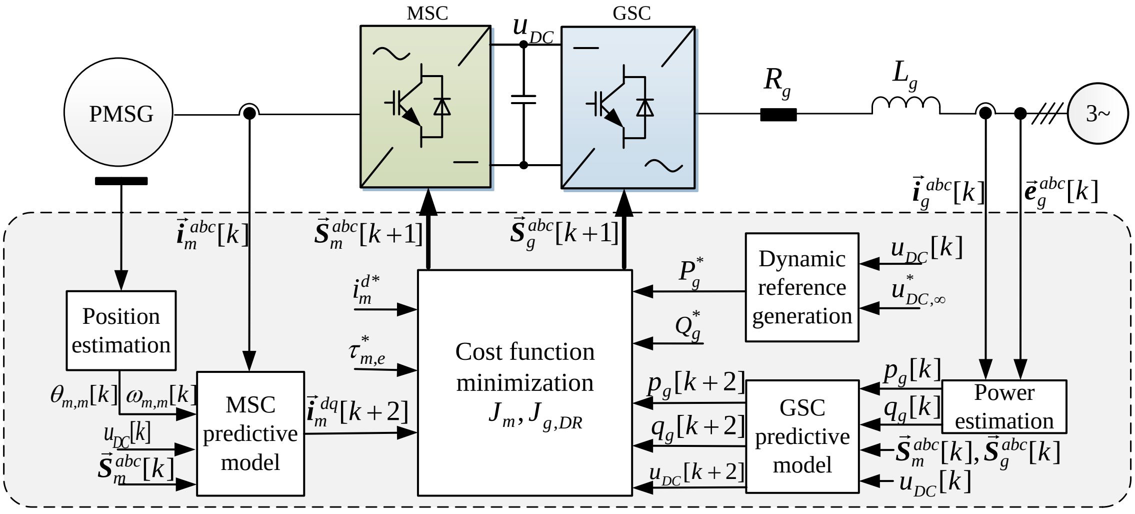

Figure 4.1: Control structure of the modified DRPC strategy.

This section introduces a modified DRPC strategy for a BTB converter-fed PMSM system, as illustrated in Fig. 4.1. DRPC offers advantages over the DC-link PI controller-based control strategy, including quick and controlled DC-link dynamics, lack of an additional PI DC-link controller, and lower control complexity.

4.2.1 Dynamic references generation

The DRPC strategy, which achieves DC-link voltage regulation directly by the cost function, is developed in [39], and it specifies the actual DC-link voltage reference of every instant according to the dynamic reference generation concept as follows

$$u_{DC}^{*} = u_{DC}[k] + \frac{1}{N_s}\left(u_{DC,\infty}^{*} - u_{DC}[k]\right) \tag{4.1}$$

where $u_{DC,\infty}^{*}$ denotes the DC-link voltage reference, u_{DC}^{*} denotes the real DC-link voltage reference of each instant, and reference prediction horizon N_s denotes the number of steps in reaching $u_{DC,\infty}^{*}$. To reach u_{DC}^{*} at the next instant, the grid-side active power reference P_g^{*} should be

$$P_g^{*} = \underbrace{\frac{2}{3}R_g\left(\frac{P_g^{*}}{e_g^{d}}\right)^{2}}_{P_{g,R}^{*}} + \underbrace{\tau_{m,e}^{*}\omega_{m,m}^{k} + u_{DC}^{*}\left(\frac{C}{T_s}\left(u_{DC}^{*} - u_{DC}[k]\right)\right)}_{P_{g,DC}^{*}} \tag{4.2}$$

where $P_{g,R}^{*}$ denotes the power consumed by grid-side resistors, e_g^{d} denotes the d-axis component of grid-side voltage, and $P_{g,DC}^{*}$ denotes the total power of PMSM and DC-link capacitor. Solving (4.2) gives the expression of P_g^{*}

$$P_g^{*} = \frac{3\left(e_g^{d}\right)^{2}}{4R_g} - \sqrt{\frac{9\left(e_g^{d}\right)^{4}}{16R_g^{2}} - \frac{3\left(e_g^{d}\right)^{2}}{2R_g}P_{g,DC}^{*}}. \tag{4.3}$$

Being applied to the two-step prediction to the discretized models of the DC-link voltage at $(k+1)^{\text{th}}$ instant, the predictive model of DC-link voltage of instant $k+2$ is expressed as

$$u_{DC}[k+2] = u_{DC}[k+1] + \frac{T_s}{C}\{\underbrace{\left(\vec{\boldsymbol{S}}_g^{abc}[k+1]\right)^{\mathrm{T}}\vec{\boldsymbol{\imath}}_g^{abc}[k+1]}_{i_{g,DC}[k+1]} - \underbrace{\left(\vec{\boldsymbol{S}}_m^{abc}[k+1]\right)^{\mathrm{T}}\vec{\boldsymbol{\imath}}_m^{abc}[k+1]}_{i_{m,DC}[k+1]}\}. \tag{4.4}$$

where C denotes the capacitance of DC-link capacitor, $i_{g,DC}$ denotes the DC-link current flowing out of GSC, and $i_{m,DC}$ denotes the DC-link current flowing into MSC. $\vec{\boldsymbol{S}}_m^{abc} = \left[S_m^{a}, S_m^{b}, S_m^{c}\right]^{\mathrm{T}}$, and S_m^{y} denotes the phase MSC phase switching state. $\vec{\boldsymbol{S}}_g^{abc} = \left[S_g^{a}, S_g^{b}, S_g^{c}\right]^{\mathrm{T}}$ and S_g^{y} denotes the GSC phase switching state.

To summarize, the cost function relies on references obtained from (4.1) and (4.3). It is worth noting that, given the references $u_{DC,\infty}^{*}$ and Q_g^{*}, the reference values P_g^{*} and u_{DC}^{*} are calculated at each time step. This allows the controller to track dynamic references. The reference prediction horizon N_s, used in (4.1), strikes a balance between response time and control effort by limiting the total change in capacitor current. If a faster tracking response is desired, then N_s should be kept small. However, this generally results in larger converter currents. The reference prediction horizon N_s moves forward in time using a moving horizon approach. From this perspective, the proposed control algorithm can be viewed as having a switching horizon of one unit, but an overall reference prediction horizon of N_s.

4.2.2 Cost function design

For steady-state error elimination, $\sum_{k=1}^{\infty}\left(U_{DC}^{*}-u_{DC}[k]\right)$ is added additionally into P_g^* to compensate for the errors caused by switching power loss, conduction power loss, etc. of power converters. The optimal voltage vector can be selected by evaluating the cost function below

$$\begin{aligned} J_{g,DRPC} = & \left\|P_g^* - p_g[k+2]\right\|^2 + \lambda_q \left\|Q_g^* - q_g[k+2]\right\|^2 + \lambda_{udc} \left\|u_{DC}^* - u_{DC}[k+2]\right\|^2 \\ & + \underbrace{\begin{cases} 0, & \|p_g[k+2]\| \le \left\|p_g^{\max}\right\| \\ \infty, & \|p_g[k+2]\| > \left\|p_g^{\max}\right\| \end{cases}}_{h_{g,conp}} + \underbrace{\begin{cases} 0, & \|q_g[k+2]\| \le \left\|q_g^{\max}\right\| \\ \infty, & \|q_g[k+2]\| > \left\|q_g^{\max}\right\| \end{cases}}_{h_{g,conq}} \end{aligned} \tag{4.5}$$

where $h_{g,conp}$ and $h_{g,conq}$ denote the constraint of active power and reactive power, respectively.

4.2.3 Dynamic reference prediction

In this DRPC strategy, the DC-link voltage tracking performance heavily depends on the reference prediction horizon N_s, and N_s serves as a trade-off between response time in dynamics against DC-link voltage ripple in steady state [39]. To improve the dynamic performance of the DRPC, a modified DRPC strategy is proposed. In the proposed modified DRPC, a dynamic prediction horizon is adopted for (4.1) to compute the actual DC-link voltage reference of each instant

$$N_s = N_{s,st} - c_{re} \left\|u_{DC,\infty}^* - u_{DC}[k]\right\| \tag{4.6}$$

where $N_{s,st}$ represents the reference prediction horizon used in steady state, and $c_{re} \in \mathrm{R}_{+}$represents the regulation coefficient. It aims to reduce the dynamic response time by reducing N_s while achieving a satisfying steady-state DC-link voltage control performance. However, tracking DC-link voltage reference by specifying the actual reference for each instant is still the core of DRPC.

4.3 Comparison between DRPC and PI-MPC

The primary comparison between DRPC strategy and PI-MPC strategies can be explained as follows.

(a) The DRPC approach is effective in preventing significant over- or under-shoot of the DC-link voltage, thanks to its gradual reference voltage generation method. This ensures that the reference voltage value $u_{DC}^*[k+1]$ stays within safe limits and avoids excessive charging or discharging currents, as power constraints are included in the cost function. Since large voltage over- or undershoot can damage DC-link capacitors, which are typically vulnerable components of a power converter, the DRPC approach is ideal for prolonging their lifespan.

(b) The DRPC approach considers all system parameters, including the load-side resistor that significantly influences the generated active power reference, when determining the DC-link and grid-side active power reference values. Compared to other approaches, the DRPC approach is more sensitive to variations in system parameters and requires more computational effort.

4.4 Experimental verification

4.4.1 Steady-state performances

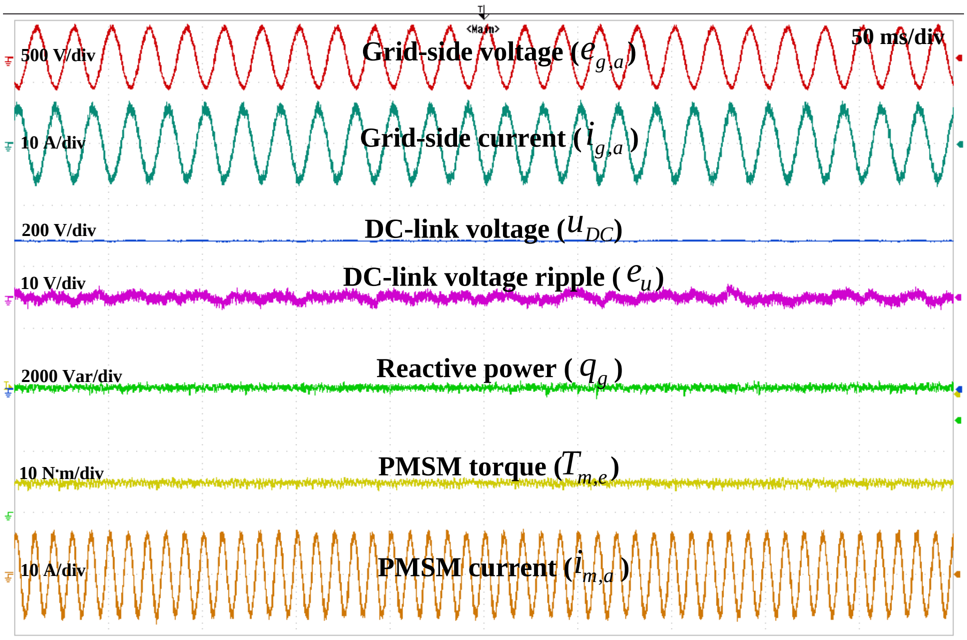

(a) Experimental waveforms.

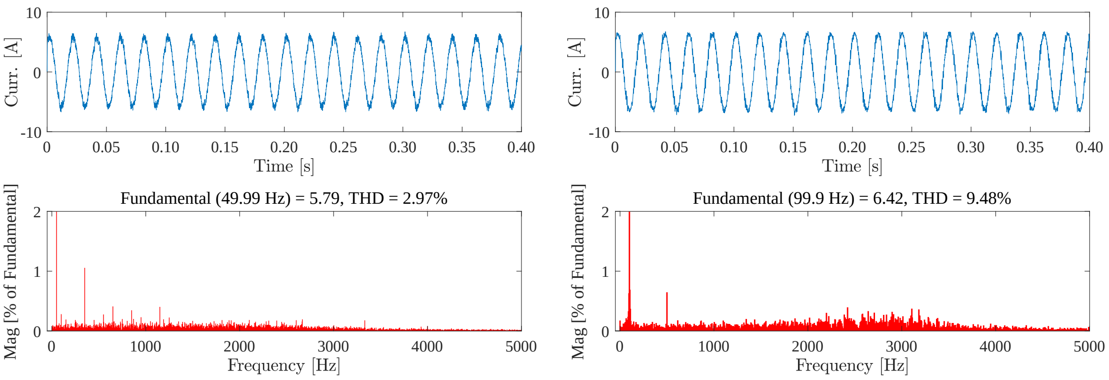

(b) Grid-side current spectrum.

(c) Machine-side current spectrum.

Figure 4.2: Steady-state experimental results of the modified DRPC strategy.

The experiment results of the modified DRPC strategy at the rated speed of 1500 r/min are presented in Fig. 4.2 to show the steady-state regulation performance. For the PMSM side, the electromagnetic torque is set to -15 N · m (the yellow dash on the upper left of the torque curve denotes 0 N · m). For the grid side, the energy produced by PMSM has been continuously transmitted into the grid to keep a stable DC-link voltage under the proposed scheme. The DC-link voltage has been boosted to 480 V, and the difference between the actual and reference DC-link voltage (i.e., $e_u = u_{dc} - u^*_{dc,\infty}$) is defined to evaluate the regulation quality of DC-link voltage, and it is observed that the DC-link voltage ripple has been regulated within ± 3 V. In this process, the sinusoidal grid-side current in the opposite phase with the grid-side voltage is obtained because the reactive power has been kept around 0 Var. The current spectrum of the grid-side current and machine-side current are shown in Fig. 4.2(b) and Fig. 4.2(c), respectively. For the grid-side, the current is 5.79 A, and the THD is 2.97 %. For the machine-side, the current is 6.42 A, and the THD is 9.48 %.

4.4.2 Step change of DC-link voltage

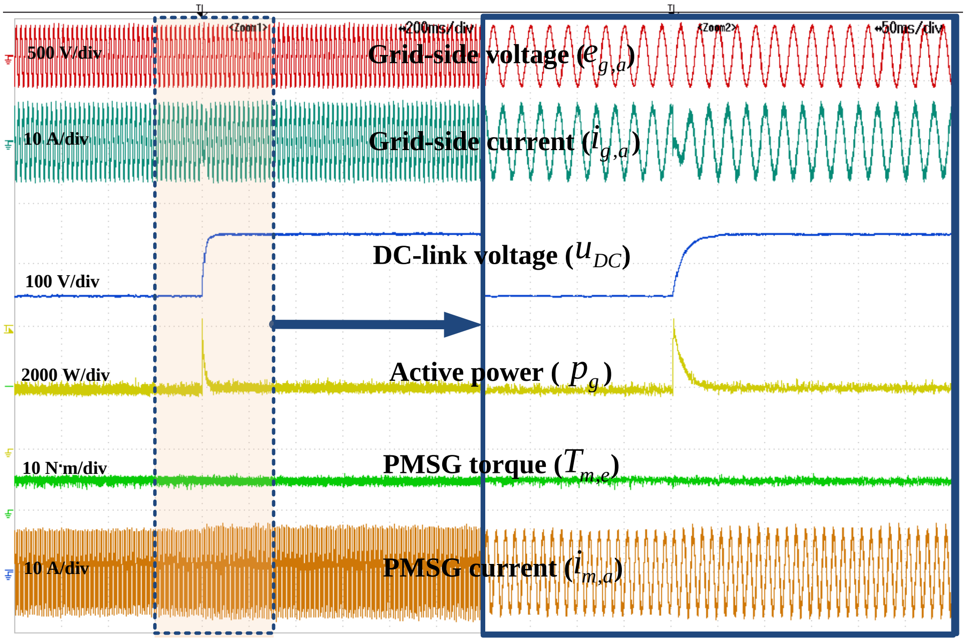

Figure 4.3: Experimental waveforms of modified DRPC strategy in the step change of DC-link voltage.

Fig. 4.3 investigates the effectiveness of a modified DRPC strategy in the DC-link voltage. In the regulation, the torque and speed of PMSM are not changed (1500 r/min, -15 N·m), which means the active power generated by PMSM does not change during this dynamic regulation. When the reference of DC-link voltage is increased from 450 V to 550 V, the active power flowing into the grid, which is controlled by GSC, should be decreased so that some of the active power generated by PMSM can be accumulated on DC-link to boost the DC-link voltage. It can be seen from the waveform that to boost the DC-link voltage quickly, not only does the active power flowing to grid decrease but the power flow direction is even reversed. That means the grid even starts to provide active power along with the PMSM to charge the DC-link capacitor as soon as possible. Once the new reference of 550 V is reached, the power flowing into grid recovers to the value before the reference is changed. It takes 60 ms for the DC-link voltage of modified DRPC strategy to increase from 450 to 550 V. The active power flowing into grid is increased in time to transfer the PMSM power into grid after reaching the voltage reference, which leads to no overshoot in voltage waveform.

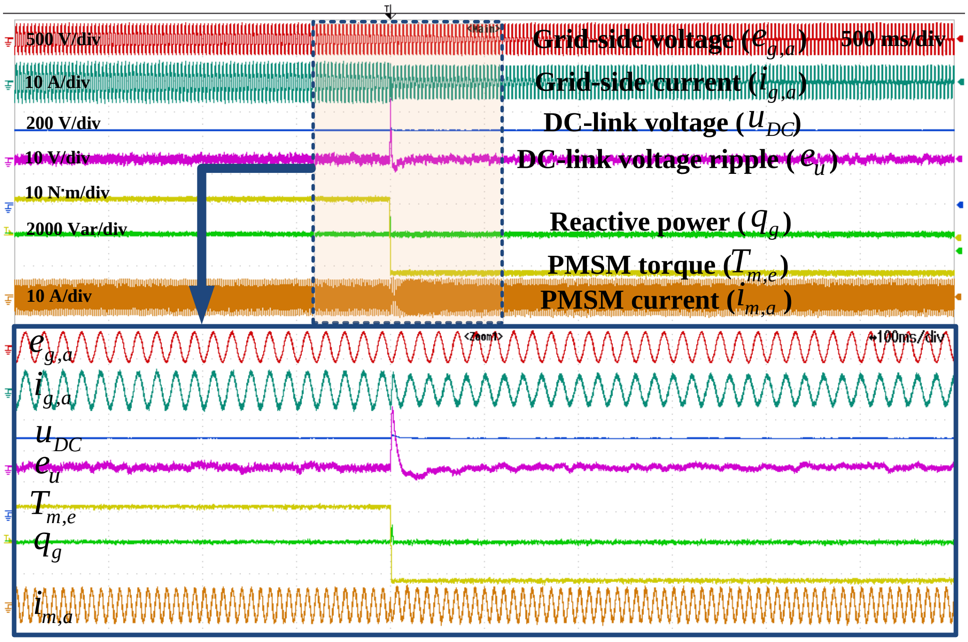

Figure 4.4: Experimental waveforms of modified DRPC strategy in the step change of torque.

4.4.3 Step change of torque

The experiment results under abrupt torque change at rated speed are shown in Fig. 4.4. The DC-link voltage increases at the moment when torque decreases from 12 to -12 N·m since PMSM suddenly starts to produce power instead of consuming power. Although the direction of active power flow is reversed under these abrupt torque changes, the DC-link voltage can be pulled back to its reference by transmitting the active power to the grid in time. As can be seen from the curves, the peak errors of DC-link voltage e_u are 20 V, and the recovery times of DC-link voltage are around 90 ms. The modified DR-MPC strategy has a better dynamic regulation performance compared with the previously mentioned control strategy (i.e., PI-MPC and PI-DBPC) since it presents a smaller peak error and faster recovery time.

4.4.4 Step change of reactive power

The experiment results under abrupt reactive power changes at the rated operating state are presented in Fig. 4.5. The change of grid-side reactive power reference from -1500 to 1500 Var affects the DC-link voltage due to the coupling between reactive power and active power. The DC-link voltage in the modified DRPC strategy presents a small decrease of 6 V. The recovery times of DC-link voltage is around 80 ms.

4.4.5 Step change of speed

Experiment results under abrupt speed changes are presented in Fig. 4.6. At -15 N·m, the operating status of the PMSM changes from generating mode to motoring mode as the speed changes from 1500 to -1500 r/min. Correspondingly, the phase of grid-side current changes

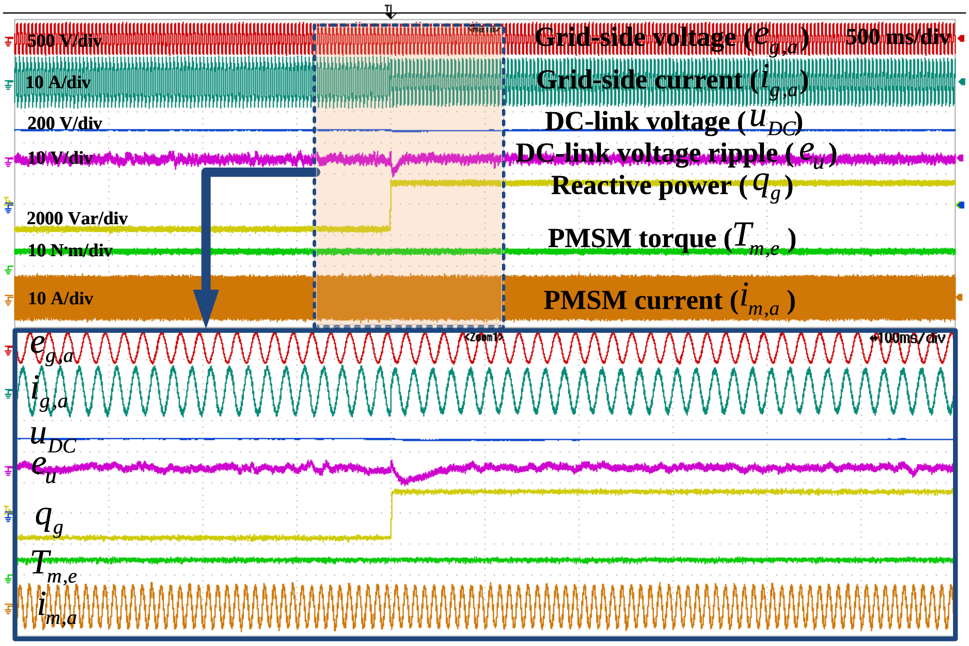

Figure 4.5: Experimental waveforms of modified DRPC strategy in the step change of reactive power.

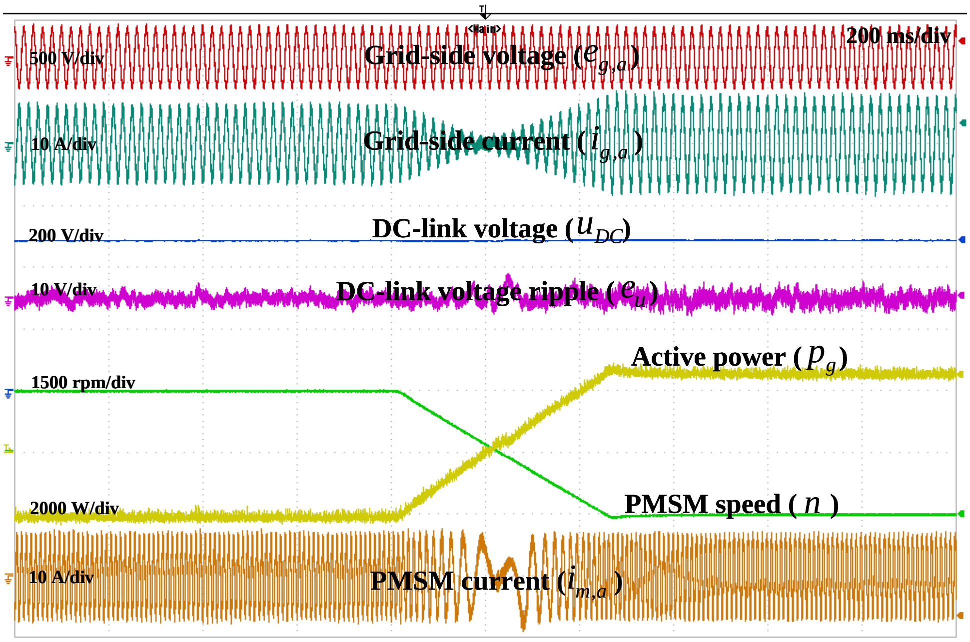

Figure 4.6: Experimental waveforms of modified DRPC strategy in the step change of speed.

from being in the opposite direction to being in the same direction as the grid-side voltage. It indicates that the operating status of GSC is changed from transmitting power in the machine-to-grid direction to providing power in the grid-to-machine direction to keep a constant DC-link voltage. Speed, unlike electromagnetic torque, is a mechanical parameter, so the change of speed direction results in a slower operating change for the system, which gives the control schemes more time to respond. It can be seen from the curves that the modified DRPC strategy presents satisfying DC-link voltage regulation performance since it yields a small voltage peak error of around 4 V during this dynamic regulation.

4.4.6 Robustness performance

To evaluate the robustness of the control strategy, experiments with mismatched parameters are conducted. As the accuracy of the dynamic model is more severely impacted by inductance variation than resistance variation, the control performance is tested under mismatched inductance. In the DRPC strategy, the grid-side inductor L_g and PMSM inductor $L_{m,s}$ values are set to linearly increase from half of their actual value to twice their actual values (i.e., from 50 % to 200 %) simultaneously at the rated operating condition.

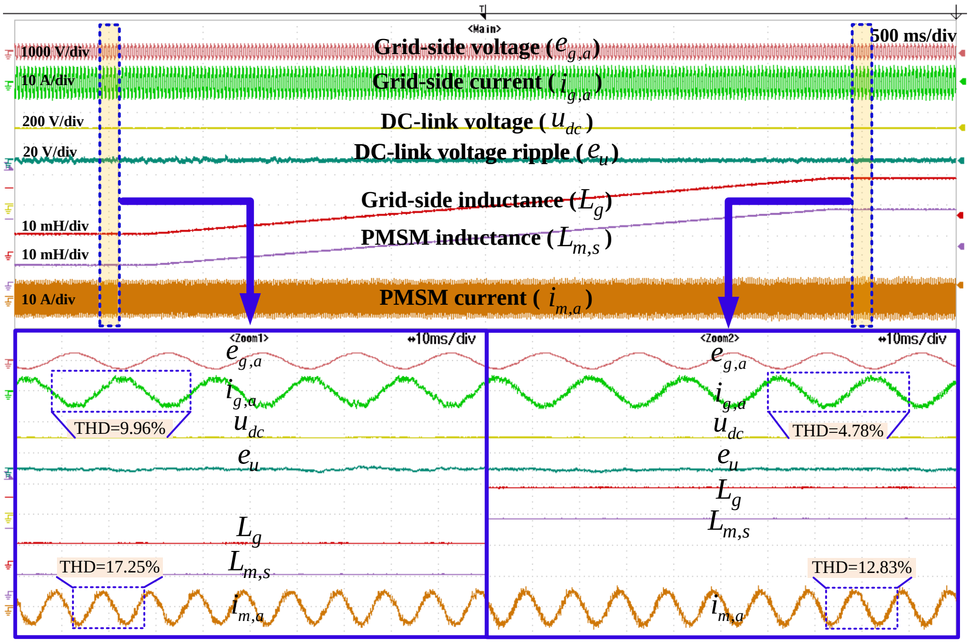

Figure 4.7: Experiment results of the modified DRPC strategy under mismatched inductances.

Fig. 4.7 illustrates the experimental results of the modified DRPC under mismatched inductances. The grid-side current THDs are approximately 2.97%, and the PMSM current THDs are around 11.6 % when the actual inductance values are used. However, when L_g and $L_{m,s}$ are set to 50% of their actual values, the grid-side current THDs rise to around 9.96 %, and the PMSM current THDs increase to approximately 17.25 %. Conversely, when L_g and $L_{m,s}$ are set to 200 % of their actual values, the grid-side current THDs decrease to around 4.78 %, and the PMSM current THDs reduce to around 12.83 %.

Despite the current THDs become worse as the inductance values deviate from their actual values, the system remains controllable. In practical systems, mismatched inductance values typically do not exceed the range of 50 % to 200 % of their actual values. As a result, the DRPC strategy exhibits comparable robustness against mismatched inductance values.

4.4.7 Current THDs and power factors

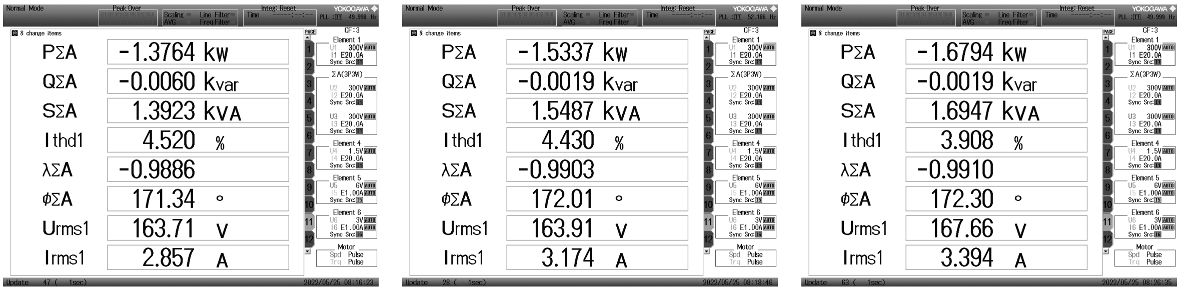

PΣA -1.3764 kW
QΣA -0.0060 kvar
SΣA 1.3923 kVA
Ithd1 4.520 %
λΣA -0.9886
ϕΣA 171.34 °
Urms1 163.71 V
Irms1 2.857 A

PΣA -1.5337 kW
QΣA -0.0019 kvar
SΣA 1.5487 kVA
Ithd1 4.430 %
λΣA -0.9903
ϕΣA 172.01 °
Urms1 163.91 V
Irms1 3.174 A

PΣA -1.6794 kW
QΣA -0.0019 kvar
SΣA 1.6947 kVA
Ithd1 3.908 %
λΣA -0.9910
ϕΣA 172.30 °
Urms1 167.66 V
Irms1 3.394 A

(a) 1000 r/min (b) 1100 r/min (c) 1200 r/min

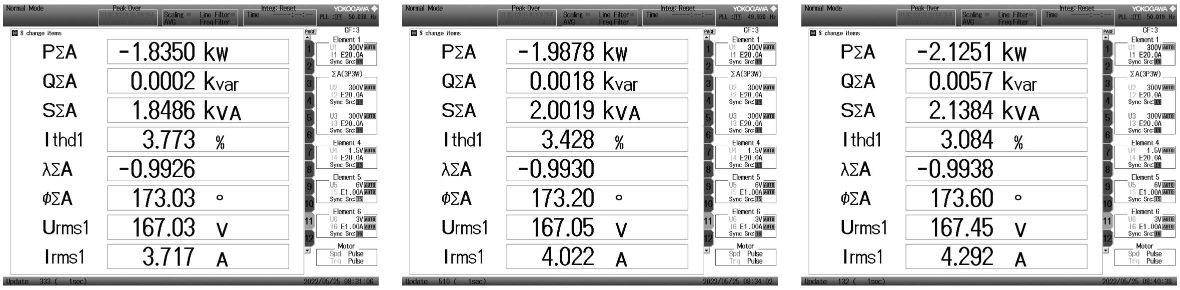

PΣA -1.8350 kW
QΣA 0.0002 kvar
SΣA 1.8486 kVA
Ithd1 3.773 %
λΣA -0.9926
ϕΣA 173.03 °
Urms1 167.03 V
Irms1 3.717 A

PΣA -1.9878 kW
QΣA 0.0018 kvar
SΣA 2.0019 kVA
Ithd1 3.428 %
λΣA -0.9930
ϕΣA 173.20 °
Urms1 167.05 V
Irms1 4.022 A

PΣA -2.1251 kW
QΣA 0.0057 kvar
SΣA 2.1384 kVA
Ithd1 3.084 %
λΣA -0.9938
ϕΣA 173.60 °
Urms1 167.45 V
Irms1 4.292 A

(d) 1300 r/min (e) 1400 r/min (f) 1500 r/min

Figure 4.8: Power analyzer screenshots of modified DRPC strategy at different speeds.

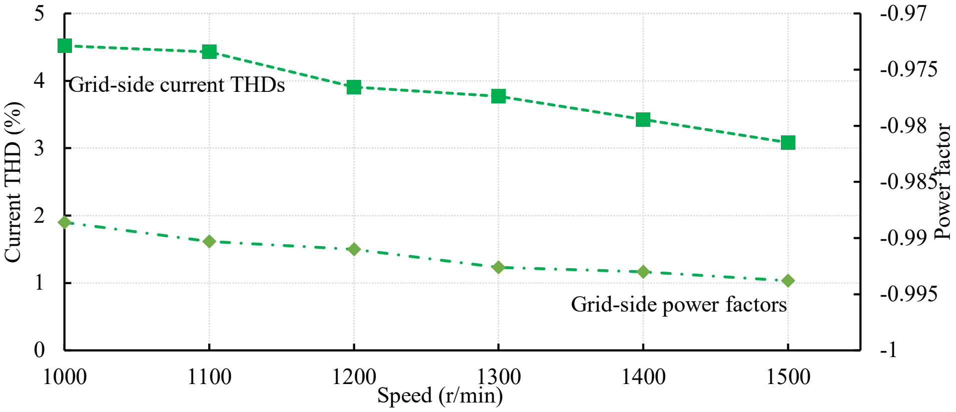

Figure 4.9: Current THDs and power factors of modified DRPC strategy.

The experimental power analyzer screenshots (Yokogawa WT1800E) of the conventional PI-MPC strategy, which reflect its steady-state performances at different operating speeds, are presented in Fig. 4.8, and the current THDs and power factors are concluded in Fig. 4.9. In the power analyzer, $\mathrm{P\Sigma A}$, $\mathrm{Q\Sigma A}$, $\mathrm{S\Sigma A}$, $\mathrm{Ithd1}$, $\lambda\Sigma\mathrm{A}$, $\phi\Sigma\mathrm{A}$, $\mathrm{Urms1}$, and $\mathrm{Irms1}$ denote the active power, reactive power, apparent power, current THD, power factor phase angle, phase voltage, and phase current of AC side, respectively. At the rated operating condition (480 V, 1500 r/min, -12 N · m, 0 Var), the grid-side current THDs are controlled below 3.1 %, the grid-side power factors are controlled around 0.9938, and the machine-side current THDs are around 9.48 %. Overall, the modified DRPC strategy can reach a satisfying steady-state control performance.

4.5 Summary

PI-MPC is one of the common solutions to control the BTB converter-fed PMSM system. It uses an additional voltage PI controller to generate the active power reference for inner power controller to track. Instead of that cascade control structure, the modified DRPC strategy only needs to evaluate the predefined cost function in which the power reference of each instant is obtained from the filtered DC-link voltage reference. For system protection, the constraints for maximum power are also included in the cost function. It can be found that the modified DRPC strategy regulates the DC-link voltage by strictly following the specified trajectories of voltage reference and power reference. Although satisfying control performance, i.e., unity grid-side power factor, low current harmonics, and stable DC-link voltage, can be realized, the response time of this strategy is still subject to the reference prediction horizon in principle.

CHAPTER 5

Direct predictive voltage control strategy for BTB converter-fed PMSM system

This chapter presents a cascade-free DPVC strategy which is proposed to further improve the dynamic response for BTB converter-fed PMSM system.

- In Sec. 5.1, the principle of the proposed DPVC strategy is explained firstly. Then, the coefficient determination is described in detail.

- In Sec. 5.2, steady-state experiments and transient-state experiments are carried out on the testbench to evaluate the effectiveness of the DPVC strategy.

- In Sec. 5.3, the performance of the proposed DPVC strategy is examined under abnormal grid scenarios, e.g., the unbalanced grid-side voltage, distorted grid-side voltage, and low voltage ride-through.

5.1 Direct predictive voltage control strategy

5.1.1 Basic principle of DPVC

Instead of using the cascade control structure of conventional PI-MPC strategy, the proposed DPVC strategy shown in Fig. 5.1 directly selects the optimal voltage vector by evaluating the

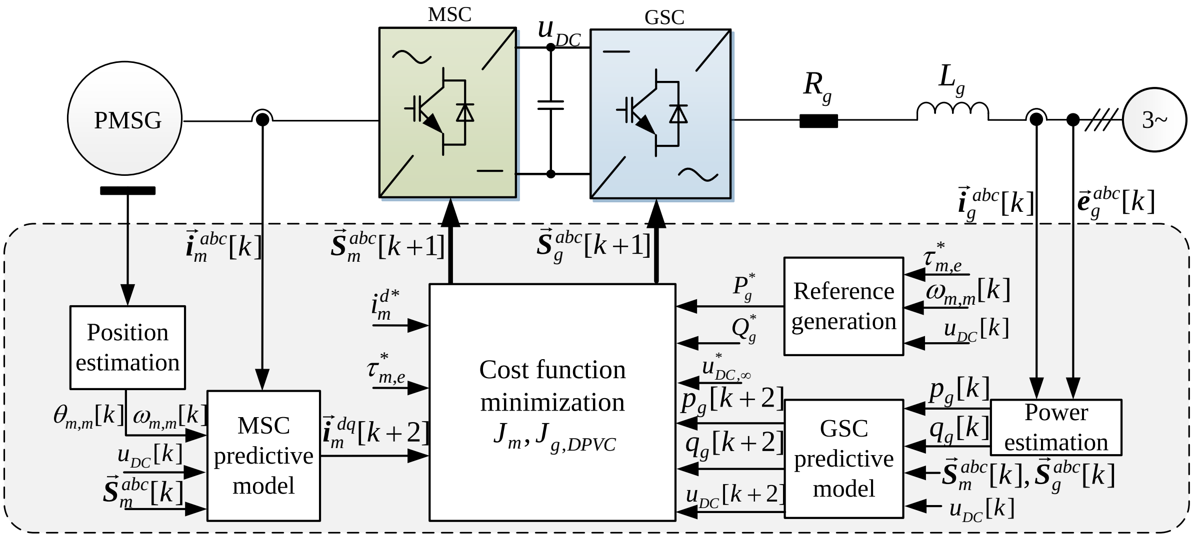

Figure 5.1: Control structure of proposed DPVC strategy.

cost function below

$$\begin{aligned}
J_{g,DPVC} = {} & \underbrace{\left\|\left(u_{DC,\infty}^* - u_{DC}[k+2]\right) + c_p\left(P_g^* - p_g[k+2]\right)\right\|^2}_{J_{g,H}} \\
& + \underbrace{\left\|u_{DC,\infty}^* - u_{DC}[k+2]\right\|^2}_{J_{g,udc}} + \lambda_q \underbrace{\left\|Q_g^* - q_g[k+2]\right\|^2}_{J_{g,q}} \\
& + \underbrace{\begin{cases} 0, & \|p_g[k+2]\| \le \left\|p_g^{\max}\right\| \\ \infty, & \|p_g[k+2]\| > \left\|p_g^{\max}\right\| \end{cases}}_{h_{g,conp}} + \underbrace{\begin{cases} 0, & \|q_g[k+2]\| \le \left\|q_g^{\max}\right\| \\ \infty, & \|q_g[k+2]\| > \left\|q_g^{\max}\right\| \end{cases}}_{h_{g,conq}}
\end{aligned} \tag{5.1}$$

where $u_{DC,\infty}^*$ is the DC-link voltage reference, P_g^* is the power generated by PMSM, namely, $\tau_{m,e}^*\omega_{m,m}^k$. $u_{DC}[k+2]$ of every vector $\boldsymbol{S}_m[k+1]$ are predicted in light of the expressions of u_{DC} of instant $k+2$, which can be obtained via shifting forward by one T_s on the discrete models of instant $k+1$. $c_p \in \mathrm{R}_+$is for active power regulation, $J_{g,udc}$ and $J_{g,H}$ are used to control DC-link voltage and active power of instant $k+2$, and $J_{g,q}$ is used to control reactive power. $h_{g,conp}$ and $h_{g,conq}$ denote the constraint of active power and reactive power, respectively.

Since MPC can regulate the terms in the cost function to approach zero to realize the reference tracking, assume that $J_{g,H}$ and $J_{g,udc}$ equal zero in the following explanation. Besides, the generating mode of PMSM, which corresponds to a negative P_g^*, is taken as an example for description. In the proposed integrated control scheme, the voltage reference $u_{DC,\infty}^*$ is directly taken as the reference in $J_{g,udc}$ to regulate the DC-link voltage for instant $k+2$, so the switching state that leads to the smaller DC-link voltage error tends to be chosen. If a switching state will generate a DC-link voltage smaller than its reference $u_{DC,\infty}^*$ at instant $k+2$ in $J_{g,udc}$, this switching state is the optimal one only when it also will transfer less power back to the grid than the generated PMSM power due to $J_{g,H}$. It means if $u_{DC,\infty}^* > u_{DC}[k+2]$ for a switching state, not all the power generated by PMSM should be transferred to grid by that switching state (i.e., $P_g^* < p_g[k+2]$). In this way, the DC-link capacitor can be charged by the remained power generated by PMSM, thereby reducing the voltage error. When $u_{DC}[k+2]$ reaches $u^*_{DC,\infty}$, $p_g[k+2]$ equals P^*_g, which means all the power generated by PMSM is transferred to the grid in steady state. But, considering the non-ignorable switching power loss, conduction power loss, etc. of MSC and GSC, a sum term $\sum_{k=1}^{\infty}\left(u^*_{DC,\infty} - u_{DC}[k]\right)$ should be added additionally into P^*_g to eliminate the steady-state error. Contrarily, if a switching state will generate a DC-link voltage larger than its reference $u^*_{DC,\infty}$ at instant $k+2$, this switching state is the optimal one only when it will also feed more active power to the grid than the generated PMSM power to discharge the capacitor. Hence, the switching state that not only will generate a DC-link voltage closer to the reference at the future instant but will generate the active power that can further reduce that voltage error is selected by the proposed control scheme.

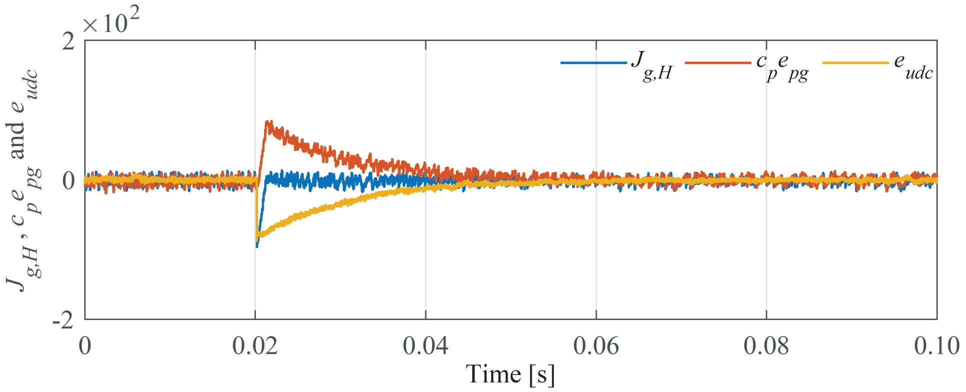

Figure 5.2: The experiment curves of $J_{g,H}$, $c_p e_{pg}$, and e_{udc} of the proposed DPVC strategy during generating mode.

The experiment curves of $J_{g,H}$, e_{udc}, $c_p e_{pg}$ when DC-link voltage is commanded to decrease are illustrated in Fig. 5.2 where e_{udc} represents the voltage error $\left(e_{udc} = u^*_{DC,\infty} - u_{DC}[k+2]\right)$ and e_{pg} represents the active power error $\left(e_{pg} = P^*_g - p_g[k+2]\right)$. After a decreased $u^*_{DC,\infty}$ is sent to controller, $J_{g,H}$ is reduced to 0 rapidly in the proposed DPVC strategy, and then the absolute value of e_{udc} is rapidly reduced by controlling how much power should be transferred to the grid to discharge the DC-link capacitor.

5.1.2 Coefficient c_p design

The determination of weighting factors is still an open question, but some rules-of-thumbs have been developed. In the method developed in [80, 81], the system containing primary term and secondary term in the cost function is defined. The term that must be achieved in order to provide a proper system behavior is called primary term, and the less important term that should also be accomplished to improve system performance, such as the terms for efficiency and power quality improvement, is called secondary term. For the BTB system, the DC-link voltage makes a direct connection between grid-side converter and machine-side converter, so DC-link voltage regulation is the not only primary control target but is the basis of a stable system as well. Therefore, the term $J_{g,H}$ and $J_{g,udc}$ for DC-link voltage regulation can be regarded as the primary term in the proposed cost function, and the term $J_{g,q}$ for reactive power regulation can be regarded as the secondary term. In this type of cost function, the weighting factor λ_q of $J_{g,q}$ can be temporarily set to a quite small value, then the optimal coefficient c_p for active power regulation in $J_{g,H}$ can be firstly determined according to the following process.

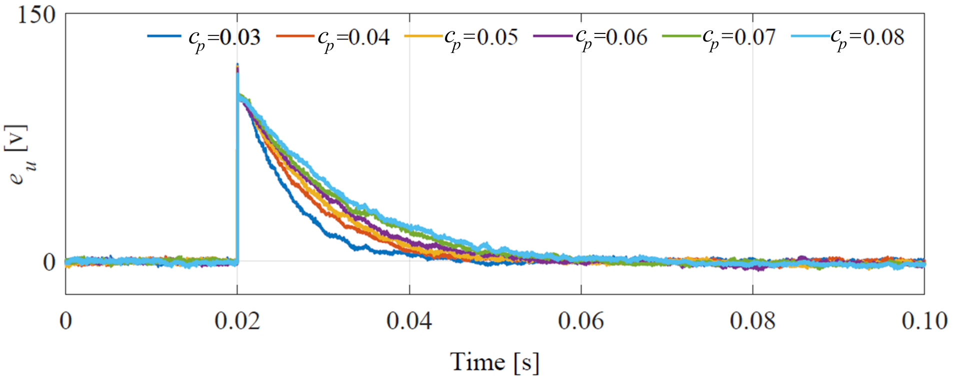

Figure 5.3: Dynamic experiment results under abrupt change of DC-link voltage from 550 V to 450 V at different c_p.

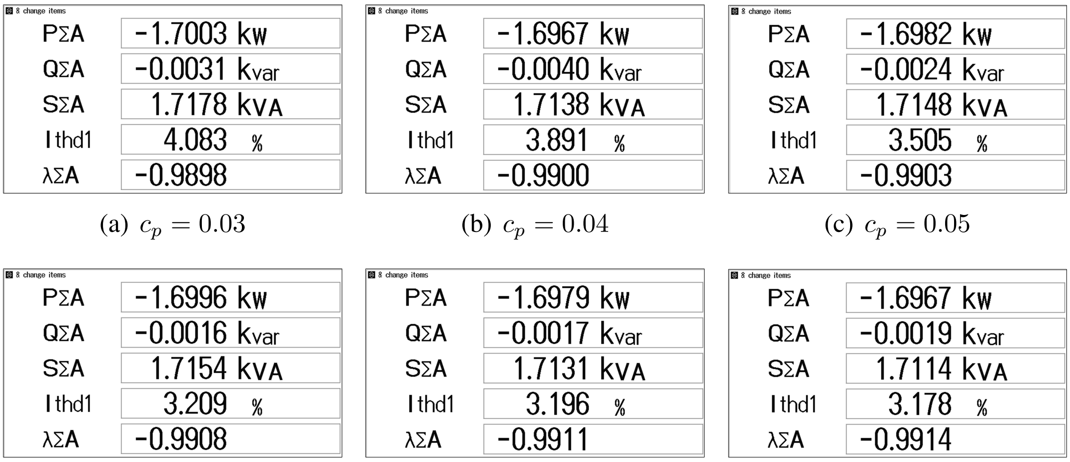

PΣA	-1.7003 kW
QΣA	-0.0031 kvar
SΣA	1.7178 kVA
Ithd1	4.083 %
λΣA	-0.9898

(a) $c_p = 0.03$

PΣA	-1.6967 kW
QΣA	-0.0040 kvar
SΣA	1.7138 kVA
Ithd1	3.891 %
λΣA	-0.9900

(b) $c_p = 0.04$

PΣA	-1.6982 kW
QΣA	-0.0024 kvar
SΣA	1.7148 kVA
Ithd1	3.505 %
λΣA	-0.9903

(c) $c_p = 0.05$

PΣA	-1.6996 kW
QΣA	-0.0016 kvar
SΣA	1.7154 kVA
Ithd1	3.209 %
λΣA	-0.9908

(d) $c_p = 0.06$

PΣA	-1.6979 kW
QΣA	-0.0017 kvar
SΣA	1.7131 kVA
Ithd1	3.196 %
λΣA	-0.9911

(e) $c_p = 0.07$

PΣA	-1.6967 kW
QΣA	-0.0019 kvar
SΣA	1.7114 kVA
Ithd1	3.178 %
λΣA	-0.9914

(f) $c_p = 0.08$

Figure 5.4: Power analyzer screenshots of steady state at different c_p.

To investigate the effect of coefficient c_p on the dynamic/steady-state performance of the system, the abrupt changes of DC-link voltage at different c_p have been set in the proposed system. The voltage error between actual DC-link voltage and its reference (i.e., $e_u = u_{DC} - u^*_{DC,\infty}$) is defined to reflect the regulation performance. Fig. 5.3 presents the experiment curves of e_u under abrupt change of DC-link voltage (from 550 to 450 V) at different c_p, and Fig. 5.4 gives the steady-state power analyzer screenshots at different c_p. It can be found from the results that the system has a fast response in tracking the changed DC-link voltage reference when c_p=0.03 (Fig. 5.3), but lower power factor and higher current THD are shown in the steady-state experiments (Fig. 5.4 (a)). When c_p=0.08, higher power factor and lower current THD are obtained in steady state, but a slow DC-link voltage reference tracking performance is presented. When c_p=0.06, both the dynamic and steady-state performances are satisfying, and this value is adopted for the system.

5.1.3 Robustness analysis

According to Kirchhoff's voltage law, the following state equations can be obtained (the models are eventually derived in discrete-time format by applying the forward Euler method of $\frac{d}{dt}x(t) = \frac{x[k+1]-x[k]}{T_s}$:

$$\boldsymbol{x}_y[k+1] = \boldsymbol{A}_y[k] \cdot \boldsymbol{x}_y[k] + \boldsymbol{B}_y[k] \cdot \boldsymbol{u}_y[k] + \boldsymbol{H}_y[k] \tag{5.2}$$

where $y \in \{m, g\}$ represents the variables of machine (m) and grid (g) sides, respectively. $\boldsymbol{x}_m[k] = \left(i_m^d[k], i_m^q[k]\right)^{\mathrm{T}}$ and $\boldsymbol{x}_g[k] = \left(p_g[k], q_g[k]\right)^{\mathrm{T}}$ are the state variable of machine and grid sides, respectively. $\boldsymbol{u}_m[k] = \left(u_m^d[k], u_m^q[k]\right)^{\mathrm{T}}$ and $\boldsymbol{u}_g[k] = \left(u_g^\alpha[k], u_g^\beta[k]\right)^{\mathrm{T}}$ are the state variable of machine and grid sides, respectively. $\boldsymbol{A}_y, \boldsymbol{B}_y$ and $\boldsymbol{H}_y$ given below are the state, input, and feed-through matrices, respectively.

$$\boldsymbol{A}_m[k] = \begin{bmatrix} 1 - \frac{T_s R_m}{L_m} & T_s \omega_e[k] \\ -T_s \omega_e[k] & 1 - \frac{T_s R_m}{L_m} \end{bmatrix} \tag{5.3a}$$

$$\boldsymbol{B}_m = \begin{bmatrix} \frac{T_s}{L_m} & 0 \\ 0 & \frac{T_s}{L_m} \end{bmatrix} \tag{5.3b}$$

$$\boldsymbol{H}_m[k] = \begin{pmatrix} 0 \\ \frac{-T_s \psi_r}{L_m} w_e[k] \end{pmatrix} \tag{5.3c}$$

$$\boldsymbol{A}_g = \begin{bmatrix} 1 - \frac{T_s R_g}{L_g} & -T_s \omega_g \\ T_s \omega_g & 1 - \frac{T_s R_g}{L_g} \end{bmatrix} \tag{5.3d}$$

$$\boldsymbol{B}_g[k] = \frac{-3T_s}{2L_g} \begin{bmatrix} e_g^\alpha[k] & e_g^\beta[k] \\ e_g^\beta[k] & -e_g^\alpha[k] \end{bmatrix} \tag{5.3e}$$

$$\boldsymbol{H}_g[k] = \frac{3T_s}{2L_g} \begin{pmatrix} \left\| e_g^{\alpha\beta}[k] \right\|^2 \\ 0 \end{pmatrix} \tag{5.3f}$$

It can be seen that the inductance is involved in the state, input, and feed-through matrices i.e., $\boldsymbol{A}_y[k]$, $\boldsymbol{B}_y[k]$, and $\boldsymbol{H}_y[k]$. The nominal inductance used in the controller is denoted as $\tilde{L}_y$ while the actual inductance value is denoted as L_y. The predicted value of the state variables based on the nominal value can be obtained as

$$\boldsymbol{x}_y^p[k+1] = \tilde{\boldsymbol{A}}_y[k] \cdot \boldsymbol{x}_y[k] + \widetilde{\boldsymbol{B}}_y[k] \cdot \boldsymbol{u}_y^p[k] + \widetilde{\boldsymbol{H}}_y[k] \tag{5.4}$$

where $\boldsymbol{x}_y^p$ and $\boldsymbol{u}_y^p$ stand for predicted values of the state and input variables, respectively. As the control period of the current loop is 50 μ s, both the inductance and resistance in the system are small enough to ignore. Thus, the system matrix $\tilde{\boldsymbol{A}}_y$ used here is simplified as $\boldsymbol{I}_2 = \mathrm{diag}(1, 1)$. Then the input voltage vectors $u^p[k]$ can be calculated by

$$\boldsymbol{u}_y^p[k] = \widetilde{\boldsymbol{B}}_y[k]^{-1} \left(\boldsymbol{x}_y^p[k+1] - \widetilde{\boldsymbol{H}}_y[k] - \tilde{\boldsymbol{A}}_y[k] \cdot \boldsymbol{x}_y[k] \right). \tag{5.5}$$

Applying (5.5) into (5.2) gives

$$\boldsymbol{x}_y^m[k+1] = \boldsymbol{A}_y[k] \cdot \boldsymbol{x}_y^m[k] + \boldsymbol{M}[k] \left(\boldsymbol{x}_y^p[k+1] - \widetilde{\boldsymbol{H}}_y[k] - \tilde{\boldsymbol{A}}_y[k] \cdot \boldsymbol{x}_y^m[k] \right) + \boldsymbol{H}_y[k] \tag{5.6}$$

where $\boldsymbol{x}_y^m$ stands for measured values of state variables, and $\boldsymbol{M}[k] = \boldsymbol{B}_y[k] \cdot \widetilde{\boldsymbol{B}}_y[k]^{-1}$. Since $\boldsymbol{x}_y^p[k+1]$ will approach $\boldsymbol{x}_y^*[k+1]$, so the following expression holds

$$\boldsymbol{x}_y^m[k+1] = \frac{\tilde{L}_y}{L_y}\boldsymbol{x}_y^*[k+1] + \left(1 - \frac{\tilde{L}_y}{L_y}\right)\boldsymbol{x}_y^m[k]. \tag{5.7}$$

The closed-loop transfer function in discrete format becomes

$$\frac{\boldsymbol{x}_y^m(z)}{\boldsymbol{x}_y^*(z)} = \frac{\frac{\tilde{L}_y}{L_y}z}{z - 1 + \frac{\tilde{L}_y}{L_y}}. \tag{5.8}$$

Based on the "Bounded-Input Bounded-Output (BIBO)" stability criteria from the classic control theory, the system in this work is stable if and only if all roots of $F(z) = z - 1 + \frac{\tilde{L}_y}{L_y}$ are inside the unit circle [82]. Thus, when $\tilde{L}_y \in (0, 2L_y)$, the system will be stable.

$$|z| = \left|1 - \frac{\tilde{L}_y}{L_y}\right| < 1. \tag{5.9}$$

5.2 Experimental verification

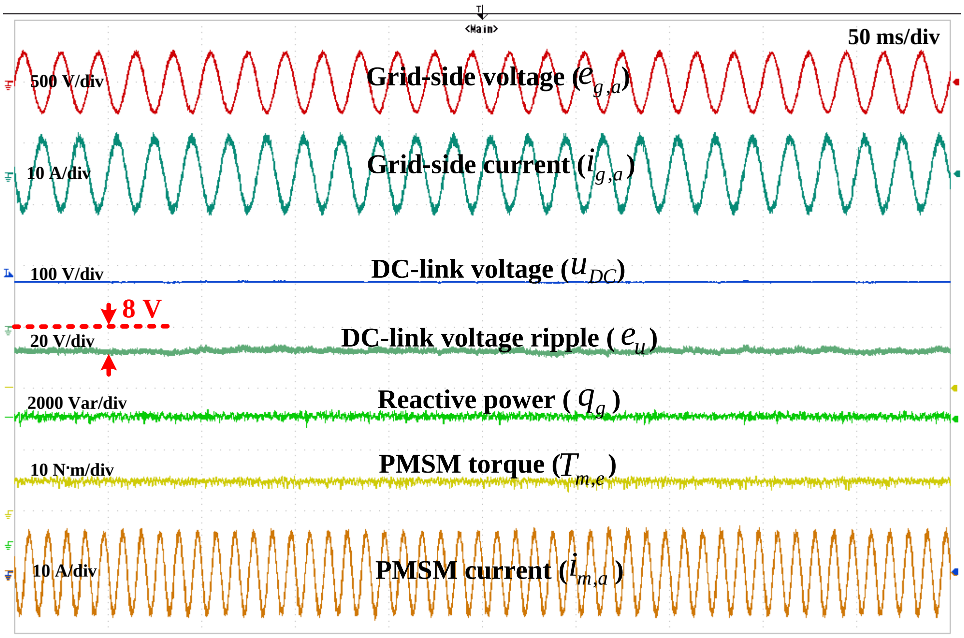

Figure 5.5: Steady-state experiment results without compensation.

In practical experiments, the converters also consume power (conduction loss, switching loss, etc.) when transferring the generated power of PMSM P_g^* into grid, which means the power that can be actually transferred into grid side is less than P_g^*. In this case, if the voltage vector

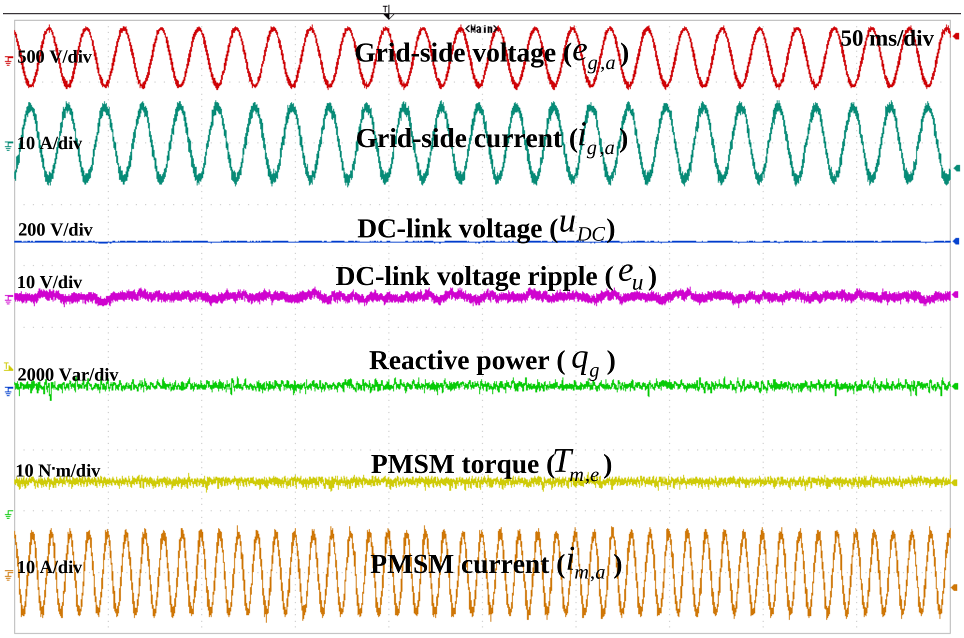

(a) Experiment waveforms.

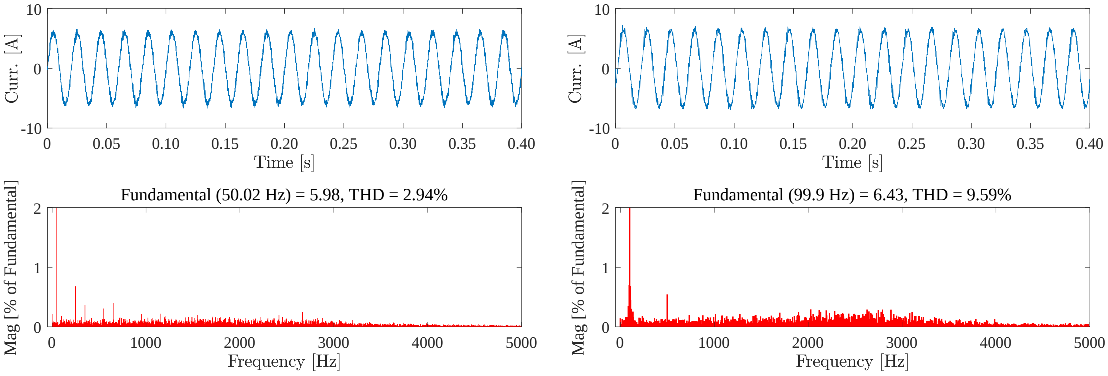

(b) Grid-side current spectrum. (c) Machine-side current spectrum.

Figure 5.6: Experimental results of the proposed DPVC strategy with the sampling frequency of 20 kHz.

that makes $p_g[k+2]$ equal to P_g^* is selected in the cost function, not only all the power coming from PMSM is sent to grid but the DC-link capacitor will be discharged to contribute its power to grid, which makes the regulated DC-link voltage lower than its reference. To address that problem, the sum term $\sum_{k=1}^{\infty}(U_{DC}^* - u_{DC}[k+2])$ is added into P_g^* to compensate for the power loss in power converters, thus eliminating the steady-state voltage error. It can be seen from Fig. 5.5 that the voltage bias of 8 V exists in the system without compensation, but the sum term can effectively eliminate the bias, as can be seen in Fig. 5.6(a).

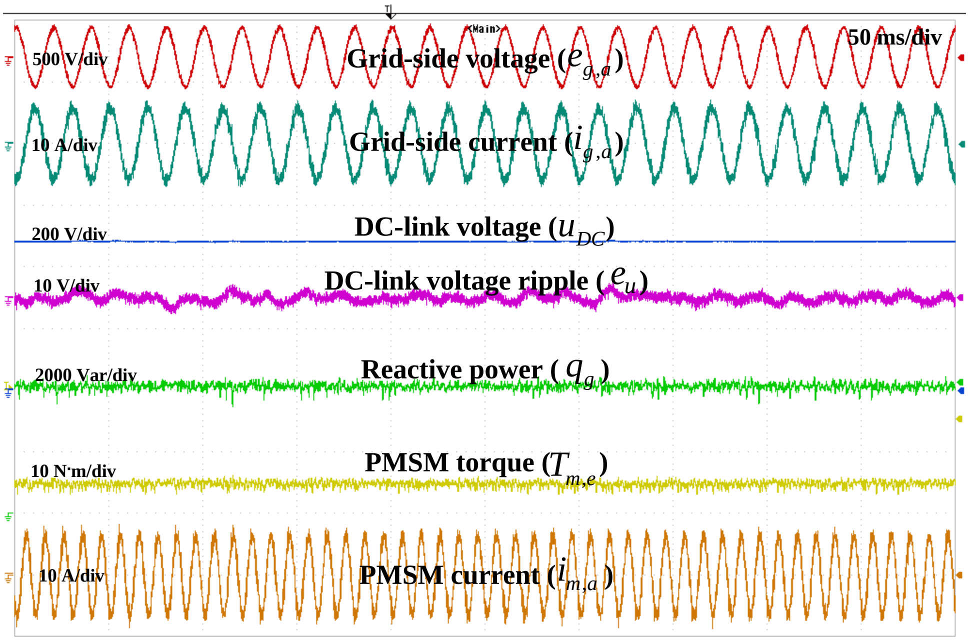

(a) Experiment waveforms.

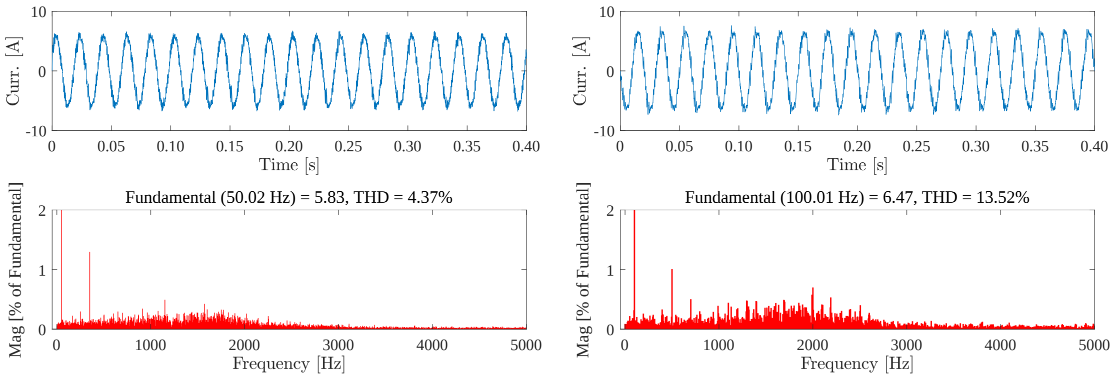

(b) Grid-side current spectrum.

(c) Machine-side current spectrum.

Figure 5.7: Experimental results of the proposed DPVC strategy with the sampling frequency of 15 kHz.

5.2.1 Steady-state performances

The steady-state experiment results of the proposed DPVC strategy (at sampling frequency f_{samp} = 20 kHz) at the rated speed of 1500 r/min is presented in Fig. 5.6. For the PMSM side, the electromagnetic torque is set to -15 N·m (the yellow dash on the left of the torque curve indicates 0 N·m), and the sinusoidal stator current is obtained to reach the reference torque. For the grid side, the energy generated by PMSM has been continuously transferred into the grid to keep a stable DC-link voltage under the proposed DPVC strategy. The DC-link voltage has been boosted to 480 V, and it is observed that the DC-link voltage ripple, which can be reflected by the error between the actual DC-link voltage and its reference (i.e., $e_u = u_{dc} - u^*_{dc,\infty}$), has been regulated within ± 2 V. In this process, the sinusoidal grid-side current in the opposite

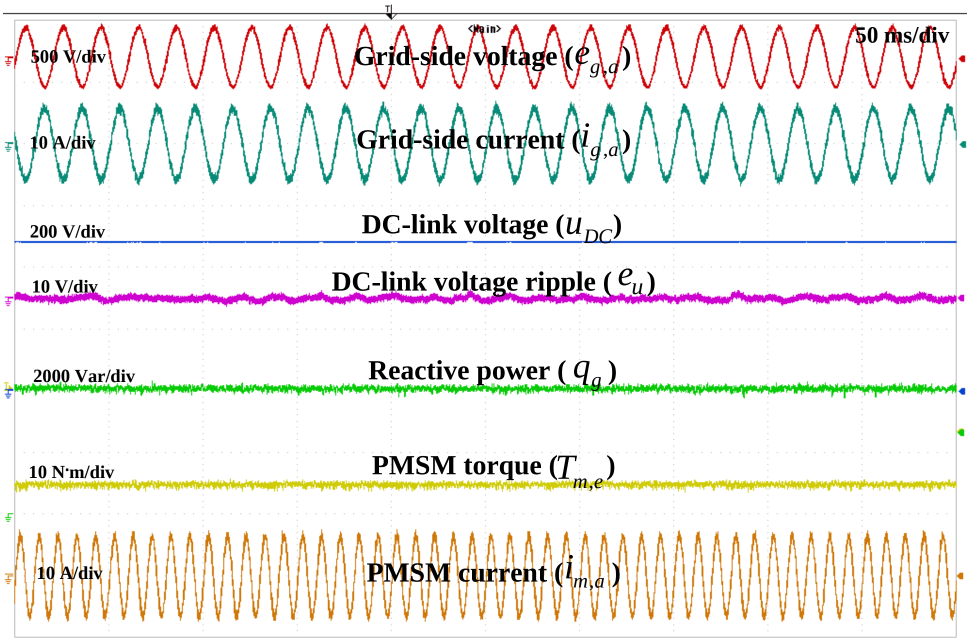

(a) Experiment waveforms.

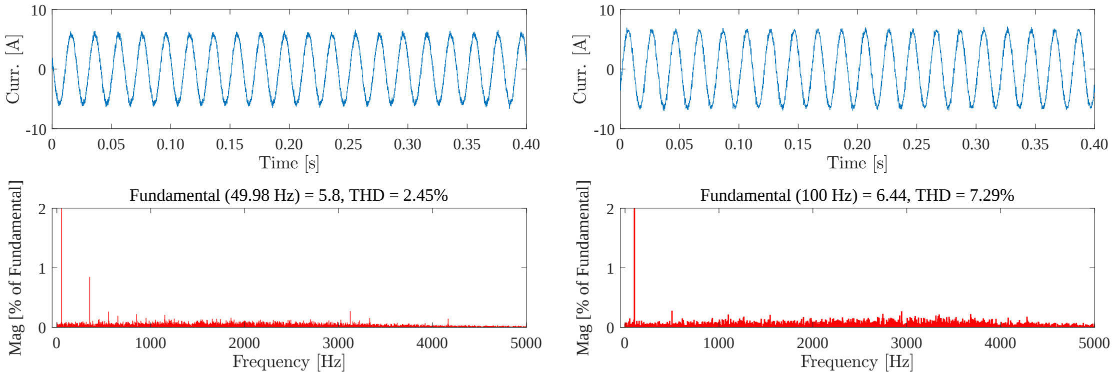

(b) Grid-side current spectrum. (c) Machine-side current spectrum.

Figure 5.8: Experimental results of the proposed DPVC strategy with the sampling frequency of 25 kHz.

phase with the grid-side voltage is obtained because the reactive power has been kept around 0 Var. The current spectrum of the grid-side current is shown in Fig. 5.6(b) and the machine-side current is shown in Fig. 5.6(c). For the grid side, the current is 5.98 A, and the THD is 2.94 %. For the machine side, the current is 6.43 A, and the THD is 9.59 %.

To test the performances of DPVC strategy at different switching frequencies, the sampling frequency has been set to 15 kHz and 25 kHz in the experiments of Fig. 5.7 and Fig. 5.8, respectively. With the sampling frequency f_{samp} = 15 kHz), the switching frequency is around 2.0 kHz. For the grid side, the current is 5.83 A, and the THD is 4.37 %. For the machine-side, the current is 6.47 A, and the THD is 13.52 %. With the sampling frequency f_{samp} = 25 kHz), the switching frequency is around 3.4 kHz. For the grid side, the current is 5.8 A, and the THD is 2.45 %. For the machine side, the current is 6.44 A, and the THD is 7.29 %. Although the increased sampling frequency improves regulation performance, 20 kHz is adopted in the manuscript after comprehensively considering the control performance and computation time.

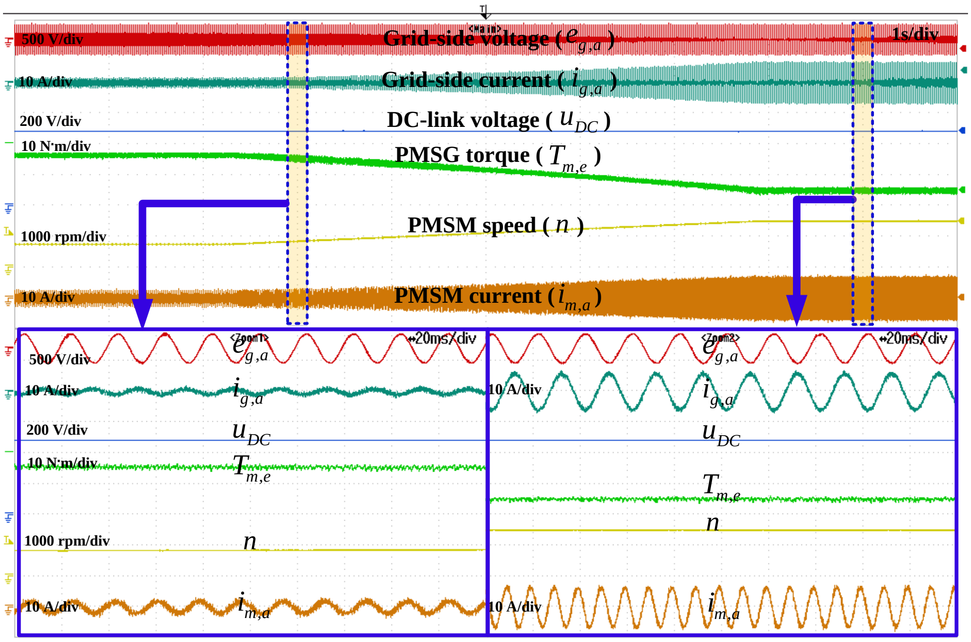

Figure 5.9: Experimental waveforms of the proposed DPVC strategy under variable speed and torque.

In the normal wind speed range of a realistic wind turbine system, the changes in the wind speed will proportionately cause changes in generator speed, and the electromagnetic torque reference should be changed correspondingly in the optimal torque control scheme in order to achieve MPPT [32]. More specifically, the electromagnetic torque reference $\tau^*_{m,e}$ should be calculated according to generator angular speed $\omega_{m,m}$ as follows

$$\tau^*_{m,e} = K_{opt}\omega^2_{m,m} \tag{5.10}$$

where K_{opt} can be calculated offline according to the datasheet of the wind turbine. To simulate this scenario of variable wind speed, a varying generator angular speed is set in the system, and the electromagnetic torque reference changes in proportional to the square of generator angular speed. In the experiment results shown in Fig. 5.9, the generator speed is set to change from 750 to 1500 r/min, and in light of (5.10), the electromagnetic torque reference correspondingly changes from -3.75 to -15 N · m (the short purple line on the left-most side of the curve indicates 0 N · m). The increased electromagnetic torque and speed increase the active power flowing inside the system, so the amplitude of grid-side current increases as well. The grid-side current is in the opposite phase with the grid-side voltage during the regulation since the reactive power has been regulated around 0 Var. The active power increases as the increases of speed and torque, which also increases the grid-side current, but the DC-link voltage can maintain at 480 V by continuously feeding the generated active power into grid.

5.2.2 Transient-state performances

The dynamic performances of proposed DPVC strategy in different operating conditions are tested and compared.

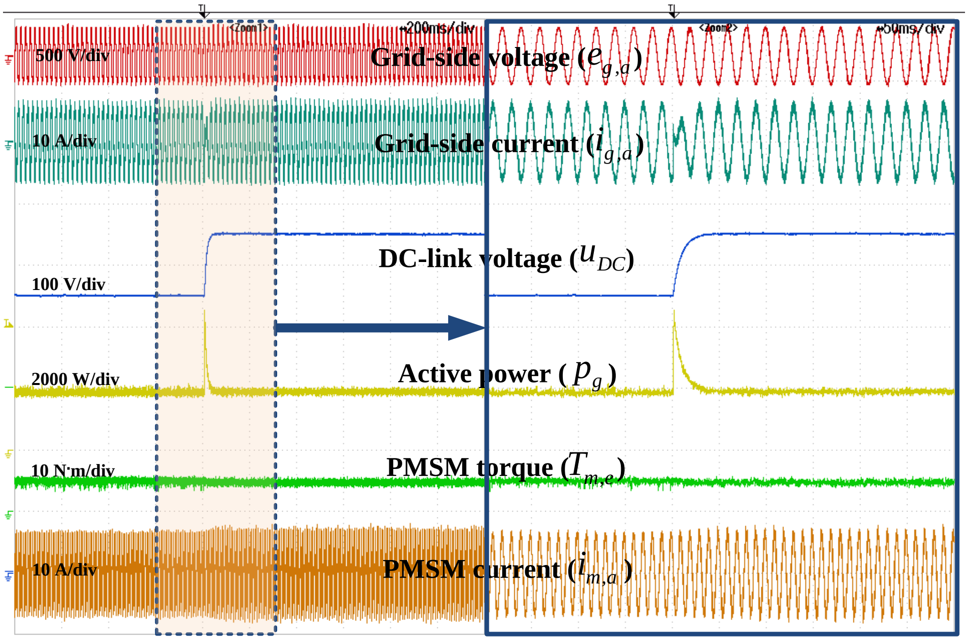

Figure 5.10: Experimental results of DPVC in the step change of DC-link voltage.

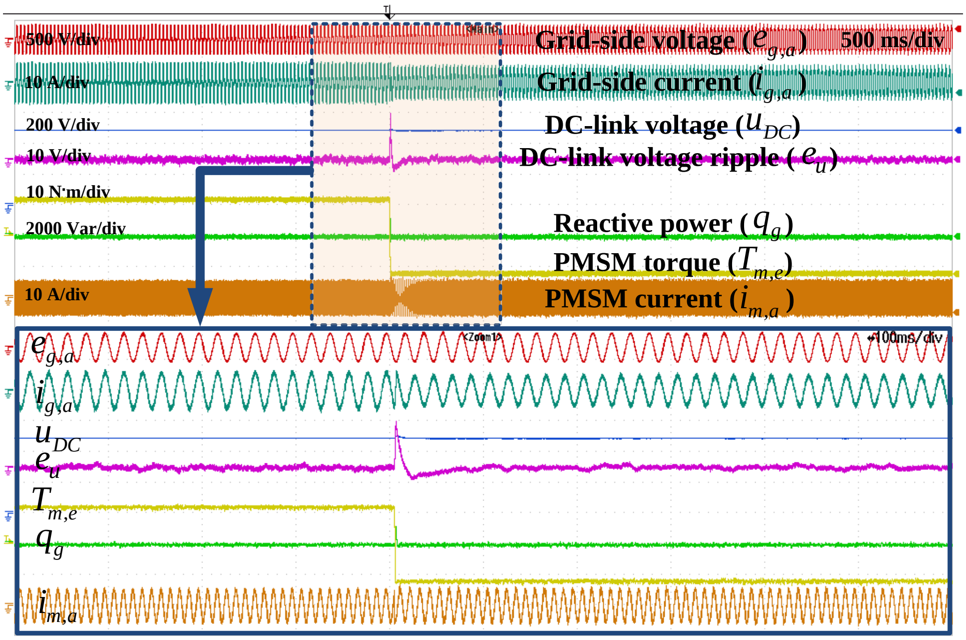

Figure 5.11: Experimental results of DPVC in the step change of torque.

5.2.2.1 Step change of DC-link voltage

To ease the description, the flowing direction of active power should be defined. When the grid provides active power, i.e., the active power flows in the grid-to-machine direction, the direction is defined as the positive direction. When the grid absorbs active power, i.e., the active power flows in the machine-to-grid direction, the direction is defined as the negative direction. Then, once the direction of power flow is mentioned, the "increase" or "decrease" indicates the increase or decrease in the absolute value.

The experimental waveforms with an enlarged zoom window in the step change of DC-link voltage (from 450 to 550 V) have been presented in Fig. 5.10. To display both the positive and negative value of active power, an offset has been added to the DAC output, and the short yellow dash with a "T" on it indicates 0 W for active power waveform. During the regulation, the torque and speed of PMSM are not changed (1500 r/min, -15 N · m), which means the active power generated by PMSM does not change during this dynamic regulation. When the reference of DC-link voltage is increased from 50 V to 550 V, the active power flowing into the grid, which is controlled by GSC, should be decreased so that some of the active power generated by PMSM can be accumulated on DC-link to boost the DC-link voltage. It can be seen from the waveform that to boost the DC-link voltage in a quick manner, not only does the active power flowing to grid decrease but the power flow direction is even reversed (the active power is changed from around -2250 W to a positive value). That means the grid even starts to provide active power along with the PMSM in order to charge the DC-link capacitor as soon as possible. Once the new DC-link voltage reference of 550 V is reached, the power flowing into grid recovers to the value before the reference is changed. There is no voltage overshoot during the regulation, and it takes around 40 ms for proposed DPVC strategy to reach the new DC-link voltage reference.

5.2.2.2 Step change of torque

Figure 5.11 illustrates the experimental results of an abrupt torque change at rated speed. The changes of electromagnetic torque lead to changes in active power, which also leads to the fluctuation in reactive power in the transient due to the coupling between active and reactive power The DC-link voltage undergoes an increase when the torque changes from 12 to -12 N·m. Since PMSM suddenly start to generate power instead of consuming power. Although the active power flow direction reverses during the abrupt torque changes, the DC-link voltage can be promptly returned to its reference value by transferring active power to the grid, thanks to the application of the DPVC strategies. Compared with the experimental results of the previous PI-MPC, PI-DBPC, modify DRPC strategies, the proposed DPVC strategy achieves better dynamic regulation performance with a smaller peak error of DC-link voltage (e_u) of 15 V and a faster recovery time of around 70 ms.

5.2.2.3 Step change of reactive power

Figure 5.12 depicts the results of an experiment conducted at the rated speed with an electromagnetic torque -15 N·m. The abrupt change in reactive power is implemented in experiments, i.e., the grid-side reactive power reference is increased from -1500 to 1500 Var. Due to the coupling between reactive power and active power, the DC-link voltage is also affected. However,

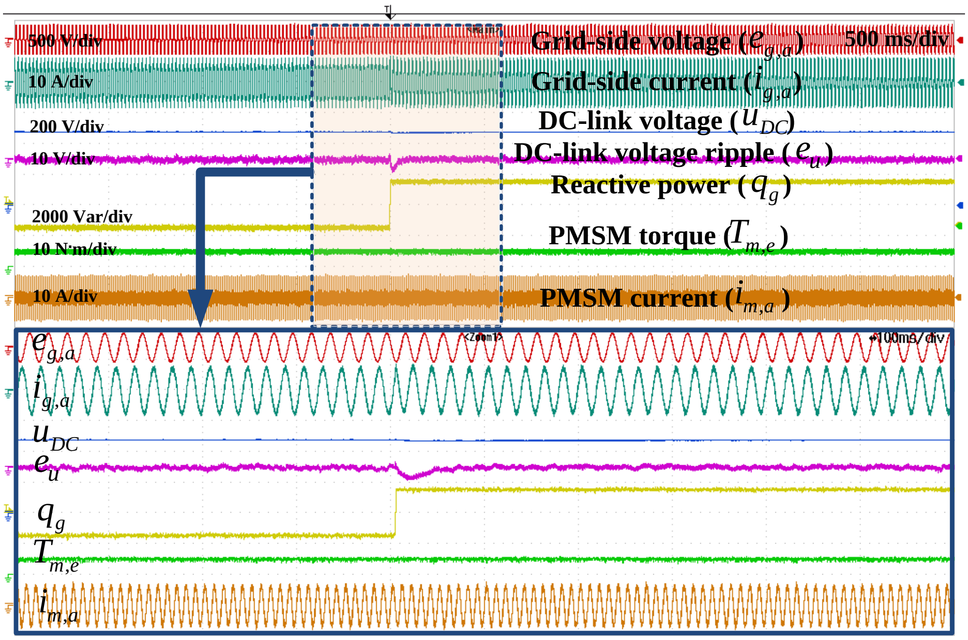

Figure 5.12: Experimental results of DPVC in the step change of reactive power.

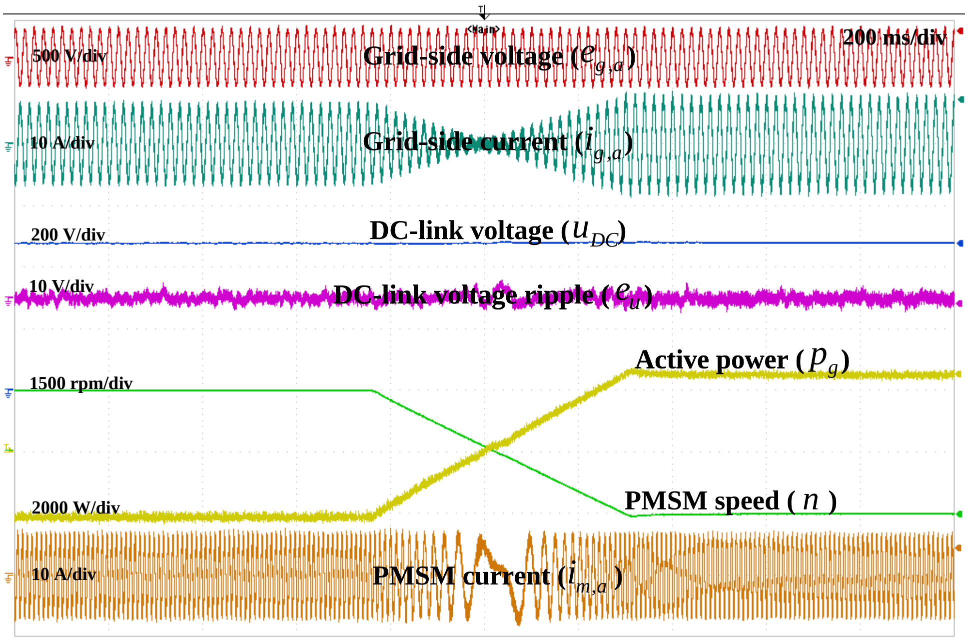

Figure 5.13: Experimental results of DPVC in the step change of speed.

the proposed DPVC strategy demonstrates superior performance as it produces a small decrease of 5 V in the DC-link voltage regulation. Accordingly, compared with the previous strategies, it also has the fastest recovery to the reference, and its recovery times of the DC-link voltage is around 50 ms.

5.2.2.4 Step change of speed

Figure 5.13 displays the experimental results under abrupt speed changes with a constant torque of -15 N·m. As the speed changes from 1500 to -1500 r/min, the operating status of the PMSM changes from generating mode to motoring mode, so the phase of the grid-side current switches from being in the opposite direction to being in the same direction as the grid-side voltage. This shift indicates a change in the operating status of the GSC from transferring power in the machine-to-grid direction to providing power in the grid-to-machine direction to maintain a constant DC-link voltage. Unlike electromagnetic torque, speed is a mechanical parameter that results in a slower operating change for the system, so it allows longer response times for control strategies. Compared with the previous control strategies, the proposed DPVC strategy demonstrates satisfying DC-link voltage regulation performance since it is minimally affected during this regulation. As seen in the waveforms, the proposed DPVC strategy yields a small voltage peak error of around 3 V during this dynamic regulation.

5.2.2.5 robustness performance

To evaluate the robustness of the control scheme, experiments with mismatched parameters are conducted. As the accuracy of the dynamic model is more severely impacted by inductance variation than resistance variation, the control performance is tested under mismatched inductance. In the DPVC strategy, the grid-side inductor L_g and PMSM inductor $L_{m,s}$ values are set to linearly increase from half of their actual value to twice their actual values (i.e., from 50 % to 200 %) simultaneously at the rated operating condition.

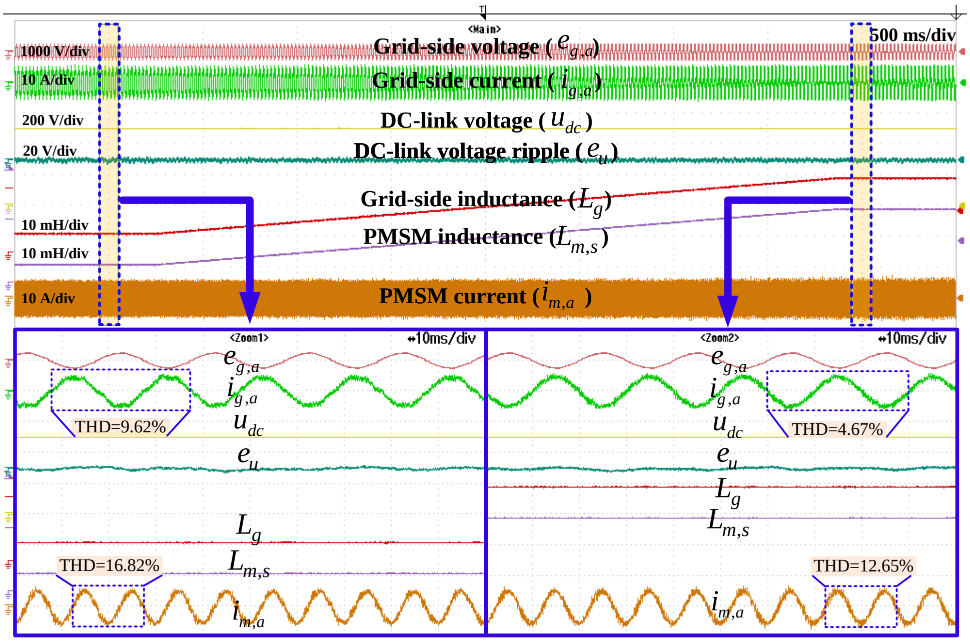

Figure 5.14: Experiment results of the DPVC strategy under mismatched inductance.

Fig. 5.14 illustrates the experimental results of the DPVC under mismatched inductance. The grid-side current THDs are approximately 2.45%, and the PMSM current THDs are around 11 % when the actual inductance values are used. However, when L_g and $L_{m,s}$ are set to 50 % of their actual values, the grid-side current THDs rise to around 9.62 %, and the PMSM current THDs increase to approximately 16.82 %. When L_g and $L_{m,s}$ are set to 200 % of their actual values, the grid-side current THDs decrease to around 4.67 %, and the PMSM current THDs are around 12.65 %. In practical systems, mismatched inductance values typically do not exceed the range of 50 % to 200 % of their actual values. As a result, the DPVC strategy exhibits comparable robustness against mismatched inductance values.

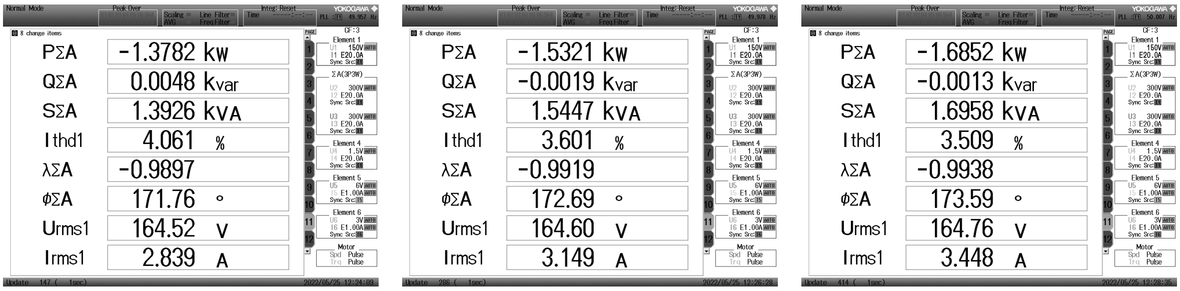

PΣA -1.3782 kW
QΣA 0.0048 kvar
SΣA 1.3926 kVA
Ithd1 4.061 %
λΣA -0.9897
φΣA 171.76 °
Urms1 164.52 V
Irms1 2.839 A

PΣA -1.5321 kW
QΣA -0.0019 kvar
SΣA 1.5447 kVA
Ithd1 3.601 %
λΣA -0.9919
φΣA 172.69 °
Urms1 164.60 V
Irms1 3.149 A

PΣA -1.6852 kW
QΣA -0.0013 kvar
SΣA 1.6958 kVA
Ithd1 3.509 %
λΣA -0.9938
φΣA 173.59 °
Urms1 164.76 V
Irms1 3.448 A

(a) 1000 r/min (b) 1100 r/min (c) 1200 r/min

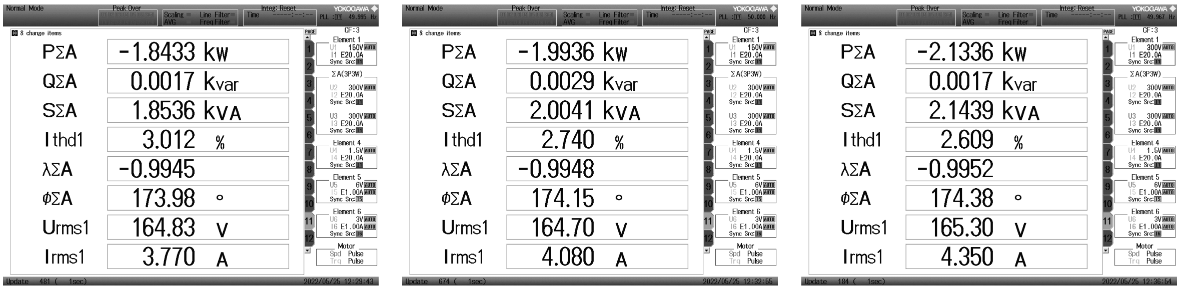

PΣA -1.8433 kW
QΣA 0.0017 kvar
SΣA 1.8536 kVA
Ithd1 3.012 %
λΣA -0.9945
φΣA 173.98 °
Urms1 164.83 V
Irms1 3.770 A

PΣA -1.9936 kW
QΣA 0.0029 kvar
SΣA 2.0041 kVA
Ithd1 2.740 %
λΣA -0.9948
φΣA 174.15 °
Urms1 164.70 V
Irms1 4.080 A

PΣA -2.1336 kW
QΣA 0.0017 kvar
SΣA 2.1439 kVA
Ithd1 2.609 %
λΣA -0.9952
φΣA 174.38 °
Urms1 165.30 V
Irms1 4.350 A

(d) 1300 r/min (e) 1400 r/min (f) 1500 r/min

Figure 5.15: Power analyzer screenshots of the DPVC strategy at different speeds.

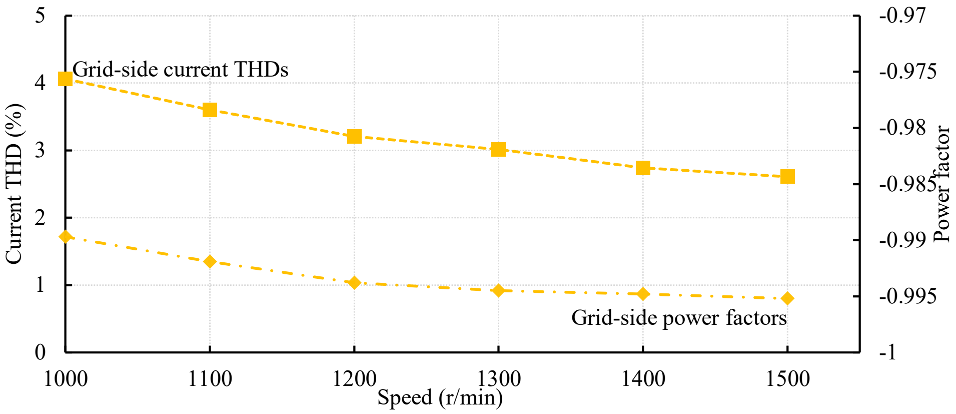

Figure 5.16: Current THDs and power factors of the DPVC strategy.

5.2.3 Current THDs and power factors

The experimental power analyzer screenshots (Yokogawa WT1800E) of the proposed DPVC strategy, which reflect it steady-state performances at different operating speeds, are presented in Fig. 5.15, and the current THDs and power factors are concluded in Fig. 5.16. In the power analyzer, $\mathrm{P\Sigma A}$, $\mathrm{Q\Sigma A}$, $\mathrm{S\Sigma A}$, $\mathrm{Ithd1}$, $\lambda\mathrm{\Sigma A}$, $\phi\mathrm{\Sigma A}$, $\mathrm{Urms1}$, and $\mathrm{Irms1}$ denote the active power, reactive power, apparent power, current THD, power factor phase angle, phase voltage and phase current of AC side, respectively. At the rated operating condition (480 V, 1500 r/min, -15 $\mathrm{N}\cdot\mathrm{m}$, 0 Var), the grid-side current THDs are controlled around 2.609 %, the grid-side power factors are controlled at around 0.9952, and the machine-side current THDs are around 9.59 %.

5.3 Control performances under abnormal grid

A BTB converter-fed PMSM drive system can face various issues under an abnormal grid, and the common issues are:

1) **Unbalanced grid-side voltage**: This indicates a case when the amplitude of the three-phase grid voltages are not equal. This can cause the PMSM drive system to operate at reduced efficiency and can even lead to damage to the system components.

2) **Distorted grid-side voltage**: This occurs when the voltage waveform is not sinusoidal, but has harmonics and/or transients present. This also can cause the PMSM drive system to operate at reduced efficiency and can even lead to damage to the system components.

3) **Low-voltage ride-through**: This occurs when the grid voltage drops below a certain level (15 % -25 % of its nominal value according to E. ON grid code), and the PMSM drive system must continue to operate without tripping or shutting down. This requires the use of appropriate power electronic devices and control strategies to ensure that the PMSM drive system can maintain its operation during these conditions.

5.3.1 Unbalanced grid-side voltage

The AC components of active power and reactive power in the system increase in the unbalanced grid-side voltage conditions [10], and a detailed explanation is as follows. The grid-side voltage $\boldsymbol{e}_g$ and current $\boldsymbol{i}_g$ can be expressed as the sum of positive and negative sequence components:

$$\begin{cases} \boldsymbol{e}_g = \boldsymbol{e}^+_{g,\alpha\beta} + \boldsymbol{e}^-_{g,\alpha\beta} = \boldsymbol{e}^+_{g,dq}e^{j\omega t} + \boldsymbol{e}^-_{g,dq}e^{-j\omega t} \\ \boldsymbol{i}_g = \boldsymbol{i}^+_{g,\alpha\beta} + \boldsymbol{i}^-_{g,\alpha\beta} = \boldsymbol{i}^+_{g,dq}e^{j\omega t} + \boldsymbol{i}^-_{g,dq}e^{-j\omega t} \end{cases} \tag{5.11}$$

$$\begin{cases} \boldsymbol{e}^+_{g,dq} = \boldsymbol{e}^+_{g,d} + j\boldsymbol{e}^+_{g,q} \\ \boldsymbol{e}^-_{g,dq} = \boldsymbol{e}^-_{g,d} + j\boldsymbol{e}^-_{g,q} \\ \boldsymbol{i}^+_{g,dq} = \boldsymbol{i}^+_{g,d} + j\boldsymbol{i}^+_{g,q} \\ \boldsymbol{i}^-_{g,dq} = \boldsymbol{i}^-_{g,d} + j\boldsymbol{i}^-_{g,q} \end{cases} \tag{5.12}$$

where ω is the angular frequency of grid-side voltage, and $\boldsymbol{e}^+_{g,\alpha\beta}, \boldsymbol{e}^-_{g,\alpha\beta}, \boldsymbol{e}^+_{g,dq}, \boldsymbol{e}^-_{g,dq}, \boldsymbol{i}^+_{g,\alpha\beta}, \boldsymbol{i}^-_{g,\alpha\beta}, \boldsymbol{i}^+_{g,dq}$, and $\boldsymbol{i}^-_{g,dq}$are the positive and negative sequence

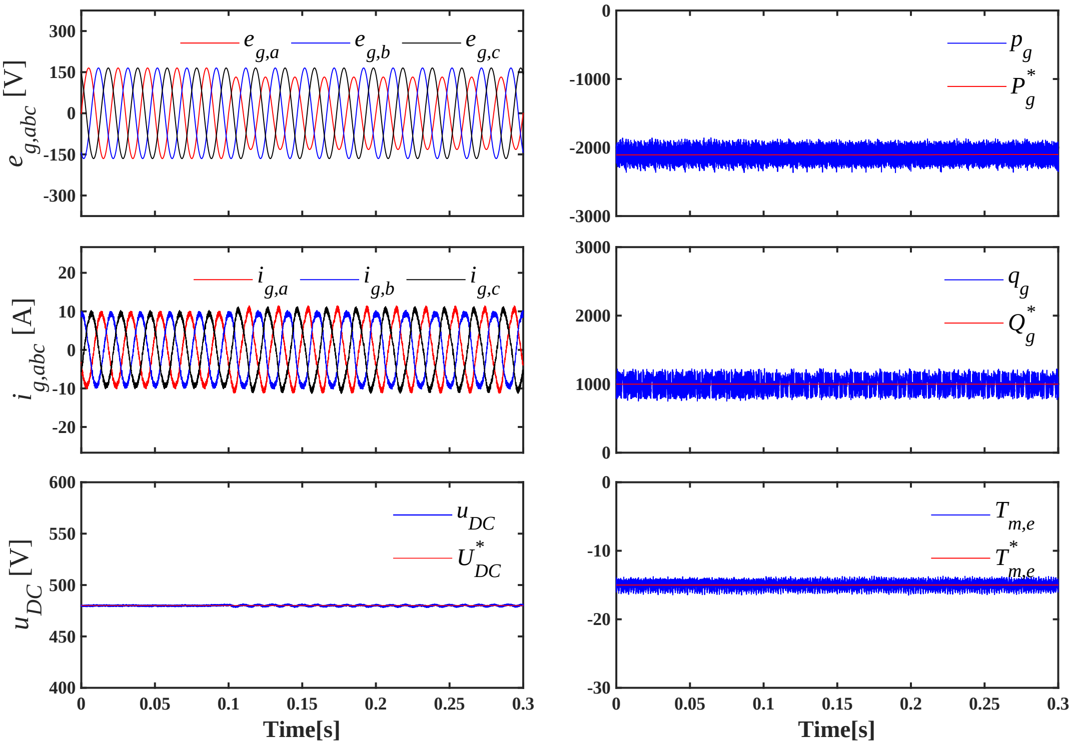

Figure 5.17: Waveforms of the proposed DPVC strategy under unbalanced grid voltage.

components of the grid-side voltage/current in $\alpha\beta$-axis and dq-axis, respectively. The grid-side power expression under power invariant transformation can be given by

$$s = p_g + jq_g = \left(\boldsymbol{e}^{+}_{g,dq}e^{j\omega t} + \boldsymbol{e}^{-}_{g,dq}e^{-j\omega t}\right) \times \left(\boldsymbol{i}^{+}_{g,dq}e^{j\omega t} + \boldsymbol{i}^{-}_{g,dq}e^{-j\omega t}\right)^{*} \tag{5.13}$$

where

$$\begin{cases} p_g = p_0 + p_{c2}\cos 2\omega t + p_{s2}\sin 2\omega t \\ q_g = q_0 + q_{c2}\cos 2\omega t + q_{s2}\sin 2\omega t \end{cases} \tag{5.14}$$

In dq rotating coordinates, by expanding (5.13) and (5.14), the expression of power can be written as [10]

$$\begin{cases} p_0 = e^{+}_{g,d}i^{+}_{g,d} + e^{+}_{g,q}i^{+}_{g,q} + e^{-}_{g,d}i^{-}_{g,d} + e^{-}_{g,q}i^{-}_{g,q} \\ p_{c2} = e^{+}_{g,d}i^{-}_{g,d} + e^{+}_{g,q}i^{-}_{g,q} + e^{-}_{g,d}i^{+}_{g,d} + e^{-}_{g,q}i^{+}_{g,q} \\ p_{s2} = e^{+}_{g,d}i^{-}_{g,q}e^{+}_{g,q}i^{-}_{g,d} + e^{-}_{g,d}i^{+}_{g,d} - e^{-}_{g,q}i^{+}_{g,q} \\ q_0 = e^{+}_{g,q}i^{+}_{g,d} - e^{+}_{g,d}i^{+}_{g,q} + e^{-}_{g,q}i^{-}_{g,d}e^{-}_{g,d}i^{-}_{g,q} \\ q_{c2} = e^{+}_{g,q}i^{-}_{g,d}e^{+}_{g,d}i^{-}_{g,q} + e^{-}_{g,q}i^{-}_{g,d}e^{-}_{g,d}i^{+}_{g,q} \\ q_{s2} = e^{+}_{g,d}i^{-}_{g,d} + e^{+}_{g,q}i^{-}_{g,q}e^{-}_{g,d}i^{+}_{g,d} - e^{-}_{g,q}i^{+}_{g,q} \end{cases} \tag{5.15}$$

Because of the limited experimental conditions, there is no programmable AC power source in the laboratory, which means the proposed DPVC strategy cannot be tested under the experiment condition of unbalanced grid-side voltage. However, the simulation with unbalanced grid-side voltage is conducted to further test the control performance of proposed strategy, and Fig. 5.17 shows the waveforms when under the condition of 20 % voltage dip. Since 0.1 s, the grid-side voltage is changed from the balanced state to the unbalanced state, and the system is still controllable when the unbalanced voltage happens in the grid.

5.3.2 Distorted grid-side voltage

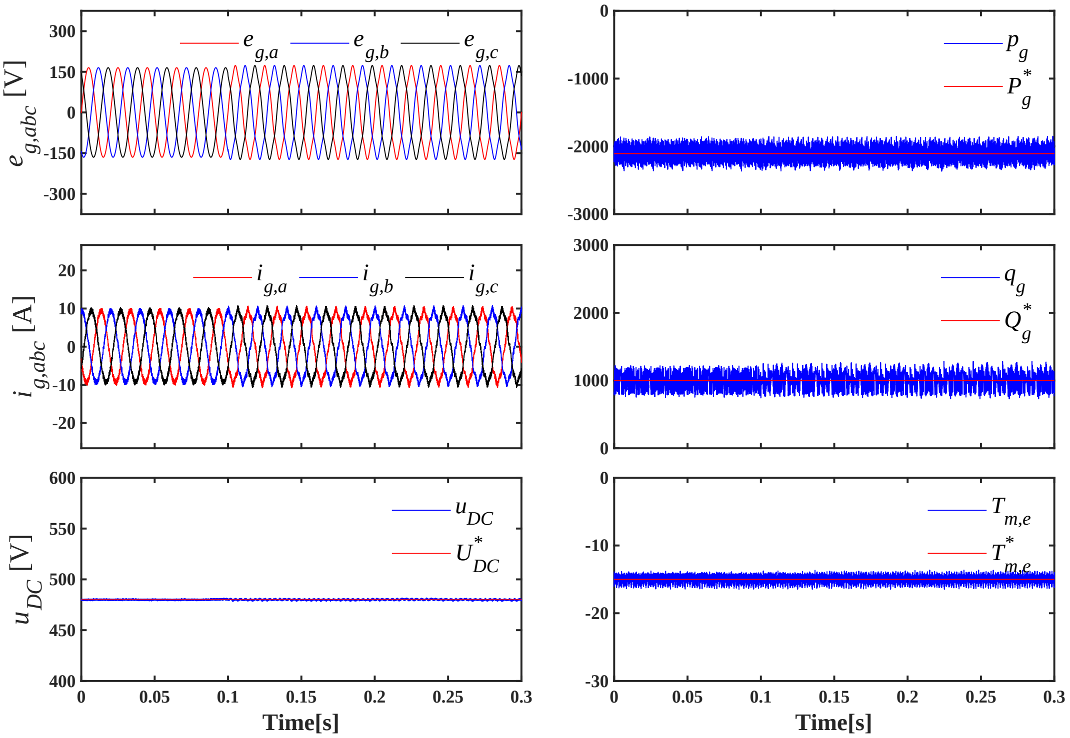

Figure 5.18: Waveforms of the proposed DPVC strategy under distorted grid-side voltage.

The simulation with distorted grid-side voltage is also conducted to test the control performance of proposed strategy. The fifth harmonics frequently appear in grid-side voltage [24], and Fig. 5.18 presents the waveforms of the simulation where the 5 % fifth-order harmonic component is injected since 0.1 s. As can be seen, although the system is still controllable when the grid-side voltage distorts, the grid-side current is also distorted since the harmonic rejection under abnormal grid-side voltage is not specially considered. To reduce the adverse effects on grid-side current, the harmonic extraction algorithm, e.g., discrete Fourier transform [83], can be utilized to extract the harmonic components from the harmonic-polluted grid- side voltage, and the power compensation method [84, 85] can be considered to be added into the proposed system to achieve the sinusoidal and symmetrical grid-side currents. These will be the focuses of our future research to further improve the system performance under abnormal grid-side voltage.

5.3.3 Low-voltage ride-through

In the Low-Voltage Ride-Through (LVRT) profile, the grid voltage becomes 15 % -25 % of its nominal value according to E. ON grid code. The LVRT capability is a grid code standard

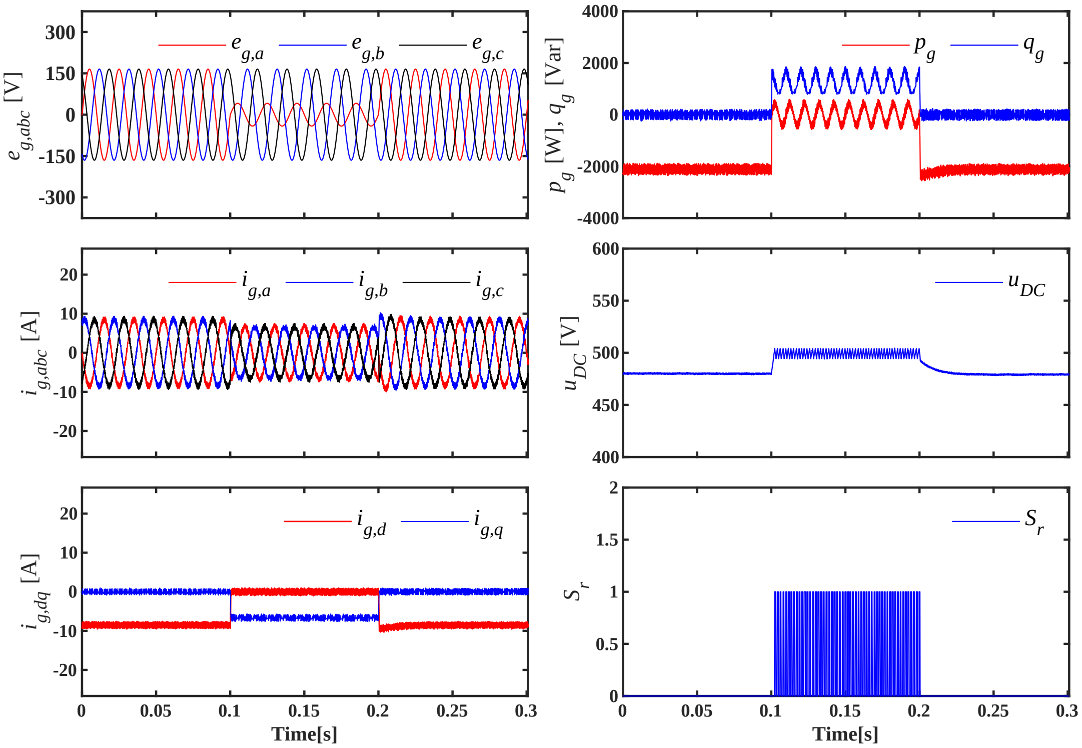

Figure 5.19: Waveforms of the proposed DPVC strategy under the crowbar LVRT method.

for most modern WECS, which requires the power generation system to be grid-connected during faults and to provide reactive power to support the WECS [32]. Generally, specialized algorithms and hardware configurations are required to meet LVRT requirements [86].

Crow-bar protection [87] is a commonly-used LVRT method in WECS. In this method, a chopper circuit along with a resistor is used across the DC-link capacitor, and a DC-link voltage PI controller is used to control the chopper circuit. Under normal operating conditions, no gate pulse is given to the chopper circuit. When LVRT happens, the DC-link voltage rises above a threshold, and the PI controller yields a nonzero duty cycle, which enables the generation of gate pulses for the chopper circuit. Therefore, the DC-link voltage is kept within safe limits by dissipating the generated power in the crow-bar resistance, and the operating of PMSM does not need to be modified [88, 89]. Many other LVRT methods [90–93] are also developed in literature.

The performance of the proposed DPVC strategy under the crowbar LVRT method is tested according to [88], and the waveforms are shown in Fig. 5.19. In the figure, $e_{g,abc}$, $i_{g,abc}$, $i_{g,dq}$, p_g, q_g, u_{DC}, and S_r denote the grid-side phase voltage, grid-side phase current, grid-side dq-axis current, grid-side active power, grid-side reactive power, DC-link voltage, and switching signal of the chopper circuit, respectively. Since 0.1 s, phase a of grid-side voltage drops to 25 % of its nominal value, and the system goes into LVRT mode. In this mode, the system remains connected to the grid and starts to provide reactive power. When phase a of grid-side voltage recovers to its nominal value, the system also recovers to its normal operating condition.

5.4 Summary

In this chapter, a DPVC strategy is proposed for the BTB converter-fed PMSM system, and its advantages are as follows:

- Achieve cascade-free control.

A DC-link voltage PI controller is always necessary to control the BTB converter with PI-MPC, which is a cascaded control structure since the inner MPC is nested within the outer voltage PI control loop. In this chapter, a DPVC strategy without outer voltage PI controller is proposed for the BTB converter-fed PMSM drive system, which realizes the well-regulated DC-link voltage, controllable power flow, sinusoidal phase current, and near-unity power factor.

- Design a new cost function.

A new cost function integrating the DC-link voltage regulation term and power regulation term together is constructed, so that the control of DC-link voltage and power can be realized by a single cost function. The desired power of PMSM motor is directly adopted for the prediction of DC-link voltage for the future time instant. During the assessment of the cost function, the switching vector, which is able to produce a DC-link voltage closer to the reference and is able to simultaneously produce an active power capable of further narrowing that voltage error, is chosen for the next time instant. Without steady-state deviations, the proposed strategy presents an effective DC-link voltage tracking performance even though the system operating state varies abruptly.

As can be seen from the experiment results, the proposed DPVC strategy presents fast dynamic performances in response to step changes of DC-link voltage, torque, reactive power, and speed while realizing a satisfying steady-state performance.

CHAPTER 6

Enhanced DPVC strategy for BTB converter-fed PMSM system

Although satisfying control performances, especially transient-state performances, are obtained by the proposed DPVC strategy in Chap. 5, there are also challenges that need to be addressed. For example, power deviation can be generated in this model-based control system because of the use of nominal values of inductor and resistor for prediction. Additionally, the adoption of weighting factor in cost functions makes it hard to achieve good performance in variable operating conditions, as it requires additional effort to tune parameters. This chapter aims to address the above two problems, thereby further enhancing the performance of DPVC strategy.

- In Sec. 6.1, the Kalman filter is integrated into DPVC strategy to eliminate the steady-state power deviation and to improve the robustness of system.
- In Section 6.2, a weighting factor-less method is used to eliminate the parameter tunning effort of the weighting factor in the DPVC strategy and ensures fast response at various operating conditions.

6.1 DPVC strategy with Kalman filter

To predict active power and reactive power accurately, the actual value of the inductor is essential. However, it is actually the nominal value of inductor that is involved in the prediction, and the actual inductance also changes during the operation due to the varying current and temperature. Both of the above two aspects will cause steady-state error in power regulation. To compensate for the steady-state error, Kalman filter is adopted to estimate the power disturbances caused by the mismatched parameters, and the estimated disturbances are used to correct the expressions of power prediction.

6.1.1 Kalman filter with reactive power compensation

The discretized power equation of GSC in $\alpha\beta$ coordinate system at $(k+1)^{\text{th}}$ instant is given by

$$\begin{aligned}\begin{pmatrix} p_g[k+1] \\ q_g[k+1] \end{pmatrix} = \frac{3T_s}{2L_g}\begin{bmatrix} e_g^{\alpha}[k] & e_g^{\beta}[k] \\ e_g^{\beta}[k] & -e_g^{\alpha}[k] \end{bmatrix}\begin{pmatrix} e_g^{\alpha}[k]-u_g^{\alpha}[k] \\ e_g^{\beta}[k]-u_g^{\beta}[k] \end{pmatrix} \\ +\begin{pmatrix} p_g[k]-\frac{T_sR_g}{L_g}p_g[k]-T_s\omega_g q_g[k] \\ q_g[k]-\frac{T_sR_g}{L_g}q_g[k]+T_s\omega_g p_g[k] \end{pmatrix}.\end{aligned} \tag{6.1}$$

Equation (6.1) holds only when the actual values of the inductor and resistor, i.e., L_g and R_g, are brought into it for prediction. However, it is actually the nominal values, i.e., $L_{g,n}$ and $R_{g,n}$, that are involved in the prediction since L_g and R_g are unknown, and it is also possible that the actual values L_g and R_g change during the operation, which causes the steady-state power error in system [94]. To address this problem, Kalman filter is added to the proposed strategy to compensate for the steady-state error by estimating the disturbances in power expression, and the aforementioned uncertainties can be regarded as the active power disturbances f_p and reactive power disturbances f_q for (6.1). Then the state space model of Kalman filter can be written as

$$\begin{aligned}\underbrace{\begin{pmatrix} p_g[k] \\ q_g[k] \\ f_p[k] \\ f_q[k] \end{pmatrix}}_{\boldsymbol{X}_d[k]} = \underbrace{\begin{bmatrix} \boldsymbol{C}_d & \boldsymbol{D}_d \\ \boldsymbol{0}_{2\times 2} & \boldsymbol{I}_2 \end{bmatrix}}_{\boldsymbol{F}_d}\underbrace{\begin{pmatrix} p_g[k-1] \\ q_g[k-1] \\ f_p[k-1] \\ f_q[k-1] \end{pmatrix}}_{\boldsymbol{X}_d[k-1]} \\ +\underbrace{\frac{T_s}{L_{g,n}}\begin{bmatrix} \boldsymbol{A}_c[k-1] \\ \boldsymbol{0}_{2\times 2}[k-1] \end{bmatrix}}_{\boldsymbol{G}_d[k-1]}\boldsymbol{B}_c[k-1]+\boldsymbol{W}_d[k]\end{aligned} \tag{6.2}$$

$$\underbrace{\begin{pmatrix} p_g[k] \\ q_g[k] \end{pmatrix}}_{\boldsymbol{Z}_d[k]} = \underbrace{\begin{bmatrix} \boldsymbol{I}_2 & \boldsymbol{0}_{2\times 2} \end{bmatrix}}_{\boldsymbol{H}_d}\boldsymbol{X}_{\boldsymbol{d}}[k]+\boldsymbol{V}_d[k] \tag{6.3}$$

where $\boldsymbol{C}_d = \begin{bmatrix} 1-\frac{T_sR_{g,n}}{L_{g,n}} & -T_s\omega_g \\ \omega_g T_s & 1-\frac{T_sR_{g,n}}{L_{g,n}} \end{bmatrix}$, $\boldsymbol{D}_d = \begin{bmatrix} \frac{-T_s}{L_{g,n}} & 0 \\ 0 & \frac{-T_s}{L_{g,n}} \end{bmatrix}$, $\boldsymbol{W}_d[k]$ is the process noise with the covariance matrix $\boldsymbol{Q}_d$: $\boldsymbol{W}_d[k] \sim N(0,\boldsymbol{Q}_d)$, and $\boldsymbol{V}_d[k]$ is measurement noise with the covariance matrix $\boldsymbol{R}_d$:$\boldsymbol{V}_d[k] \sim N(0,\boldsymbol{R}_d)$. Then the predicted (a priori) estimate of state vector can be obtained as below based on the mathematical model

$$\hat{\boldsymbol{X}}_d^-[k] = \boldsymbol{F}_d\hat{\boldsymbol{X}}_d[k-1]+\boldsymbol{G}_d[k-1]\boldsymbol{B}_c[k-1] \tag{6.4}$$

where $\hat{\boldsymbol{X}}_d^-[k]$ represents the priori estimate of state vector $\boldsymbol{X}_d$, and $\hat{\boldsymbol{X}}_d[k-1]$ represents the posteriori estimate of state vector calculated within interval $[k-1,k)$. The accuracy covariance of the priori estimate of state vector is defined, i.e., $\boldsymbol{P}_d^-[k] = E[(\boldsymbol{X}_d[k]-\hat{\boldsymbol{X}}_d^-[k])(\boldsymbol{X}_d[k]-\hat{\boldsymbol{X}}_d^-[k])^T]$ and it can be calculated by

$$\boldsymbol{P}_d^-[k] = \boldsymbol{F}_d\boldsymbol{P}_d[k-1]\boldsymbol{F}_d^T+\boldsymbol{Q}_d \tag{6.5}$$

where $\boldsymbol{P}_d[k-1]$ is the accuracy covariance of the posteriori estimate of state vector obtained in $[k-1,k)$. Then in the correction stage, Kalman gain $\boldsymbol{K}_d[k]$ and the posteriori estimate of state vector $\hat{\boldsymbol{X}}_d[k]$ can be calculated by

$$\boldsymbol{K}_d[k] = \frac{\boldsymbol{P}_d^-[k]\boldsymbol{H}_d^T}{\boldsymbol{H}_d\boldsymbol{P}_d^-[k]\boldsymbol{H}_d^T + \boldsymbol{R}_d} \tag{6.6}$$

$$\hat{\boldsymbol{X}}_d[k] = \hat{\boldsymbol{X}}_d^-[k] + \boldsymbol{K}_d[k](\boldsymbol{Z}_d[k] - \boldsymbol{H}_d\hat{\boldsymbol{X}}_d^-[k]) \tag{6.7}$$

$$\boldsymbol{P}_d[k] = (\boldsymbol{I} - \boldsymbol{K}_d[k]\boldsymbol{H}_d)\boldsymbol{P}_d^-[k] \tag{6.8}$$

where $\boldsymbol{P}_d[k]$ is updated to be used in the next sampling period. Through this process, $f_p[k]$ and $f_q[k]$ are estimated and used to correct the expressions for power prediction.

6.1.2 Kalman filter without DC-link voltage error

The proposed DVPC strategy can regulate the terms in its cost function to approach zero to realize the tracking of references. However, the converters also consume power (conduction loss, switching loss, etc.) when transferring the generated power of PMSM P_g^* into grid, which means the power that can be actually transferred into grid side is less than P_g^*. In this case, if the voltage vector that makes $p_g[k+2]$ equal to P_g^* is selected, not only all the power coming from PMSM is sent to grid but the DC-link capacitor will be discharged to contribute its power to grid, which makes the regulated DC-link voltage lower than its reference. To address that problem, the sum term, which has been mentioned in Chap. 5, should be added into P_g^* to compensate for the power loss in power converters, thus eliminating the steady-state voltage error. Alternatively, the sum term also can be removed by correcting the prediction model of DC-link voltage through the Kalman filter for parameter mismatch.

Based on power balance, the following equation holds in an ideal case

$$u_{DC}C\frac{du_{DC}}{dt} = p_g - \tau_{m,e}^*\omega_{m,m} \tag{6.9}$$

However, the switching loss, conduction loss, etc. in the realistic case are not considered in the above expression, which causes the steady-state error in DC-link voltage. To address this problem, Kalman filter is used to compensate for the steady-state voltage error. The unconsidered power loss can be regarded as the active power disturbances f_{udc}, then (6.9) can be modified as

$$u_{DC}C\frac{du_{DC}}{dt} = \frac{1}{2}C\frac{du_{DC}^2}{dt} = p_g - \tau_{m,e}^*\omega_{m,m} + f_{udc}. \tag{6.10}$$

The discrete form of (6.10) is

$$(u_{DC}[k])^2 = \frac{2T_s}{C}\left(p_g[k-1] - \tau_{m,e}^*\omega_{m,m}[k-1] + f_{udc}[k-1]\right) + (u_{DC}[k-1])^2. \tag{6.11}$$

Then the Kalman filter, which can simultaneously realize parameter mismatch compensation and voltage steady-state error elimination, can be obtained as follows by adding (6.11) into the state space model of the Kalman filter for parameter mismatch

$$\underbrace{\begin{pmatrix} p_g[k] \\ q_g[k] \\ (u_{DC}[k])^2 \\ f_p[k] \\ f_q[k] \\ f_{udc}[k] \end{pmatrix}}_{\boldsymbol{X}_d[k]} = \underbrace{\begin{bmatrix} \boldsymbol{C}_d & \boldsymbol{D}_d \\ \mathbf{0}_{3\times 3} & \boldsymbol{I}_3 \end{bmatrix}}_{\boldsymbol{F}_d} \underbrace{\begin{pmatrix} p_g[k-1] \\ q_g[k-1] \\ (u_{DC}[k-1])^2 \\ f_p[k-1] \\ f_q[k-1] \\ f_{udc}[k-1] \end{pmatrix}}_{\boldsymbol{X}_d[k-1]} + \underbrace{\frac{T_s}{L_{g,n}} \begin{bmatrix} \boldsymbol{A}_c[k-1] \\ \mathbf{0}_{3\times 3} \end{bmatrix}}_{G_d[k-1]} \boldsymbol{B}_c[k-1] + \boldsymbol{W}_d[k] \tag{6.12}$$

$$\underbrace{\begin{pmatrix} p_g[k] \\ q_g[k] \\ u_{dc}[k] \end{pmatrix}}_{\boldsymbol{Z}_d[k]} = \underbrace{\begin{bmatrix} \boldsymbol{I}_3 & \mathbf{0}_{3\times 3} \end{bmatrix}}_{\boldsymbol{H}_d} \boldsymbol{X}_d[k] + \boldsymbol{V}_d[k] \tag{6.13}$$

where

$$\boldsymbol{A}_c[k-1] = \frac{3}{2} \times \begin{bmatrix} e_{g,\alpha}[k-1] & e_{g,\beta}[k-1] & 0 \\ e_{g,\beta}[k-1] & -e_{g,\alpha}[k-1] & 0 \\ 0 & 0 & -\frac{4L_{g,n}}{3C} \end{bmatrix} \tag{6.14a}$$

$$\boldsymbol{B}_c[k-1] = \begin{pmatrix} e_{g,\alpha}[k-1] - u_{g,\alpha}[k-1] \\ e_{g,\beta}[k-1] - u_{g,\beta}[k-1] \\ \tau^*_{m,e}\omega_{m,m}[k-1] \end{pmatrix} \tag{6.14b}$$

$$\boldsymbol{C}_d = \begin{bmatrix} 1 - \frac{T_s R_{g,n}}{L_{g,n}} & -T_s\omega_g & 0 \\ \omega_g T_s & 1 - \frac{T_s R_{g,n}}{L_{g,n}} & 0 \\ \frac{2T_g}{C} & 0 & 1 \end{bmatrix} \tag{6.14c}$$

$$\boldsymbol{D}_d = \begin{bmatrix} -\frac{T_s}{L_{g,n}} & 0 & 0 \\ 0 & -\frac{T_s}{L_{g,n}} & 0 \\ 0 & 0 & \frac{2T_s}{C} \end{bmatrix} \tag{6.14d}$$

The following implementation steps are the same as the steps described in Sec. 6.1.1. Through this process, f_{udc} can be estimated and used to correct the power reference of PMSM in (5.1) as follows

$$P_g^* = \tau^*_{m,e}\omega_{m,m}[k] - f_{udc}[k] \tag{6.15}$$

Fig. 6.1 and Fig. 6.2 present the experimental waveforms and power analyzer screenshots of DPVC strategy at the rated operating condition, respectively. In Fig. 6.1, the short green dash on the left-most side of the reactive power curve indicates 0 Var. As can be seen from Fig. 6.1(a) and Fig. 6.2(a), for the system without Kalman filter, the reactive power deviates its setpoint (0V) by 260 Var, which correspondingly leads to a decreased power factor, and DC-link voltage deviates its setpoint by 8V when the sum term is not added to the power reference in the cost function for compensation. However, as can be seen from Fig. 6.1(b) and Fig. 6.2(b),

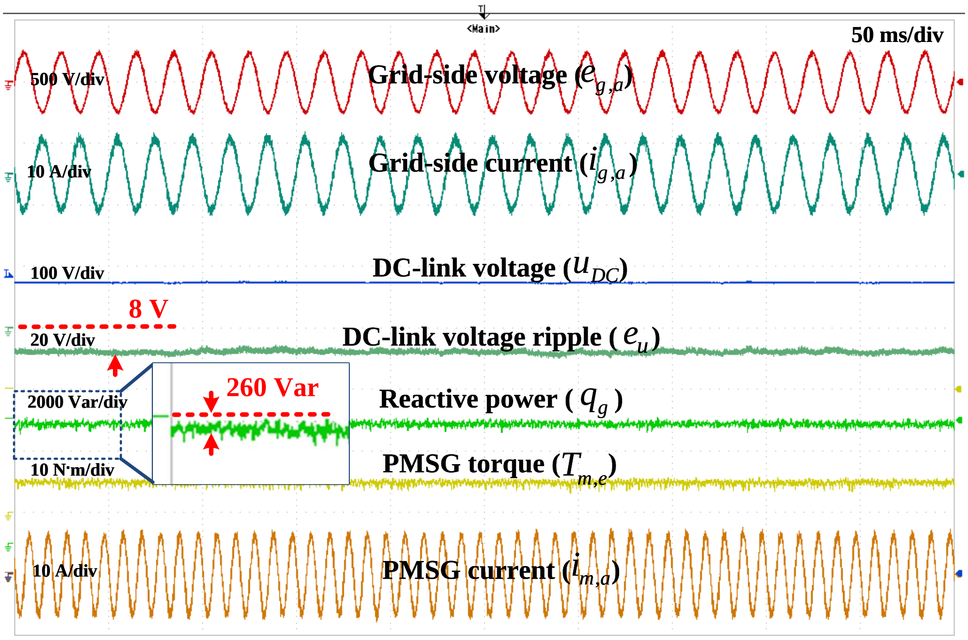

(a) Without Kalman filter.

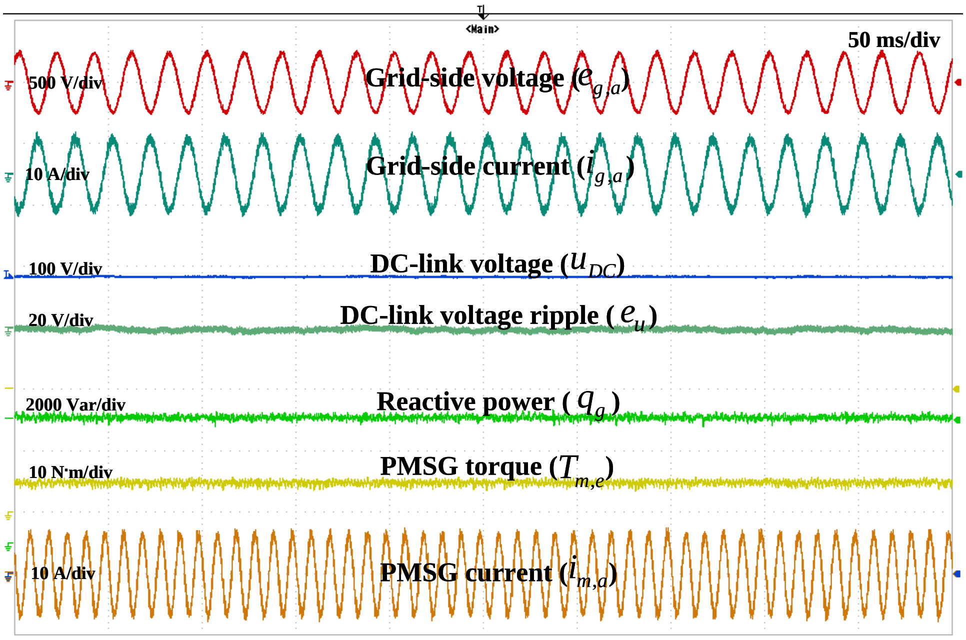

(b) With Kalman filter.

Figure 6.1: Experiment waveforms of DPVC strategy at the rated operating condition.

the reactive power error and DC-link voltage error can be effectively removed by adopting the proposed Kalman filter. With the Kalman filter, the reactive power is regulated strictly to around 0 Var, and DC-link voltage also is able to track its setpoint without deviation.

The mismatched parameters are experimentally tested on the DPVC strategy with Kalman filter in the rated operating condition. Since the inductance variation has a more serious effect

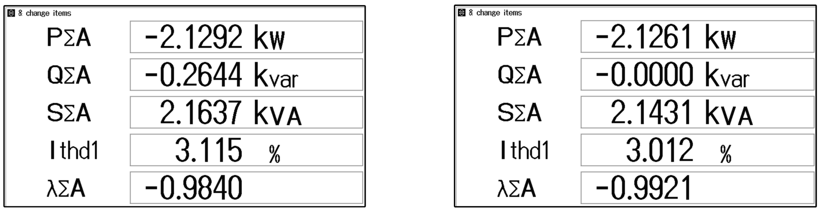

8 change items

PΣA	-2.1292 kW
QΣA	-0.2644 kvar
SΣA	2.1637 kVA
Ithd1	3.115 %
λΣA	-0.9840

8 change items

PΣA	-2.1261 kW
QΣA	-0.0000 kvar
SΣA	2.1431 kVA
Ithd1	3.012 %
λΣA	-0.9921

(a) Without Kalman filter. (b) With Kalman filter.

Figure 6.2: Power analyzer screenshots of DPVC strategy at rated operating condition.

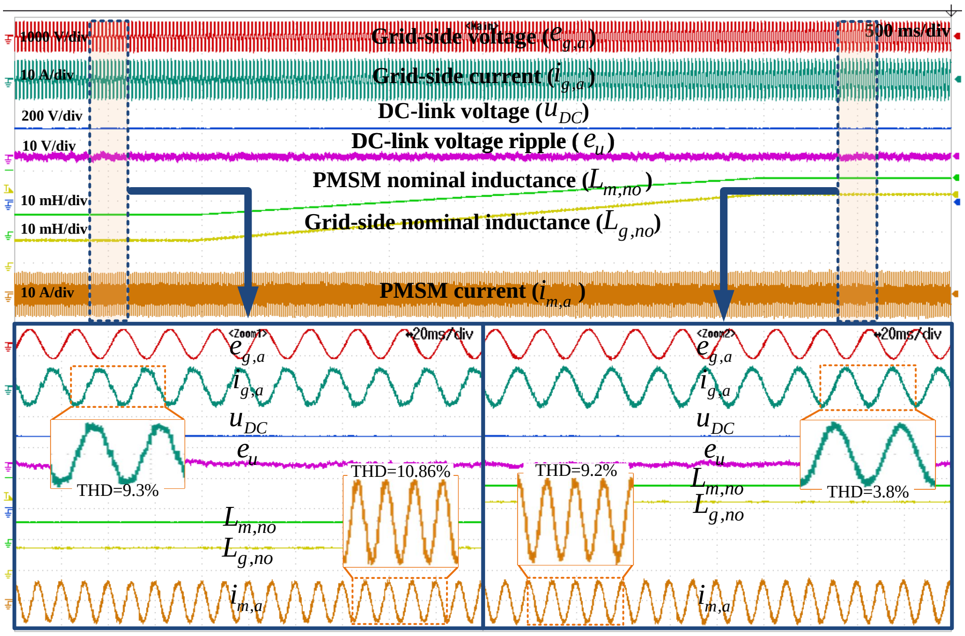

Figure 6.3: Experimental waveforms of DPVC strategy with Kalman filter under mismatched inductances.

on the model accuracy than resistance variation, the control performance under mismatched inductance is tested and presented in Fig. 6.3. The nominal values of grid-side inductor $L_{g,n}$ and PMSM inductor $L_{m,n}$ are set to linearly increase from 50% to 150% of their actual values at the same time inside the controller. The grid-side current THDs are around 2.94% and the PMSM current THDs are around 9.59% if $L_{g,n}$ and $L_{m,n}$ are adopted. When $L_{g,n}$ and $L_{m,n}$ are set to 50% and 150%, grid-side current THDs are around 9.3% and 3.8%, respectively, and the PMSM current THDs are around 10.86% and 9.2%, respectively. The control performance does degrade as the inductances deviate from their actual values, but the system remains stable. Besides, there is no steady-state error in the reactive power even though the mismatched parameters are adopted for prediction, as can be found in Fig. 6.4.

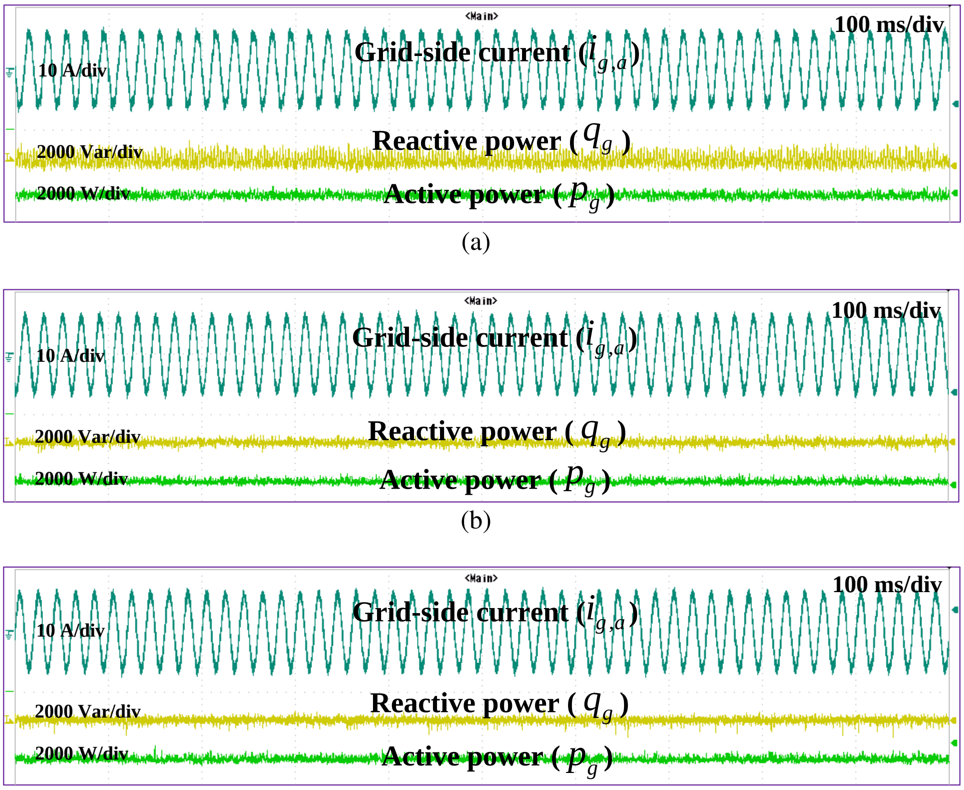

(a)

(b)

(c)

Figure 6.4: Experimental power waveforms of DPVC strategy with Kalman filter under mismatched inductances. (a) $L_{g,n}$ and $L_{m,n}$ decrease to 50% ($L_{g,n}$=7.5 mH, $L_{m,n}$=6 mH). (b) $L_{g,n}$ and $L_{m,n}$ are adopted ($L_{g,n}$=15 mH, $L_{m,n}$=12 mH). (c) $L_{g,n}$ and $L_{m,n}$ increase to 150% ($L_{g,n}$=22.5 mH, $L_{m,n}$=18 mH).

6.2 DPVC strategy without weighting factor

One crucial part in MPC algorithm is the cost function design which includes the determination of regulated variables and tuning of the weighting factor according to the desired behavior of system. The cost function design can be extremely complex especially when many constraints need to be used to guarantee the performance, but it only depends on the control objects of the application under study. Generally, a large number of simulations or experiments is necessary to find the proper value of the weighting factor [81], which lacks sufficient theoretical basis and is also a time-consuming process. To address the above problem, some researches have presented the guideline about how to obtain the well-designed weighting factor based on a specific standard [95, 96]. However, the system performance with a constant weighting factor cannot be guaranteed in different operating conditions. The others focus on how to get rid of the weighting factor from cost function. In [97], one single regulated variable is chosen to supersede the original two regulated variables in conventional cost function and the weighting factor is naturally eliminated from cost function. In [98], the proposed parallel predictive method separately calculates the flux criterion and torque criterion. In [99], two vectors are sequentially implemented in one control period. The first vector is for power regulation and the second is for neutral point balance regulation. A time modulation controlled by a proportional controller is used to adjust its duty cycle in a control period. However, it is hard to implement this method due to the variable switching point between the two vectors. In [100], the method, which uses a ranking table to determine the importance of each objective in the cost function, is proposed in the Model Predictive Torque Control (MPTC). It achieves independence from the weighting factor, but it may miss relative magnitude errors because the ranking table is discrete. Another way to avoid using weighting factors is to convert the different objectives in the cost function into a reference vector with the same magnitude [101]. Other researchers propose controlling the torque and stator flux indirectly by controlling the direct and quadrature stator current, which have objectives of the same magnitude [102]. In [103], a modified MPTC is suggested where the electrical torque and stator flux are controlled by controlling the torque and reactive torque. Both have the same order of magnitude, so a weighting factor is not needed.

To avoid the challenge of selecting appropriate weighting factors in multiobjective control, the sequential MPTC (SMPTC) method has been proposed in [104]. The SMPTC has two control objectives: the electromagnetic torque τ_c and amplitude of the stator flux Ψ_s. Two optimum vectors that minimize the torque criterion are chosen from eight possible vectors firstly and the one of the two that gets the smaller result from flux criterion is selected as the finalized vector to be applied to the system. The two cost functions used in SMPTC are

$$\begin{aligned} J_\tau &= (\Delta\tau_c)^2 = (\tau_c^* - \tau_c[k+1])^2 \\ J_\Psi &= (\Delta\Psi_s)^2 = (\Psi_s^* - \Psi_s[k+1])^2 \end{aligned} \tag{6.16}$$

This SMPTC can be described in three simple steps: First, the electromagnetic torque for the next control period is predicted using all possible vectors of the 2L-VSI and the discrete-time model of the stator flux and torque. Second, the cost function J_τ is evaluated, and the two vectors that minimize this cost function are selected for the next optimization stage. Finally, the two optimal vectors found in the previous step are evaluated in the cost function J_Ψ, and the vector that minimizes J_Ψ is selected as the optimal vector to be applied in the 2L-VSI in the next control period. With this method, the need for weighting factors is eliminated, while still achieving good performance in the motor drive.

6.2.1 Basic principle

The weighting factor in the cost function is generally determined based on trial and error procedures, which are empirical and time-consuming. Besides, a fixed weighting factor cannot be suitable for various operating conditions. Therefore, the weighting factor is further eliminated from the cost function of the proposed DPVC, and the system control strategy is shown in Fig. 6.5. To achieve that, the five terms in (5.1) are firstly classified into the following two categories according to their regulation objectives

$$\begin{aligned} J_{g,pro\_a} = &\underbrace{\left\| \left(u_{DC,\infty}^* - u_{DC}[k+2]\right) + c_p\left(P_g^* - p_g[k+2]\right) \right\|^2}_{J_{g,H}} \\ &+ \underbrace{\left\| u_{DC,\infty}^* - u_{DC}[k+2] \right\|^2}_{J_{g,udc}} + \underbrace{\begin{cases} 0, & \|p_g[k+2]\| \le \left\|p_g^{\max}\right\| \\ \infty, & \|p_g[k+2]\| > \left\|p_g^{\max}\right\| \end{cases}}_{h_{g,conp}} \end{aligned} \tag{6.17}$$

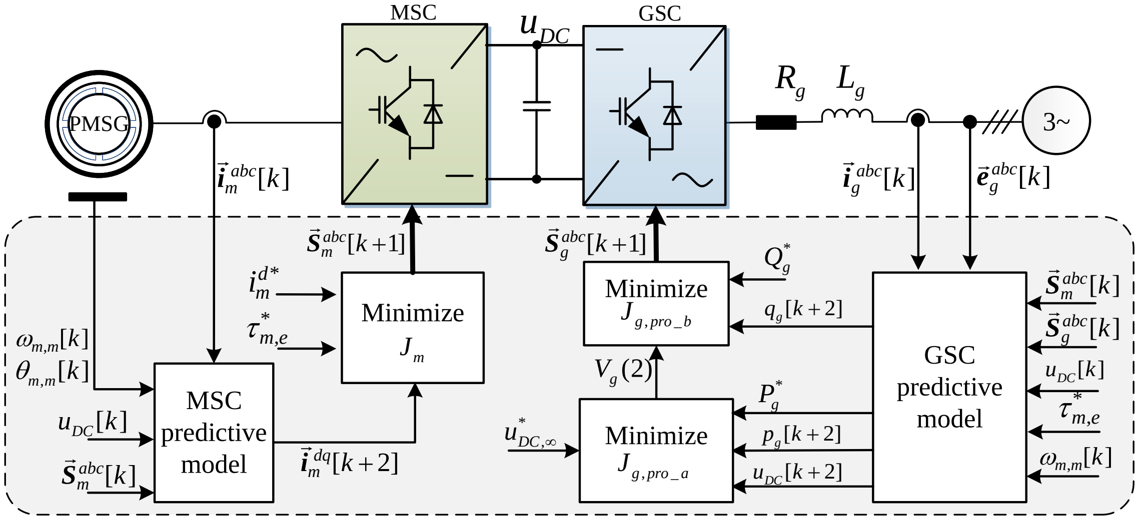

Figure 6.5: Proposed DPVC strategy without weighting factor.

$$J_{g,pro\_b} = \lambda_q \underbrace{\left\|Q_g^* - q_g[k+2]\right\|^2}_{J_{g,q}} + \underbrace{\begin{cases} 0, & \|q_g[k+2]\| \le \left\|q_g^{\max}\right\| \\ \infty, & \|q_g[k+2]\| > \left\|q_g^{\max}\right\| \end{cases}}_{h_{g,conq}} \tag{6.18}$$

where J_{g,pro_a} includes the terms related to DC-link voltage regulation, and J_{g,pro_b} includes the terms related to reactive power regulation. Since DC-link voltage regulation is not only the primary control target but is the basis of a stable system as well, J_{g,pro_a} is evaluated firstly by calculating the effect every voltage vector has on it, and the best two vectors that minimize J_{g,pro_a} are selected to form the vector pool $V_g(2)$. Afterward, the effect of every vector in $V_g(2)$ have on J_{g,pro_b} is evaluated, and the optimal voltage vector that minimizes J_{g,pro_b} will be selected to be implemented at instant $k+1$, which fulfills the controllable reactive power.

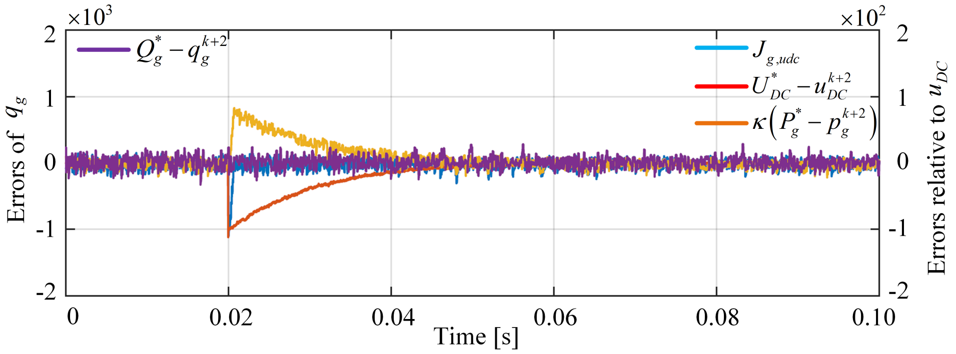

Figure 6.6: The experimental waveforms relevant to DC-link voltage and reactive power regulations in the DPVC strategy without weighting factor.

Fig. 6.6 illustrates waveforms relevant to DC-link voltage and reactive power regulations in the DPVC strategy without weighting factor when a reduced DC-link voltage reference is commanded. It can be seen that $J_{g,udc}$ deviates from 0 at the beginning stage after a changed reference, but it is soon pulled back to around 0 within a short time. Meanwhile, the error of DC-link voltage is quickly reduced under the regulation, and active power approaches P_g^* as the DC-link voltage approaches U_{DC}^*. The reactive power can be kept around 0 Var during the regulation.

In the proposed control strategy, the best two vectors that minimize J_{g,pro_a} are selected to form the vector pool $V_g(2)$, and used in the evaluation of J_{g,pro_b}. Selecting three voltage vectors $V_g(3)$ from the evaluation of J_{g,pro_a} is also feasible, and compared with selecting two voltage vectors, it focuses more on reactive power regulation since more candidate vectors are left to be evaluated by J_{g,pro_b}. In contrast, selecting two voltage vectors focuses more on the DC-link voltage regulation.

Fig. 6.7 presents the experimental waveforms of DPVC strategy without weighting factor in the step change of torque, and Fig. 6.8 presents the steady-state experimental waveforms of DPVC strategy without weighting factor at the rated operating condition. As can be seen in Fig. 6.7(a) and 6.7(b), selecting two voltage vectors helps in reducing the peak error and recovery time of DC-link voltage during the dynamic regulation. Although a slight improvement in reactive power is made by selecting three voltage vectors in Fig. 6.8, the DC-link voltage ripple also gets worse. More importantly, for the BTB system, the DC-link voltage makes a direct connection between the GSC and MSC, and the control performances of both GC and MC depend on a well-regulated DC-link voltage. Thus, satisfying DC-link voltage regulation performance is the not only primary control target but is the basis of a well-controlled system as well. That means selecting two vectors is more conducive to achieving the control target. Besides, since the bubble sort is adopted to obtain the best three or two vectors during the evaluation of J_{g,pro_a}, selecting the best three vectors costs much more computation effort, which adds burden on the microcontroller. Comprehensively considering the importance of DC-link voltage and computation effort, selecting two vectors is adopted in the proposed strategy.

6.2.2 Experimental verification

The necessary implementation steps of the DPVC strategy without weighting factor during k th interrupt are listed as the following quasi-code:

6.2.2.1 Steady-state performances

The steady-state experimental results of the DPVC strategy without weighting factor are given in Fig. 6.9. The DC-link voltage has been manipulated to 480 V, and the PMSM is driven to its rated speed of 1500 r/min with the torque of -15 N·m. The electric power generated by PMSM is transferred onto DC-link and then sent into the grid by controlling the grid-side active power to a negative value while keeping a stable DC-link voltage. The DC-link voltage ripple, which can be reflected by the error between the real value and reference of DC-link voltage, is within ± 2.5 V. The current spectrum of the grid-side current is shown in Fig. 6.9(b), and the machine-side current is shown in Fig. 6.9(c). For the grid side, the current is 5.81 A, and the THD is 3.15 %. For the machine side, the current is 6.41 A, and the THD is 9.69 %.

To test the performance of the DPVC strategy without weighting factor in the application of wind turbine system, the experiment under variable speed and torque is conducted. In wind tur-

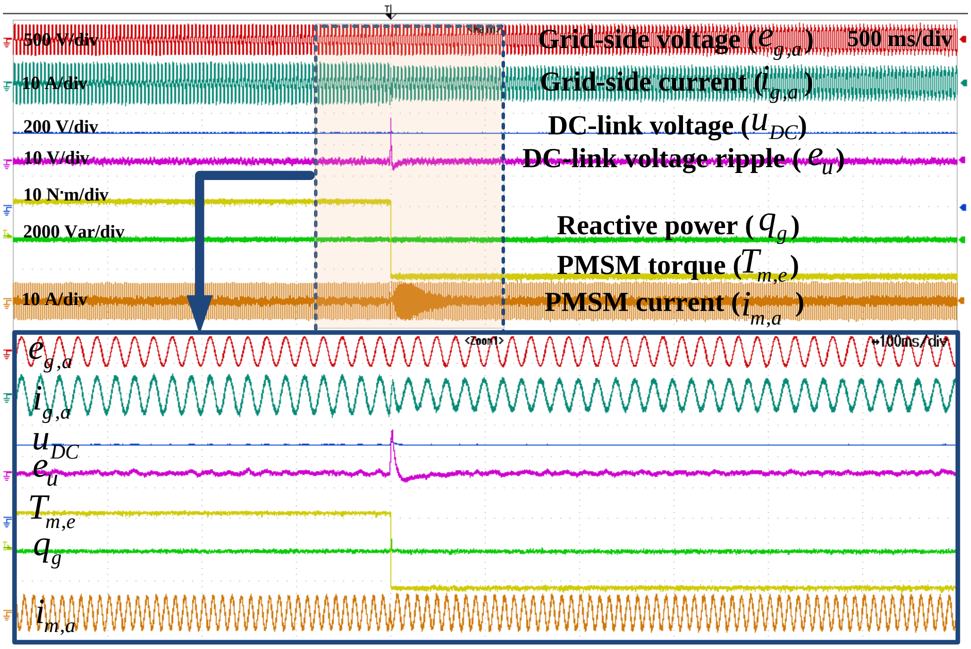

(a) Selecting two vectors.

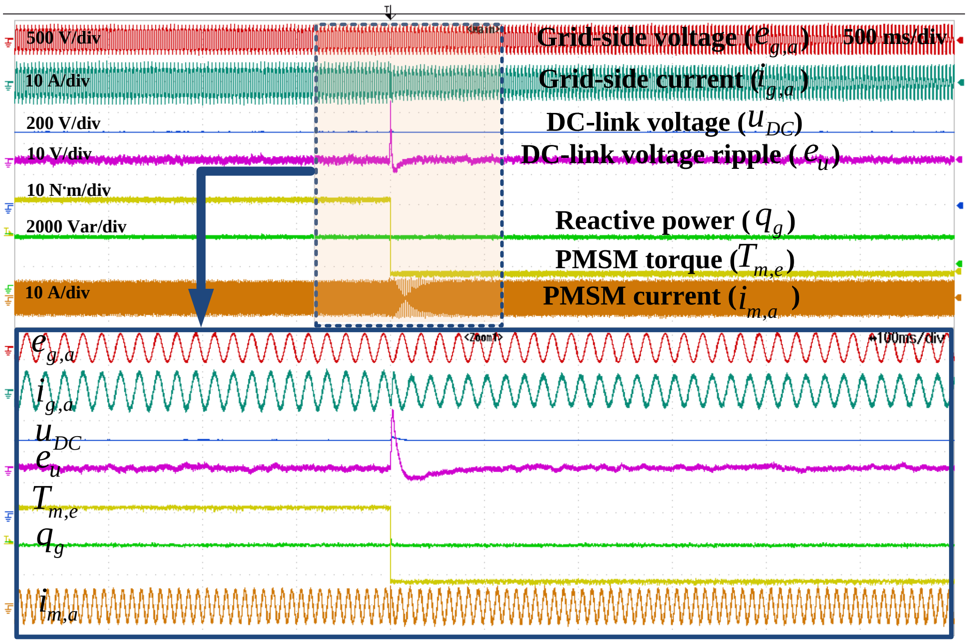

(b) Selecting three vectors

Figure 6.7: Experimental waveforms of DPVC strategy without weighting factor in the step change of torque.

bine system, the changes in wind speed will proportionately cause changes in generator speed $\omega_{m,m}$, and the electromagnetic torque reference $\tau^*_{m,e}$ should be changed correspondingly to achieve maximum power point tracking [32]. More specifically, $\tau^*_{m,e}$ should be the product of a coefficient and the square of $\omega_{m,m}$. In order to simulate the variable wind speed, a generator an-

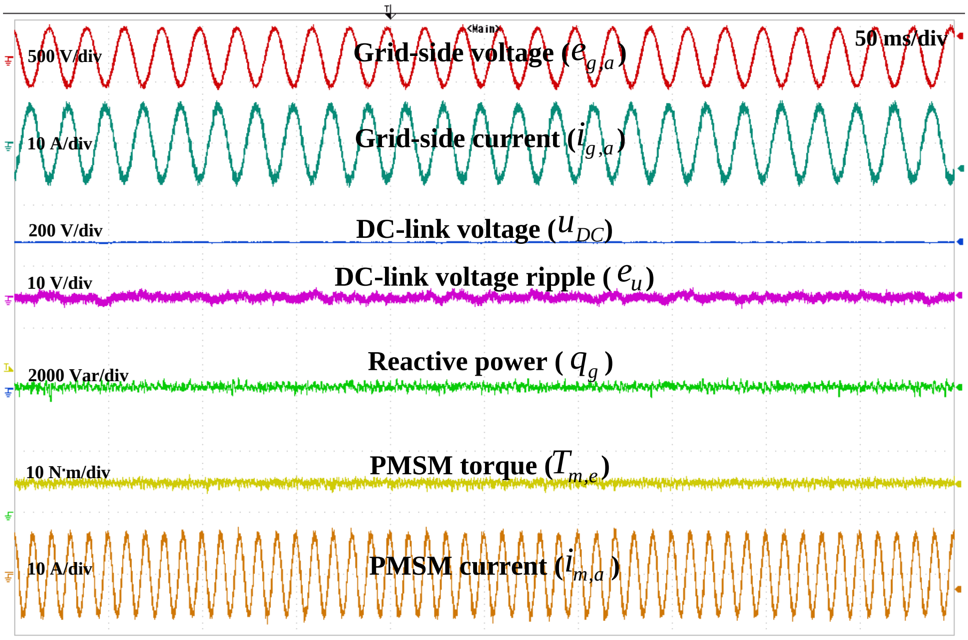

(a) Selecting two vectors.

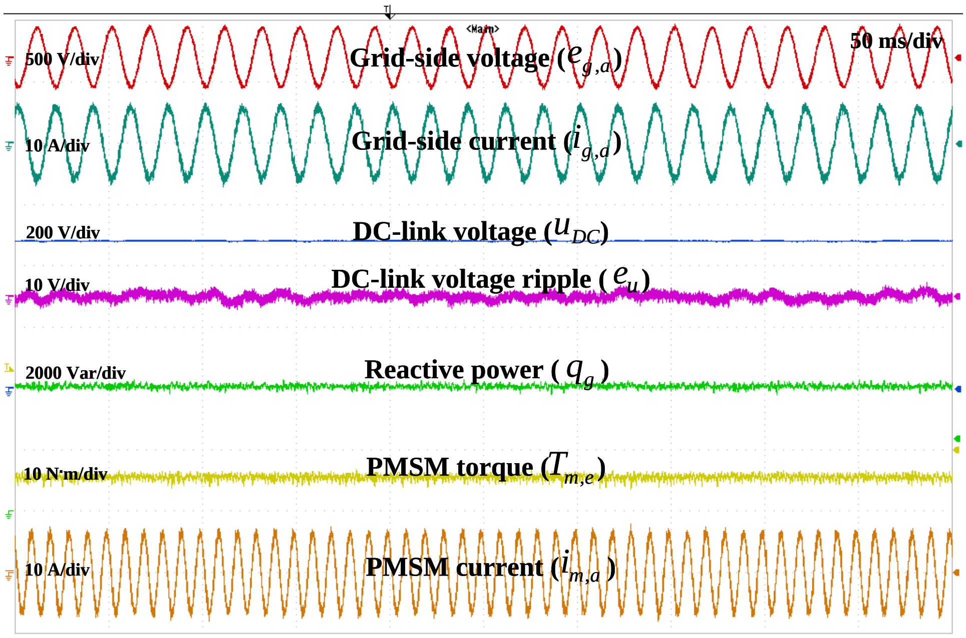

(b) Selecting three vectors.

Figure 6.8: Experimental waveforms of DPVC strategy without weighting factor in steady-state.

gular speed changing from 750 to 1500 r/min is set in the experiment, and $\tau^*_{m,e}$ correspondingly changes from -3.75 to -15 N·m in light of the aforementioned expression. The experimental waveforms are shown in Fig. 6.10. The active power increases as the increases of speed and torque, which also increases the grid-side current, but the DC-link voltage can maintain at 480

```
function: DPVC strategy without weighting factor ($k$, $u^*_{DC,\infty}$, $u_{DC}[k]$, $Q^*_g$, $i^{d*}_m$, $\tau^*_{m,e}$,
        $\theta_{m,m}[k]$, $\omega_{m,m}[k]$, $\vec{\boldsymbol{e}}^{abc}_g[k]$, $\vec{\boldsymbol{i}}^{abc}_g[k]$, $\vec{\boldsymbol{i}}^{abc}_m[k]$, $\vec{\boldsymbol{S}}^{abc}_g[k]$, $\vec{\boldsymbol{S}}^{abc}_m[k]$)
Apply $\vec{\boldsymbol{S}}^{abc}_m[k]$ and $\vec{\boldsymbol{S}}^{abc}_g[k]$
Compute $\vec{\boldsymbol{i}}^{dq}_m[k]$, $\vec{\boldsymbol{u}}^{dq}_m[k]$
Estimate $\vec{\boldsymbol{i}}^{dq}_m[k+1]$, with $\vec{\boldsymbol{S}}^{abc}_m[k]$
for $i = 1$ to $7$
    Predict $\vec{\boldsymbol{i}}^{dq}_m[k+2]$
    Minimize $J_m$
end for
Store $\vec{\boldsymbol{S}}^{abc}_m[k+1]$
Compute $\vec{\boldsymbol{e}}^{\alpha\beta}_g[k]$, $\vec{\boldsymbol{i}}^{\alpha\beta}_g[k]$, $P^*_g$, $p_g[k]$, $q_g[k]$
Estimate $p_g[k+1], q_g[k+1]$ and $u_{DC}[k+1]$ with $\vec{\boldsymbol{S}}^{abc}_g[k]$ and $\vec{\boldsymbol{S}}^{abc}_m[k]$
for $j = 1$ to $7$
    Predict $p_g[k+2]$ and $u_{DC}[k+2]$
    Evaluate $J_{g,pro\_a}$
end for
Sort $\vec{\boldsymbol{S}}^{abc}_g$ and build $V_g(2)$
for $l = 1$ to $2$
    Predict $q_g[k+2]$
    Evaluate $J_{g,pro\_b}$
end for
Sort $V_g(2)$ and Store $\vec{\boldsymbol{S}}^{abc}_g[k+1]$
```

V by continuously feeding the generated active power into grid. The grid-side current is kept in opposite phase with the voltage due to the well-controlled reactive power.

6.2.2.2 Step change of DC-link voltage

Fig. 6.11 presents the experimental waveforms in the step change of DC-link voltage (from 450 V to 550 V). In the regulation, the torque and speed of PMSM are not changed (1500 r/min, -15 N·m), which means the active power generated by PMSM does not change during this dynamic regulation. When the reference of DC-link voltage is increased from 450 V to 550 V, the active power flowing into the grid, which is controlled by GSC, should be decreased so that some of the active power generated by PMSM can be accumulated on DC-link to boost the DC-link voltage. It can be seen from the waveform that to boost the DC-link voltage quickly, not only does the active power flowing to grid decrease but the power flow direction is even reversed (the active power is changed from around -2250 W to a positive value). That means the grid even starts to provide active power along with the PMSM to charge the DC-link capacitor as soon as possible. Once the new reference of 550 V is reached, the power flowing into grid recovers to the value before the reference is changed. It takes 25 ms for the DC-link voltage of DPVC strategy without weighting factor to increase from 450 to 550 V. The active power flowing into grid is increased in time to transfer the PMSM power into grid after reaching the

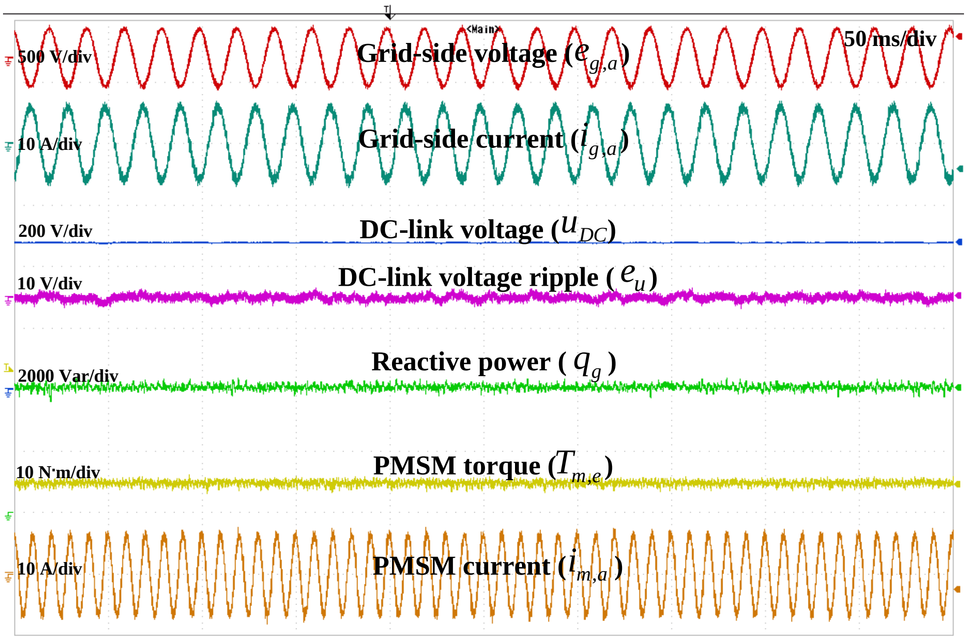

(a) Steady-state experimental results

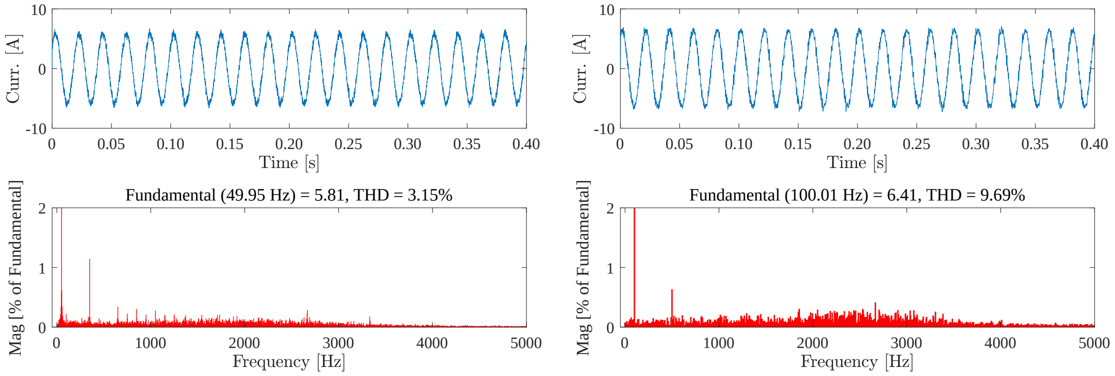

(b) Grid-side current spectrum.

(c) Machine-side current spectrum.

Figure 6.9: Steady-state experimental results of the DPVC strategy without weighting factor.

voltage reference, which leads to no overshoot in voltage waveform. Compared with the DPVC strategy, the DPVC strategy without weighting factor shows a faster regulation in pulling the voltage to reference.

6.2.2.3 Step change of torque

Fig. 6.12 presents the experimental waveforms in the step change of electromagnetic torque. The changes of electromagnetic torque lead to changes in active power, which also leads to the fluctuation in reactive power in the transient due to the coupling between active and reactive power [30]. The load-side machine changes from motoring mode to generating mode as the torque changes from 12 N·m to -12 N·m. While the electromagnetic power is identical in generating and motoring modes, the stator current is a little bit higher in motoring mode than in generating mode due to the power loss in MSC and GSC. At the beginning of the switching of

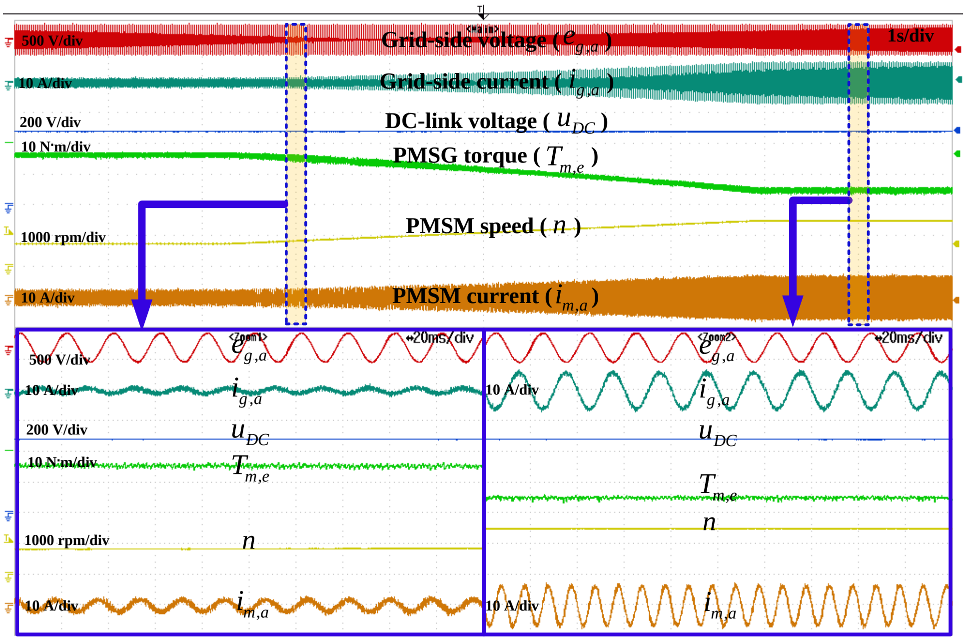

Figure 6.10: Experimental waveforms of the DPVC strategy without weighting factor under variable speed and torque.

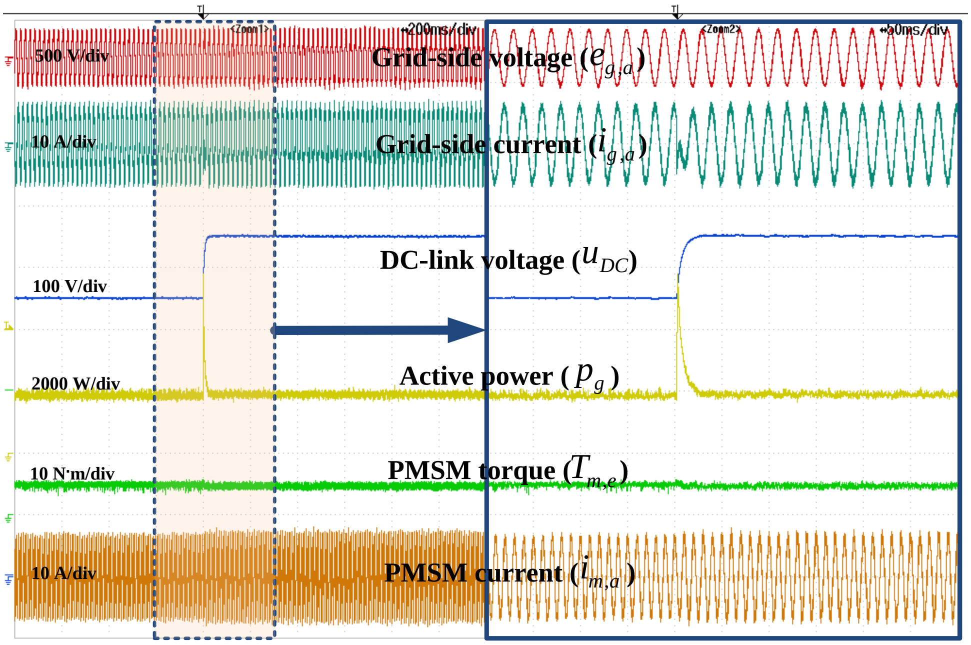

Figure 6.11: Experimental waveforms of DPVC strategy without weighting factor in the step change of DC-link voltage.

the operating mode, the generated energy is accumulated on the DC-link, which causes the increase of the DC-link voltage. Compared with the previous control strategy, the DPVC strategy without weighting factor shows the faster response (50 ms) to the step change of torque, and the DC-link deviates (12 V) less from its reference in Fig.6.12.

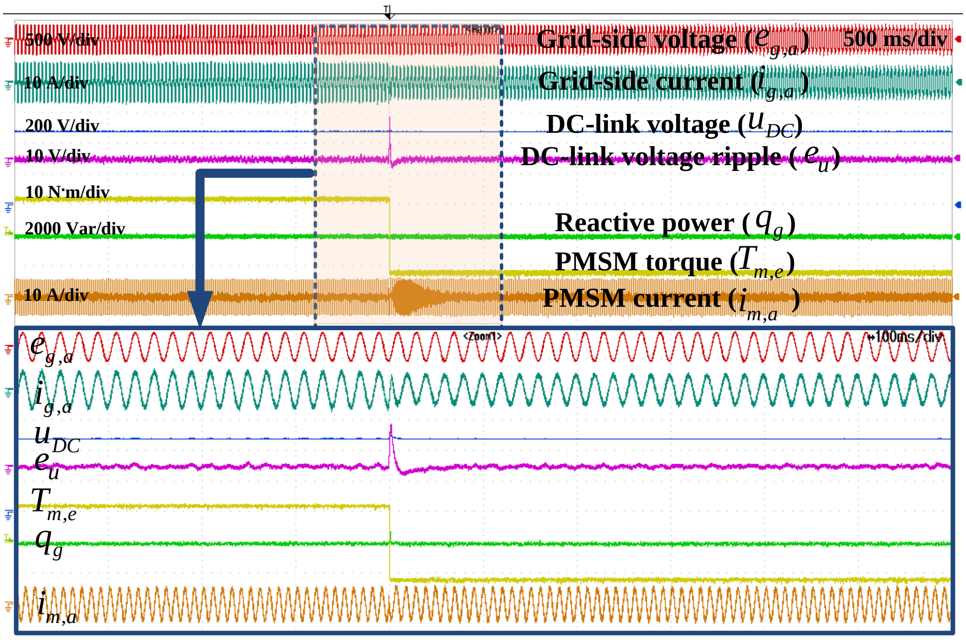

Figure 6.12: Experimental waveforms of DPVC strategy without weighting factor in the step change of torque.

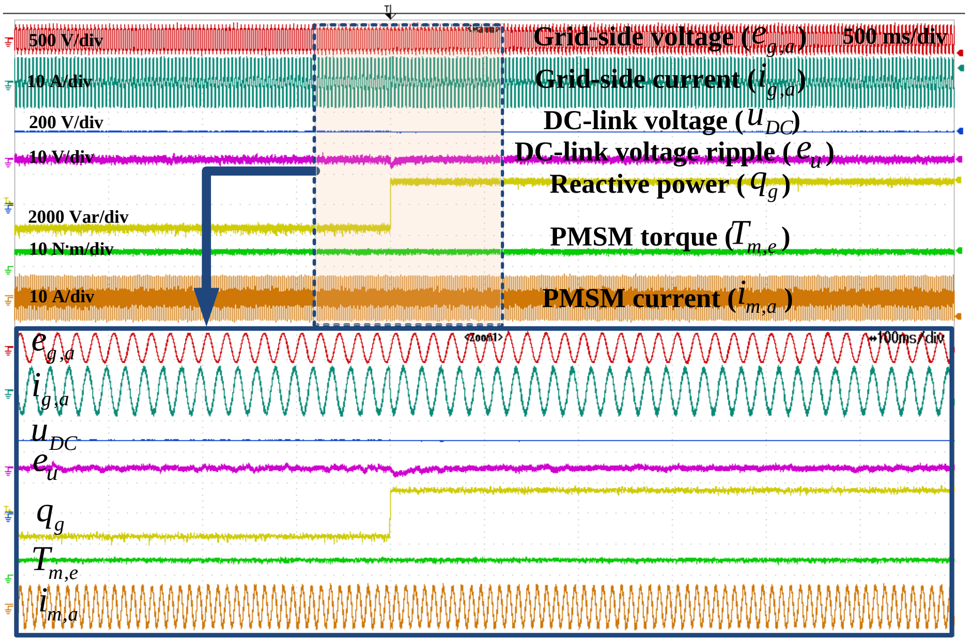

Figure 6.13: Experimental waveforms of DPVC strategy without weighting factor in the step change of reactive power.

6.2.2.4 Step change of reactive power

Fig. 6.13 presents the experimental waveforms in the step change of reactive power. In tests, the grid-side reactive power reference is changed from -1500 to 1500 Var in the rated operating

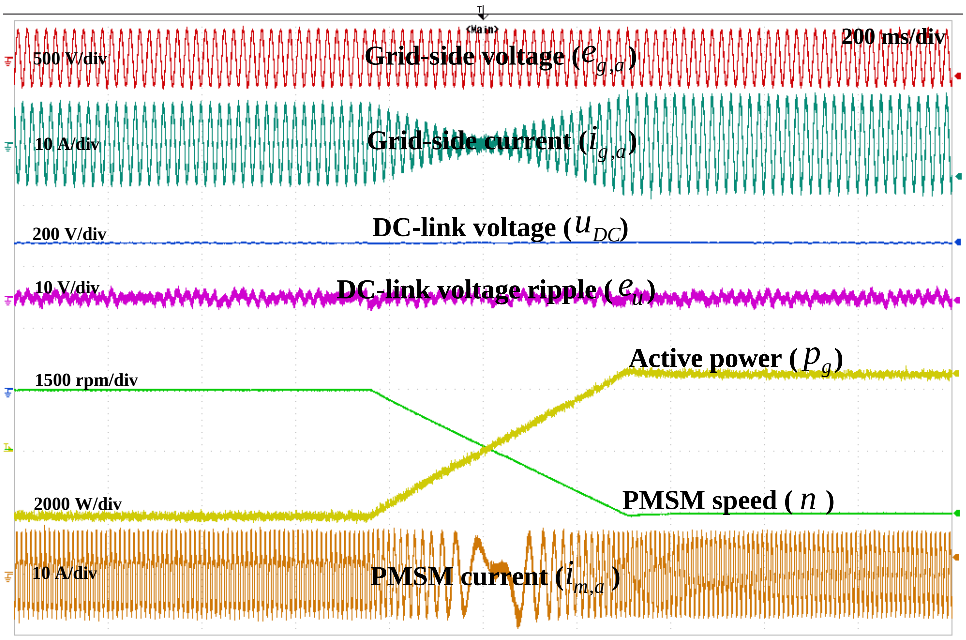

Figure 6.14: Experimental waveforms of DPVC strategy without weighting factor in the step change of speed.

condition. The reactive power follows the new references under regulations, but the step change of reactive power disturbs DC-link voltage due to the coupling between active and reactive power. The DPVC strategy without weighting factor has a fast regulation performance on DC-link voltage. It takes 30 ms for DPVC strategy without weighting factor to recover to the voltage reference, and a smaller disturbance of 3 V is presented, in comparison with the 5 V of the DPVC strategy. It is difficult for the fixed weighting factor to be optimal in various operating conditions, and removing the weighting factor from DPVC strategy does enhance the system dynamic performance to some extent and save the effort of the tuning of weighting factor.

6.2.2.5 Step change of speed

Fig. 6.14 presents the experimental waveforms in the step change of speed. When the speed of PMSM is commanded to reverse from -1500 to 1500 r/min with the rated torque, the machine state is changed from generating power to consuming power, and the direction of grid-side active power changes correspondingly in order to keep the DC-link voltage constant. In this case, the DC-link voltage fluctuates with a peak error of 3 V in DPVC strategy during the regulation, which is hardly affected in DPVC strategy without weighting factor. For the same reason as in the case of step torque change, the current amplitude of PMSM ineluctably increases after the speed reverses because of the power loss in MSC and GSC.

6.2.2.6 Current THDs and power factors

The experimental power analyzer screenshots (Yokogawa WT1800E) of the DPVC strategy without weighting factor, which reflect it steady-state performances at different operating speeds, are presented in Fig. 6.15, and the current THDs and power factors are concluded

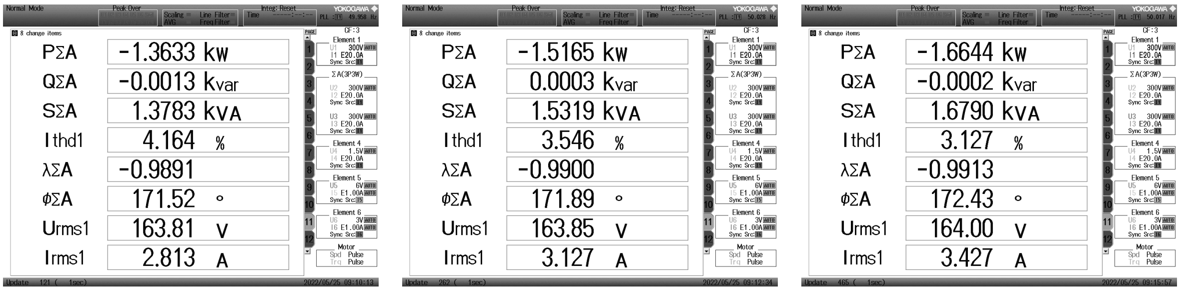

PΣA -1.3633 kW
QΣA -0.0013 kvar
SΣA 1.3783 kVA
Ithd1 4.164 %
λΣA -0.9891
ϕΣA 171.52 °
Urms1 163.81 V
Irms1 2.813 A

PΣA -1.5165 kW
QΣA 0.0003 kvar
SΣA 1.5319 kVA
Ithd1 3.546 %
λΣA -0.9900
ϕΣA 171.89 °
Urms1 163.85 V
Irms1 3.127 A

PΣA -1.6644 kW
QΣA -0.0002 kvar
SΣA 1.6790 kVA
Ithd1 3.127 %
λΣA -0.9913
ϕΣA 172.43 °
Urms1 164.00 V
Irms1 3.427 A

(a) 1000 r/min (b) 1100 r/min (c) 1200 r/min

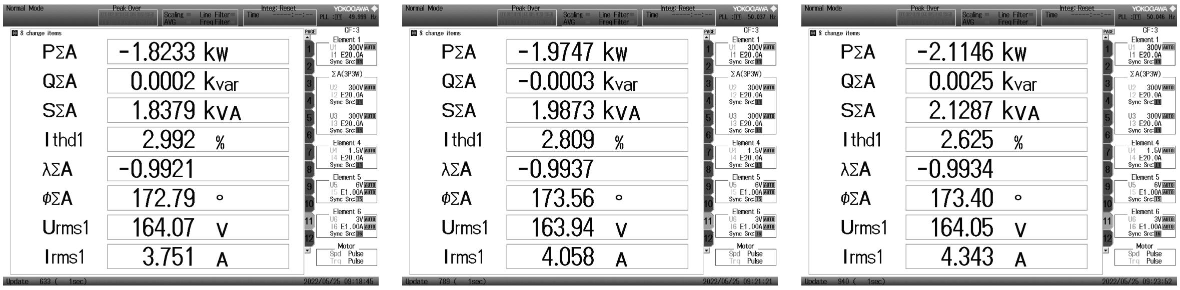

PΣA -1.8233 kW
QΣA 0.0002 kvar
SΣA 1.8379 kVA
Ithd1 2.992 %
λΣA -0.9921
ϕΣA 172.79 °
Urms1 164.07 V
Irms1 3.751 A

PΣA -1.9747 kW
QΣA -0.0003 kvar
SΣA 1.9873 kVA
Ithd1 2.809 %
λΣA -0.9937
ϕΣA 173.56 °
Urms1 163.94 V
Irms1 4.058 A

PΣA -2.1146 kW
QΣA 0.0025 kvar
SΣA 2.1287 kVA
Ithd1 2.625 %
λΣA -0.9934
ϕΣA 173.40 °
Urms1 164.05 V
Irms1 4.343 A

(d) 1300 r/min (e) 1400 r/min (f) 1500 r/min

Figure 6.15: Power analyzer screenshots of DPVC strategy without weighting factor at different speeds.

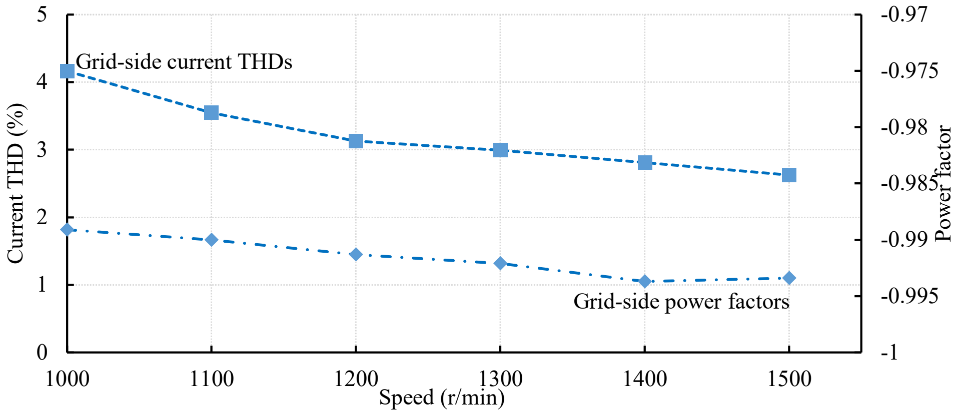

Figure 6.16: Current THDs and power factors of DPVC strategy without weighting factor.

in Fig. 6.16. In the power analyzer, $\mathrm{P\Sigma A}$, $\mathrm{Q\Sigma A}$, $\mathrm{S\Sigma A}$, $\mathrm{Ithd1}$, $\lambda\Sigma\mathrm{A}$, $\phi\Sigma\mathrm{A}$, $\mathrm{Urms1}$, and $\mathrm{Irms1}$ denote the active power, reactive power, apparent power, current THD, power factor phase angle, phase voltage, and phase current of AC side, respectively. At the rated operating condition (480 V, 1500 r/min, -15 N $\cdot$ m, 0 Var), the grid-side current THDs are controlled around 2.625 %, the grid-side power factors are controlled above 0.9934, and the machine-side current THDs are around 9.69 %. Therefore, the DPVC strategy without weighting factor can reach a good steady-state control performance.

6.3 Summary

In this chapter, the DPVC strategy is enhanced from the following two aspects:

-Compensation for errors caused by mismatched parameter.

The mathematical model for prediction is accurate when actual values of inductor and resistor are adopted. However, it is actually the nominal values involved in the prediction since the actual values are unknown, and it is also possible that the actual values change during the operation, which causes the steady-state error in the system. To address this problem, Kalman filter is added to the proposed strategy. The disturbances caused by mismatched parameters are estimated via Kalman filter and used to correct the power expressions, thus compensating for the steady-state power error.

-Removal of the weighting factor.

The weighting factor in the cost function is generally determined based on trial and error procedures, which are empirical and time-consuming. The weighting factor is removed from the proposed DPVC strategy by sorting the terms of cost function into two groups and independently evaluating each group separately, which gets rid of the empirical weighting factor tuning procedures and ensures fast dynamic performance.

CHAPTER 7

Integrated power control for BTB converter-fed high-speed SRM system

An integrated power control strategy for BTB converter-fed high-speed SRM system is presented in this chapter.

- In Sec. 2.3, the drive topology and the mathematical modeling of the BTB converter-fed high-speed SRM drive system are explained. This includes the detailed description of the VSR and AHBC, which work together to realize the control objectives of power quality improvement and SRM regulation.
- In Sec. 7.2, the proposed power control strategy, which builds the direct power connection between front-end VSR and back-end SRM, is presented. It integrally controls the front-end VSR and SRM together by controlling the system power flow so that the unity power factor, low current harmonic, and stable speed regulation can be realized in one control structure simultaneously.
- In Sec. 7.3, the experimental waveforms of the proposed control strategy are presented.

7.1 Background

High-speed electrical machine drives have been extensively adopted in the fields of aerospace, transportation, domestic appliances, and hand-held electrical tools due to the continuous need for increased power density, smaller size, higher efficiency, and lower maintenance cost. PMSMs and IMs are popular selections as high-speed drives. However, because of the permanent magnet blocks mounted on the rotor, the temperature and mechanical stress characteristics of PMSMs should be cautiously analyzed. In many practical high-speed applications, the specially-designed cooling path and rotor sleeves must be considered for PMSMs to guarantee the safety of the whole system. As for the IMs, the non-ignorable copper loss of rotor winding and the low starting torque limit their applications to some extent. The development of SRMs is later than that of the PMSMs [105, 106] and IMs [107, 108], but SRMs driven by reluctance torque have their distinctive benefits [109, 110]. Firstly, SRMs have a very simple structure. There are neither permanent magnet blocks nor windings on the rotor, which not only gives them sufficient robustness in high-temperature and high-speed applications but lows their manufacturing costs. Moreover, without the need for field weakening control, SRMs can achieve high-speed operation easily by just adjusting the turn-on and turn-off angle of each phase. In addition, SRMs are known to be fault-tolerant by their nature, which means they can keep operating even in open-circuit situations. All the aforementioned merits make SRMs a strong competitor in high-speed applications. Comprehensively considering cost, switching loss, and control performance, two-phase SRMs are the most ideal candidates for high-speed operation against other multi-phase SRMs [111, 112].

Grid-side power quality is a high priority for electrical drive. Some investigations have been conducted to make improvements on grid-side current harmonics and power factor for the SRM drive system. In [113], a power switch and a fast recovery diode are added into the DBR-fed single-phase asymmetric half-bridge (ASHB) converter to form a new drive topology in which the output port of the AC-DC rectifier and the DC bus storage capacitor are separated. The improvements in power factor and crest factor are validated via a 6/6 SRM drive system, but the grid-side current harmonics are still high. In [114], a quasi Z-source converter is developed, and the magnetization voltage is regulated according to the operation modes. The peak current control method, which coordinates with the voltage controller, is used to correct the grid-side power factor. In [115], a three-level AC-DC converter with dual output is developed, but an additional controller for the balancing of DC bus capacitors must be added to ensure the regular operation of the back-end power converter of SRM. Besides, its DC bus voltage is not fully utilized for winding excitation because of the adoption of the midpoint converter. The single-phase and three-phase switch-mode rectifiers are developed to feed the SRM converter in [116] and [117], respectively. However, the magnetization port and demagnetization port are heavily coupled through shared switches in these topologies. Moreover, the three-phase inductance in [117] is not conducive to system volume reduction, and the experimental grid-side power factors are not very satisfying. In [118], a converter combining the Cuk and SEPIC circuit together is constructed to provide two balanced output voltages and one neutral point for the SRM midpoint converter, but its DC bus voltage still is not fully utilized for excitation. In [119], a three-phase Vienna converter is developed to drive the SRMs. Although nice current THDs are obtained, the capacitor balancing on the DC bus also should be considered for high-performance drive.

The aforementioned SRM drive systems with power quality improvements regulate the front-end Power Factor Correction (PFC) converter and SRM converter as two self-contained control units, which makes the whole control system complicated. Additionally, bi-directional power flow is not allowed in those systems, which means the current just can flow from the grid side to SRM.

This chapter presents a system control strategy where the modeling and control are completed in the stationary coordinate plane. This eliminates the need for phase locking and rotatory transformation for variables. More importantly, since the SRM drive can be viewed as a load of the VSR, a power direct connection between front-end VSR and back-end SRM is established, and the SRM is then controlled by manipulating instantaneous active power flowing to motor side.

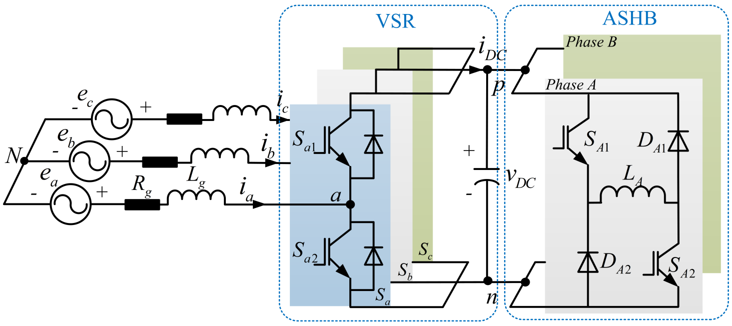

Figure 7.1: The drive topology of BTB converter-fed high-speed SRM system.

To achieve the tracking of power references, Predictive Deadbeat Power Control (P-DBPC) with an online observer is employed. Errors between predicted and actual power are treated as disturbances and compensated through feed-forward action by adding estimated disturbance term to calculated voltage reference.

7.2 Integrated power control strategy

The drive topology of BTB converter-fed high-speed SRM system, which consists of a VSR and ASHB converter, is illustrated in Fig. 7.1. In this section, a deadbeat power control strategy is designed to simultaneously govern the front-end PFC converter and back-end SRM for the drive topology. By controlling the instantaneous active power in the drive system, stable SRM control can be realized and the enhanced grid-side power quality is achieved by directly reducing the instantaneous reactive power. The disturbance observer compensates for the errors caused by the inaccurate inductance and resistance, thus providing robust control.

7.2.1 Control strategy description

The proposed integrated power control strategy for BTB converter-fed high-speed SRM drive system is shown in Fig. 7.2. Through the signals acquired from the encoder mounted on the rotor shaft, the mechanical rotor position and rotational speed can be estimated. According to the position, the switching signals of single pulse pattern [120] are generated for the ASHB converter to conduct every phase winding alternately for excitation, and the pair of turn-on and turn-off angles are obtained from a predetermined lookup table. The current limitation is configured in hardware circuit to serve as winding protection [121]. In the proposed control strategy, rotational speed and grid-side power factor are regulated by directly manipulating the active power and reactive power, respectively. The angular velocity ω_r is used to generate torque reference T^* through a speed PI controller, and the product of T^* and the angular velocity is the reference input active power P^* of grid. The reference input reactive power Q^* is set to 0 Var to restrain the grid-side reactive power flow in the system.

P-DBPC strategy with disturbance observer, which realizes independent control of the grid-side active power and reactive power, is to make the actual active power and reactive power track P^* and Q^*, respectively. According to instantaneous power theory, the active power and reactive power of a three-phase system in $\alpha\beta$ reference frame is given by [122]

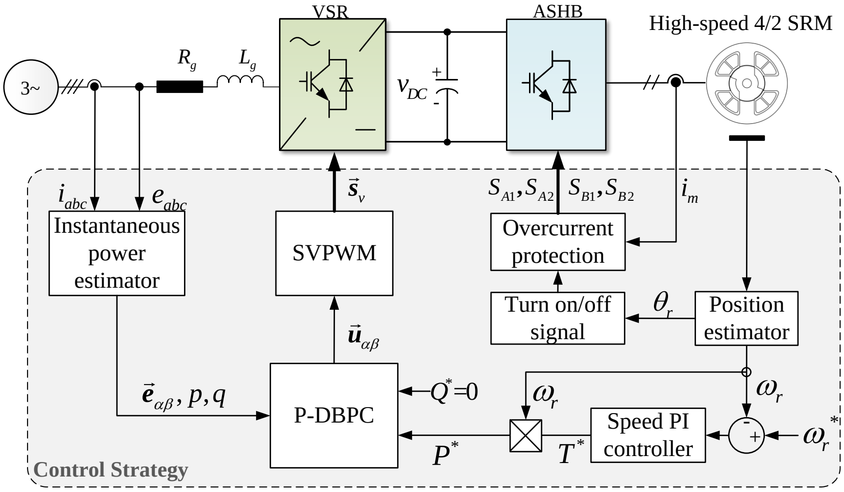

Figure 7.2: The proposed control system of BTB converter-fed high-speed SRM system based on P-DBPC.

$$\begin{pmatrix} p(t) \\ q(t) \end{pmatrix} = \frac{3}{2} \begin{bmatrix} e_\alpha(t) & e_\beta(t) \\ e_\beta(t) & -e_\alpha(t) \end{bmatrix} \overrightarrow{\boldsymbol{i}}_{\alpha\beta}(t) \tag{7.1}$$

The relationship between e_α and e_β can be described by

$$\frac{d}{dt} \begin{pmatrix} e_\alpha(t) \\ e_\beta(t) \end{pmatrix} = \begin{pmatrix} -\omega_g e_\beta(t) \\ \omega_g e_\alpha(t) \end{pmatrix} \tag{7.2}$$

Equation (2.26) can be rewritten as:

$$\frac{d}{dt}\vec{\boldsymbol{i}}_{\alpha\beta}(t) = \frac{1}{L_g}(\vec{\boldsymbol{e}}_{\alpha\beta}(t) - R_g\vec{\boldsymbol{i}}_{\alpha\beta}(t) - \vec{\boldsymbol{u}}_{\alpha\beta}(t)) \tag{7.3}$$

Substituting (7.2) and (7.3) into (7.1) gives

$$\begin{aligned} \frac{d}{dt} \begin{pmatrix} p(t) \\ q(t) \end{pmatrix} =& \frac{3}{2L_g} \begin{bmatrix} e_\alpha(t) & e_\beta(t) \\ e_\beta(t) & -e_\alpha(t) \end{bmatrix} \begin{pmatrix} e_\alpha(t) - u_\alpha(t) \\ e_\beta(t) - u_\beta(t) \end{pmatrix} \\ &+ \begin{pmatrix} -\frac{R_g}{L_g} p(t) - \omega_g q(t) \\ -\frac{R_g}{L_g} q(t) + \omega_g p(t) \end{pmatrix}. \end{aligned} \tag{7.4}$$

(7.4) can be transformed into the following form after being applied with the backward Euler discretization.

$$\begin{aligned} \begin{pmatrix} p[k+1] \\ q[k+1] \end{pmatrix} =& \frac{3T_s}{2L_g} \begin{bmatrix} e_\alpha[k] & e_\beta[k] \\ e_\beta[k] & -e_\alpha[k] \end{bmatrix} \begin{pmatrix} e_\alpha[k] - u_\alpha[k] \\ e_\beta[k] - u_\beta[k] \end{pmatrix} \\ &+ \begin{pmatrix} p[k] - \frac{T_s R_g}{L_g} p[k] - T_s \omega_g q[k] \\ q[k] - \frac{T_s R_g}{L_g} q[k] + T_s \omega_g p[k] \end{pmatrix} \end{aligned} \tag{7.5}$$

(7.5) holds when the actual values of the inductor and resistor, i.e., L_g and R_g, are brought into the expression. However, it is actually the nominal values, i.e., $L_{g,no}$ and $R_{g,no}$, are involved in the calculation of the prediction since L_g and R_g are unknown. Considering those uncertainties as a dynamic disturbance, (7.5) can be rewritten as

$$\begin{aligned}\begin{pmatrix} p[k+1] \\ q[k+1] \end{pmatrix} = \frac{3T_s}{2L_{g,no}} \begin{bmatrix} e_\alpha[k] & e_\beta[k] \\ e_\beta[k] & -e_\alpha[k] \end{bmatrix} \begin{pmatrix} e_\alpha[k]-u_\alpha[k] \\ e_\beta[k]-u_\beta[k] \end{pmatrix} \\ + \begin{bmatrix} 1-\frac{T_sR_{g,no}}{L_{g,no}} & -T_s\omega_g \\ \omega_g T_s & 1-\frac{T_sR_{g,no}}{L_{g,no}} \end{bmatrix} \begin{pmatrix} p[k] \\ q[k] \end{pmatrix} - \frac{T_s}{L_{g,no}} \begin{pmatrix} g_p[k] \\ g_q[k] \end{pmatrix}\end{aligned} \tag{7.6}$$

where the subscript $"no"$ represents the nominal value, and g_p and g_q are the disturbances. Assuming that the values of g_p and g_q are constant during each sampling interval [123], [124], so Luenberger disturbance observer can be constructed as below

$$\begin{aligned}\begin{pmatrix} \hat{p}[k+1] \\ \hat{q}[k+1] \\ \hat{g}_p[k+1] \\ \hat{g}_q[k+1] \end{pmatrix} = \frac{3T_s}{2L_{g,no}} \begin{bmatrix} e_\alpha[k] & e_\beta[k] \\ e_\beta[k] & -e_\alpha[k] \\ 0 & 0 \\ 0 & 0 \end{bmatrix} \begin{pmatrix} e_\alpha[k]-u_\alpha[k] \\ e_\beta[k]-u_\beta[k] \end{pmatrix} \\ + \boldsymbol{E} \begin{pmatrix} \hat{p}[k] \\ \hat{q}[k] \\ \hat{g}_p[k] \\ \hat{g}_q[k] \end{pmatrix} + \begin{bmatrix} l_1 & 0 & 0 & 0 \\ 0 & l_1 & 0 & 0 \\ 0 & 0 & l_2 & 0 \\ 0 & 0 & 0 & l_2 \end{bmatrix} \begin{pmatrix} p[k]-\hat{p}[k] \\ q[k]-\hat{q}[k] \\ p[k]-\hat{p}[k] \\ q[k]-\hat{q}[k] \end{pmatrix}\end{aligned} \tag{7.7}$$

where $\boldsymbol{E} = \begin{bmatrix} 1-\frac{T_sR_{g,no}}{L_{g,no}} & -T_s\omega_g & -\frac{T_s}{L_{g,no}} & 0 \\ \omega_g T_s & 1-\frac{T_sR_{g,no}}{L_{g,no}} & 0 & -\frac{T_s}{L_{g,no}} \\ 0 & 0 & 1 & 0 \\ 0 & 0 & 0 & 1 \end{bmatrix}$, and the gains ($l_1$, l_2) of the observer can be selected by the pole placement method [125], and $\hat{\zeta}$, $\zeta \in \{p, q, g_p, g_q\}$ represents the estimated variable. Deadbeat control is to calculate the desired variables by presuming that the system attains the intended behavior at the very end of every control period. Hence the desired voltage vector can be calculated by bringing $p[k+1] = P^*$ and $q[k+1] = Q^* = 0$ into (7.6)

$$\begin{aligned}\vec{\boldsymbol{u}}_{\alpha\beta}[k] =& \vec{\boldsymbol{e}}_{\alpha\beta}[k] - \frac{2L_{g,no}}{3T_s \left\|\vec{\boldsymbol{e}}_{\alpha\beta}[k]\right\|^2} \begin{bmatrix} e_\alpha[k] & e_\beta[k] \\ e_\beta[k] & -e_\alpha[k] \end{bmatrix} \\ & \cdot \begin{pmatrix} P^* - p[k] + \frac{T_sR_{g,no}}{L_{g,no}} p[k] + T_s\omega_g q[k] + \frac{T_s}{L_{g,no}} \hat{g}_p[k] \\ Q^* - q[k] + \frac{T_sR_{g,no}}{L_{g,no}} q[k] - T_s\omega_g p[k] + \frac{T_s}{L_{g,no}} \hat{g}_q[k] \end{pmatrix}.\end{aligned} \tag{7.8}$$

The error caused by the mismatched parameters is considered as the disturbance to correct the expression of the desired converter voltage, thereby providing a robust control. The implementation of P-DBPC with disturbance observer within instant k is described as follows. Firstly, $p[k]$ and $q[k]$ are computed according to the measured $\vec{\boldsymbol{e}}_{\alpha\beta}[k]$ and $\vec{\boldsymbol{i}}_{\alpha\beta}[k]$. $\hat{g}_p[k]$ and $\hat{g}_q[k]$ in (7.8) are estimated disturbances that are already obtained in the interval of $[k-1, k]$. Then with the above values, the desired converter voltage $\vec{\boldsymbol{u}}_{\alpha\beta}[k]$ can be calculated by bringing updated P^* and Q^* into (7.8). Besides, in order to prepare the calculation for the next instant (i.e., instant $k+1$), $\hat{p}[k+1]$, $\hat{q}[k+1]$, $\hat{g}_p[k+1]$, and $\hat{g}_q[k+1]$ should be predicted based on (7.7) where $\hat{p}[k]$ and $\hat{q}[k]$ are already obtained in the interval of $[k-1,k]$. Since $\hat{g}_p[k]$ and $\hat{g}_q[k]$ are obtained from the last interval, both $\hat{g}_p[0]$ and $\hat{g}_q[0]$ equal 0 in the calculation of $\vec{\boldsymbol{u}}_{\alpha\beta}[0]$ within the initial instant $k=0$. Finally, through synthesizing and applying the calculated $\vec{\boldsymbol{u}}_{\alpha\beta}[k]$, the active and reactive power can reach their references without steady-state error.

7.2.2 Speed controller design

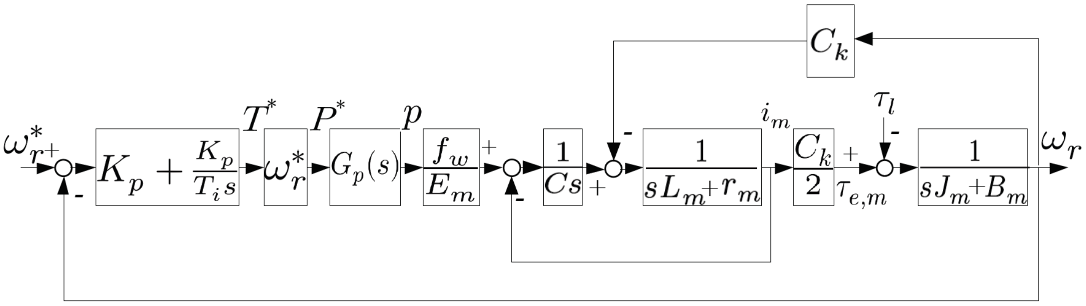

Figure 7.3: Block diagram of BTB converter-fed high-speed SRM drive based on P-DBPC.

The system block diagram is presented in Fig. 7.3. A PI controller is adopted for speed regulation

$$T^* = k_p e + \frac{k_p}{T_i}\int e dt, \qquad e = \omega_r^* - \omega_r \tag{7.9}$$

with transfer function $F(s) = k_P(1 + 1/(T_i s))$ is used. The relationship between active power p and d-axis component of grid-side current in the proposed system can be expressed as below through applying the magnitude-invariant version of Clarke transformation and Park transformation to (7.1)

$$i_d = \frac{2p}{3E_m} \tag{7.10}$$

where E_m represents the amplitude of the grid-side voltage. With the control frequency of 20 kHz, the actual active power in P-DBPC can track the active power reference with fast response by directly calculating the desired converter voltages, so the transfer function of the deadbeat control can be modeled as unity gain [126]– [127], namely, $G_p(s) = 1$. For point p on DC-link shown in Fig. 7.1, the following current expression holds [128]

$$\frac{dv_{DC}}{dt} = \frac{3f_\omega i_d}{2C} - \frac{i_m}{C} \tag{7.11}$$

where $f_\omega \in [0,1]$ is a constant in steady condition [129], C represents the capacitance of the DC-link capacitor. The electromagnetic torque of SRM can be expressed by [58]

$$\tau_{e,m} = \frac{1}{2}C_k i_m \tag{7.12}$$

where $C_k = \frac{d\psi_m}{d\theta_r}$. Then, given the system parameters, the open-loop transfer function can be derived as

$$F_{ol}(s) = \frac{k_P(T_i s + 1)}{T_i s} \frac{k_A}{k_B s^2 + k_C s} \tag{7.13}$$

where $k_A = \frac{C_k \omega_r^* f_\omega}{2}$, $k_B = Cr_m J_m E_m$, $k_C = \frac{C_k^2 E_m C}{2} + J_m E_m$. To ease the analysis, (7.13) is rewritten into the form expressed by the multiplication of three terms:

$$F_{ol}(s) = G_{ol}(s) H_{ol}(s) I_{ol}(s) \tag{7.14}$$

where $G_{ol}(s) = \frac{k_A}{k_C} \frac{k_P(T_i s+1)}{T_i s}$, $H_{ol}(s) = \frac{1}{s}$, $I_{ol}(s) = \frac{1}{\frac{k_B}{k_C}s+1}$. In light of [130] – [131], a maximum phase margin φ_m can show at the crossover frequency $\omega_{f,c}$ of $F_{ol}(s)$ in the phase frequency characteristic by making sure the following expressions hold

$$\omega_{g,c} = \frac{1}{\gamma}\omega_{f,c} = \frac{1}{T_i} \tag{7.15}$$

$$\omega_{i,c} = \gamma\omega_{f,c} = \frac{k_C}{k_B} \tag{7.16}$$

where $\omega_{g,c}$, $\omega_{i,c}$ represent the crossover frequency of $G_{ol}(s)$ and $I_{ol}(s)$, respectively, and γ is generally within the interval of [2, 4]. Thus, combining (7.15) and (7.16) gives the integral time constant of the speed PI controller

$$T_i = \gamma^2 \frac{k_B}{k_C} \tag{7.17}$$

Since $|F_{ol}(j\omega_{f,c})| = |G_{ol}(j\omega_{f,c}) H_{ol}(j\omega_{f,c}) I_{ol}(j\omega_{f,c})| = 1$ at $\omega_{f,c}$, the following expression holds

$$\frac{k_P k_A}{k_C} = \frac{k_C}{\gamma k_B}. \tag{7.18}$$

(7.18) gives the proportional gain of the speed PI controller

$$k_P = \frac{k_C^2}{\gamma k_A k_B}. \tag{7.19}$$

7.2.3 Power flow in the proposed system

In the proposed drive system, SRM drive can be regarded as the load of the VSR, so the output active power of VSR (denoted as P_{VSR}) is the sum of the active power consumed by DC-link capacitors (denoted as P_C) and the active power consumed by SRM drive (denoted as P_M), i.e., $P_{VSR} = P_M + P_C$. Suppose $P_{VSR} > P_M$, the DC-link voltage will increase since $P_C > 0$. Then, P_M will increase since the DC-link voltage is applied to the winding terminal in every conduction region, and the increased P_M will reduce P_C. The P_M will continue to rise until $P_{VSR} = P_M$, i.e., $P_C = 0$. Similarly, suppose $P_{VSR} < P_M$, the DC-link voltage will decrease since $P_C < 0$. Then, P_M will decrease, which makes P_C gradually approach zero, and P_M will stop decreasing when $P_{VSR} = P_M$. It can be found that P_{VSR} always can regulate P_M, and constant P_{VSR} indicates constant P_M. Based on the above, the SRM is proposed to be regulated by directly controlling the active power flowing to the motor side. Specifically, the torque reference T^* obtained from the speed controller is multiplied by the motor angular velocity ω_r to compute the active power reference P^*, and P^* is supplied by VSR through the active power control in P-DBPC. In this way, a direct connection of power between the front-end VSR and back-end SRM is built. The P-DBPC can make sure the active power flowing to the motor side follows the reference P^*. The energy feedback can be fulfilled so that the excess active power can be transferred back to the grid. The improvements in grid-side power factor and current harmonics can be realized by further setting $Q^* = 0$ in P-DBPC.

7.3 Experimental evaluation

7.3.1 Testbench parameters and pseudocode

A practical laboratory setup is constructed to validate the effectiveness of the proposed control system. Table 7.1 present the photograph and hardware configuration of the constructed testbench, respectively. The experimental parameters concerning the drive system are given in Table 7.2, and the control frequency equals the sampling frequency in the experiments. The necessary implementation steps of the proposed high-speed SRM drive based on P-DBPC during kth interrupt are listed as the following quasi-code:

```
function Proposed P-DBPC ($\vec{e}_{\alpha\beta}[k]$, $\vec{i}_{\alpha\beta}[k]$, $\theta_r[k]$, $k$)
    if $\theta_{m,on} \leq \theta_r[k] \leq \theta_{m,off}, m \in A, B$ then
        Set $S_{m1} = 1$; $S_{m2} = 1$[1]
    else then
        Set $S_{m1} = 0$; $S_{m2} = 0$[2]
    end if
    Estimate $\omega_r[k]$
    Refresh $T^*[k]$
    Calculate $P^* = \omega_r[k]T^*[k]$
    Calculate $p[k]$ and $q[k]$ according to (7.1)
    Calculate $\vec{u}_{\alpha\beta}[k]$ according to (7.8)
    Estimate $\hat{p}[k+1]$, $\hat{q}[k+1]$, $\hat{g}_p[k+1]$, and $\hat{g}_q[k+1]$ according to (7.7)
    Implement SVPWM
end function
```

[1] Turn on the switch of phase m of SRM. [2] Turn off the switch of phase m of SRM.

7.3.2 Experimental results

In this section, certain parts of the main windows in the left or top side of the experimental figures are shown in a larger version by the oscilloscope to present the control performance as thoroughly as possible, and the same curve shares the same scale.

Table 7.1: Hardware configuration

Function	Producer	Type
Digital Signal Processor (DSP)	TEXAS INSTRUMENTS	TMS320F28335
VSR	INFINEON	FS100R06
Insulated Gate Bipolar Transistor	IXYS	IXGH60N60
Fast recovery diodes	IXYS	DSEI60-06A
High-speed incremental encoder	HEIDENHAIN	ERO1420

Table 7.2: Testbench parameters of the high-speed SRM drive based on P-DBPC.

Description	Parameter	Value
Grid-side voltage frequency	$\omega_r(\mathrm{rad/s})$	100π
Grid-side filter resistance	$R_{g,no}(\Omega)$	0.3
Grid-side phase voltage	$e_g(\mathrm{V})$	50
Grid-side filter inductor	$L_{g,no}(\mathrm{mH})$	2
DC-link capacitor	$C(\mu\mathrm{F})$	1360
Control period	$T_s(\mu\mathrm{s})$	50
Rated torque of the high-speed SRM	$\tau_{e,m}(\mathrm{N}\cdot\mathrm{m})$	0.12
Rated speed of the high-speed SRM	$n_r(\mathrm{r/min})$	25000

7.3.2.1 Steady-state performances

The steady-state test waveforms when the proposed drive system operates at 20000r/min and 25000r/min are presented in Fig. 7.4 and Fig. 7.5, respectively. Low grid-side current THD and near-unity power factor have been obtained by properly controlling grid-side active power and reactive power. Constant active and reactive power suggests low current harmonics, and low reactive power suggests high power factor. In Fig. 7.4, the active power is about 190 W when the SRM operates at 20000 r/min, and the reactive power ripples up and down around 0 Var. The grid-side current is about 4.7 A, which is not only a sine waveform with little distortion but in the same phase as the grid-side voltage. Fig. 7.5 displays the steady-state test waveforms when the motor runs at the rated condition, namely, 25000 r/min. The DC-link voltage ripple is regulated to approximately $\pm$ 1 V. The active power is raised to about 390 W to supply sufficient power for SRM operation. The reactive power is still well manipulated to correct the power factor. Not only can the high-speed SRM control be achieved in the proposed drive system, but nice grid-side power quality is obtained. It is evident that the fluctuation frequency of the DC-link voltage is double that of the electrical frequency (defined as the reciprocal of the electrical period) of the SRM. One fluctuation period can be divided into three distinct sections based on its variation trend. In section “ab”, the energy stored in the magnet field of the motor flows back to the capacitor due to the demagnetization of phase winding, which leads to the rise of DC-link voltage. The winding current descends quickly within a short time after being switched off, so the energy flowing back is relatively big. In section “bc”, the rotor position

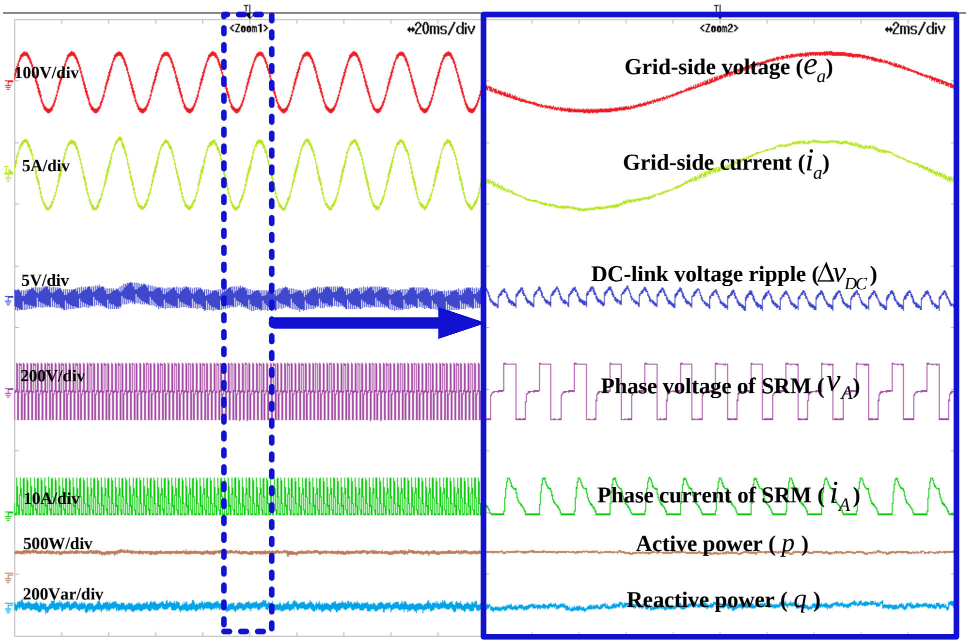

Figure 7.4: Steady-state experiment results of proposed system at 20000 r/min.

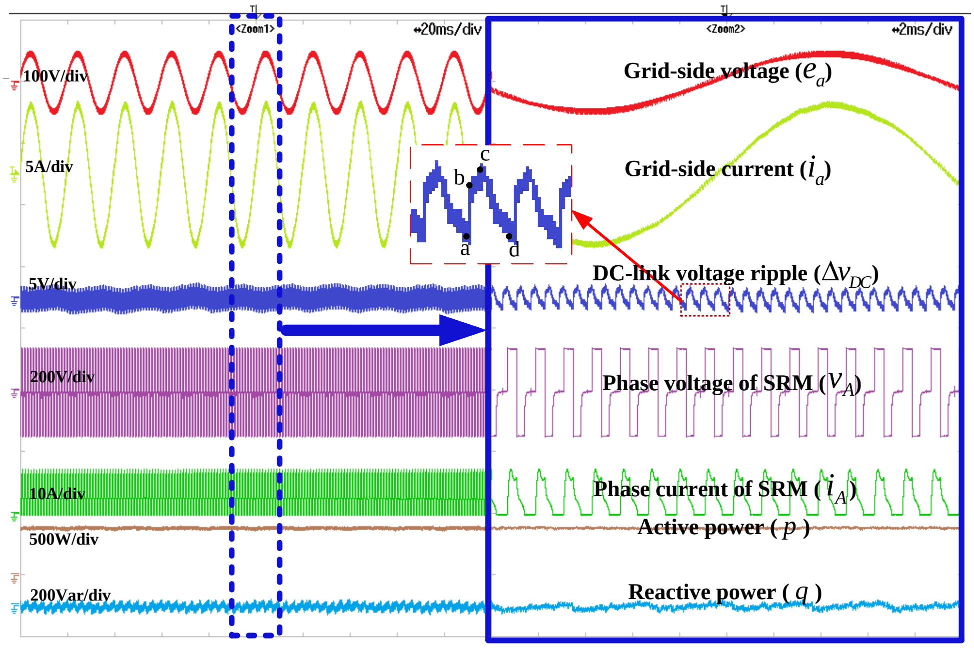

Figure 7.5: Steady-state experiment results of proposed system at 25000 r/min.

goes into the maximum inductor region, so the drop of winding current becomes slow, which reduces the rising rate of the DC-link voltage. In section “cd”, the DC-link voltage declines due to the current establishment of the incoming phase.

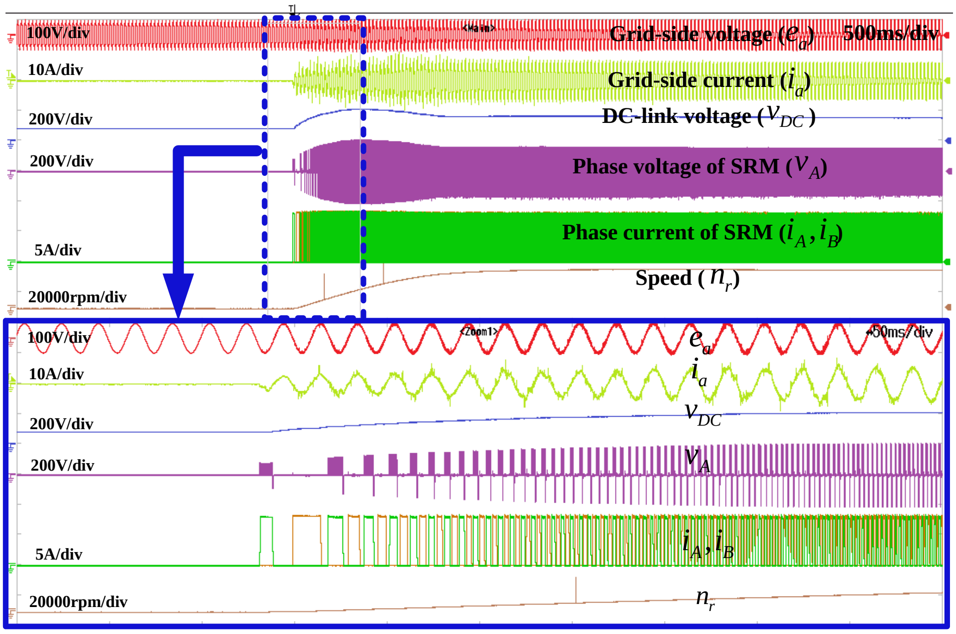

Figure 7.6: Experimental results when the SRM starts from standstill to 25000 r/min.

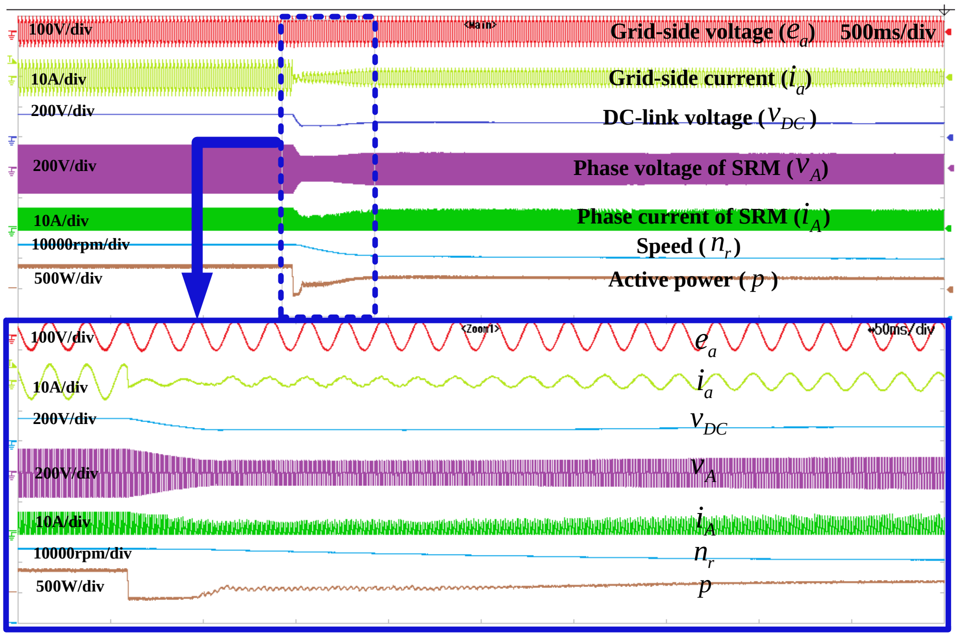

Figure 7.7: Experimental results when SRM speed changes from 25000 to 20000 r/min.

7.3.2.2 Transient-state performances

Fig. 7.6 shows the test waveforms when the speeds start from 0 to 25000 r/min. It can be seen from the Main window locating at the upper part of Fig. 7.6 that the input active power of the system is increased suddenly to enable the starting when the reference speed is commanded, and the speed reaches steady state after approximately 1 second. Moreover, it can be seen

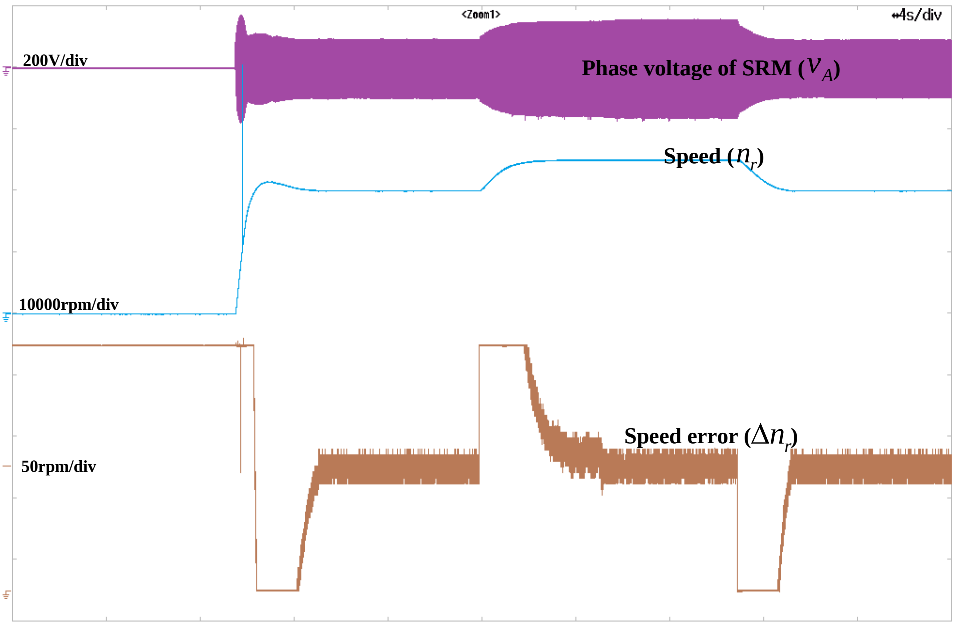

Figure 7.8: Dynamic experiment results when SRM speed changes from 0 r/min to 20000 r/min to 25000 r/min to 20000 r/min.

from the detailed view on Zoom 1 window locating at the lower part of Fig. 7.6 that the phase of grid-side current tightly follows the phase of grid-side voltage from the beginning of the starting in the proposed system. At the start of acceleration, winding current in motor reaches protection threshold of 7.5 A and is subsequently chopped by hardware overcurrent protection. This ensures that motor operates safely within its specified limits.

Figures 7.7 display dynamic test results of proposed system when motor is commanded to decelerate. The short line on the left-hand side of active power curve represents 0 W. At the instant of deceleration in Fig. 7.7, a negative active power reference is generated. In order to follow the negative active power reference, the direction of the grid-side current flow is changed from the positive direction (namely, being in phase with the grid-side voltage) to the negative direction (namely, having a phase shift of 180° with the grid-side voltage) to produce the negative instantaneous active power. In this way, the speed is quickly decreased by feeding the excess energy back toward the grid side.

In Fig. 7.8, the curve of speed tracking errors between reference speed and actual speed during dynamic speed regulation is shown along with the curve of speed. The short brown line on the leftmost end of the waveform denotes 0 r/min for speed tracking error. The display range of the digital-to-analog converter chip is 100 r/min in the setting. As can be seen, the absolute value of the speed error remains under ± 15 r/min in the steady state, indicating a good speed regulation strategy.

7.3.2.3 Parameter sensitivity

The parameter sensitivity experiments are performed, and the experimental waveforms, screenshots of power analyzer, and current harmonic analysis are presented in Fig. 7.9, Fig. 7.10, and

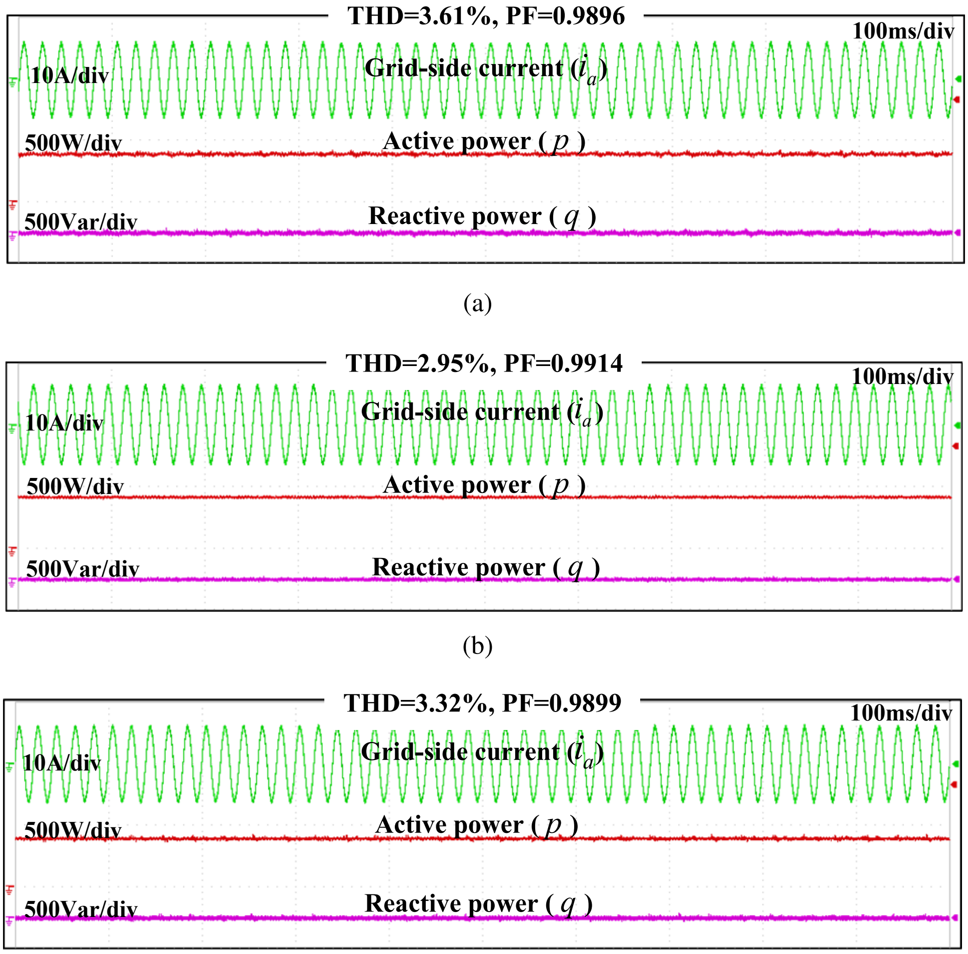

(a)

(b)

(c)

Figure 7.9: Waveforms of parameter sensitivity experiments in the rated operating condition (25000 r/min). (a) $L_{g,no}$ decreases to 50% and $R_{g,no}$ decreases to $50\% \, (L_{g,no} = 1\text{mH}, R_{g,no} = 0.15\Omega)$. (b) $L_{g,no}$ and $R_{g,no}$ are adopted $(L_{g,no} = 2\text{mH}, R_{g,no} = 0.3\Omega)$. (c) $L_{g,no}$ increases to 150 % and $R_{g,no}$ increases to $150\% \, (L_{g,no} = 3\text{mH}, R_{g,no} = 0.45\Omega)$.

Fig. 7.11, respectively.

In the experiments, three pairs of mismatched parameters are configured when the SRM runs in its rated operating condition, in order to test the system performance. With the disturbance observer, the prediction error caused by the mismatched parameters can be estimated online to compensate for deadbeat control. Therefore, as can be seen from Fig. 7.9, there is still no steady-state error in reactive power even if $L_{g,no}$ and $R_{g,no}$ are decreased to 50 % and increased to 150 % simultaneously in experiments. According to Fig. 7.10 and Fig. 7.11, satisfying power factor $\lambda\Sigma A$ and current THD can be got when the mismatched parameters are used in the system, which proves the validity of the disturbance observer.

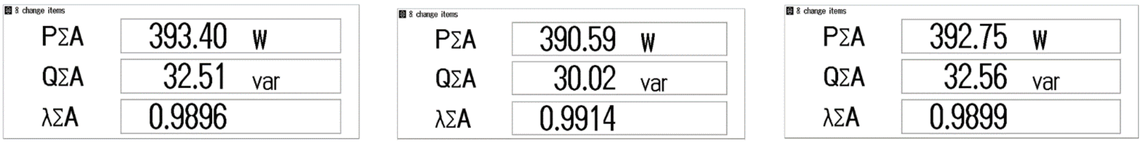

8 change items
PΣA 393.40 W
QΣA 32.51 var
λΣA 0.9896

8 change items
PΣA 390.59 W
QΣA 30.02 var
λΣA 0.9914

8 change items
PΣA 392.75 W
QΣA 32.56 var
λΣA 0.9899

(a) (b) (c)

Figure 7.10: Screenshots of power analyzer in parameter sensitivity experiments in the rated operating condition. (a) $L_{g,no}$ decreases to 50% and $R_{g,no}$ decreases to $50\%\,(L_{g,no} = 1\text{mH}, R_{g,no} = 0.15\Omega)$. (b) $L_{g,no}$ and $R_{g,no}$ are adopted $(L_{g,no} = 2\text{mH}, R_{g,no} = 0.3\Omega)$. (c) $L_{g,no}$ increases to 150% and $R_{g,no}$ increases to $150\%\,(L_{g,no} = 3\text{mH}, R_{g,no} = 0.45\Omega)$.

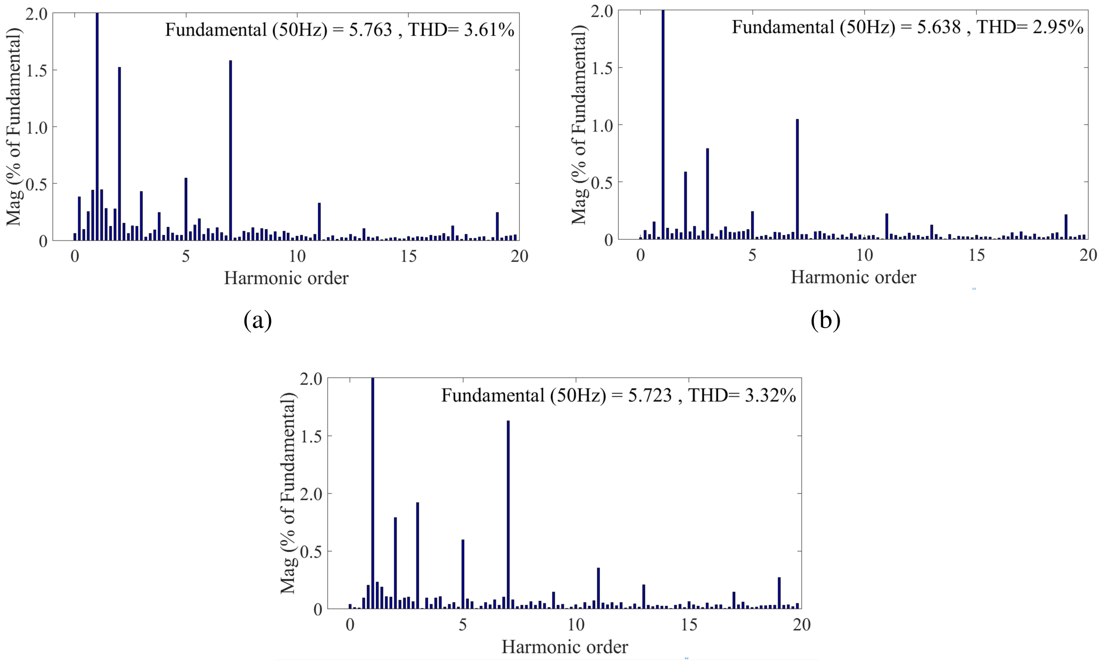

(a) (b)

(c)

Figure 7.11: Grid-side current harmonic analysis in parameter sensitivity experiments in the rated operating condition. (a) $L_{g,no}$ decreases to 50% and $R_{g,no}$ decreases to $50\%\,(L_{g,no} = 1\text{mH}, R_{g,no} = 0.15\Omega)$. (b) $L_{g,no}$ and $R_{g,no}$ are adopted $(L_{g,no} = 2\text{mH}, R_{g,no} = 0.3\Omega\ )$. (c) $L_{g,no}$ increases to 150% and $R_{g,no}$ increases to $150\%\,(L_{g,no} = 3\text{mH}, R_{g,no} = 0.45\Omega)$.

7.4 Summary

In this chapter, a power control strategy is proposed for the BTB converter-fed high-speed SRM system to govern the front-end PFC converter and back-end SRM simultaneously for system simplification. Stable SRM control is achieved by controlling the instantaneous active power in the drive system. Enhanced grid-side power quality is achieved by directly reducing the instantaneous reactive power. P-DBPC with disturbance observer can make sure the active and reactive power can follow their references at the same time without steady-state error even if the inaccurate system parameter is adopted in the calculation. As a result, satisfying SRM control performance can be realized while keeping a unity power factor and low current harmonics. Additionally, the energy feedback, which is beneficial to the motor drive system, can be realized in the proposed drive system so that the excess active power can be transferred back to the grid. The experimental results have verified the effectiveness of the proposed strategy.

CHAPTER 8

Conclusions

This dissertation focuses on the predictive control of BTB converter-fed electrical machine systems, and low current THDs, controllable reactive power, and well-regulated electrical machine are the main control goals.

In Chapter 2, the mathematical modelings concerning the two-level BTB converter-fed PMSM system and SRM system have been introduced in terms of both continuous and discrete forms to ease the system analysis and controller design presented in the chapters after. Besides, the lab-constructed testbench on which the control strategies are validated is presented in detail.

In Chapter 3, the conventional PI-MPC, which selects the optimal voltage vector by evaluating the cost function, is described. In this strategy, an outer voltage PI controller is applied to generate power/current reference, and the inner MPC controller is applied to achieve reference tracking. In addition, another model-based control strategy PI-DBPC, which calculates the desired variables by presuming that the system attains the intended behavior at the very end of every control period, is introduced. The experiments of these two strategies are carried out on the testbench to show their regulation performances, and the waveforms are adopted as references to compare with that of the following proposed strategies.

In Chapter 4, the DRPC, which removes the outer PI controller by updating the reference of every instant, is described. The trajectory of its temporary DC-link voltage reference is specially designated, and the temporary active power reference involved in the cost function is estimated correspondingly by adding the load power and capacitor power together. Whereas the reference prediction horizon limits its dynamic response to some extent. To improve its dynamic performance, a modified DRPC is proposed, which adopts a dynamic reference prediction horizon for the calculation of DC-link voltage reference so that the dynamic response time can be reduced by increasing the system power flow at the beginning stage when a new reference is given.

In Chapter 5, instead of adopting the cascade control structure, a DPVC strategy, which directly regulates the DC-link voltage and power flow within a newly-defined cost function, is proposed. By evaluating the newly-defined cost function, the strategy selects the voltage vector which not only will generate a DC-link voltage closer to its reference at instant k+2 but will generate an active power capable of further reducing that voltage error for the future instant. Consequently, well-regulated DC-link voltage and controllable power can be achieved within one cost function.

Although the cascade-free control strategy has been proposed in Chapter 5, the weighting factor is still requisite in its cost function. The determination of weighting factor is generally based on trial and error procedures, which are empirical and time-consuming. Moreover, additional tuning effort is also necessary in order to perform well in various operating conditions. To further improve the control performance of DPVC strategy, the weighting factor is removed by sorting the terms of cost function into two groups and independently evaluating each group separately in Chapter 6. Moreover, to cope with the mismatch between the actual and nominal parameters, Kalman filter has been added to DPVC strategy to compensate for the steady-state error caused by parameter mismatch through estimating the disturbances in power expression. By this way, the Kalman filter is adopted to estimate the power loss in MSC and GSC in real time for DC-link voltage error elimination.

Due to the structural characteristics of SRM, the BTB converter-fed SRM system is also researched considering its suitability in high-speed application. In Chapter 7, a centralized P-DBPC is proposed to simplify the control structure of the BTB converter-fed high-speed SRM drive system. Regarding the front-end converter and the SRM converter as one single control unit, it controls the whole drive system by manipulating the power flow. Specifically, the speed controller of the SRM generates the torque reference, and the active power reference is obtained by multiplying the torque reference by the angular velocity. By transferring the desired instantaneous power required by the motor side from the grid, P-DBPC builds a direct power connection between the front-end VSR and back-end SRM so that SRM regulation, grid-side power factor correction, and current harmonic restraint can be fulfilled simultaneously.

The proposed control strategies have been verified on the testbench. The DPVC strategies present more satisfying regulation performance than the conventional PI-MPC strategy, PI-DBPC in dynamic experiments. Through the DPVC strategies, the tracking error of DC-link voltage is kept around ± 2.5 V, the grid-side current THDs are around 3.1 %, and the winding current THDs are around 7.5 % at the rated operating condition of the BTB converter-fed PMSM system. Furthermore, compared with DPVC strategy with weighting factor, DPVC strategy without weighting factor is capable of achieving better control performance in responding to the step changes of DC-link voltage, torque, speed, and reactive power. For the BTB converter-fed SRM drive system, a stable SRM drive is fulfilled by controlling the instantaneous power flow inside the system, and the speed tracking error is kept within ± 15 r/min at the rated operating condition of 25000 r/min. The grid-side power factors have been increased to near 1, and the current distortions have been reduced to below 5 %.

In future work, long-horizon predictive control can be considered to be applied to BTB converter-fed electrical machine system for switch frequency reduction and further control performance improvements. In addition, to improve the reliability and availability of the whole system, fault diagnosis and post-fault operation can be further studied when a short circuit or open switch fault is detected in the BTB converter.

APPENDIX A

List of publications

A.1 Journal papers

- **Y. He**, Y. Tang, X. Gao, H. Xie, F. Wang, J. Rodriguez, and R. Kennel, “ Direct Predictive Voltage Control for Grid-Connected Permanent Magnet Synchronous Generator System", *Industrial Electronics, IEEE Transactions on*, vol. 70, no. 11, pp. 10860-10870, Nov. 2023.
- **Y. He**, Y. Tang, X. Gao, H. Xie, F. Wang, J. Rodriguez, and R. Kennel, “ A Cascade-Free Model Predictive Control Scheme for Back-to-Back Converter-Fed PMSM Drive System", *Power Electronics, IEEE Transactions on*, vol. 39, no. 4, pp. 4590-4600, Apr. 2024.
- **Y. He**, Y. Tang, H. Xie, F. Wang, J. Rodriguez, and R. Kennel, “ Single-phase H-bridge Rectifier fed High-speed SRM System based on Integrated Power Control", *Energy conversion, IEEE Transactions on*, vol. 38, no. 1, pp. 519-529, March 2023.
- Y. Tang, **Y. He**, F. Wang and R. Kennel, “Voltage-sourced Converter fed High-speed SRM Drive System with Energy Feedback and Near-Unity Power Factor", *Industrial Electronics, IEEE Transactions on*, vol. 69, no. 4, pp. 3460–3470, Apr. 2022.
- Y. Tang, **Y. He**, F. Wang, H. Xie, J. Rodriguez and R. Kennel, “A Drive Topology for High-speed SRM with Bidirectional Energy Flow and Fast Demagnetization Voltage", *Industrial Electronics, IEEE Transactions on*, vol. 68, no. 10, pp. 9242–9253, Oct. 2021.
- Y. Tang, **Y. He**, F. Wang, G. Lin, J. Rodriguez and R. Kennel, “A Centralized Control Strategy for Grid-connected High-speed Switched Reluctance Motor Drive System with Power Factor Correction", *Energy conversion, IEEE Transactions on*, vol. 36, no. 3, pp. 2163–2171, Sep. 2021.

- Y. Tang, **Y. He**, F. Wang, D. Lee, J. Ahn, and R. Kennel, “ Back-EMF-based sensorless control system of hybrid SRM for high-speed operation", *IET Elect. Power Appl*, vol. 12, no. 6, pp. 867–873, Jul. 2018.
- H. Xie, L. Liu, **Y. He**, F. Wang, J. Rodríguez and R. Kennel, "Gradient Descent-Based Objective Function Reformulation for Finite Control Set Model Predictive Current Control With Extended Horizon," *Industrial Electronics, IEEE Transactions on*, vol. 69, no. 9, pp. 8667-8678, Sept. 2022.
- F. Wang, G. Lin and **Y. He**, "Passivity-Based Model Predictive Control of Three-Level Inverter-Fed Induction Motor," *Power Electronics, IEEE Transactions on*, vol. 36, no. 2, pp. 1984-1993, Feb. 2021.
- H. Xie, F. Wang, **Y. He**, J. Rodríguez and R. Kennel, "Encoderless Parallel Predictive Torque Control for Induction Machine Using a Robust Model Reference Adaptive System," *Energy conversion, IEEE Transactions on*, vol. 37, no. 1, pp. 232-242, March 2022.
- H. Xie, F. Wang, Q. Xun, **Y. He**, J. Rodríguez and R. Kennel, "A Low-Complexity Gradient Descent Solution With Backtracking Iteration Approach for Finite Control Set Predictive Current Control," *Industrial Electronics, IEEE Transactions on*, vol. 69, no. 5, pp. 4522-4533, May 2022.
- H. Xie, F. Wang, Q. Xun, **Y. He**, J. Rodríguez and R. Kennel, "Iterative Gradient Descent-Based Finite Control Set Predictive Current Control With Least-Squares Optimized Duty Cycles," *IEEE J. Emerg. Sel. Topics Power Electron.*, vol. 10, no. 2, pp. 1422-1433, April 2022.
- H. Xie, F. Wang, Q. Chen, **Y. He**, J. Rodríguez and R. Kennel, "Computationally Efficient Predictive Current Control with Finite Set Extension using Derivative Projection for IM Drives," *IEEE J. Emerg. Sel. Topics Power Electron.*, vol. 11, no. 2, pp. 1345-1357, April 2023.

A.2 Conference papers

- **Y. He**,Y. Tang, H. Xie, D. Ke, and F. Wang, “Rotor optimization for two-phase high-speed switched reluctance motor", in *proc. IEEE ECCE Asia*, Singapore, May 2021, pp. 2100-2103.
- **Y. He**,Y. Tang, H. Xie, D. Ke, F. Wang, and R. Kennel, “Power quality improvement for grid-connected high-speed switched reluctance drive system", in *proc. IEEE ECCE Asia*, Singapore, May 2021, pp. 2406-2409.
- **Y. He**,Y. Tang, Q. Chen, F. Wang, and R. Kennel, “Deadbeat direct power control of voltage- sourced rectifier with reduced switching frequency", in *proc. IEEE ICEMS*, Hamamatsu, Japan, Dec. 2020, pp. 1511-1515.

- **Y. He**,Y. Tang, H. Xie, F. Wang, and R. Kennel, “Weighting-factor-less model predictive direct power control for three-level NPC rectifier", in *proc. IEEE ICEMS*, Hamamatsu, Japan, Dec. 2020, pp. 581-586.
- **Y. He**,Y. Tang, H. Xie, F. Wang, J. Rodriguez, and R. Kennel, “Performance evaluation for an optimized 4/2 high-speed SRM fed by active front-end rectifier", in *proc. IEEE ICEM*, Gothenburg, Sweden, Dec. 2020, pp. 1192-1198.
- Q. Chen, Y. Tang, **Y. He**, P. Stolze, and R. Kennel, “An assessment of finite control set predictive current control with concept of variable switching point or parallel cost function for induction motor", in *proc. IEEE ECCE Europe*, Ghent, Belgium, Oct. 2021, pp. 1-6.
- H. Xie, F. Wang, **Y. He**,Y. Tang, J. Rodriguez, and R. Kennel, “Extended kalman filter based encoderless predictive current control for induction machine drives", in *proc. IEEE ECCE Asia*, Singapore, Jul. 2021, pp. 865-868.
- H. Xie, F. Wang, **Y. He**,Y. Tang, J. Rodriguez, and R. Kennel, “Sliding-mode disturbance observer based parallel predictive torque controller for induction machine drives", in *proc. IEEE ECCE Asia*, Singapore, Jul. 2021, pp. 1511-1514.
- H. Xie, F. Wang, **Y. He**, L. Liu, J. Rodriguez and R. Kennel, "Cascaded Predictive Current Control with a Piecewise Approach for Induction Machine Drives," in *proc. IEEE PRECEDE*, Jinan, China, 2021, pp. 81-85.
- G. Lin, F. Wang, **Y. He** and J. Rodríguez, "A Cascaded Extended State Observer for Three-level Back-to-back Converter with Surface Mounted Permanent Magnet Synchronous Motor," in *proc. IEEE ICEMS*, Harbin, China, 2019, pp. 1-6.

APPENDIX B

List of symbols and abbreviations

B.1 List of symbols

i_m	Stator current
u_m	Stator voltage
ψ_r	Permanent magnet flux linkage
R_m	Stator resistor
L_m	Stator inductor
$\omega_{m,e}$	Electrical angular velocity
$\boldsymbol{I}_m$	Stator current reference
$T_{m,e}$	Electromagnetic torque
$\overrightarrow{\boldsymbol{S}}_m^{abc}$	Switching state of MSC
ψ_m	Phase flux linkage
ω_r	Mechanical angular velocity
θ_r	Rotor position
N_s	Number of stator poles
N_r	Number of rotor poles
τ_l	Load torque
J_m	Rotor inertia
B_m	Friction coefficient

u_{dc}	DC-link voltage
i_{dc}	DC-link current
ω_g	Frequency of grid side voltage
R_g	Grid-side filter resistance
e_g	Grid-side voltage
L_g	Grid-side filter inductance
C	DC-link capacitor
u_{DC}	Voltage on DC-link capacitor
Δv	Deviation of neutral voltage
p_g	Instantaneous active power
q_g	Instantaneous reactive power
P^*	Active power reference
Q^*	Reactive power reference
$\overrightarrow{\boldsymbol{S}}_g^{abc}$	Switching state of GSC

B.2 List of abbreviations

AC	Alternating Current
AHBC	Asymmetric Half-Bridge Converter
ANNs	Artificial Neural Networks
BTB	Back-to-Back
BIBO	Bounded-Input Bounded-Output
CT	Continuous-Time
DAC	Digital-to-Analog Converter
DB	Dead-beat
DBPC	Deadbeat Predictive Control
DBR	Diode Bridge Rectifier
DC	Direct Current
DPVC	Direct Predictive Voltage Control
DRPC	Dynamic Reference Predictive Control
DSP	Digital Signal Processor
DT	Discrete-Time
DTC	Direct Torque Control
DPC	Direct Power Control
EMF	Electromotive Force
EMI	Electromagnetic Interference
FOC	Field-Oriented Control
FCS-MPC	Finite Control-Set Model Predictive Control
GaN	Gallium Nitride
GSC	Grid-side Converter
HIL	Hardware-in-the-Loop
IGBT	Insulated Gate Bipolar Transistor
IGCT	Insulated Gate Commutated Thyristor
IM	Induction Machine
IPMs	Intelligent Power Modules
KCL	Kirchhoff's Current Law
KVL	Kirchhoff's Voltage Law
LTI	Linear Time Invariant
LTV	Linear Time Variant
LV	Low-Voltage
LVRT	Low-Voltage Ride-Through
MTPA	Maximum Torque Per Ampere
MPC	Model Predictive Control
MPCC	Model Predictive Current Control
MPPC	Model Predictive Power Control
MPTC	Model Predictive Torque Control
MSC	Machine-side Converter
MV	Medium-Voltage
NPC	Neutral Point Clamped
PCB	Printed Circuit Board

P-DBPC	Predictive Deadbeat Power Control
PFC	Power Factor Correction
PI	Proportional Integral
PTC	Predictive Torque Control
PMSM	Permanent Magnet Sychronous Machine
PWM	Pulse-Width Modulation
RQC-DMPC	Revised Quasi-Centralized Direct Model Predictive Control
SiC	Silicon Carbide
SMC	Sliding Mode Control
SMPTC	sequential Model Predictive Torque Control
SPWM	Sinusoidal Pulse Width Modulation
SRM	Switched Reluctance Machine
SVPWM	Space Vector Pulse Width Modulation
THD	Total Harmonic Distortion
VSC	Voltage-Sourced Converter
VSI	Voltage-Source Inverter
VSR	Voltage-Source Rectifier
VOC	Voltage-Oriented Control
WECS	Wind Energy Conversion System
ZOH	Zero-Order Hold

APPENDIX C

Performance Comparison

Table C.1: Comparison Data under Various Conditions

Experiment	Control strategy	Peak error of DC-link voltage(V)	Recovery time(ms)
Step change of voltage (from 450 to 550 V)	PI-MPC	Overshoot(10V)	90
	PI-DBPC	Overshoot(12V)	100
	DRPC	No overshoot	60
	DPVC-1	No overshoot	40
	DPVC-2	No overshoot	25
Step change of torque (from 12 to -12N·m)	PI-MPC	28	200
	PI-DBPC	35	300
	DRPC	20	90
	DPVC-1	15	70
	DPVC-2	12	50
Step change of reactive power (from -1500 to 1500 Var)	PI-MPC	-10	200
	PI-DBPC	-12	250
	DRPC	-6	80
	DPVC-1	-5	50
	DPVC-2	-3	30
Step change of speed (from 1500 to -1500 r/min)	PI-MPC	6	-
	PI-DBPC	8	-
	DRPC	4	-
	DPVC-1	3	-
	DPVC-2	3	-

The experimental data of PI-MPC, PI-DBPC, modified DRPC, DPVC (DPVC-1), and DPVC without weighting factor (DPVC-2) in the aforementioned dynamic tests, which reflects their transient performances, is summarized in Table C.1. It can be found that the dynamic regulation performances presented in all four MPC-based strategies (PI-MPC, DRPC, DPVC-1, and DPVC-2) are obviously better than that of the PI-DBPC strategy. This means that the dynamic performance of the MPC controller is significantly better than that of the controller with modulator. Furthermore, compared with the PI-MPC, the proposed control strategies (DRPC, DPVC-1, and DPVC-2) present faster dynamic performances in responding to the abrupt changes of torque, reactive power, and speed since it presents smaller peak errors and shorter recovery time. Therefore, the dynamic response of the cascade-free controller without outer voltage loop is better than that of the cascaded PI-MPC strategy, and the dynamic performance of DPVC-2 without weighting factor is better than that of DPVC-1 with weighting factor.

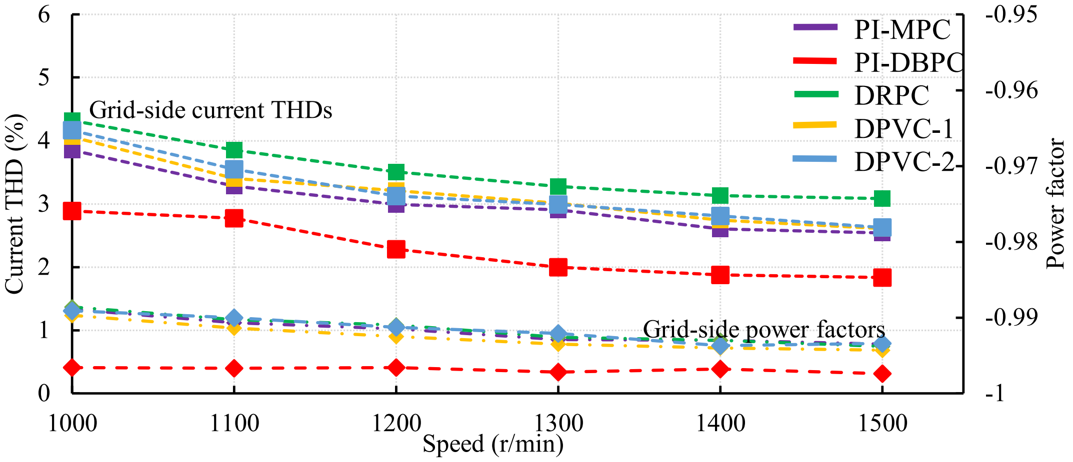

Figure C.1: Current THDs and power factors.

As can be seen from the current THDs and power factors in Fig. C.1, the PI-DBPC with modulator has a slightly better steady-state regulation performance than the other four MPC-based strategies at the same switching frequency, but it has the slowest regulation performance in transients, which is shown in Table C.1. However, the steady-state performances of the four MPC-based strategies are comparable to that of the PI-DBPC since the MPC-based strategies also can regulate the current THDs below 3 % and regulate the grid-side power factors above 0.993 at the rated operating condition.

List of Figures

List of Tables

Bibliography

[1] B. Bilgin, J. W. Jiang, and A. Emadi, “Electric motor industry and switched reluctance machines,” in *Switched Reluctance Motor Drives*, 1st ed. Boca Raton, FL, USA: CRC, ch. 1, pp. 1-31, 2019.

[2] B. Bilgin and A. Sathyan, “Fundamentals of electric machines,” in *Advanced Electric Drive Vehicles*, 1st ed. Boca Raton, FL: CRC Press, ch. 5, pp. 107-186, 2014.

[3] V. Yaramasu and B. Wu, “Control of PMSG WECS with back-to-back connected converters,” in *Model Predictive Control of Wind Energy Conversion Systems*, 1st ed. Hoboken, NJ, USA: Wiley-IEEE Press, ch. 1, pp. 285-328, 2017.

[4] L. Shen, S. Bozhko, G. Asher, C. Patel, and P. Wheeler, “Active DC-link capacitor harmonic current reduction in two-level back-to-back converter,” *IEEE Transactions on Power Electronics*, vol. 31, no. 10, pp. 6947–6954, 2015.

[5] P. Sanchis, A. Ursæa, E. Gubía, and L. Marroyo, “Boost DC-AC inverter: a new control strategy,” *IEEE Transactions on Power Electronics*, vol. 20, no. 2, pp. 343–353, 2005.

[6] C.-H. Hsieh, T.-J. Liang, S.-M. Chen, and S.-W. Tsai, “Design and implementation of a novel multilevel DC-AC inverter,” *IEEE Transactions on Industry Applications*, vol. 52, no. 3, pp. 2436–2443, 2016.

[7] J. Chivite-Zabalza, C. Gironés, A. Cárcar, I. Larrazabal, E. Olea, and M. Zabaleta, “Comparison of power conversion topologies for a multi-megawatt off-shore wind turbine, based on commercial power electronic building blocks,” in *IECON 2013-39th Annual Conference of the IEEE Industrial Electronics Society*. IEEE, 2013, pp. 5242–5247.

[8] X. Xu, Z. Zheng, K. Wang, B. Yang, and Y. Li, “A comprehensive study of common mode voltage reduction and neutral point potential balance for a back-to-back three-level NPC converter,” *IEEE Transactions on Power Electronics*, vol. 35, no. 8, pp. 7910–7920, 2019.

[9] A. Yazdani and R. Iravani, “A neutral-point clamped converter system for direct-drive variable-speed wind power unit,” *IEEE Transactions on Energy Conversion*, vol. 21, no. 2, pp. 596–607, 2006.

[10] S. Alepuz, A. Calle, S. Busquets-Monge, S. Kouro, and B. Wu, “Use of stored energy in PMSG rotor inertia for low-voltage ride-through in back-to-back NPC converter-based wind power systems,” *IEEE Transactions on Industrial Electronics*, vol. 60, no. 5, pp. 1787–1796, 2012.

[11] S. Kouro, M. Malinowski, K. Gopakumar, J. Pou, L. G. Franquelo, B. Wu, J. Rodriguez, M. A. Pérez, and J. I. Leon, “Recent advances and industrial applications of multilevel converters,” *IEEE Transactions on Industrial Electronics*, vol. 57, no. 8, pp. 2553–2580, 2010.

[12] J. Rodriguez, S. Bernet, P. K. Steimer, and I. E. Lizama, “A survey on neutral-point-clamped inverters,” *IEEE transactions on Industrial Electronics*, vol. 57, no. 7, pp. 2219–2230, 2009.

[13] F. Blaabjerg and K. Ma, “Future on power electronics for wind turbine systems,” *IEEE Journal of Emerging and Selected Topics in Power Electronics*, vol. 1, no. 3, pp. 139–152, 2013.

[14] V. Yaramasu and B. Wu, “Overview of digital control techniques,” in *Model Predictive Control of Wind Energy Conversion Systems*, 1st ed. Hoboken, NJ, USA: Wiley-IEEE Press, ch. 1, pp. 3-58, 2017.

[15] C.-T. Pan and T.-Y. Chang, “An improved hysteresis current controller for reducing switching frequency,” *IEEE Transactions on Power Electronics*, vol. 9, no. 1, pp. 97–104, 1994.

[16] A. Shukla, A. Ghosh, and A. Joshi, “Hysteresis modulation of multilevel inverters,” *IEEE Transactions on Power Electronics*, vol. 26, no. 5, pp. 1396–1409, 2010.

[17] G. K. Singh, K. Nam, and S. Lim, “A simple indirect field-oriented control scheme for multiphase induction machine,” *IEEE Transactions on Industrial Electronics*, vol. 52, no. 4, pp. 1177–1184, 2005.

[18] R. Kadri, J.-P. Gaubert, and G. Champenois, “An improved maximum power point tracking for photovoltaic grid-connected inverter based on voltage-oriented control,” *IEEE Transactions on Industrial Electronics*, vol. 58, no. 1, pp. 66–75, 2010.

[19] L. Zhong, M. F. Rahman, W. Y. Hu, and K. Lim, “Analysis of direct torque control in permanent magnet synchronous motor drives,” *IEEE Transactions on Power Electronics*, vol. 12, no. 3, pp. 528–536, 1997.

[20] J. Alonso-Martinez, J. E.-G. Carrasco, and S. Arnaltes, “Table-based direct power control: A critical review for microgrid applications,” *IEEE Transactions on Power Electronics*, vol. 25, no. 12, pp. 2949–2961, 2010.

[21] X. Zhang, L. Sun, K. Zhao, and L. Sun, “Nonlinear speed control for PMSM system using sliding-mode control and disturbance compensation techniques,” *IEEE Transactions on Power Electronics*, vol. 28, no. 3, pp. 1358–1365, 2012.

[22] J. Rodriguez, J. Pontt, C. A. Silva, P. Correa, P. Lezana, P. Cortés, and U. Ammann, "Predictive current control of a voltage source inverter," *IEEE Transactions on Industrial Electronics*, vol. 54, no. 1, pp. 495–503, 2007.

[23] N. Jin, C. Gan, and L. Guo, "Predictive control of bidirectional voltage source converter with reduced current harmonics and flexible power regulation under unbalanced grid," *IEEE Transactions on Energy Conversion*, vol. 33, no. 3, pp. 1118–1131, 2018.

[24] Y. Zhang and Z. Min, "Model-free predictive current control of a PWM rectifier based on space vector modulation under unbalanced and distorted grid conditions," *IEEE Journal of Emerging and Selected Topics in Power Electronics*, vol. 10, no. 2, pp. 2319–2329, 2022.

[25] S. Xu, S. Tao, W. Zheng, Y. Chai, M. Ma, and L. Ding, "Multiple open-circuit fault diagnosis for back-to-back converter of PMSG wind generation system based on instantaneous amplitude estimation," *IEEE Transactions on Instrumentation and Measurement*, vol. 70, pp. 1–13, 2021.

[26] N. M. A. Freire and A. J. M. Cardoso, "A fault-tolerant direct controlled PMSG drive for wind energy conversion systems," *IEEE Transactions on Industrial Electronics*, vol. 61, no. 2, pp. 821–834, 2014.

[27] J.-S. Lee and K.-B. Lee, "Open-switch fault tolerance control for a three-level NPC/T-type rectifier in wind turbine systems," *IEEE Transactions on Industrial Electronics*, vol. 62, no. 2, pp. 1012–1021, 2015.

[28] Z. Zhang, H. Xu, M. Xue, Z. Chen, T. Sun, R. Kennel, and C. M. Hackl, "Predictive control with novel virtual-flux estimation for back-to-back power converters," *IEEE Transactions on Industrial Electronics*, vol. 62, no. 5, pp. 2823–2834, 2015.

[29] R. Portillo, M. Prats, J. Leon, J. Sanchez, J. Carrasco, E. Galvan, and L. Franquelo, "Modeling strategy for back-to-back three-level converters applied to high-power wind turbines," *IEEE Transactions on Industrial Electronics*, vol. 53, no. 5, pp. 1483–1491, 2006.

[30] A. Yazdani and R. Iravani, "Back-to-back HVDC conversion system," in *Voltage-Sourced Converters in Power Systems: Modeling, Control, and Applications*, 1st ed. Hoboken, NJ, USA: Wiley-IEEE Press, ch. 12, pp. 69-107, 2010.

[31] I. Jlassi and A. J. M. Cardoso, "Fault-tolerant back-to-back converter for direct-drive PMSG wind turbines using direct torque and power control techniques," *IEEE Transactions on Power Electronics*, vol. 34, no. 11, pp. 11 215–11 227, 2019.

[32] V. Yaramasu and B. Wu, "Basics of wind energy conversion systems," in *Model Predictive Control of Wind Energy Conversion Systems*, 1st ed. Hoboken, NJ, USA: Wiley-IEEE Press, ch. 1, pp. 3-58, 2017.

[33] M. E. Zarei, D. Ramírez, M. Prodanovic, and G. M. Arana, "Model predictive control for PMSG-based wind turbines with overmodulation and adjustable dynamic response time," *IEEE Transactions on Industrial Electronics*, vol. 69, no. 2, pp. 1573–1585, 2022.

[34] I. Jlassi and A. J. Marques Cardoso, "Enhanced and computationally efficient model predictive flux and power control of PMSG drives for wind turbine applications," *IEEE Transactions on Industrial Electronics*, vol. 68, no. 8, pp. 6574–6583, 2021.

[35] A. Calle-Prado, S. Alepuz, J. Bordonau, P. Cortes, and J. Rodriguez, "Predictive control of a back-to-back NPC converter-based wind power system," *IEEE Transactions on Industrial Electronics*, vol. 63, no. 7, pp. 4615–4627, 2016.

[36] J. Rodriguez, J. Pontt, P. Correa, P. Lezana, and P. Cortes, "Predictive power control of an AC/DC/AC converter," in *Fourtieth IAS Annual Meeting. Conference Record of the 2005 Industry Applications Conference, 2005.*, vol. 2, 2005, pp. 934–939 Vol. 2.

[37] M. Liu, K. W. Chan, J. Hu, W. Xu, and J. Rodriguez, "Model predictive direct speed control with torque oscillation reduction for PMSM drives," *IEEE Transactions on Industrial Informatics*, vol. 15, no. 9, pp. 4944–4956, 2019.

[38] H. Abu-Rub, M. Malinowski, and K. Al-Haddad, "Model predictive speed control of electrical machines," in *Power Electronics for Renewable Energy Systems, Transportation and Industrial Applications*, 1st ed. Hoboken, NJ, USA: Wiley-IEEE Press, ch. 19, pp. 608-627, 2014.

[39] D. E. Quevedo, R. P. Aguilera, M. A. Perez, P. Cortes, and R. Lizana, "Model predictive control of an AFE rectifier with dynamic references," *IEEE Transactions on Power Electronics*, vol. 27, no. 7, pp. 3128–3136, 2012.

[40] X. Liu, D. Wang, and Z. Peng, "Cascade-free fuzzy finite-control-set model predictive control for nested neutral point-clamped converters with low switching frequency," *IEEE Transactions on Control Systems Technology*, vol. 27, no. 5, pp. 2237–2244, 2019.

[41] Z. Zhang, F. Wang, T. Sun, J. Rodríguez, and R. Kennel, "FPGA-based experimental investigation of a quasi-centralized model predictive control for back-to-back converters," *IEEE Transactions on Power Electronics*, vol. 31, no. 1, pp. 662–674, 2016.

[42] Z. Zhang, T. Sun, F. Wang, J. Rodríguez, and R. Kennel, "A computationally efficient quasi-centralized DMPC for back-to-back converter PMSG wind turbine systems without DC-link tracking errors," *IEEE Transactions on Industrial Electronics*, vol. 63, no. 10, pp. 6160–6171, 2016.

[43] T. Wildi, "Active, reactive, and apparent power," in *Electrical Machines, Drives and Power Systems*, 5th ed. Upper Saddle River, NJ, USA: Prentice Hall, ch. 7, pp. 134-144, 2002.

[44] D.-H. Lee, Z.-G. Lee, J. Liang, and J.-W. Ahn, "Single-phase SRM drive with torque ripple reduction and power factor correction," *IEEE Transactions on Industry Applications*, vol. 43, no. 6, pp. 1578–1587, Nov. 2007.

[45] M. Mohamadi, A. Rashidi, S. M. S. Nejad, and M. Ebrahimi, “A switched reluctance motor drive based on quasi Z-source converter with voltage regulation and power factor correction,” *IEEE Transactions on Industrial Electronics*, vol. 65, no. 10, pp. 8330–8339, Oct. 2018.

[46] Y. Tang, Y. He, F. Wang, G. Lin, J. Rodríguez, and R. Kennel, “A centralized control strategy for grid-connected high-speed switched reluctance motor drive system with power factor correction,” *IEEE Transactions on Energy Conversion*, vol. 36, no. 3, pp. 2163–2172, Jan. 2021.

[47] J.-Y. Chai and C.-M. Liaw, “Development of a switched-reluctance motor drive with PFC front end,” *IEEE Transactions on Energy Conversion*, vol. 24, no. 1, pp. 30–42, Mar. 2009.

[48] J.-Y. Chai, Y.-C. Chang, and C.-M. Liaw, “On the switched-reluctance motor drive with three-phase single-switch switch-mode rectifier front-end,” *IEEE Transactions on Power Electronics*, vol. 25, no. 5, pp. 1135–1148, May 2010.

[49] A. Anand and B. Singh, “Power factor correction in cuk–sepic-based dual-output-converter-fed SRM drive,” *IEEE Transactions on Industrial Electronics*, vol. 65, no. 2, pp. 1117–1127, Feb. 2018.

[50] A. Aniket and S. Bhim, “Cuk-SEPIC based bridgeless PFC dual output converter fed SRM drive,” in *Proc. IEEE IICPE*, Jaipur, India, Oct. 2018, pp. 1–7.

[51] M. Changizian, S. Rezazade, A. Saleki, and M. T. Bina, “Application of vienna converter to a double-driven SRMs under one PFC compensator,” in *2018 9th Annual Power Electronics, Drives Systems and Technologies Conference*. IEEE, 2018, pp. 294–299.

[52] A. Anand and B. Singh, “Modified dual output cuk converter-fed switched reluctance motor drive with power factor correction,” *IEEE Transactions on Power Electronics*, vol. 34, no. 1, pp. 624–635, Jan. 2019.

[53] F. Z. Peng and J.-S. Lai, “Generalized instantaneous reactive power theory for three-phase power systems,” *IEEE transactions on instrumentation and measurement*, vol. 45, no. 1, pp. 293–297, 1996.

[54] H. Akagi, Y. Kanazawa, and A. Nabae, “Instantaneous reactive power compensators comprising switching devices without energy storage components,” *IEEE Transactions on industry applications*, no. 3, pp. 625–630, 1984.

[55] A. Yazdani and R. Iravani, “Space phasors and two-dimensional frames,” in *Voltage-sourced converters in power systems: modeling, control, and applications*, 1st ed. Hoboken, NJ, USA: Wiley-IEEE Press, ch. 4, pp. 69-107, 2010.

[56] R. Burgos and E. Wiechmann, “Extended voltage swell ride-through capability for PWM voltage-source rectifiers,” *IEEE Transactions on Industrial Electronics*, vol. 52, no. 4, pp. 1086–1098, 2005.

[57] K. Nam, “PMSM control methods,” in *AC Motor Control and Electrical Vehicle Applications*, 2nd ed. Boca Raton, FL, USA: CRC, ch. 7, pp. 243-274, 2018.

[58] R. Krishnan, “Principle of operation of the switched reluctance motor,” in *Switched Reluctance Motor Drives: modeling, Simulation, Analysis, Design, and Applications*, 1st ed. Boca Raton, FL, USA: CRC, ch. 1, pp. 229-294, 2001.

[59] P. Alemi, Y.-C. Jeung, and D.-C. Lee, “DC-link capacitance minimization in T-type three-level AC/DC/AC PWM converters,” *IEEE Transactions on Industrial Electronics*, vol. 62, no. 3, pp. 1382–1391, 2014.

[60] B. Wittig, W.-T. Franke, and F. Fuchs, “Design and analysis of a DC/DC/AC three phase solar converter with minimized DC link capacitance,” in *2009 13th European Conference on Power Electronics and Applications*. IEEE, 2009, pp. 1–9.

[61] Y. Dote, T. Sriram, and R. G. Hoft, “Parameter and state estimation for dead-beat DC drive speed control,” in *1980 IEEE Power Electronics Specialists Conference*. IEEE, 1980, pp. 335–340.

[62] K. P. Gokhale, A. Kawamura, and R. G. Hoft, “Dead beat microprocessor control of PWM inverter for sinusoidal output waveform synthesis,” *IEEE Transactions on Industry Applications*, no. 5, pp. 901–910, 1987.

[63] P. Cortés, M. P. Kazmierkowski, R. M. Kennel, D. E. Quevedo, and J. Rodríguez, “Predictive control in power electronics and drives,” *IEEE Transactions on Industrial Electronics*, vol. 55, no. 12, pp. 4312–4324, 2008.

[64] J. Rodriguez, R. M. Kennel, J. R. Espinoza, M. Trincado, C. A. Silva, and C. A. Rojas, “High-performance control strategies for electrical drives: An experimental assessment,” *IEEE Transactions on Industrial Electronics*, vol. 59, no. 2, pp. 812–820, 2012.

[65] L. Yan, F. Wang, M. Dou, Z. Zhang, R. Kennel, and J. Rodriguez, “Active disturbance-rejection-based speed control in model predictive control for induction machines,” *IEEE Transactions on Industrial Electronics*, vol. 67, no. 4, pp. 2574–2584, 2019.

[66] S.-K. Sul, “Design of regulators for electric machines and power converters,” in *Control of Electric Machine Drive Systems*, 1st ed. Piscataway, NJ, USA: Wiley-IEEE Press, ch. 4, pp. 154-230, 2011.

[67] L. Malesani, P. Mattavelli, and S. Buso, “Robust dead-beat current control for pwm rectifiers and active filters,” in *IEEE Industry Applications Conference*, vol. 2. IEEE, 1998, pp. 1377–1384.

[68] S. A. Davari, F. Wang, and R. M. Kennel, “Robust deadbeat control of an induction motor by stable MRAS speed and stator estimation,” *IEEE Transactions on Industrial Informatics*, vol. 14, no. 1, pp. 200–209, 2017.

[69] J.-F. Stumper, V. Hagenmeyer, S. Kuehl, and R. Kennel, “Deadbeat control for electrical drives: A robust and performant design based on differential flatness,” *IEEE Transactions on Power Electronics*, vol. 30, no. 8, pp. 4585–4596, 2014.

[70] F. Grimm, Z. Zhang, and R. Kennel, “Sphere decoding based long-horizon predictive control of three-level NPC back-to-back PMSG wind turbine systems,” in *2018 International Power Electronics Conference*. IEEE, 2018, pp. 2895–2900.

[71] T. Geyer, “Predictive control with long horizons,” in *Model Predictive Control of High Power Convertersand Industrial Drives*, 1st ed. Chichester, West Sussex, UK: Wiley, ch. 5, pp. 195-216, 2016.

[72] J. Hu, J. Zhu, and D. G. Dorrell, “Predictive direct power control of doubly fed induction generators under unbalanced grid voltage conditions for power quality improvement,” *IEEE Transactions on Sustainable Energy*, vol. 6, no. 3, pp. 943–950, 2014.

[73] Y. Zhang, Z. Li, W. Xu, J. Hu, and J. Zhu, “Grid synchronization of DFIG using model predictive direct power control,” in *2011 International Conference on Electrical Machines and Systems*. IEEE, 2011, pp. 1–6.

[74] P. Kou, D. Liang, J. Li, L. Gao, and Q. Ze, “Finite-control-set model predictive control for DFIG wind turbines,” *IEEE Transactions on Automation Science and Engineering*, vol. 15, no. 3, pp. 1004–1013, 2017.

[75] B. Hu, L. Kang, J. Liu, J. Zeng, S. Wang, and Z. Zhang, “Model predictive direct power control with fixed switching frequency and computational amount reduction,” *IEEE Journal of Emerging and Selected Topics in Power Electronics*, vol. 7, no. 2, pp. 956–966, 2019.

[76] I. Jlassi and A. J. M. Cardoso, “Enhanced and computationally efficient model predictive flux and power control of PMSG drives for wind turbine applications,” *IEEE Transactions on Industrial Electronics*, vol. 68, no. 8, pp. 6574–6583, 2020.

[77] X. Liu, D. Wang, and Z. Peng, “Cascade-free fuzzy finite-control-set model predictive control for nested neutral point-clamped converters with low switching frequency,” *IEEE Transactions on Control Systems Technology*, vol. 27, no. 5, pp. 2237–2244, 2018.

[78] M. Liu, K. W. Chan, J. Hu, W. Xu, and J. Rodriguez, “Model predictive direct speed control with torque oscillation reduction for PMSM drives,” *IEEE Transactions on Industrial Informatics*, vol. 15, no. 9, pp. 4944–4956, 2019.

[79] T. Hagglund and K. J. Astrom, “PID controllers: theory, design, and tuning,” *ISA-The Instrumentation, Systems, and Automation Society*, 1995.

[80] J. Rodriguez and C. Estay, “Weighting factor design,” in *Predictive Control of Power Converters and Electrical Drives*, 1st ed. Chichester West Sussex UK, Hoboken N.J.: IEEE/Wiley, ch. 1, pp. 3-16, 2012.

[81] P. Karamanakos and T. Geyer, “Guidelines for the design of finite control set model predictive controllers,” *IEEE Transactions on Power Electronics*, vol. 35, no. 7, pp. 7434–7450, 2020.

[82] Z. Zhang, Z. Li, M. P. Kazmierkowski, J. Rodríguez, and R. Kennel, “Robust predictive control of three-level NPC back-to-back power converter PMSG wind turbine systems with revised predictions,” *IEEE Transactions on Power Electronics*, vol. 33, no. 11, pp. 9588–9598, 2018.

[83] H. Liu, H. Hu, H. Chen, L. Zhang, and Y. Xing, “Fast and flexible selective harmonic extraction methods based on the generalized discrete fourier transform,” *IEEE Transactions on Power Electronics*, vol. 33, no. 4, pp. 3484–3496, 2017.

[84] Y. Zhang and Z. Min, “Model-free predictive current control of a pwm rectifier based on space vector modulation under unbalanced and distorted grid conditions,” *IEEE Journal of Emerging and Selected Topics in Power Electronics*, vol. 10, no. 2, pp. 2319–2329, 2022.

[85] S. Yan, Y. Yang, S. Hui, and F. Blaabjerg, “A review on direct power control of pulsewidth modulation converters,” *IEEE Transactions on Power Electronics*, vol. 36, no. 10, pp. 11 984–12 007, 2021.

[86] R. Basak, G. Bhuvaneswari, and R. R. Pillai, “Low-voltage ride-through of a synchronous generator-based variable speed grid-interfaced wind energy conversion system,” *IEEE Transactions on Industry Applications*, vol. 56, no. 1, pp. 752–762, 2020.

[87] J. Esch, “High-power wind energy conversion systems: State-of-the-art and emerging technologies,” *Proceedings of the IEEE*, vol. 103, no. 5, pp. 736–739, 2015.

[88] A. Zhou, Y. W. Li, and Y. Mohamed, “Mechanical stress comparison of PMSG wind turbine LVRT methods,” *IEEE Transactions on Energy Conversion*, vol. 36, no. 2, pp. 682–692, 2021.

[89] M. M. Mahmoud, A. Mohamed Hemeida, and A.-M. M. Abdel-Rahim, “Behavior of PMSG wind turbines with active crowbar protection under faults,” in *2019 Innovations in Power and Advanced Computing Technologies*, vol. 1, 2019, pp. 1–6.

[90] K.-H. Kim, Y.-C. Jeung, D.-C. Lee, and H.-G. Kim, “LVRT scheme of PMSG wind power systems based on feedback linearization,” *IEEE Transactions on Power Electronics*, vol. 27, no. 5, pp. 2376–2384, 2012.

[91] V. Yaramasu, B. Wu, S. Alepuz, and S. Kouro, “Predictive control for low-voltage ride-through enhancement of three-level-boost and NPC-converter-based pmsg wind turbine,” *IEEE Transactions on Industrial Electronics*, vol. 61, no. 12, pp. 6832–6843, 2014.

[92] C. Kim and W. Kim, “Enhanced low-voltage ride-through coordinated control for PMSG wind turbines and energy storage systems considering pitch and inertia response,” *IEEE Access*, vol. 8, pp. 212 557–212 567, 2020.

[93] S. Alepuz, A. Calle, S. Busquets-Monge, S. Kouro, and B. Wu, “Use of stored energy in PMSG rotor inertia for low-voltage ride-through in back-to-back NPC converter-based wind power systems,” *IEEE Transactions on Industrial Electronics*, vol. 60, no. 5, pp. 1787–1796, 2013.

[94] M. Norambuena, P. Lezana, and J. Rodriguez, "A method to eliminate steady-state error of model predictive control in power electronics," *IEEE Journal of Emerging and Selected Topics in Power Electronics*, vol. 7, no. 4, pp. 2525–2530, 2019.

[95] S. A. Davari, D. A. Khaburi, and R. Kennel, "An improved FCS-MPC algorithm for an induction motor with an imposed optimized weighting factor," *IEEE Transactions on Power Electronics*, vol. 27, no. 3, pp. 1540–1551, 2011.

[96] L. M. Caseiro, A. M. Mendes, and S. M. Cruz, "Cooperative and dynamically weighted model predictive control of a 3-level uninterruptible power supply with improved performance and dynamic response," *IEEE Transactions on Industrial Electronics*, vol. 67, no. 6, pp. 4934–4945, 2019.

[97] P. Acuna, L. Morán, M. Rivera, R. Aguilera, R. Burgos, and V. G. Agelidis, "A single-objective predictive control method for a multivariable single-phase three-level NPC converter-based active power filter," *IEEE Transactions on Industrial Electronics*, vol. 62, no. 7, pp. 4598–4607, 2015.

[98] F. Wang, H. Xie, Q. Chen, S. A. Davari, J. Rodriguez, and R. Kennel, "Parallel predictive torque control for induction machines without weighting factors," *IEEE Transactions on Power Electronics*, vol. 35, no. 2, pp. 1779–1788, 2019.

[99] Y. He, Y. Tang, H. Xie, F. Wang, and R. Kennel, "Weighting-factor-less model predictive direct power control for three-level NPC rectifier," in *2020 23rd International Conference on Electrical Machines and Systems*. IEEE, 2020, pp. 581–586.

[100] T. Geyer, "Algebraic weighting factor selection for predictive torque and flux control," in *2017 IEEE Energy Conversion Congress and Exposition*. IEEE, 2017, pp. 357–364.

[101] Y. Zhang and H. Yang, "Two-vector-based model predictive torque control without weighting factors for induction motor drives," *IEEE Transactions on Power Electronics*, vol. 31, no. 2, pp. 1381–1390, 2015.

[102] Y. Zhang, S. Gao, and W. Xu, "An improved model predictive current control of permanent magnet synchronous motor drives," in *2016 IEEE Applied Power Electronics Conference and Exposition*. IEEE, 2016, pp. 2868–2874.

[103] L. Guo, X. Zhang, S. Yang, Z. Xie, L. Wang, and R. Cao, "Simplified model predictive direct torque control method without weighting factors for permanent magnet synchronous generator-based wind power system," *IET Electric Power Applications*, vol. 11, no. 5, pp. 793–804, 2017.

[104] M. Norambuena, J. Rodriguez, Z. Zhang, F. Wang, C. Garcia, and R. Kennel, "A very simple strategy for high-quality performance of AC machines using model predictive control," *IEEE Transactions on Power Electronics*, vol. 34, no. 1, pp. 794–800, 2018.

[105] C. Candelo-Zuluaga, J.-R. Riba, A. G. Espinosa, and P. T. Blanch, "Customized PMSM design and optimization methodology for water pumping applications," *IEEE Transactions on Energy Conversion*, vol. 37, no. 1, pp. 454–465, Mar. 2022.

[106] A. Beltran-Pulido, D. Aliprantis, I. Bilionis, A. R. Munoz, F. Leonardi, and S. M. Avery, “Uncertainty quantification and sensitivity analysis in a nonlinear finite-element model of a permanent magnet synchronous machine,” *IEEE Transactions on Energy Conversion*, vol. 35, no. 4, pp. 2152–2161, Dec. 2020.

[107] H. Xie, F. Wang, Y. He, J. Rodríguez, and R. Kennel, “Encoderless parallel predictive torque control for induction machine using a robust model reference adaptive system,” *IEEE Transactions on Energy Conversion*, vol. 37, no. 1, pp. 232–242, Mar. 2022.

[108] F. Wang, S. Li, X. Mei, W. Xie, J. Rodríguez, and R. M. Kennel, “Model-based predictive direct control strategies for electrical drives: An experimental evaluation of PTC and PCC methods,” *IEEE Transactions on Industrial Informatics*, vol. 11, no. 3, pp. 671–681, Jun. 2015.

[109] M. Korkosz, P. Bogusz, and J. Prokop, “Complex performance analysis and comparative study of very high-speed switched reluctance motors,” *IEEE Transactions on Magnetics*, vol. 55, no. 8, pp. 1–14, Aug. 2019.

[110] F. J. Marquez-Fernandez, J. H. J. Potgieter, A. G. Fraser, and M. D. McCulloch, “Experimental validation of a thermal model for high-speed switched reluctance machines for traction applications,” *IEEE Transactions on Industry Applications*, vol. 54, no. 4, pp. 3235–3244, Jul. 2018.

[111] D.-H. Lee, T. H. Pham, and J.-W. Ahn, “Design and operation characteristics of four-two pole high-speed SRM for torque ripple reduction,” *IEEE Transactions on Power Electronics*, vol. 60, no. 9, pp. 3637–3643, Sep. 2013.

[112] Y. Tang, Y. He, F. Wang, and R. Kennel, “Voltage-sourced converter fed high-speed switched reluctance motor drive system with energy feedback and near-unity power factor,” *IEEE Transactions on Industrial Electronics*, vol. 69, no. 4, pp. 3460–3470, Apr. 2022.

[113] B. Singh and A. Anand, “Power factor correction in modified sepic fed switched reluctance motor drives,” *IEEE Transactions on Industry Applications*, vol. 54, no. 5, pp. 4494–4505, 2018.

[114] M. Mohamadi, A. Rashidi, S. M. S. Nejad, and M. Ebrahimi, “A switched reluctance motor drive based on quasi z-source converter with voltage regulation and power factor correction,” *IEEE Transactions on Industrial Electronics*, vol. 65, no. 10, pp. 8330–8339, 2017.

[115] B. Singh and M. Rajesh, “Analysis, design and control of single-phase three-level power factor correction rectifier fed switched reluctance motor drive,” *IET Power Electronics*, vol. 7, no. 6, pp. 1499–1508, June 2014.

[116] J.-Y. Chai, Y.-C. Chang, and C.-M. Liaw, “On the switched-reluctance motor drive with three-phase single-switch switch-mode rectifier front-end,” *IEEE Transactions on Power Electronics*, vol. 25, no. 5, pp. 1135–1148, 2009.

[117] G. K. Andersen and F. Blaabjerg, “Current programmed control of a single-phase two-switch buck-boost power factor correction circuit,” *IEEE Transactions on Industrial Electronics*, vol. 53, no. 1, pp. 263–271, 2006.

[118] A. Anand and B. Singh, “Cuk-sepic based bridgeless pfc dual output converter fed srm drive,” in *2018 8th IEEE India International Conference on Power Electronics (IICPE)*. IEEE, 2018, pp. 1–7.

[119] A. Anan and B. Sing, “Modified dual output cuk converter-fed switched reluctance motor drive with power factor correction,” *IEEE Transactions on Power Electronics*, vol. 34, no. 1, pp. 624–635, 2018.

[120] B. Bilgin, J. W. Jiang, and A. Emadi,, “Switched reluctance motor and drive design examples,” in *Switched Reluctance Motor Drives: Fundamentals to Applications*, 1st ed. Boca Raton, FL, USA: CRC Press, ch. 16, pp. 183-195, 2018.

[121] T. J. Miller, “Drive development and test,” in *Electronic Control of Switched Reluctance Machines*, 1st ed. Oxford, UK: Newnes, ch. 9, pp. 201-226, 2001.

[122] A. Yazdani and R. Iravani, “Grid-imposed frequency VSC system: control in $\alpha\beta$-frame,” in *Voltage-Sourced Converters in Power Systems: Modeling, Control, and Applications*, 1st ed. Hoboken, NJ, USA: Wiley-IEEE Press, ch. 7, pp. 160-200, 2010.

[123] K.-J. Lee, B.-G. Park, R.-Y. Kim, and D.-S. Hyun, “Robust predictive current controller based on a disturbance estimator in a three-phase grid-connected inverter,” *IEEE Transactions on Power Electronics*, vol. 27, no. 1, pp. 276–283, Jan. 2012.

[124] A. Nikoobin and R. Haghighi, “Lyapunov-based nonlinear disturbance observer for serial n-link robot manipulators,” *Journal of Intelligent and Robotic Systems*, vol. 55, pp. 135–153, 2009.

[125] C. Xia, M. Wang, Z. Song, and T. Liu, “Robust model predictive current control of three-phase voltage source PWM rectifier with online disturbance observation,” *IEEE Transactions on Industrial Informatics*, vol. 8, no. 3, pp. 459–471, Aug. 2012.

[126] L. Yan, F. Wang, M. Dou, Z. Zhang, R. Kennel, and J. Rodriguez, “Active disturbance-rejection-based speed control in model predictive control for induction machines,” *IEEE Transactions on Industrial Electronics*, vol. 67, no. 4, pp. 2574–2584, Apr. 2020.

[127] L. Harnefors, S. E. Saarakkala, and M. Hinkkanen, “Speed control of electrical drives using classical control methods,” *IEEE Transactions on Industry Applications*, vol. 49, no. 2, pp. 889–898, Mar. 2013.

[128] W. Xu, H. Kaizheng, Y. Shijie, and X. Bin, “Simulation of three-phase voltage source PWM rectifier based on the space vector modulation,” in *2008 Chinese Control and Decision Conference*. IEEE, 2008, pp. 1881–1884.

[129] P. Verdelho and G. D. Marques, “DC voltage control and stability analysis of PWM-voltage-type reversible rectifiers,” *IEEE Transactions on Industrial Electronics*, vol. 45, no. 2, pp. 263–273, Apr. 1998.

[130] B. Chandra, M. Marta, J. A. Suul, and T. M. Undeland, “Understanding of tuning techniques of converter controllers for VSC-HVDC,” in *Nordic Workshop on Power and Industrial Electronics*, Helsinki, Finland, Jun. 2008, pp. 1–8.

[131] W. Leonhard, “Control of a separately excited DC machine,” in *Control of Electrical Drives*, 3rd ed. Broadway Frnt, NY, USA: Springer, ch. 7, pp. 77-96, 2001.